Studies on Magnetoelectric-Multiferroic Properties of Bi-substituted Co_2MnO_4

Thesis
Submitted to the University of Calicut, Kerala
in partial fulfillment of the requirements
for the award of the Degree of Doctor of Philosophy
in
PHYSICS
under the Faculty of Science

By

N.E. RAJEEVAN

Supervising Teacher

Dr. P.P. PRADYUMNAN
Department of Physics
University of Calicut, Kerala

Co-Supervisor

Dr. RAVI KUMAR
Materials Science Division
Inter University Accelerator Centre, New Delhi

DEPARTMENT OF PHYSICS
UNIVERSITY OF CALICUT
KERALA, INDIA

FEBRUARY - 2009

Dedicated to

my wife, daughters, teachers & well wishers

Department of Physics
UNIVERSITY OF CALICUT

CERTIFICATE

This is to certify that the thesis entitled, **Studies on Magnetoelectric-Multiferroic Properties of Bi-substituted Co_2MnO_4** is a bonafide research work carried out by **N. E. Rajeevan** under my supervision together with **Dr. Ravi Kumar,** Scientist F, Inter University Accelerator Centre, New Delhi in partial fulfillment of the requirements for the award of the degree of **Doctor of Philosophy** in **Physics** under the faculty of Science of University of Calicut, Kerala. It is also certified that this work has not been submitted for the award of any other degree or diploma earlier.

DR. P. P. PRADYUMNAN
Supervising Teacher
Reader
Department of Physics
University of Calicut
Kerala 673635

Calicut University
February 2009

CERTIFICATE

This is to certify that the Ph.D. thesis entitled, "Studies on magnetoelectric (multiferroic) properties of Bi-substituted Co_2MnO_4" submitted by N.E.Rajeevan in partial fulfillment of the degree of Doctor of Philosophy in Physics of University of Calicut, Kerala, is a bona fide report of the Ph.D. research work carried out by the candidate under my supervision, together with Dr.P.P.Pradyumnan, Reader, Department of Physics, University of Calicut, Kerala. This work has not been submitted in part or full for any degree or diploma of any university.

DR. RAVI KUMAR

(Co-supervisor)

Inter-University Accelerator Centre

Aruna Asaf Ali Marg, P.B. -10502

New Delhi-110067, INDIA

New Delhi
February 2009

DECLARATION

I hereby declare that this thesis entitled "**Studies on Magnetoelectric Multiferroic Properties of Bi-substituted Co_2MnO_4**" is a record of the research work carried out by me under two joint supervision and guidance of Dr. P.P. Pradyumnan, Reader, Department of Physics, University of Calicut, Kerala and Dr. Ravi Kumar, Scientist F, Materials Science Division, Inter University Accelerator Centre, New Delhi. No part of this thesis has been presented for any other degree or diploma earlier.

Calicut University, **N.E. Rajeevan**

February 2009.

Acknowledgements . . .

I am deeply indebted to my family, friends, teachers and students for whatever little I was able to achieve in the exciting field of rising science. Many academic institutions and progressive organizations gave me great support to explore a new route in scientific research. I express my sincere gratitude to my supervisors Dr. P.P. Pradyumnan, University of Calicut, Kerala and Dr. Ravi Kumar, Inter University Accelerator Centre (IUAC), New Delhi for the training, constructive criticism and constant encouragement that improved my strength in experimental research. This thesis would not have been accomplished without thesis support and guidance. Dr. P.P. Pradyumnan guided me in the right way and it was his suggestion and initiation that led me to go for collaborative research work at IUAC.

I am fortunate and privileged to have been able to work with Dr. Ravi Kumar, my Co-supervisor. Dr. Ravi Kumar is a great teacher with his deep insight and knowledge in Magnetism and Super Conductivity, an excellent experimentalist with intuitive capability that helped me to save a lot of time. Above all his humble and jovial character sufficiently soothed and strengthened me to face all the tough situations during my research carrier. I am grateful and obliged to this senior scientist of IUAC for my achievements in the field of multiferroics.

I wish to express my sincere regards to Dr. Amit Roy, Director, IUAC, New Delhi for providing me the experimental facilities for this work. My very special thanks go to Pelletron group at IUAC for the specific supports during the irradiation experiments. It gives me great pleasure to extend my gratitude to Dr. D. Kanjilal, Dr. D.K. Avasthi and Dr. Sundeep Chopra for their support. Dr. D. Kanjilal's generosity and encouraging words were the strongest reasons that compelled me to continue my research carrier at IUAC against many odds especially during the initial stages. I sincerely thank all scientists, Engineers and Administrative staff of IUAC especially Dr. Ajith Kumar, Dr. Sugathan, Dr. Kabiraj, Dr. Ambuj Tripati, Golda, Indra Sulania, Pawan Kulriya, Lakshmi, Jacob Chacko, Rajesh Kumar, S. K. Saini, M.B. Joseph, Jimson Zacharias, Suresh Babu, N. J. Jose and Ponnappan for their timely help and cooperation whenever required. Abhilash, Engineer at IUAC, spent a lot of his time and resources for me and his company gave the feeling that I was not away from my home state. I sincerely acknowledge his cooperation and affection.

Words will not suffice to express my gratitude to Dinesh Kumar Shukla, my co-researcher at IUAC without whom I doubt whether I could complete the thesis. This young dynamic researcher helped me a lot even during his busiest research activity to do experiments, data analysis and documentation; sharing his experience in experimental research. I express my gratitude to him from the core of my heart. I was fortunate to be in Dr. Ravi Kumar's research group which comprised of the entire regional

spectrum of India; from Kashmir to Kanyakumari. So it was not only just a laboratory of Physics research but a real unity in diversity that I experienced there. I also thank Dr. S.K. Sharma and Dr. Shalendra Kumar who were the senior research scholars in Dr. Ravi Kumar's group for their timely help and encouragement. I should thank my other co-researchers Feroz, Abida, Abhinav, Aditya, Ghazala, Prikshit, Yogesh and Bhagvati for their good company and support during the long hours of experiments. I was benefited much from their experimental skills and I fervently wish their names will come to be reckoned with in experimental research. I am also grateful to Dr. Y. K. Mishra, Dr. D. C. Agarwal, Dr. Rishi, and Dr. Yashpal for giving their time for fruitful discussion regarding the research work. Hardev, Apanna Babu, Rohith, JaiPrakash, and Shiv Poojan Patel were good pals at the corridors and canteen of IUAC and their interactions were much useful.

I extend my sincere gratitude to Dr. S.K. Arora and Prof. I.V. Shvets, CRANN, Trinity College, Dublin, Ireland for accurately performing the lengthy magnetization measurements described in this work. I thank Dr.P. Thakur, Prof. Chae, Prof. Choi, Prof. Brooks and S. Gautam at Pohang Light Source KIST, Korea and ESRF, France for being kind enough in performing all the synchrotron measurements presented in this thesis. I am also thankful to Dr. Ajay Gupta (Director), Dr. R.J. Chaubhury, Dr. D.M. Phase, Dr. V. Sathe, Dr. Awasti, Suresh Bharadwaj, Ram Prakash, Shelja Tiwari, Vikram Singh, Manoj Kumar and Sarath Lal ; IUC Indore for always extending their support to carry out thin film deposition, Raman scattering and DSC studies used for this thesis. I should also thank Dr. Patnaik, S.D. Kaushik, A.K. Singh, Shiv and Sreekala for rendering their support and very patiently helping during the lengthy magnetoelectric measurements done at Department of Physics, School of Physical Sciences, JNU, New Delhi. I should also express my gratitude to Dr. G. V. S. Murthy, NML, Jamshedpur, for the SEM characterization of the bulk samples. I have to acknowledge Dr. Raj Mohan, RRCAT, Indore; my former student for getting me many of the journal publications relevant to the presented thesis at the earliest.

Prof. K. M. Varier, Prof. B. R. S. Babu and Dr. Vishnumayya Bannur from Department of Physics, University of Calicut showed genuine interest on the progress of my work and it is my pleasure to thank them for their valuable suggestions. I also thank all the faculty members, library and office staff of the Department for the help they rendered during the entire course of my research study. The Zamorin's Guruvayurappan College, a cultural symbol of Kozhikode has ever remained in the forefront of academic enrichment of its faculty. The Management of the College, Prof. C.M. Sathyavathy (former principal), Prof. M. Sumathy, Principal and Prof. K. Vijayalakshmi, Head of the department of Physics deserve special mention for granting the permission to undergo the Ph. D course under the Faculty Improvement Programme. I would also like to thank my colleagues in the Department of Physics, Z.G. College for not only their keen interest and encouragement in my research work but also for

engaging my classes during leave on deputation, for the Ph. D research work. I also express my gratitude to all other teaching and non teaching staff for encouragement and support they rendered upon me. A special mention is to Dr. Pushpa Mohandas, for checking important portions of this thesis that improved the quality of presentation.

I wish also to place on record my special thanks to the University Grants Commission (UGC), New Delhi, and also to the Government of Kerala for granting teacher fellowship and sanctioning deputation without which this work would have been impossible, and KSCSTE under the state government of Kerala for their support. The opportunity to do quality research when IUAC, New Delhi, accepted my thesis proposal as collaborative research was a blessing to me. I sincerely acknowledge this leading scientific institution of our country, under UGC, for providing the experimental facilities, accommodation and TA-DA for all the visits. I would like to express special regards my co-researchers Udayanandan, Abdulla, Sethumadhavan, Jeena and Bipin at University of Calicut. I also thank KSCSTE, Trivandrum, for their support during the initial stages of the research work.

This would not be complete without extending my sincere regards to my uncle Sri. N.E. Balakrishna Marar and my cousin Sri. N.E.Manohar, my friends Sri. T. Ramachandran, Dr. Jacob Alapatt, my good neighbors Sri. Madan Menon and Adv. Sidharthan, and above all Chalappuram Raksha Samithi for their whole hearted support, especially during my lengthy home-away stay at IUAC, New Delhi, which was really a relief and confidence to my family at Calicut. I thank Sri. Ratnakaran, Balu and Vinesh, for their timely help in improving the quality of the manuscript of the thesis.

Finally I must express my regards and gratitude to my family members for letting me to fulfill my long cherished wish of doing Ph. D in Physics. My wife Sindhu, and daughters Gayathri and Haritha were in Calicut and managing themselves without any complaints during my long stay in Delhi, for the research. They always stood by me giving care, love and support, without which this thesis could not be realized. I am very much fortunate to be a brother, loved by three sisters Reetha, Rajasree and Shanthi. The affection showered to me by their family has always been a great inspiration to take up academic endeavors. My mother Santhakumari has always concerned about my health and success. But I have greatly felt the loss of my father, father in law, mother in law, and one of my aunts who taught me the first syllables of learning, during the initial stages of the Ph. D work. For reasons too personal and unaccountable to enumerate I wish to express my indebtedness to them for being my mentors who helped me to grow and advance in the academic field. This thesis is a dedication to all my family members and well wishers.

N. E. Rajeevan

Preface

Technological advancements realized through discoveries and inventions are inevitable for the modern living. Furthermore man's natural inquisitiveness has always been a driving force in the innovations and deeper understanding of a physical system. The present era is developing amongst three main technologies; Information technology, Biotechnology and Nanotechnology. For each of these technologies, information storage and access is of great importance. Its efficiency depends upon how fast and economic it can be. Most widely, access and storage of information is implemented through binary logic based FERAM (ferroelectric random access memory), MRAM (magnetic random access memory) and various other auxiliary magnetic memory systems. FERAMs are activated by electric field, where as MRAMs and auxiliary magnetic memory units are energized with magnetic field. Now scientists are trying to cross couple these two types of memories and energizing fields. The spark for this initiative can be traced way back from Maxwell's equations in electrodynamics. The formal equivalence of four differential equations of electrostatics and magnetostatics in polarizable media explained numerous similarities in the thermodynamics of ferroelectrics and ferromagnets, for example their behaviour in external fields, anomalies at a critical temperature, and domain structures. The proposal to couple the electric and magnetic fields for tuning the material property was put forward even in 1950s, but due to the lack of availability of materials exhibiting both ferroelectric (FE) and ferromagnetic (FM) the idea could not be realized. This was due to the apparently different origins of ferroelectricity and magnetism. Magnetism is related to ordering of spins of electrons in incomplete ionic shells, whereas, ferroelectricity results from relative shifts of negative and positive ions that induce surface charges, which made them mutually exclusive. Anyhow the beginning of the 21^{st} century witnessed the growth of the different series of materials, with FE and FM co-existing, and the name multiferroic was coined. Many of the multiferroics exhibited magnetoelectric coupling, where, electric polarization could be induced by magnetic field and vice versa due to the interplay between electric and magnetic properties. The search for these materials is driven by the prospect of controlling charges by applied magnetic

fields and spins by applied voltages, and using these to construct new forms of multifunctional devices. However, the effort to synthesize new multiferroic materials is being carried out by many research groups. The magnetoelectric responses of the existing multiferroics are either relatively weak or occurs at temperatures too low for practical applications. In the research work presented here, for the first time synthesization and characterization of single phase Bi-substituted Co_2MnO_4 is undertaken, as a multiferroic material. In view of the practical device applications, both the bulk targets and thin films were characterized for magnetoelectric properties. Finally, the magnetoelectric multiferroic properties were tuned by swift heavy ion (SHI) irradiation. Both Bi-substitution and SHI irradiation have improved the magnetoelectric properties of this cobalt based spinel oxide. Basically, the modifications observed in the magnetoelectric prospects can be attributed to the frustration in the magnetic ordering, which is strongly influenced by the non-magnetic Bi ion, along with the enhanced electric polarization. So this spinel oxide material, Bi-substituted Co_2MnO_4, is supposed to assure its candidature in multiferroic applications.

Bulk samples of single phase $Bi_xCo_{2-x}MnO_4$ ($0 \leq x \leq 0.3$) were synthesized using conventional solid-state reaction technique; whereas the polycrystalline thin films of the same on different substrate have been grown using Pulsed Laser Deposition (PLD) technique. The structural, electrical, electronic structure and magnetic characterizations of both the bulk and thin film samples have been performed using different techniques such as x-ray diffraction (XRD), near edge x-ray absorption fine structure (NEXAFS) spectroscopy, dielectric, dc magnetization and magnetocapacitance measurements. Further, to understand the morphological features, scanning electron microscopy (SEM) and atomic force microscopy (AFM) have been used for bulk samples and thin films respectively. X-ray magnetic circular dichroism (XMCD) has been used for confirmation of magnetic ordering in the thin films. For the modification of magnetoelectric properties, the thin films were irradiated with SHI irradiation using the 15 UD Pelletron Accelerator at IUAC, New Delhi. Chapter 1 describes the general introduction to the present thesis work and the relevant theoretical background, comprising origins of different types of

magnetism, dielectric polarization, ferroelectricity and magnetoelectric behaviour of the magnetically frustrated oxides. Structure of spinel oxides and brief introduction to magnetoelectric multiferroics is also given. Chapter 2 covers experimental details of various techniques related to structural electrical, magnetic and magnetoelectric properties of the systems studied along with a concise description of the swift heavy ion (SHI) irradiation facility utilized for this work. Chapter 3 comprises the experimental results that include the structural and electrical properties of bulk samples prepared by the solid-state reaction technique. In chapter 4, Raman spectroscopy and NEXAFS studies are included to explain structural distortion and cationic distribution in the synthesized bulk spinel oxide to describe the magnetic and magnetoelectric behaviour. Chapter 5 highlights the structural, electrical, magnetic and magnetoelectric characteristics of $Bi_xCo_{2-x}MnO_4$ thin films grown by PLD. Chapter 6 briefly describes the effect of 200 MeV, Ag^{15+} ion irradiation on electrical and magnetic behaviour of the thin films. Finally, the concluding chapter is an overview of the previous chapters and offers scope for future work.

CONTENTS

LIST OF TABLES

`LIST OF FIGURES

Chapter 1

General Introduction

This chapter presents a brief description of the different categories of magnetism, dielectric and ferroelectric properties, and cubic spinel oxides along with magnetoelectric behaviour to understand a phenomenon where both magnetism (ferromagnetism/and antiferromagnetism) and ferroelectricity co-exist known as magnetoelectric-multiferroic materials.

1.1 Introduction

The rapidly advancing science and technology front demands new generation materials to cater its expanding requirements in device fabrication. Magnetoelectric multiferroic materials, which possess both magnetic and ferroelectric ordering have found wide ranging applications in magnetoelectric sensors, magnetocapacitive devices, and electrically driven magnetic data storage and recording [1-3]. Many of the oxide materials have characteristic ferroelectric and magnetic properties, and have been investigated by the researchers during the last few years. Recently, there has been upsurge in research on multiferroic systems due to its good magnetoelectric coupling exhibited by thin films of some of the transition metal oxides [2-3]. Ferroelectric polarization and magnetization are used to encode binary information in FeRAMs (ferroelectric random access memories) and MRAMs (magnetic random access memories), respectively and the coexistence of magnetization and polarization in a multiferroic material allows the realization of four-state logic devices [3]. Magnetoelectric property originates from the coupled action of charge as well as spin nature of electrons that leads to alliance of electrical and magnetic properties in the same material. The recent advancements in the characterization techniques and materials processing techniques have expanded the realm of materials functionality. One of such new generation materials used to realize smart devices possessing multifunctional properties, is the multiferroic materials, with sufficient amount of coupling among elasticity, charge and spin degree of freedoms. Unlike the natural multiferroics having weak magnetoelectric coupling, the newly developed multiferroic composites yield giant magnetoelectric coupling response near to the room temperature, enabling them ready for wider technological applications [1, 2].

In this chapter, a short review of the origin of magnetism and definition of its subcategories such as; the phenomenon of diamagnetism, paramagnetism, ferromagnetism, antiferromagnetism and ferrimagnetism is presented. Curie-Weiss law, for the antiferromagnetic and ferro/ferrimagnetic materials are described in

detail. Dielectric and ferroelectric materials are also discussed to understand the phenomenon where both magnetism (ferro/ferrimagnetism and antiferromagnetism) and ferroelectricity coexists known as multiferroic materials. A brief description is provided about Cobalt based cubic spinel oxides on which the present thesis is based. At the end, magnetoelectric effect is discussed in terms of Dsyaloshinskii-Moriya interactions, applicable for the magnetically frustrated systems, like complex multiferroic oxides.

1.2 Magnetic materials

In general, magnetism is exhibited by all the materials. The magnetic nature of a material is determined by the magnetic moment of the electrons, atoms and ions in the material. An understanding of the mechanism of magnetic behaviour is necessary to modify the magnetic properties of the materials [4].

The magnetic moment of an atom originates mainly from two contributions: orbital angular momentum of electrons circulating the nucleus and spin magnetic moment arising from their 'spin'. The spin and orbital angular moments are coupled to yield the total magnetic moment, based on Pauli's exclusion principle, Hund's rules and different coupling schemes like spin-orbit(L-S), Russel-Saunders coupling(R-S) and total angular momentum coupling (j-j). The response of a material to an applied magnetic filed H, is given by magnetic induction B, as

$$B = \mu_0 (H + M) \text{ or simply } B = \mu H \text{ (in SI system)} \quad \text{---- (1.1)}$$

where M is the magnetization of the material, μ is the material dependent characteristic called magnetic permeability and μ_0 is the permeability of free space. μ & μ_0 are related through relative permeability, μ_r, of the medium as $\mu_r = \mu / \mu_0$ [5]. For a magnetic material of volume v, with net magnetic moment m, magnetization is obtained as,

$$M = \frac{m}{V} \quad \text{emu}/cm^3 \quad \text{---- (1.2)}$$

The magnetic susceptibility (χ) of a material is defined as

$$\chi = \frac{M}{H} \quad \text{emu}/cm^3/\text{Oe} \quad \text{---- (1.3)}$$

Magnetic materials are classified into four main categories, namely, diamagnetic, paramagnetic, ferro/ferrimagnetic and antiferromagnetic. All materials in broad sense, belongs to any one of these types of magnetism (Fig 1.1 a-f), and their behaviour depends on both the individual magnetic moments of constituent ions, atoms or molecules and on how these dipole moments interact in response to applied magnetic field.

1.2.1 Diamagnetism

Diamagnetism is the weak form of magnetism and occurs in all atoms including atoms with completely filled electron shells. It is induced by a change in the orbital motion of electrons due to an applied magnetic field. The induced magnetic moment is extremely small and is in the direction opposite to that of the applied field. However, in other type of magnetic materials diamagnetic effect is overshadowed by much stronger magnetic interactions. Owing to the weak magnetic capability, diamagnetic materials do not find wide range of applications, apart from the newly explored applications in the magnetic field-induced alignment of liquid crystals [6]. Nevertheless, the use of these materials in the scientific applications and research is of great importance, as most of the superconductors are diamagnetic.

1.2.2 Paramagnetism

Paramagnetism is characterized by a positive susceptibility and a magnetic permeability greater than μ_0. In paramagnetic materials, constituent atoms or molecules will be having individual magnetic moments, but weakly coupled to each other and thermal energy causes the random alignment of the magnetic moments. When a magnetic field is applied, a fraction of the individual moments are aligned into the field direction. χ_{para} is around 10^{-4} and μ_r is slightly greater than 1. Curie-Weiss law for the paramagnetic materials can be expressed as,

$$\chi_{para} = \frac{C}{T-\theta} \qquad \text{---- (1.4)}$$

T = θ, represents the phase transition into the spontaneously ordered state and $C = \frac{Nm^2}{3k_B}$ is the Curie constant (m is the magnitude of the individual magnetic moment). Langevin's theory and Curie-Weiss law provide the accurate description of most of

the paramagnetic materials including transition metal oxides. Also, there is a category of temperature independent paramagnetic materials like Na, Al etc, called Pauli paramagnets, which needs quantum mechanical explanations [7]. Paramagnetic materials are used in the production of very low temperature, by adiabatic demagnetization. The quick removal of an applied magnetic field, forces the spins to randomize, which necessitates the work against the remaining field at the expense of their own internal energy and get cooled.

1.2.3 Ferromagnetism

Ferromagnetic (FM) ordering occurs when all the moments contribute equally to the spontaneous magnetization. FM materials exhibit parallel alignment of magnetic moments to one another resulting in net spontaneous magnetization even in the zero magnetic field. If the magnetic moment is large enough, an applied dc magnetic field can force a nearest neighbor to align in the same direction provided the interaction is larger than the thermal energy, $k_B T$, of the atom in the lattice. The interaction between atomic magnetic moments is of two types: the dipolar interaction and exchange interaction, which represents the difference in the Coulomb energy between two electrons with spins that are parallel and antiparallel. The Curie temperature (T_C) is the temperature at which the interaction energy is greater than the thermal energy so ferromagnetism occur. Ferromagnetic materials exhibit paramagnetism above the Curie temperature [8]. χ_{ferro} is always positive and high. Classically FM materials obey the Curie-Weiss law based on molecular field. Above Curie temperature $T_C \sim \theta$, they turn into paramagnetic. Molecular field in this case is strong enough to magnetize the substance even in the absence of externally applied magnetic field. Following Langevin's theory and Curie-Weiss law, T_C can be obtained in terms of molecular field constant, γ as

$$T_C = \frac{\gamma N m^2}{3k_B} \qquad \text{---- (1.5)}$$

It is obvious that a large value for γ leads to a high T_C revealing that FM materials with strongly interacting magnetic moments require a large thermal energy to disrupt their magnetic ordering and to induce phase transition to paramagnetic

phase. Greater accuracy can be obtained in the expression for FM T_C, by coupling the quantum mechanical Brillouin function with Langevin's theory, along with appropriate choice of *J*, as

$$T_C = \frac{\gamma N g^2 J(J+1)\mu_B{}^2}{3k_B} \quad \text{---- (1.6)}$$

However, Langevin's theory and Curie-Weiss law, as applied in the above case of localized magnetic moments is found inadequate to explain the fractional magnetic moment/atom exhibited by some FM materials. Fractional magnetic moments were explained later on the basis of collective electron theory, also called band theory. Here the mechanism of inducing magnetism is identified with an exchange energy that gives rise to Hund's rule for spin allocation in atoms [7]. The exchange energy is minimized when all the electrons have the same spin. The exchange interaction in transition metals can be considered as the shift in energy of the 3*d* band for electrons with one spin direction. If the Fermi energy lies within the 3*d* band, then the band displacement will lead to more electrons of the lower energy spin direction, resulting in spontaneous magnetic moment in the ground state and external magnetic field is not required to induce magnetization.

The magnetization exhibited by a bulk FM material below T_C, is less than what would have been, if every atomic moment were aligned in the same direction. This is due to the existence of domains, which are regions where all the atomic moments align in the same direction so that within each domain the magnetization is saturated (possessing its maximum possible value). However, the magnetization vectors of different domains in the sample are not all parallel to each other, so the total magnetization is less than the value for the complete alignment of all the moments [5].

When the dc magnetic field is applied, it increases the magnetic moment of the sample. Initially, as H increases, M increases until a saturation point, M_S is reached. When H is decreased from the saturation point, M does not decrease to the same value as it possess while increasing the field. It is higher on the curve of the decreasing field, creating a hysteresis, as shown in Fig.1.1 (d). This effect occurs

because the domains that were aligned with the increasing field do not return to the original orientation when the field is lowered. When H is returned to zero, the material still has a magnetization, referred as remnant magnetization; M_r. In order to remove remnant magnetization, a field is to be applied in the opposite direction to the internal field. This field is known as coercive field (H_C) [9]. A full cycle of magnetization (M) of a material in response to an applied magnetic field (H) is called a hysteresis loop. M_S, M_r and H_C, all strongly depend on the ferromagnetic material and the condition by which they are synthesized.

1.2.4 Antiferromagnetism

Antiferromagnetic (AF) materials are characterized by having weak magnetic susceptibility of the order of paramagnetic materials. In AF materials, the interaction between magnetic moments tends to align the moments antiparallel to each other. These materials can be considered as a system consisting two interpenetrating but identical sublattices of magnetic ions, in which one set of magnetic ions is spontaneously magnetized below a critical temperature called Neel temperature, T_N and the second set is spontaneously magnetized by the same amount in the opposite direction. Consequently, AF materials have zero net magnetization. $\chi_{antiferro}$ is positive with very low value. In fact Curie-Weiss theory is found more suitable for AF materials since most of them are ionic salts with localized magnetic moments, but with a negative value for θ.

$$\chi_{antiferro} = \frac{C}{T-(-\theta)} = \frac{C}{T+\theta} \qquad \text{---- (1.7)}$$

Negative value of θ is suggestive of the negative Weiss molecular field that causes the magnetic moments to align antiparallel. Below T_N, $\chi_{antiferro}$ is found to decrease slightly with temperature. If A and B are the two interpenetrating sublattices of magnetic ions, on the assumption of the domination of nearest neighbour interactions A-B, from Curie-Weiss law it is possible to obtain magnetization of A-sublattice in terms of magnetization of B-sublattice as,

$$M_A = -\frac{\theta M_B}{T_N} \quad \text{---- (1.8)}$$

At $T_N = \theta$, $M_A = -M_B$; anyhow in practice θ is found larger than T_N. This necessitates the inclusion of next nearest neighbor interaction in addition to the A-B interactions. Also magnetic anisotropy plays an important role in AF materials which results in the preferred alignment of magnetic moments perpendicular rather than parallel to the applied magnetic field, with spins 'pinning' along the preferred axis [7]. A higher external magnetic field is required to overcome the pinning. In the case of magnetic oxides, a superexchange interaction between magnetic cations mediated through O^{2-}, leads into the overall AF alignment in which oxygen donates up-spin and down-spin electrons from its 2*p*-orbital to the 3d-orbital of magnetic ions, like Mn^{2+}, Co^{2+} ions. AF materials are now explored for spin-valve applications.

1.2.5 Ferrimagnetism

Ferrimagnets also behave like FM and exhibits spontaneous magnetization below a critical temperature, T_C, even in absence of external magnetic field. They are also related to AF materials, in that exchange coupling between adjacent magnetic ions results in antiparallel alignments of the localized moments. The overall magnetization exhibited by the ferrimagnetic materials is because of the imbalance in the magnetization of the oppositely aligned sublattices. Ferrimagnetic materials also can be better explained using Weiss molecular field theory, as most of these materials are ionic solids with largely localized electrons. Ferrimagnetic theory was developed by Neel, in continuation with the theory on AF.

However, in the case of ferrimagnetic materials, three interactions are considered as the A and B sublattices are not structurally identical. This consists of nearest neighbor A-B interactions that align the magnetic moments of the two sublattices antiparallel, and FM-next nearest neighbor A-A and B-B interactions. Here A and B represents the atoms/ions at the sites of different symmetry, like tetrahedral and octahedral sites in cubic spinel lattice.

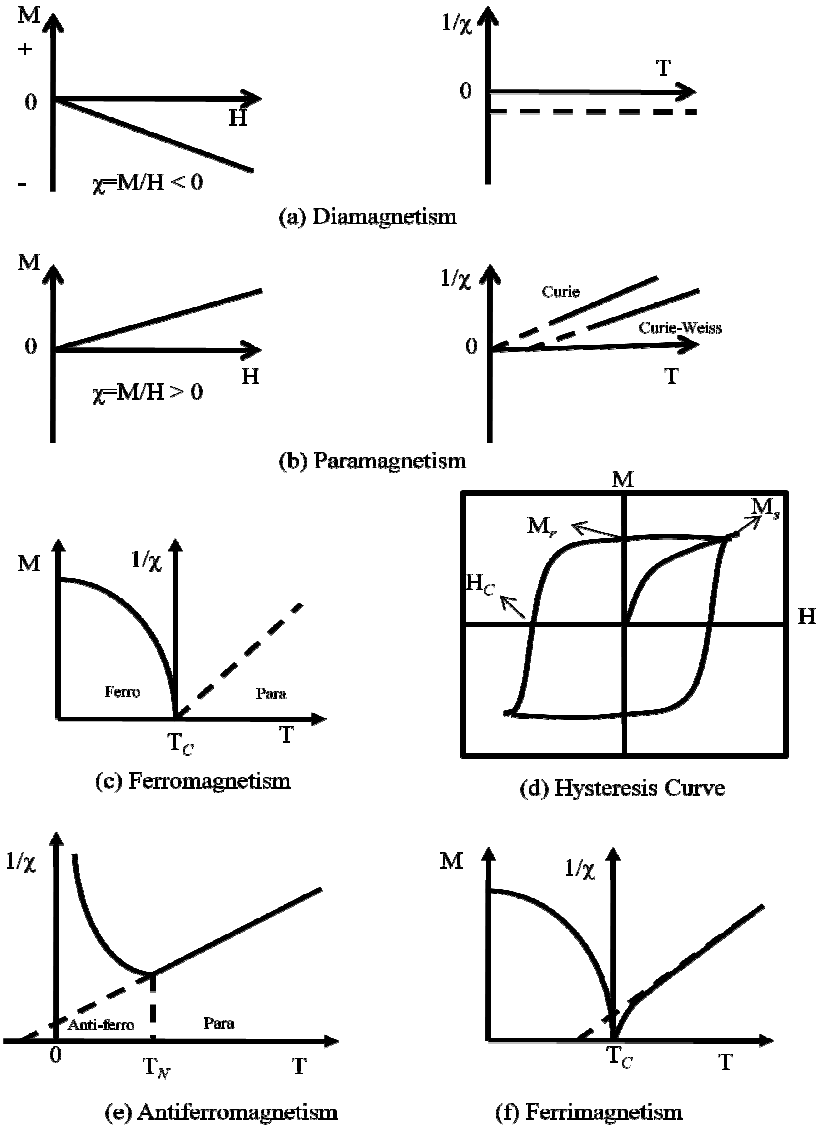

Fig. 1.1(a-f). *Behavior of different kinds of magnetism in response to magnetic field and temperature.*

Curie-Weiss law for ferrimagnetic materials up to T_C is,

$$\chi_{ferri} = \frac{C}{T + \left(\frac{C}{\chi_0}\right)} \qquad \text{---- (1.9)}$$

where χ_0 is a constant based on total molecular field arising from all the three types of interactions. The intersection of $\frac{1}{\chi_{ferri}}$ vs. T plot on temperature axis is the

ferrimagnetic Curie-Weiss constant, θ. Below T_C both A and B sublattices have spontaneous magnetizations M_A and M_B respectively, resulting into a net non-zero magnetization, M [7]. The dependence of M with T need not be monotonic, as M_A and M_B depend upon all the molecular field constants and distribution of A and B type ions. Often seen, especially in the case of many cubic spinel oxides, is the typical increase in the spontaneous magnetization with temperature, rising to a maximum and then falling to zero at T_C .

1.3 Electric polarization in solids

Electric polarization refers to a phenomenon of the relative displacement of the negative and positive charges of atoms or molecules, the orientation of existing dipoles toward the direction of the field, or the separation of mobile charge carriers at the interfaces of impurities or other defect boundaries, caused by an external electric field. Electric polarization can also be thought of as charge redistribution in a material caused by an external electric field. Charge redistribution and the energy loss involved in the redistribution process require energy [10]. Polarization process is performed at the expense of the potential energy released because the total potential energy of the system in an electric field is smaller after the electric polarization than before it.

1.3.1 Dielectric material

One of the important electrical properties of dielectric materials is permittivity (or relative permittivity, which is generally referred to as the dielectric constant). For most materials, the dielectric constant is independent of the electric field strength for fields below a certain critical field. From the basics of electrostatics and Gauss's law, one can determine the dielectric constant of a material considering the geometry of a parallel plate capacitor as,

$$\varepsilon_r \text{ or } \varepsilon' = \frac{\sigma_s}{\varepsilon_0 E} \qquad \text{---- (1.10)}$$

where σ_s is the surface charge density on the capacitor plates and ε_0 is the permittivity of free space or vacuum. The dielectric constant depends strongly on the

frequency of the alternating electric field or the rate of the change of the time-varying field. It depends on the chemical structure and the imperfections (defects) of the material, as well as on other physical parameters including temperature, pressure, etc. Polarization in a dielectric material is given by,

$$P = \alpha E \quad \text{---- (1.11)}$$

where α is the polarizability. Dielectric properties is also expressed in terms of relative permittivity, $\varepsilon' = \varepsilon/\varepsilon_0 = 1 + \chi$, where $\chi = \frac{N\alpha}{\varepsilon_0}$, is the electrical susceptibility. The polarization due to the elastic displacement of electron clouds of atoms and molecules require a very little time, while the polarization involving the orientation of permanent dipoles or the migration of electrons or ions, requires a much longer time to perform. All types of polarization encounter inertia that counter the change and, involve some dielectric loss.

1.3.2 Complex permittivity

When a time-varying electric field is applied across a parallel-plate capacitor with the plate area of one unit and a separation of *d* between the plates, then the total current is given by,

$$J_T = J + \frac{dD}{dt} = J + \varepsilon^* \frac{dE}{dt} \quad \text{---- (1.12)}$$

where J is the conduction current and ε^* is the complex permittivity, which is introduced to allow for dielectric losses due to the friction accompanying polarization and orientation of electric dipoles. This may be written as,

$$\varepsilon^* = (\varepsilon' + j\varepsilon'')\,\varepsilon_0 \quad \text{---- (1.13)}$$

in which ε' is called the dielectric constant and ε'' the dielectric loss. The sinusoidal monochromatic ac field applied be represented as,

$$E = E_m \exp(j\omega t) \quad \text{---- (1.14)}$$

Then from eqn.1.12 and 1.13,

$$J_T = (\sigma + \omega\varepsilon'')E + j\omega\varepsilon' E \quad \text{---- (1.15)}$$

where σ is the electrical conductivity of the material (see the equivalent circuit depicting the response of the parallel plate capacitor shown in Fig.1.2). The first term on the RHS is a loss component due to the inelastic scattering of conducting charge carriers during their migration, which is present at all frequencies, including ω = 0 (dc fields); the second term is also a loss component due to the friction in the polarization processes, which disappears when ω = 0 and increases with ω; and the third term is a lossless component which is, in fact, the displacement current [10]. In most cases the contribution of the first term can be neglected. Then loss factor,

$$\tan \delta = \varepsilon'' / \varepsilon' \qquad \text{---- (1.16)}$$

Generally, $\varepsilon'' / \varepsilon'$ 1, $\tan \delta$ δ, called as loss angle.

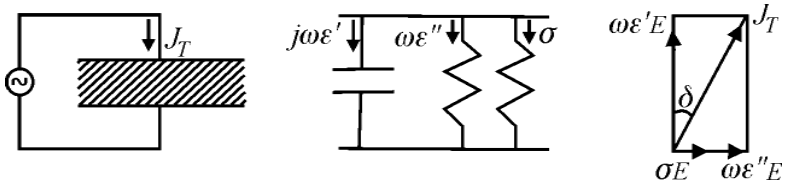

Fig. 1.2. *The response of a parallel plate capacitor with unit plate area and its equivalent circuit under an alternating electric field.*

1.3.3 Real dielectric material

In reality, there is no perfect dielectric material. All real dielectric materials contain some mobile charge carriers. If such a real material has the total charge carriers *n* per unit volume, each carrying a charge *q* and having an average mobility *v*, then the conductivity of this material σ is *nqv*. For dielectric material of low conductivity, an equivalent circuit (Fig.1.3) can be used to describe the response of the material under the applied field between the two charged metal plates [10]. R_c is the leakage resistance of the material, $C =$ ε′/d is the capacitance per unit area, R_d is the resistance per unit area. Both ε′ and R_d varies with time, and are derived directly from the polarization process.

Thus, at $t = 0$, just after the insertion of the material into the vacuum space, $\varepsilon' \to \varepsilon_\infty$ and $R_d \to \infty$, and at $t = t_s$, $\varepsilon' \to \varepsilon_s$ and $R_d \to \infty$. The value of the resistance R_d is finite only during the period $0 < t < t_s$.

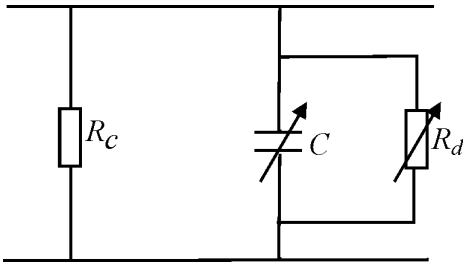

Fig.1.3. *The equivalent circuit of a real dielectric material.*

But the leakage current through the leakage resistance R_c will continue to drain the charge from plate A to plate B, making σ_s decay with time, as

$$\sigma_s(t) = \sigma_s(0) \qquad \text{---- (1.17)}$$

where $= \rho\varepsilon_s$ is the dielectric relaxation time and ρ is the resistivity of the material. is the time required for the originally induced charge to decay 36.7% of its original value. can be very large, for materials with a very high resistivity (i.e., low conductivity).

1.3.4 Various types of polarization in a dielectric material

The various mechanisms of electric polarization in a dielectric medium can be categorized as, 1) Electronic polarization, 2) Atomic or ionic polarization, 3) Dipolar polarization, 4) Spontaneous polarization and 5) Interface or space charge polarization. As each type of polarization requires time to perform, the degree of the overall polarization depends on the time variation of the electric field [10].

Electronic polarization (optical polarization): The electric field causes deformation or translation of the originally symmetrical distribution of the electron clouds of atoms or molecules. This is essentially the displacement of the outer electron clouds with respect to the inner positive atomic cores.

Atomic or ionic polarization: The electric field causes the atoms or ions of a polyatomic molecule to be displaced relative to each other. This is essentially the distortion of the normal lattice vibration, and is also referred to as vibrational polarization.

Orientational polarization: This polarization occurs only in materials consisting of molecules or particles with a permanent dipole moment. The electric field causes the reorientation of the dipoles toward the direction of the field.

Space charge polarization: At higher fields, carrier injection becomes important. For materials consisting of a high concentration of charge carriers, polarization due to the migration of charge carriers to form space charges at interfaces or grain boundaries becomes important. This type of polarization is called space charge polarization.

Electronic polarization is always present in atoms or molecules in all kinds of materials; ionic polarization is present only in materials made of two or more different kinds of atoms that form ions due to the sharing of the valence electrons of one or more atoms with the others. For both electronic and ionic polarizations, the dipole moments are induced by electric fields, so they are classified as induced dipole moments. In short, both electronic and ionic polarizations are due to the translation (or deformation) of the valence electron clouds from their original thermal equilibrium state to a new equilibrium state. These types of polarization are only slightly dependent on temperature because they are intramolecular phenomena. However, orientational polarization occurs only in the materials composed of molecules with an asymmetrical structure in which the centroid of the negative charge (mainly electrons) and that of the positive charge (mainly nuclei) are not coincident, so they possess permanent dipole moments in the absence of external fields. The directions of these permanent dipole moments are randomly distributed in the material. An electric field will cause them to reorient toward the direction of the field, resulting in orientational polarization. The net polarization will return to zero after the removal of the external field because thermal agitation tends to randomize the alignment. This is why polarization decreases with increasing temperature. The total polarizability of material a comprises four components [10],

$$\alpha = \alpha_e + \alpha_i + \alpha_o + \alpha_d \qquad \text{---- (1.18)}$$

where α_e , α_i , α_o and α_d are the polarizabilities due to electronic, atomic, orientational, and space charge polarizations, respectively. For ferroelectric

materials, there is also a component, called spontaneous polarization, under certain conditions.

The two possible ways in which space charge polarization manifested are hopping polarization and interfacial polarization. In a dielectric material, localized charges (ions and vacancies, or electrons and holes) can hop from one site to the neighboring site, creating so-called hopping polarization [11]. These charges are capable of moving freely from one site to another site for a short time, then becoming trapped in localized states and spending most of their time there. Occasionally, these charges make a jump surmounting a potential barrier to other sites. In fact, the movement of ions or vacancies in ionic crystals and the movement of electrons and holes in glasses and amorphous semiconductors are essentially due to the hopping process [12]. Interfacial polarization is produced by the separation of mobile positively and negatively charged particles under an applied field, which form positive and negative space charges in the bulk of the material or at the interfaces between different materials. These space charges, in turn, modify the field distribution. This is relevant for composite dielectric like a specimen comprising layers of different materials.

1.3.5 Maxwell-Wagner interfacial polarization

To measure the dielectric constant of a complex oxide system, a capacitor structure has to be made so that an ac electric field can be applied to it. The response to the electric field will contain at least one capacitive (dielectric) term and one resistive (leakage) term. Since the work functions of electrode and dielectric material are rarely identical, band bending may occur near the electrode-dielectric interfaces, causing charge injection from the electrode into the dielectric or vice versa (charge depletion). In either case, the outcome would be the formation of a layer near the electrode interface with a different density of charge carriers, and hence different resistivity than that of the core. If the dielectric is not a very good insulator, this can cause the electric field to be mostly dropped in the charge-depleted interfacial area rather than in the core of the material, yielding artificially high apparent dielectric constants. This effect has been documented in several oxide

materials, including manganites [13-15] and may happen not only at dielectric-electrode interfaces but also at grain boundaries in ceramics [16] and inter-slab interfaces in superlattices [17]. The dielectric property of this kind of heterogeneous materials can be described by the Maxwell-Wagner (M-W) capacitor model. This effectively consists of two leaky capacitors in series (Fig. 1.4). The dielectric constant (the real part of complex impedance) of such a system under an ac field can be obtained as [17, 18],

$$\varepsilon'(\omega) = \frac{1}{C_0(R_i + R_b)} \frac{\tau_i + \tau_b - \tau + \omega^2 \tau_i \tau_b \tau}{1 + \omega^2 \tau^2} \qquad \text{---- (1.19)}$$

where subscripts *i* and *b* refer to the interfacial-like and bulk-like layers, respectively, R = resistance, C = capacitance, ω = ac frequency, $\tau_i = C_i R_i$, $\tau_b = C_b R_b$, $\tau = (\tau_i R_b + \tau_b R_i) / (R_i + R_b)$, $C_0 = \varepsilon_0 A / t$, A = area of the capacitor, and t = thickness. In this equation the absolute thickness is actually irrelevant, what counts instead is the thickness ratio t_i / t_b. The frequency dependence can be interpreted as follows. At high frequencies charge carriers do not have time to respond to the field, so that the measured capacitance is simply that of two (insulating) capacitors in series. At low frequencies, on the other hand, the charge carriers in the low resistivity layer do respond, so that most of the field is dropped across the layers with bigger resistivity, and thus the apparent decrease in dielectric thickness results in an increased capacitance. This suggests that intrinsic capacitance should be measurable at frequencies faster than the conductivity cutoff (*RC* time constant). It is also worth noticing that the capacitance is maximal around the 1/*RC* frequency.

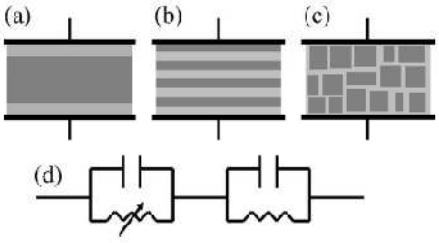

Fig. 1.4. *Capacitor systems with Maxwell-Wagner behavior: (a) homogeneous material with charge-depleted interfacial layers, (b) superlattice, and (c) clustered material or fine-grained ceramic with depleted grain boundaries and modeled by two leaky capacitors in series (d).*

Since resistance changes with temperature, capacitance will show a peak when 1/*RC* coincides with the measurement frequency. The temperature and frequency dependent dielectric behavior can also mimic that of relaxors, but in fact, it is only a resistive artifact [17, 19].

1.3.6 Dielectric relaxation

All types of polarization may be grouped into two major regimes: the resonance regime and the relaxation regime. Polarizations associated with vibrations of electrons (i.e., electronic or optical polarization) or with vibrations of atoms or ions (i.e., atomic or ionic polarization) belong to the resonance regime because in the polarization a resonance will occur when the frequency of the excitation field is close to the natural frequency of the vibration or oscillation of system. Polarizations involving the movements of charges either by orientation (i.e., orientational polarization) or through the migration of charge carriers (i.e., hopping or space charge polarization) belong to the relaxation regime because during the polarization or depolarization processes, a relaxation phenomenon occurs due to the time required for the charge carriers to overcome the inertia arising from the surrounding medium in order to proceed in their movement. The variation of ε', ε'' and $tan\delta$ with frequency shown in the Fig.1.5 illustrates schematically the typical dispersion behavior for polarizations in the relaxation regime [10], for cases with negligible contribution of σ due to carrier migration.

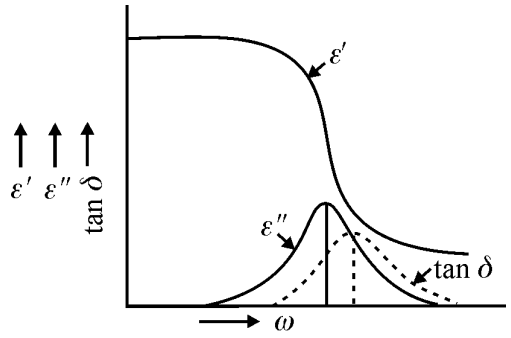

Fig. 1.5. *ε', ε'' and tan δ as functions of frequency (ω).*

It is likely that not all dipoles in a solid are situated in the same environment, so some are more free to move than others. Even in a single crystal, dipoles may find

certain orientations more favorable than others and certain transitions between orientations easier than others. The variation of such local transition probabilities reflects the variation of the activation energy for dipole orientation and hence owes different relaxation times (τ). In a different way C.G.Koops [20] proposed a phenomenological theory to explain the observed dispersion behaviour of Zn-Ni ferrite system, where electrodes were not influential on dielectric properties. He assumed a dielectric solid to consist well conducting grains (1) separated by poorly conducting layers (2), while the current is assumed to flow along the parallel alignments of the grains, as in Fig.1.6 [20].

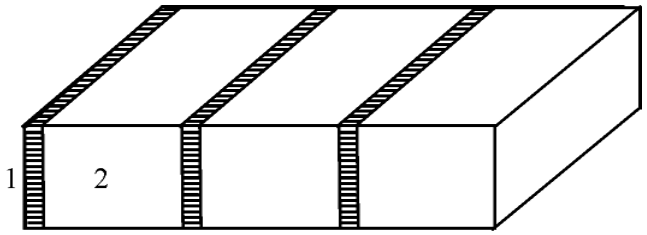

Fig.1.6. *Grain structured conductor. Poorly conducting layers separate the grains.*

He calculated the theoretical frequency dispersion of ε and tan δ (see Fig.1.5), by taking proper values to the thicknesses, resistivities and dielectric constants of conducting and non conducting regions, and assuming solid consisting only two relaxation times. A good agreement between theoretical and experimental dispersion were observed and the deviation hence means more than two relaxation time constants and even a distribution of relaxation time constants.

1.4 Ferroelectric materials

A ferroelectric material is normally in single crystalline or polycrystalline form and possesses a reversible spontaneous polarization over a certain temperature range. There is a critical temperature, called Curie temperature, which marks the transition from the ordered to the disordered phase. At this temperature, the dielectric constant may reach values three to four orders of magnitude higher than in the disordered phase. The order–disorder phase transition involves the displacement of atoms so that crystals or crystallites exhibiting ferroelectric phenomena must be noncentrosymmetric. This implies that a phase transition will induce a mechanical

strain, tending to change not only the volume and the shape of the material body, but also the optical refractive index. Thus, ferroelectric materials exhibit not only ferroelectric phenomena, but also piezoelectric, pyroelectric, and electro-optic effects, which can be used for many technological applications. In general, ferroelectric materials also have electrically induced polarizations, but these are negligibly small compared to spontaneous polarization. Like ferromagnetics, ferroelectrics exhibit a spontaneous electric polarization below the Curie temperature, a hysteresis loop, and an associated mechanical strain. However, ferroelectrics differ from ferromagnetic in their fundamental mechanisms and also in some of their applications.

Ferroelectric behavior is delimited by a transition point called the Curie temperature, T_c. At temperatures above T_c, the crystal is no longer ferroelectric and exhibits normal dielectric behavior. Ferroelectric materials usually, but not always, exist in a nonpolar state at temperatures above T_c, and have anomalously high dielectric constants, especially near the Curie temperature. Typical dielectric constant–temperature characteristic is shown in Fig.1.7 [10]. The dielectric constant increases very rapidly to a very high peak value at T_c. At $T > Tc$, anomalous behavior follows closely the Curie–Weiss relation,

$$\varepsilon' = \frac{C}{T - T_c} \qquad \text{---- (1.20)}$$

where C is known as the Curie constant. At the transition points, there are anomalies not only in the dielectric constant and polarization, but also in piezoelectric and elastic constants and specific heat, because of the change in crystal structure. Ferroelectrics are characterized with reversible spontaneous polarization. The word *reversible* refers to the direction of the spontaneous polarization that can be reversed by an applied field in opposite direction. The spontaneous polarization P_s usually increases rapidly on crossing the transition point and then gradually reaches a saturation value at lower temperatures. The most prominent features of ferroelectric properties are hysteresis and nonlinearity in the relation between the polarization P and the applied electric field E.

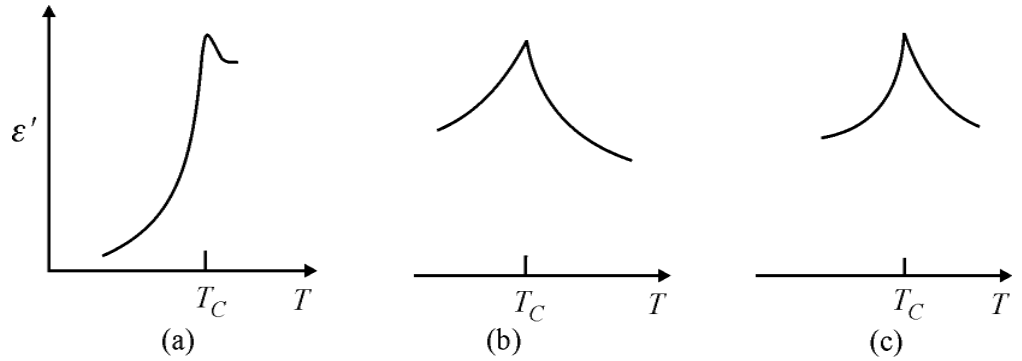

Fig. 1.7. *Schematic illustration of the variation of the dielectric constant ε´ with temperature for three typical ferroelectric crystals: (a) Barrium titanate-$BaTiO_3$ with T_c = 120°C, (b) KDP-KH_2PO_4 with T_c = -150°C, and (c) Rochelle Salt-$KNaC_4H_4O_6$-$4H_2O$ with T_c = 24°C.*

A typical hysteresis loop is shown in Fig. 1.8 [10]. When the field is small, the polarization increases linearly with the field. This is mainly due to field-induced polarization; because the field is not large enough to cause orientation of the domains (portion *OA*). At fields higher than the low-field range, polarization increases nonlinearly with increasing field, because all domains start to orient toward the direction of the field (portion *AB*). At high fields, polarization will reach a state of saturation corresponding to portion *BC*, in which most domains are aligned toward the direction of the poling field.

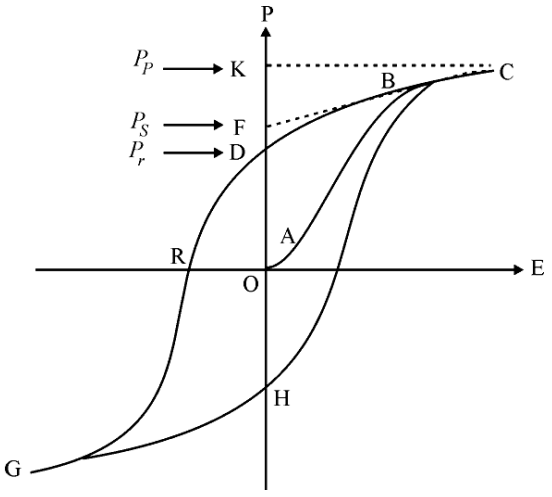

Fig.1.8. *Schematic diagram of a typical ferroelectric hysteresis loop.*

Now, if the field is gradually decreased to zero, the polarization will decrease, following the path *CBD*. By extrapolating the linear portion *CB* to the polarization axis (or zero-field axis) at *F*, *OF* represents the spontaneous polarization P_s and *OD* represents the remnant polarization P_r. The linear increase in polarization from P_s to P_p is due to the normal field-induced dielectric polarization. P_r is smaller than P_s because when the field is reduced to zero, some domains may return to their original positions due to the strain situation, thus reducing these domains' contribution to the net polarization. For most ferroelectric materials, the component due to the normal field-induced dielectric polarization is very small compared to the spontaneous polarization; therefore, for most applications, this component can be ignored. The field required to bring the polarization to zero is called the coercive field E_c (portion *OR* on zero polarization axis). E_c depends not only on temperature, but also on the measuring frequency and the waveform of the applied field. When the field in the opposite direction decreases to zero, the polarization is reversed, indicating that domains have already been formed before poling and that the motion of the domain walls results in the change of direction of polarization. The hysteresis arises from the energy needed to reverse the metastable dipoles during each cycle of the applied field. The area of the loop represents the energy dissipated inside the specimen as heat during each cycle (hysteresis loop is measured with AC fields at low frequencies, 60 Hz or lower, to avoid heating the specimen).

In general, ferroelectricity is harder to demonstrate in polycrystalline materials composed of crystallites, such as ceramics, than in a single crystal because of the random orientation of crystallites. This is why in some single crystals the polarization reverses quite abruptly to form a square loop while in most ceramics the loop is rounded because of the more sluggish reversal, which is due partly to the axes of the unit cells in the randomized arrangement of the non uniform crystallites [10]. It is quite natural that the hysteresis loop becomes gradually diminished at $T > T_C$, eventually degenerating to a straight line at T much larger than T_C, when the ferroelectric behavior disappears completely. However, some ferroelectric materials can be driven from the paraelectric state to a ferroelectric state at $T > T_C$ by applying a large electric field.

1.4.1 Capacitance-Voltage (C-V) loop:

C-V loop has been used for many of the multiferroic material [21-27], to demonstrate the ferroelectric nature. Fu *et al* [26] has modeled dielectric non-linearity of the ferroelectric materials using C-V loop and has been verified with the data of barium strontium titanate thin films. A typical butterfly C-V loop shown in Fig. 1.9 [27] is a signature of ferroelectricity. C-V measurement can be performed with the help of a precision LCR meter.

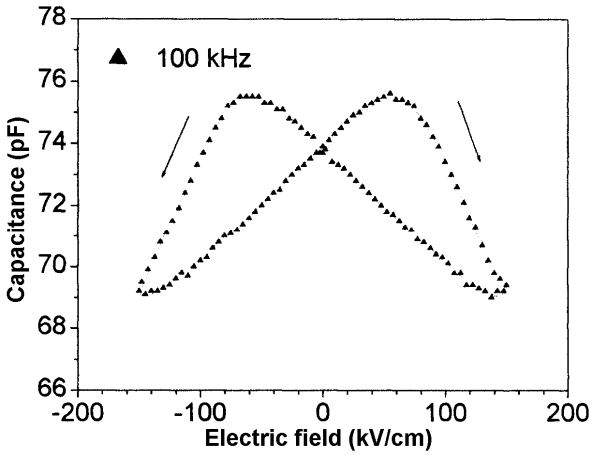

Fig. 1.9. *Butterfly shaped Capacitance-Voltage (C-V) loop exhibited by* $Bi_{3.25}La_{0.75}Ti_3O_{12}$ *thin films.*

1.4.2 Effect of Bi-lone pair on ferroelectricity

The "lone pair" in Bi-based oxides is believed to form due to the hybridization of 6*s* and 6*p* atomic orbitals with $6s^2$ electrons filling one of the resulting orbitals in Bi or Pb in their oxides. The lone pair is then considered to be chemically inactive, not taking part in the formation of bonds but sterically active. The hybridization causes the lone pair to lose its spherical symmetry and is projected out on one side of the cation, resulting in an asymmetry of the metal coordination and distorted crystal structures. Thus the stereochemically active lone-pair electrons results into the displacements of the Bi atoms from the centrosymmetric to the noncentrosymmetric structure and leads to polarization, consequently ferroelectricity [28].

1.5 Cobalt based cubic spinel oxides

Cobalt based cubic spinel oxides are mixed valent metal oxides with chemical species contained in the general formula AB_2O_4, where A and B represent divalent and trivalent cations respectively. They exhibit a variety of interesting functional properties depending on the species and stoichiometry of cations occupying the two cation sites, A and B, such as multiferroic properties, thermoelectric property, Colossal magnetoresistivity (CMR), superconductivity, spintronics, magnetic recording, etc [29-35]. These complex oxides mainly crystallize into normal spinel with a space group O_h^7-$Fd\bar{3}m$ [36] and each unit cell contains 8[AB_2O_4] formula units and therefore 32 O^{2-} ions. This close packing contains 64 tetrahedral interstices and 32 octahedral interstices coordinated with O^{2-} ions (Fig. 1.10). The charge distribution of the normal spinel is represented by $[A^{2+}]_{8a}[B_2{}^{3+}]_{16d}[O_4{}^{2-}]_{32e}$, in which Wyckoff positions 8*a* denote the tetrahedral sites and 16*d* the octahedral sites surrounded by O^{2-}ions at 32*e* sites. Empty interstitial space is comprised of 16 octahedral sites (16*c*) and 56 tetrahedral sites (8*b* and 48*f*). The substituted trivalent metal ion occupies the octahedral sites while cobalt ions are distributed over both octahedral (diamagnetic Co^{3+} ions in low spin t_{2g}^6 state) and tetrahedral sites (magnetic Co^{2+} ions in high spin $e_g^4 t_{2g}^3$ state). All spinel-like structures are characterized by an oxygen parameter *u* having a value around 0.375. For $u = 0.375$, the arrangement of O^{2-} ions is exactly a cubic close packing (FCC structure).

In actual spinel lattice, there is deviation from the ideal pattern, with $u > 0.375$, resulting in a deformation of oxygen tetrahedrons and octahedrons [36, 37]. $CoCr_2O_4$, $CoMn_2O_4$, Co_2MnO_4, $CoFe_2O_4$, $NiCo_2O_4$, $CuMnCoO_4$ and $InFeCoO_4$ are some of the important cobalt based ferrimagnetic spinel oxides, investigated by many of the research groups[29-35] owing to their variety of interesting functional properties.

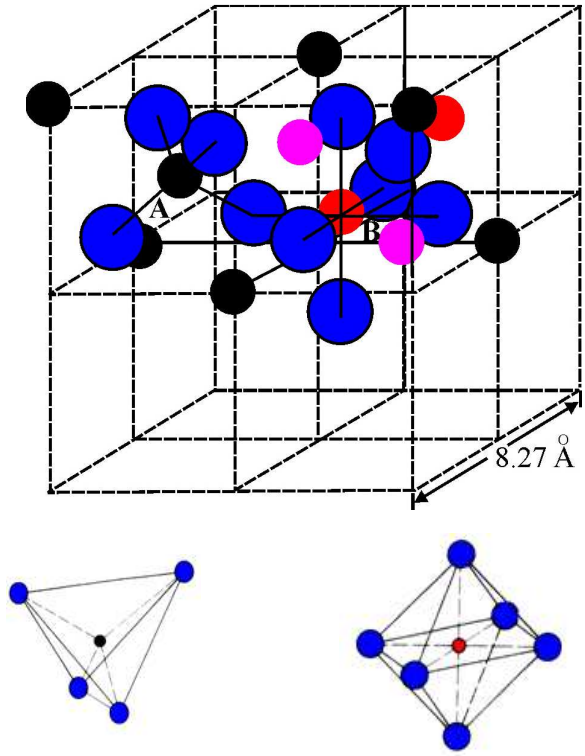

Tetrahedral A-site **Octahedral B-site**

Fig. 1.10. *Crystal Structure of a cubic spinel.*

1.5.1 Magnetic interactions in spinel oxides

In order to understand the origin and nature of the magnetic behaviour associated with spinel oxides, mainly three types of magnetic interactions are considered between the transition metal ions at A- and B-sites through the intermediate oxygen ions (O^{2-}) i.e., superexchange interaction. These are A-A, A-B, and B-B interactions. Since cation-cation distances are large, direct interactions are negligible. It has been verified experimentally that these interaction energies are negative favouring antiferromagnetism when the *d* orbital of the metal ions are half filled or more than half filled, while a positive interaction accompanied by ferrimagnetism results when *d* orbital is less than half filled.

The magnitude of the interaction energy between two magnetic ions M^I and M^{II} depends upon the following,

(a) The distances of these ions to the oxygen ions through which interaction occurs.

(b) The angle M^I-O-M^{II} represented by θ as shown in Fig. 1.11. For θ = 180°, where the interatomic distance is shortest, the exchange energy is found to be highest. The energy decreases rapidly with increasing the distance and decreasing the angle towards 90°.

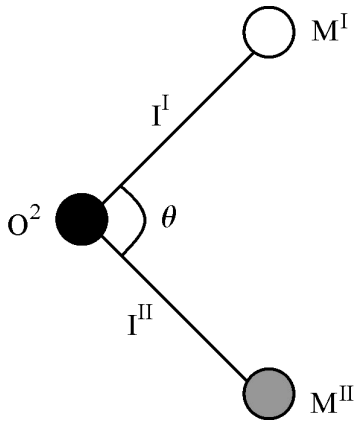

Fig. 1.11. *M^I-O-M^{II} angles in spinel oxides.*

In spinel structure, the A-O-B angle is in the neighbourhood of 180°, while A-O-A and B-O-B angles are closer to 90°. Thus, with A-O-B interaction predominating, the spins of the A-and B-site ions will be oppositely magnetized with a resultant magnetic moment equal to the difference between those of A-and B-site ions. Gorter [38] gave various possible configurations of the ion pair in spinel oxides with favorable distances and angles for an effective magnetic interaction. In general, it is found that the magnitude of A-B, B-B and A-A interactions are negative with |A-B|>>|B-B|>>|A-A|.

1.6 Magnetoelectric multiferroics

Multiferroic materials are simultaneously ferromagnetic and ferroelectric, often ferroelastic too. In magnetoelectric material, electric polarization is induced by

the application of an external magnetic or vice-versa, providing an additional degree of freedom for the design of new devices. Pierre Curie first postulated this effect at the end of the nineteenth century. Following the theoretical prediction by Dzyaloshinskii [39] in 1959 and the first experimental observation by Astrov [40] in 1960, the magnetoelectric effect was studied intensively in the 1960s and 1970s [41] and has attracted continuing interest for more than four decades. In recent years, however, the term magnetoelectric-multiferroics has become more popular, this term comprises not only ferro-electromagnets but also all the materials in which any two of the following ferroic orders co-exist.

i. Ferroelectric materials possessing a spontaneous polarization which can be switched hysteretically by an applied electric field.

ii. Antiferroelectric materials that possess ordered dipole moments which cancel each other completely within each crystallographic unit cell.

iii. Ferromagnetic materials possessing a spontaneous magnetization which can be switched hysteretically by an applied magnetic field.

iv. Antiferromagnetic materials having ordered magnetic moments that cancel each other completely within each magnetic unit cell.

v. Ferrimagnetic materials in which the magnetic moment cancellation is incomplete in such a way that they possess net magnetization that can be switched hysteretically by an applied magnetic field.

vi. Ferroelastic materials that exhibits a spontaneous deformation that is stable and can be switched hysteretically by an applied stress.

Several multiferroics have been identified to date. Examples are some boracites; $Ni_3B_7O_{13}I$, $Co_3B_7O_{13}I$, etc [42], some fluorides; $BaMF_4$ (M = Mn, Fe, Co, and Ni) [43, 44], magnetite Fe_3O_4 [45], hexagonal manganites;$YMnO_3$, $HoMnO_3$, etc. [46-47], perovskites ABO_3 having a Bi or Pb ion at the A site and transition metal at the B site; $BiFeO_3$ [48], and $BiMnO_3$ [49], $CdCr_2S_4$ [50] and hexagonal ferrites; $LuFe_2O_4$ [51]. Even though, the magnetoelectric effect and magnetoelectric multiferroics have been studied for more than four decades, still in most of the multiferroics, the temperature scale for ferroelectric order is much larger than for magnetic order (Table 1.1), and the origins of these orders are quite different and do

not strongly interfere with each other [52, 53]. Fig.1.12 schematically represents a relationship between multiferroic and magnetoelectric materials and Table 1.1 depicts important multiferroic oxides and their ferroelectric and magnetic transition temperatures.

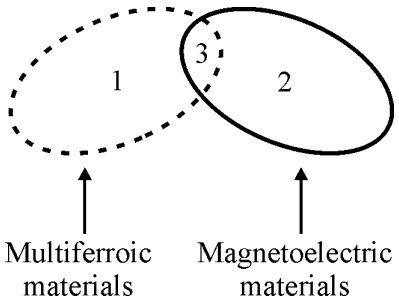

Fig.1.12. *Relationship between multiferroic and linear magnetoelectric materials. Multiferroic materials (area 1) and linear magnetoelectric materials (area2) may overlap giving rise to an enhancement of the interplay between dielectric and magnetic properties (area 3).*

Table 1.1. *Multiferroic materials and transition temperatures.*

Material	Ferroelectric transition(T_{C-FE})	Antiferromagnetic transition(T_N)	Ferro/ferrimagnetic transition(T_{C-FM})
$BiFeO_3$ [48]	1103K	647K	-
$BiMnO_3$ [54]	750K	-	105K
$YMnO_3$ [55]	950K	80K	-
$YCrO_3$ [26]	440K	140K	-
$ErMnO_3$ [56]	830K	80K	-
$TbMnO_3$ [57]	28K	43K	-
$DyMnO_3$ [58]	19K	39K	-
$LuMnO_3$ [59]	900K	90K	-
$HoMnO_3$ [60]	875K	72K	
$GaFeO_3$ [61]	220K	-	225K
$BiMn_2O_5$ [62]	35K	39K	-
$GdMn_2O_5$ [63]	30K	40K	-
$TbMn_2O_5$ [64]	39K	42K	-
$CoCr_2O_4$ [29]	26K		93K
*$Bi_{0.1}Co_{1.9}MnO_4$[65]	366K	-	184K

**From the series investigated in this thesis.*

Most ferroelectrics are transition metal oxides, in which transition ions have empty *d* shells. These positively charged ions tend to form 'molecules' with one or several of the neighbouring negative oxygen ions. This collective shift of cations and anions inside a periodic crystal induces bulk electric polarization. The mechanism of the covalent bonding (electronic pairing) in such molecules is the virtual hopping of electrons from the filled oxygen shell to the empty *d* shell of a transition metal ion. Magnetism, on the contrary, requires transition metal ions with partially filled *d* shells, as the spins of electrons occupying completely filled shells add to zero and do not participate in magnetic ordering. The exchange interaction between uncompensated spins of different ions, giving rise to long range magnetic ordering, also results from the virtual hopping of electrons between the ions. This reveals a kind of similarity in the nature of origin of the two mechanisms, but obviously, at the experimental level one cannot simply do away with the difference in filling of the *d* shells required for ferroelectricity and magnetism, which makes these two ordered states mutually exclusive. In the normal ferroelectrics materials, structural instability towards the polar state, associated with the electronic pairing, is the main driving force of the transition. On the other hand, polarization is only a part of a more complex lattice distortion related to magnetic ordering, for magnetoelectric systems [66].

The field of magnetoelectric multiferroics gained interest in recent years after the observation of gigantic ferroelectric polarization in one of the conventional multiferroics, $BiFeO_3$ [67], and the discovery of a new class of multiferroics showing a large magnetoelectric effect. A large magnetoelectric effect (a sudden change of electric polarization by the application of magnetic fields) has been observed at the onset field in $BiFeO_3$. It was established recently that, in a class of materials known as 'frustrated magnets', like the perovskites $RMnO_3$, RMn_2O_5 (R: rare earths), $Ni_3V_2O_8$, $CuFeO_2$, spinel $CoCr_2O_4$, $MnWO_4$, and hexagonal ferrite $(Ba,Sr)_2Zn_2Fe_{12}O_{22}$ [29, 68-74], the control of electric properties by magnetic fields can be easily achieved. However it is to be mentioned that uniqueness of these materials is not the strength of the magnetoelectric coupling or high magnitude of

electric polarization (in fact electric polarization is two to three orders of magnitude smaller than in typical ferroelectrics), rather, it is the high sensitivity of the dielectric properties achievable by the characteristic complex spin structures of frustrated magnets in an applied magnetic field [70, 75–81]. These studies indicate the emergence of a new class of ferroelectrics with magnetically controlled ferroelectricity, which is quite different from known ferroelectrics. This magnetically induced ferroelectricity leads to strong magnetoelectric coupling and consequently large magnetoelectric effects. Such materials, in which electric polarization can be tuned by magnetic ordering, are the best candidates for useful multiferroic device applications.

From the fundamentals of electricity and magnetism, it is known that the electric polarization **P** and electric field **E** change sign on the inversion of all coordinates, $\mathbf{r} \rightarrow -\mathbf{r}$, but remain invariant on time reversal, $t \rightarrow -t$, while the magnetization **M** and magnetic field **H** transform in precisely the other way: with the time reversal changing the sign and spatial inversion leaving them unchanged. Because of this difference in transformation properties, the linear coupling between (**P**, **E**) and (**M**, **H**) described by Maxwell's equations is only possible when these vectors vary both in space and in time: like, the spatial derivatives of **E** are proportional to the time derivative of **H** and vice versa. The coupling between static **P** and **M** can only be nonlinear. Nonlinear coupling results from the interplay of charge, spin, orbital and lattice degrees of freedom. For cubic crystals, the allowed form of the magnetically induced electric polarization is [76, 77, and 80],

$$\mathbf{P} \propto [(\mathbf{M} \cdot \nabla)\,\mathbf{M} - \mathbf{M}(\nabla \cdot \mathbf{M})] \qquad \text{---- (1.21)}$$

Here the frustration induces spatial variations of magnetization. The period of magnetic states in frustrated systems depends on strengths of competing interactions and is often incommensurate with the period of crystal lattice. For example, a spin chain with a ferromagnetic interaction $J < 0$ between neighbouring spins has a uniform ground state with all parallel spins.

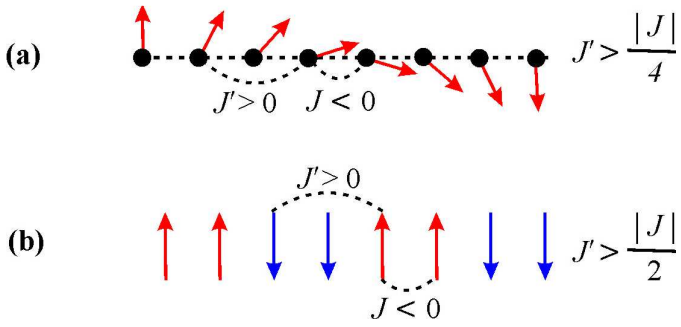

Fig. 1.13. *Frustrated spin chains with the nearest-neighbour FM and next nearest-neighbour AFM interactions J and J´ (**a**) ground state is a magnetic spiral for J´ /|J | > 1/4 (**b**) The chain has the up–up–down–down ground state for J´ /|J | > ½.*

An antiferromagnetic next-nearest-neighbour interaction $J' > 0$ frustrates this simple ordering, and when sufficiently strong, stabilizes a spiral magnetic state, S_n (see Fig. 1.13a & b) [66]. Similar to the other types of magnetic ordering, the magnetic spiral spontaneously breaks time-reversal symmetry. In addition it breaks inversion symmetry, because the change of the sign of all coordinates inverts the direction of the rotation of spins in the spiral. Thus, the symmetry of the spiral state allows for a simultaneous presence of electric polarization, the sign of which is coupled to the direction of spin rotation [66].

Spiral states are characterized by two vectors: the wave vector **Q** and the axis **e** around which spins rotate. When **Q** is parallel to the chain direction, as shown in Fig 1.13(a) and 1.14(c), induced electric dipole moment, which will be orthogonal both to **Q** and **e,** can be obtained as,

$$\mathbf{P} \parallel \mathbf{e} \times \mathbf{Q} \qquad \text{---- (1.22)}$$

Ferroelectricity induced in many of the magnetic spirals was attributed to the antisymmetric Dzyaloshinskii–Moriya (DM) interaction [78-82], which is determined as $\mathbf{D}_{n,n+1} \cdot \mathbf{S}_n \times \mathbf{S}_{n+1}$, where $\mathbf{D}_{n,n+1}$ is the Dzyaloshinskii vector [83, 84]. This interaction is a relativistic correction to the usual superexchange interaction and its strength is proportional to the spin–orbit coupling constant. The DM interaction favours non-collinear spin ordering. It generates weak ferromagnetism in antiferromagnetic layers of La_2CuO_4, the parent compound of many of the high-

temperature superconductors [85]. It also transforms the collinear Néel state in ferroelectric $BiFeO_3$ into a magnetic spiral [86]. Ferroelectricity induced by spiral magnetic ordering is the inverse effect, resulting from exchange-striction; that is, lattice relaxation in a magnetically ordered state. The exchange between spins of transition metal ions is usually mediated by ligands, like oxygen ions, forming bonds between pairs of transition metals. The Dzyaloshinskii vector $\mathbf{D}_{n,n+1}$ is proportional to $\mathbf{x} \times \mathbf{r}_{n,n+1}$, where $\mathbf{r}_{n,n+1}$ is a unit vector along the line connecting the magnetic ions n and $n+1$, and $\mathbf{x}$ is the shift of the oxygen ion from this line (see Fig. 1.14a) [66]. Consequently, the energy of the DM interaction increases with $\mathbf{x}$, depicting that the degree of inversion symmetry breaks at the oxygen site. In the spiral state the vector product $\mathbf{S}_n \times \mathbf{S}_{n+1}$ has the same sign for all pairs of neighbouring spins. So DM interaction pushes negative oxygen ions in one direction perpendicular to the spin chain formed by positive magnetic ions, and induces electric polarization perpendicular to the chain [81] (see Fig. 1.14b) [66]. Generally, ferroelectricity owing to magnetic frustration is found more probable in perovskite $RMnO_3$, with rare earth, R of lower ionic radius.

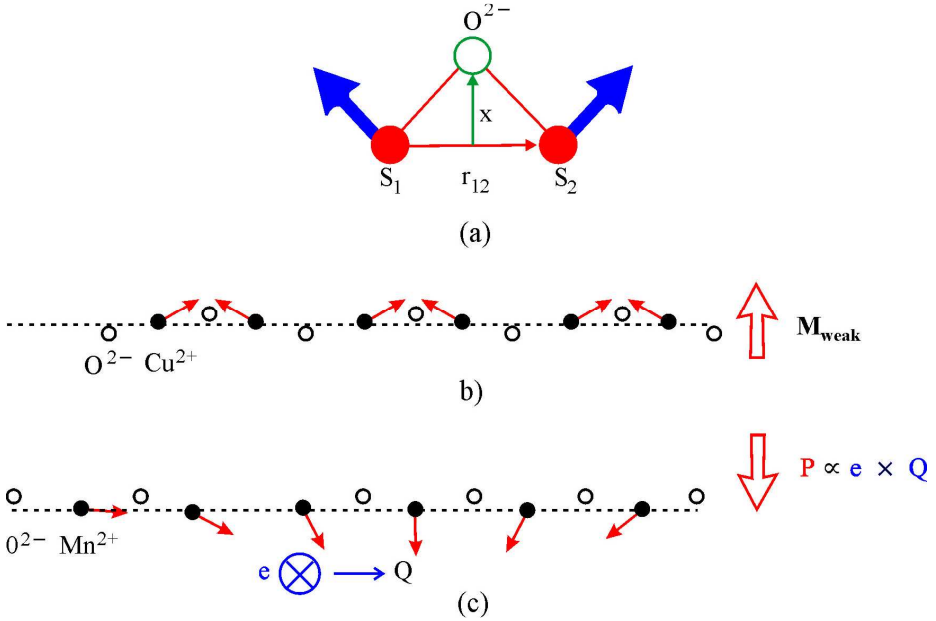

Fig.1.14. *Effects of the antisymmetric Dzyaloshinskii–Moriya interaction. (a) Dsyaloshinskii–Moriya interaction (b) Weak ferromagnetism ($LaCu_2O_4$) and (c) Weak ferroelectricity ($RMnO_3$).*

Fig.1.14 (a) [66] represents the interaction $H_{DM} = \mathbf{D}_{12} \cdot [\mathbf{S}_1 \times \mathbf{S}_2]$. The Dzyaloshinskii vector $\mathbf{D}_{12}$ is proportional to spin-orbit coupling constant λ, and depends on the position of the oxygen ion (open circle) between two magnetic transition metal ions (filled circles), $\mathbf{D}_{12} \alpha \lambda \mathbf{x} \times \mathbf{r}\hat{}_{12}$. Weak ferromagnetism in antiferromagnets (for example, $LaCu_2O_4$ layers, as in Fig.1.14b) results from the alternating Dzyaloshinskii vector, whereas (weak) ferroelectricity can be induced by the exchange striction in a magnetic spiral state, which pushes negative oxygen ions in one direction transverse to the spin chain formed by positive transition metal ions. In other words, two non-collinearly coupled magnetic moments (canted spin configuration) displace the oxygen sandwiched by the two moments through the electron – lattice interaction, as pointed out by Sergienko & Dagotto [81]. Thus, canted spin configuration polarizes the oxygen ligand through electron-lattice interaction.

1.7 Aim of present work.

It is well known from the literature that till date there is no material which has magnetoelectric properties i.e. ferroelectricity and ferromagnetism in the same phase at practically useful temperatures. So, the development of such type of material, which has magnetoelectric properties in same phase at useful temperatures, will be a milestone for the modern technology. The aim of the present work is to develop a new multiferroic material.

These materials have potential applications in the memory devices where one can write ferroelectrically and read magnetically and vice versa. In the present thesis we have taken the magnetic Co_2MnO_4 having spinel structure and substituted magnetic cations with non-magnetic Bi^{3+} having stereochemically active $6s^2$ lone pair of electrons. The motivation behind Bi-substitution is the electric polarization it can induce through non-centrosymmetric charge ordering and the magnetic frustration through lattice distortion, in the selected cubic spinel oxide. A detailed study on the magnetoelectric multiferroic properties of Co-based spinel oxides is rarely found in the literature. $CoCr_2O_4$, $CoMn_2O_4$, Co_2MnO_4, $CoFe_2O_4$, $NiCo_2O_4$, $CuMnCoO_4$, $InFeCoO_4$ are some of the important cobalt based ferrimagnetic spinel oxides investigated owing to the variety of exciting functional properties. These materials are time honored systems due to their amazing magnetic and electric

properties in which one can certainly envisage magnetoelectric property that can be tuned by changing the chemical composition through cation redistribution [87, 88].

This thesis presents such a detailed investigation of the structural, electrical and magnetic properties, starting from the scrap. For any technological application, thin films with good electrical and magnetic properties are desired, which necessitates the fabrication of thin films of spinel oxides. Of the several growth techniques available in this context, pulsed laser deposition stands far ahead than any other technique by virtue of its stoichiometry maintaining nature in the film as that of the target and non equilibrium nature of its interaction with the target.

Further, the interest in the swift heavy ion (SHI) irradiation on spinel oxides is because of the effect of irradiation on the superexchange interactions, which are highly sensitive to any disorder in such materials. The multifunctional properties of the magnetoelectric materials (ferroelectric or ferromagnetic properties) are known to be tunable by introducing some defects. The swift heavy ion irradiation is known to create the controlled defects in the materials depending on the choice of ion and its energy. SHI has been widely used to understand the damage structure and the modification in the physical properties of the materials. Moreover, SHI has been proved a good source to produce a wide variety of defects which can create structural strain and disorder in oxide materials, responsible for modifying the physical properties of materials.

By considering all the above mentioned issues the present thesis aims:

1. Substitution of non-magnetic Bi^{3+} having stereochemically active $6s^2$ lone pair of electrons in Co_2MnO_4 spinel oxide, in order to introduce ferroelectricity along with magnetic frustration, and to understand structural, electrical, electronic, magnetic and magnetoelectric properties.

2. From the application point of view, the synthesization of thin films using pulsed laser deposition (PLD). First, the optimization of growth conditions and then characterization of the thin films.

3. To investigate the effect of swift heavy ion (SHI) irradiation on the structural and magnetic properties and setting up the optimized parameters such as ions, fluence, energy etc. for engineering multiferroic properties of materials.

References

1. Ce-Wen Nan, M. I. Bichurin, S. Dong, D. Viehland, and G. Srinivasan, J. Appl. Phys. **103** (2008) 031101.

2. R. Ramesh, N. A. Spaldin, Nature mater. **6** (2007) 21.

3. M. Gajek, M. Bibes, S. Fusil, K. Bouzehouane, J. Fontcuberta, A. Barthélémy, and A. Fert, Nature Mater. **6** (2007) 296.

4. J. I. Gersten and F. W. Smith, *The Physics and Chemistry of Materials*. John Wiley & Sons, Inc. (2001).

5. C. Kittel, *Introduction to Solid State Physics, Seventh Edition.* John Wiley & Sons, Inc. (1996).

6. S. H. Tolbert, A. Firouzi, G. D. Stucky, and B. F. Chmelka, Science **278** (1997) 264.

7. N. Spaldin, *Magnetic Materials, First Edition.* Cambridge University Press, UK (2006).

8. J. R. Hook and H. E. Hall, *Solid State Physics, Second Edition*. JohnWiley & Sons, Inc. (1991).

9. B. D. Cullity, *Introduction to Magnetic Materials.* Addison-Wesley Publishing Co.,Inc.(1972).

10. K. C. Kao, *Dielectric Phenomena in Solids.* Elsevier Academic Press, UK (2004).

11. A. K. Jonscher, *Dielectric Relaxation in Solids.* Chelsea Dielectric Press, London (1983).

12. N. F. Mott and E. A. Davis, *Electronic Processes in Non-Crystalline Materials*. Clarendon, Oxford (1974).

13. R. S. Freitas, J. F. Mitchell, and P. Schiffer, Phys. Rev. B **72** (2005) 144429.

14. P. Lunkenheimer, V. Bobnar, A. V. Pronin, A. I. Ritus, A. A. Volkov, and A. Loidl, Phys. Rev. B **66** (2002) 052105.

15. N. Biškup, A. de Andrés, J. L. Martinez, and J. L. Perca, Phys. Rev. B **72** (2005) 024115.

16. D. C. Sinclair, T. B. Adams, F. D. Morrison, and A. R. West, Appl. Phys. Lett. **80** (2002) 2153.

17. G. Catalan, D. O'Neill, R. M. Bowman, and J. M. Gregg, Appl. Phys. Lett. **77** (2000) 3078.

18. A. Von Hippel, *Dielectrics and Waves*. Artech House, London (1995).

19. G. Catalan, Appl. Phys. Lett. **88** (2006) 102902.

20. C. G. Coops, Phy. Rev. **83** (1951) 121.

21. M. S. Tomar, R. E. Melgarejo, and A. Hidalgo, Appl. Phys. Lett. **83** (2003) 341.

22. C. Fu, F. Pan, H. Chen, S. Feng, W. Cai and C. Yang, International Journal of Infrared and Millimeter Waves, **28** (2007) 229.

23. A. Bartasyte, R. Bouregba, E. Dogheche, M. Boudard, G. Poullain, C. Jimenez, V. Plausinaitiene, D. Remiens, A. Abrutis, F. Weiss, O. Chaix-Pluchery and Z. Saltyte, Surface and Coatings Technology **201** (2007) 9340.

24. Q. Du, J.Y. Li, W. Nothwang and M. W. Cole, Acta Materialia **54** (2006) 2577.

25. C. R. Serrao, A. K. Kundu, S. B. Krupanidhi, U. V. Waghmare, and C. N. R. Rao, Phys. Rev. B **72**, (2005) 220101-R.

26. C. Fu, C. Yang, H. Chen, and L. Hu, J. Appl. Phys. **97** (2005) 034110.

27. J. S. Kim, S. S. Kim and T. K. Song, J. Korean Phys. Soc. **43** (2003) 548.

28. P. Ravindran, R. Vidya, A. Kjekshus, and H. Fjellvåg, Phys. Rev. B **74** (2006) 224412.

29. Y. Yamasaki, S. Miyasaka, Y. Kaneko, J. P. He, T. Arima, and Y. Tokura, Phys. Rev. Lett **96** (2006) 207204.

30. M. Matvejeff, J. Linden, T. Motohashi, M. Karppinen and H. Yamauchi, **144** (2007) 249.

31. A. K. M. Akther Hossain, M. Seki, T. Kawai, and H. Tabata, J.Appl.Phys **96** (2004) 1273.

32. D. C. Johnston, H. Prakash, W. H. Zachariasen, and R. Viswanathan, Mater.Res.Bull **8** (1973) 777.

33. S. A. Wolf, D. D. Awschalom, R. A. Buhrman, J. M. Daughton, S. von Molnár, M. L. Roukes, A. Y. Chtchelkanova, D. M. Treger, Science **294** (2001) 1488.

34. M.J. Carey, S.Maat, P.Rice, R.F.C.Farrow, R.F.Marks, A.Kellock, P.Nguyen and B.A.Gumey, Appl. Phys. Lett **81**(2002) 1044.

35. M. L. Kahn and Z. J. Zhang, Appl. Phys. Lett **78** (2001) 3651.

36. Y. Ikedo, J. Sugiyama, H. Nozaki, H. Itahara, J. H. Brewer, E. J. Ansaldo, G. D. Morris, D. Andreica, and A. Amato, Phys. Rev B **75** (2007) 054424.

37. E. J. W. Verwey and E. L. Heilmann., J. Chem. Phys. **15** (1947) 174.

38. E. W. Gorter, Philips. Res. Rept., **9** (1954) 321.

39. I. E.Dsyaloshonskii, Sov. Phys. JETP **10** (1960) 628.

40. D. N.Astrov, Sov. Phys. JETP **11** (1960) 708.

41. T. H.O'Dell, *The electrodynamics of magnetoelectric media*. Amsterdam (1970).

42. E. Ascher, H. Rieder, H. Schmid and H. Stossel, J.Appl.Phys. **37**(1966) 1404.

43. D. L. Fox and J. F.Scott, J. Phys. C **10** (1997) L329.

44. D. L. Fox, D. R. Tilley, J. F. Scott and H. J. Guggenheim, Phys. Rev. B **21** (1980) 2926.

45. K. Kato, S. Iida, K. Yanai and K. Mizushima, J.Mag.Mag.Mater. **31** (1983) 783.

46. I. G. Istnailza and S. A. Kizhaev, Sov.Phys.Solid State **7** (1965) 236.

47. J. Huang, Y. Cao, Y. Y. Sun, Y. Y. Xue and C.W. Chu, Phys. Rev. B **56** (1997) 2623.

48. J. R. Teague, R. Gerson and W. J. James, Solid State Commun. **8** (1970) 1073.

49. A. M. Dos Santos, S. Parashar, A. R. Raju, Y. S. Zhao, A. K. Cheetham and C. N.R. Rao, Solid State Commun. **122** (2002) 49.

50. J. Hemberger, P. Lunkenheimer, R. Fichtl, H. A. K von Nidda, V. Tsurkan and A. Loidl, Nature **434** (2005) 364.

51. N. Ikeda, H. Ohsumi, K. Ohwada, K. Ishii and T. Inami, Nature, **436** (2006) 1136.

52. T. Katsufuji, S. Mori, M. Masaki, Y. Moritomo, N. Yamamoto and H. Takagi, Phys. Rev. B **64** (2001) 104419.

53. T. Kimura, S. Kawamoto, I. Yamada, M. Azuma, M. Takano and Y. Tokura, Phys. Rev. B **67** (2003) 180401.

54. K. Ramesha, A. Llobet, Th. Proffen, C. R. Serrao and C. N. R. Rao, J. Phys.: Condens. Matter **19** (2007) 102202.

55. H. Fukumura, S. Matsui, H. Harima, K. Kisoda, T. Takahashi, T. Yoshimura and N. Fujimura, J. Phys.: Condens. Matter **19** (2007) 365239.

56. J. Vermette, S. Jandl and M. M. Gospodinov, J. Phys.: Condens. Matter **20** (2008) 425219.

57. N. Abe, K. Taniguchi, S. Ohtani, T. Takenobu, Y. Iwasa, and T. Arima, Phys. Rev. Lett. **99** (2007) 227206.

58. J. Strempfer, B. Bohnenbuck, M. Mostovoy, N. Aliouane, D. N. Argyriou, F. Schrettle, J. Hemberger, A. Krimmel, and M. V. Zimmermann, Phys. Rev. B **75** (2007) 212402.

59. D. G. Ramakrishnan, G.J. Nieuwenhuys and J. A. Mydosh, J. Phys.: Condens. Matter **13** (2001) 4543.

60. O. P. Vajk , M. Kenzelmann, J. W. Lynn, S. B.Kim and S. W. Cheong, Phys Rev. Lett. **94** (2005) 087601.

61. Z. H. Sun, B. L. Cheng, S. Dai and L. Z. Cao, J. Phys. D: Appl. Phys. **39** (2006) 2481.

62. D. K. Shukla, S. Mollah, Ravi Kumar, P. Thakur, K. H. Chae, W. K. Choi, and A. Banerjee, J. Appl. Phys. 104 (2008) 033707.

63. E. Golovenchits and V. Sanina, J. Phys.: Condens. Matter **16** (2004) 4325.

64. R. Valdés Aguilar, A. B. Sushkov, S. Park, S.-W. Cheong, and H. D. Drew, Phys. Rev. B **74 (**2006) 184404.

65. N. E. Rajeevan, P. P. Pradyumnan, R. Kumar, D. K. Shukla, S. Kumar, A. K.Singh, S. Patnaik, S. K. Arora, and I. V. Shvets, Appl. Phys. Lett. **92** (2008) 102910.

66. S. W. Cheong and M. Mostovoy, Nature Materials, **6** (2007) 13.

67. J. Wang, J. B. Neaton, H. Zheng, V. Nagarajan and S. B. Ogale, Science, **299** (2003) 1719.

68. T. Kimura, T. Goto, H. Shintani, K. Ishizaka, T. Arima and Y. Tokura, Nature **426** (2003) 55.

69. N. Hur, S. Park, P. A. Sharma, J. S. Ahn, S. Guha and S-W. Cheong, Nature **429** (2004) 392.

70. G. Lawes, A. B. Harris, T. Kimura, N. Rogado, R. J. Cava, A. Aharony, O. Entin-Wohlman, T. Yildirim, M. Kenzelmann, C. Broholm, and A. P. Ramirez, Phys. Rev. Lett. **95** (2005) 087205.

71. T. Kimura, J. C. Lashley and A. P. Ramirez, Phys. Rev. B **73** (2006) 220401(R).

72. K. Taniguchi, N. Abe, T. Takenobu, Y. Iwasa and T. Arima, Phys. Rev. Lett. **97** (2006) 097203.

73. O. Heyer, N. Hollmann, I. Klassen, S. Jodlauk, L. Bohatý, P. Becker, J. A. Mydosh, T. Lorenz and D. Khomskii, J. Phys.: Condens. Matter. **18** (2006) L471.

74. T. Kimura, G. Lawes and A. P. Ramirez, Phys. Rev. Lett. **94** (2005) 137201.

75. V. G. Bar'yakhtar and I. E. Chupis, Sov. Phys. Solid State **10** (1969) 2818.

76. V. G. Bary'achtar, V. A. L'vov and D. A. Jablonskii, JETP Lett. **37** (1983) 673.

77. E. P Stefanovskii and D. A. Jablonskii, Sov. J. Low Temp. Phys. **12** (1986) 478.

78. H. Katsura, N. Nagaosa and V. Balatsky, Phys. Rev. Lett. **95** (2005) 057205.

79. A. B.Harris, T. Yildirim, A. Aharony and O. E. Wohlman, Phys. Rev. B **73** (2006) 184433.

80. Mostovoy, M. Phys. Rev. Lett. **96** (2006) 067601.

81. I. A. Sergienko and E. Dagotto, Phys. Rev. B **73** (2006) 094434.

82. M. Kenzelmann, A. B. Harris, S. Jonas, C. Broholm, J. Schefer, S. B. Kim, C. L. Zhang, S. W. Cheong, O. P. Vajk, and J. W. Lynn, Phys. Rev. Lett. **95** (2005) 087206.

83. I. Dzyaloshinskii, Sov. Phys. JETP **19** (1964) 960.

84. T. Moriya, Phys. Rev. **120** (1960) 91.

85. S. W. Cheong, J. D. Thompson and Z. Fisk, Phys. Rev. B **39** (1989) 4395.

86. A. M. Kadomtseva, JETP Lett. **79** (2004) 571.

87. B. Antic, G. F. Goya, H. R. Rechenberg, V. Kusigerski, N. Jovic and M. Mitric**,** J. Phys.: Condense. Matter. **16** (2004) 651.

88. S. Kumar, Alimuddin, R. Kumar, Anjana Dogra, V.R.Reddy and A. Banerjee, J. Appl. Phys. **99** (2006) 08M910.

Chapter 2

Experimental Techniques for Preparation and Characterization

This chapter presents a brief description of material processing techniques; solid-state reaction route for the polycrystalline bulk samples and pulsed laser ablation technique for thin films. An outline of swift heavy ion irradiation is also provided. The characterization techniques opted for the study of structural, electrical, magnetic and magnetoelectric properties of bulk and thin films have been discussed.

2.1 Synthesis of bulk materials

2.1.1 Solid-state reaction technique

Various types of methods are known for the synthesis of the bulk materials such as solid-state reaction [1-6], sol gel [7] and co-precipitation [8, 9]. In the present thesis, the polycrystalline bulk samples of Bi-substituted Co_2MnO_4 have been synthesized by solid-state reaction technique, which involves a simple and straightforward process. This process is carried out in various steps such as:

(i) Mixing the required oxide powders in appropriate stoichiometric proportion

(ii) Calcination

(iii) Pelletization

(iv) Sintering

(i) Mixing of powders

For the preparation of $Bi_xCo_{2-x}MnO_4$ samples, high purity (> 99.99% pure) fine powders of cobalt oxide (Co_3O_4), manganese oxide (MnO_2) and bismuth oxide (Bi_2O_3) were weighed and mixed in stoichiometric proportion thoroughly. This was followed by grinding in highly pure acetone using a mortar and pestle. This process is carried out for several hours in order to achieve good homogeneity in the mixed powder.

(ii) Calcination

The decomposition of the mixed powder by heating below its melting point is known as calcination. The intention of calcination procedure is to felicitate the decomposition of the substituent oxides/carbonates and loss of moisture in order to establish the course of nucleation for the grain growth. Mixed powders were kept in alumina crucible and heated in the box furnace in ambient environment. During calcination, homogeneously mixed powder is heated to an intermediate high temperature, lower than the final sintering temperature. For $Bi_xCo_{2-x}MnO_4$ samples, the powders were calcined at 800 °C for 12 hours. Calcination was repeated three to four times with intermediate grinding and every time calcination temperature was kept higher than the previous step.

(iii) Pelletization

In order to increase the solid state reaction among the oxides used and for the purpose of the experimental characterizations, the calcined powders must be brought into the required high densities and shapes, before the final sintering process. This is achieved by using die-press technique in which a die of proper shape was filled with calcined powder and pressed using hydraulic press at 5 ton. In the present case, pelletization was done using a dye of 10 mm and 15 mm diameter and circular pellets of thickness ~ 2 to 3 mm were made.

(iv) Sintering

After pelletization of the calcined powder, the pellets are sintered at relatively higher temperature and for longer duration. This is followed by slow cooling with a suitable predefined rate, which is essential and important to bring in the required oxygen content in the material. For $Bi_xCo_{2-x}MnO_4$ bulk pellets, the final sintering temperature was maintained at 1000 °C for 24 hours followed by slow cooling at the rate of 5 °C /minute and the heat treatment was repeated twice with intermediate grinding. Fig. 2.1 shows the flow chart used for the preparation of bulk samples.

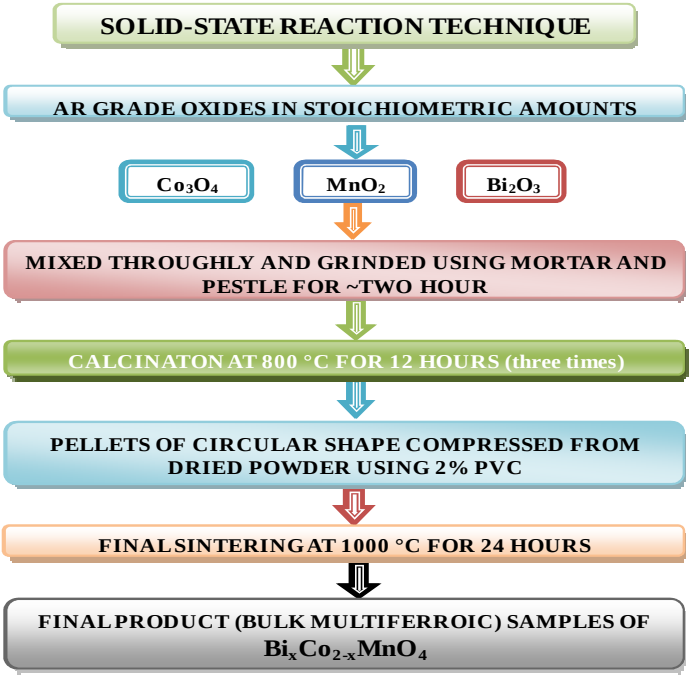

Fig. 2.1. *Flow chart for the preparation of bulk samples*

2.2 Thin film deposition: Pulsed Laser Deposition (PLD) Technique

The various techniques for thin film deposition are pulsed laser deposition (PLD) [10-15], chemical vapour deposition (CVD), metal organic chemical vapour deposition (MOCVD) [16-20], DC and RF sputtering [21-25], molecular beam epitaxy (MBE) [26], thermal evaporation [27], sol-gel [28] etc. Among these techniques, PLD is one of the most commonly used for the thin film growth of multicomponent systems. The basic process involved in all the film deposition techniques is to evaporate the material to provide atomic or molecular species in sufficient background pressure and carry them to the properly heated substrate of particular choice. The choice of substrate for the thin film deposition is guided by the lattice parameter of the compound and substrate as well as the orientation of the substrate. It has been established that high quality thin films of multicomponent oxides such as Fe_3O_4, $CoFe_2O_4$, $BiFeO_3$, $A_xMg_{1-x}Fe_2O_4$ (A = Zn, Ti), Sr_2CoO_4, $MnFe_2O_4$, $YBa_2Cu_3O_{7-\delta}$ and several other materials can be successfully grown by PLD [29-36].

The advantage of PLD technique lies in the fact that it maintains the target stoichiometry in the films, which has been found difficult for other conventional techniques such as evaporation, sputtering, etc. Excimer lasers such as XeF (λ = 352 nm); XeCl (λ = 308 nm); KrF (λ = 248 nm); KrCl (λ = 222 nm); ArF (λ = 193 nm); and F_2 (λ = 157 nm) are commercially available and can be used for thin film deposition. It uses a pulsed laser beam, usually but not necessarily, from an ultraviolet Excimer laser with pulse energy of about 1 J. The typical duration of the laser pulse is a few tens of nanosecond. Because of such a short duration of pulse, tremendous power (~ 10 - 100 MW/pulse) is delivered to the target. This is because of the nonequilibrium nature of PLD, in the sense that the absorption of energy and ablation take place in a very short time, usually within a nanosecond, before thermodynamic equilibrium is reached.

When a laser beam of energy density above the material dependent critical value is incident on the target, a large amount of energy is deposited into a few hundred-nanometer depth from the surface within a very short time scale. Due to

such a transient energy transfer, temperature of the surface layers is raised to a sufficiently high value (higher than the melting temperature of the material) and thus the melting of material starts at the surface. The process taking place in a very short duration of time scale causes a rapid ejection of the laser-induced plasma of materials at right angle from the surface of the target in the forward direction towards the substrate. The plasma plume contains various excited atoms, molecules, ions and neutral species. This plasma quickly expands away from the target towards the substrate where the adiabatic expansion of plasma at the surface of the heated substrate takes place and leads to the growth of the desired thin film. While PLD is recognized to transport the stoichiometry from the target to the film, there are several parameters, which immensely influence the growth and properties of thin films.

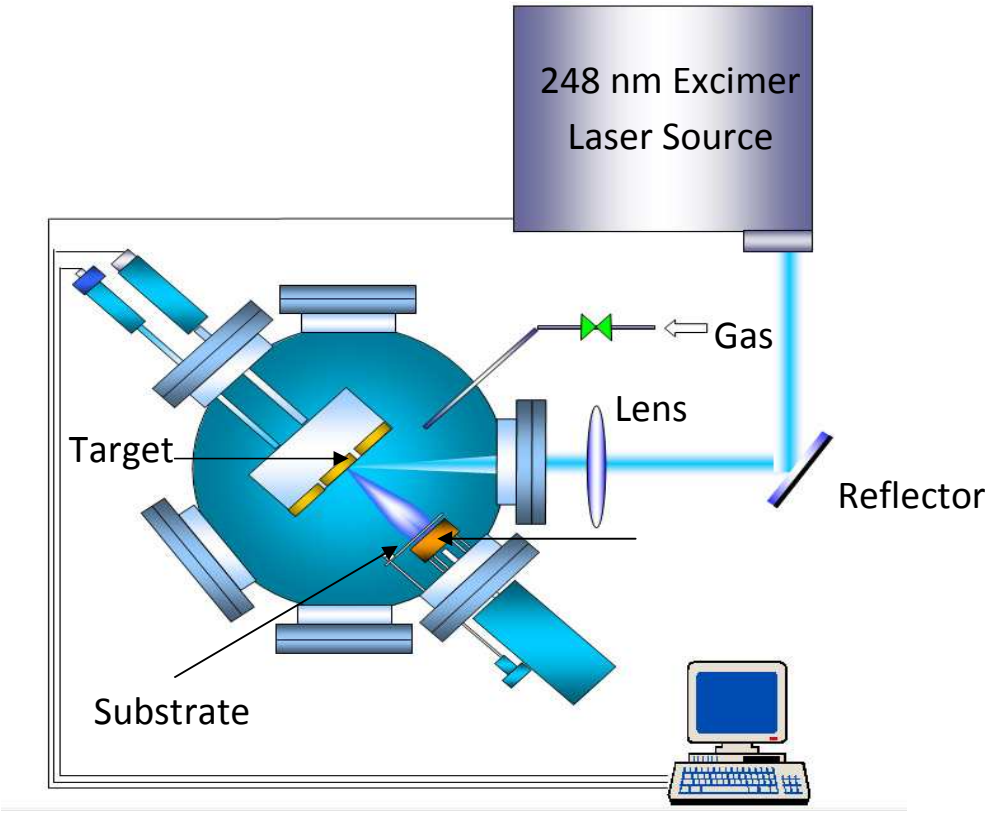

Fig. 2.2. *A schematic view of pulsed laser deposition technique.*

These parameters are laser energy density falling on the surface of the target, ambient background pressure during and after deposition, pulse repetition rate, temperature of the substrate, choice and orientation of the substrate itself, target to substrate distance etc. Laser energy density is a vital factor, which affects the properties of films. If the energy density is low, the complex target molecules do not evaporate congruently and if very high, droplet kind of particles is deposited on the substrate. The oxygen partial pressure too is critical for the thin film growth of the multiferroics to compensate the loss of oxygen in the ceramic target itself or during the course of transfer of the excited atomic/molecular species from the target to the substrate.

For this research work, thin films of Bi-substituted Co_2MnO_4 were grown by PLD technique. Typical schematic of the pulsed laser deposition technique is shown in Fig. 2.2. The thin film deposition was performed at UGC-DAE Consortium for Scientific Research, Indore, India.

2.3 Characterization techniques

2.3.1 X-ray diffraction

X-ray diffraction (XRD) was first demonstrated by Von Laue in 1912. Today, x-ray diffraction [37] is a routine technique for the characterization of the materials. A rich variety of information can be extracted from XRD. This is an appropriate technique for both forms of samples i.e. thin film as well as bulk. Using this technique, one can get the information regarding the crystallinity of the material, nature of the phase present, lattice parameter and grain size [38]. In the case of the thin films, the change in the lattice parameter with respect to the bulk indicates the nature of the strain present in the films.

The basic principle behind XRD is explained by the Bragg's equation which gives the condition for the constructive interference for the scattered x-ray from the successive atomic planes formed by the crystal lattice of the material. The Bragg's diffraction condition is given by

$$2d\sin\theta = n\lambda \qquad \text{---- (2.1)}$$

where λ is the wavelength of the incident X-ray, d is the distance between interatomic planes, θ is the glancing angle and *n* is an integer representing the order of diffraction.

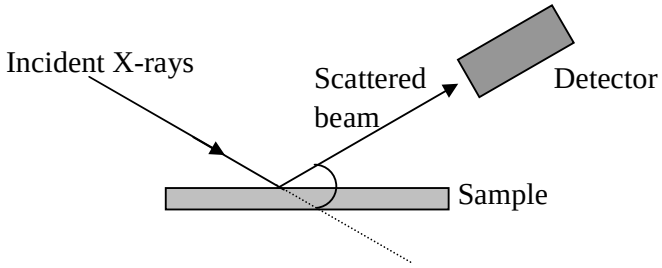

Fig. 2.3. *A representation of X-ray diffraction.*

In thin films, X-rays are diffracted by the oriented crystallites at a particular angle to satisfy the Bragg's condition. By knowing the value of θ and λ, one can calculate the interplanar spacing. The XRD pattern can be taken in various modes such as θ - 2θ scan mode, θ - 2θ rocking curve, and ϕ scan. In the θ - 2θ scan mode, a monochromatic beam of X-ray is incident on the sample at an angle of θ with the sample surface. The detector motion is coupled with the X-ray source in such a way that it always makes an angle 2θ with the incident direction of the X-ray beam (Fig. 2.3). The resulting spectrum is a plot between the intensity recorded by the detector versus 2θ.

Fig. 2.4. *X-ray diffractometer machine used for this work.*

In this work, Bruker D8 Advanced Diffractometer (see Fig.2.4) with Cu K_α (λ = 1.542 Å) was used for the phase detection of bulk powders and thin films at Inter-University Accelerator Centre, New Delhi. Room temperature powder X-ray diffraction (XRD) studies of the samples were performed within the 2θ range of 15^o to 75^o. The lattice spacing *d* was calculated using Bragg's equation (see eqn. 2.1), which is further utilized to calculate lattice constant. The analysis of the XRD pattern was done using Powder-X software [39].

2.3.2 Near Edge X-ray Absorption Fine Structure Spectroscopy (NEXAFS) studies

X-ray absorption fine structure (XAFS) refers to the details of how x-rays are absorbed by an atom at energies near and above the core-level binding energies of that atom [40]. When the x-rays hit a sample, the oscillating electric field of the electromagnetic radiation interacts with the electrons which are bound in an atom. Either the radiation will be scattered by these electrons or absorbed, which excite the electrons. A narrow parallel monochromatic x-ray beam of intensity $\boldsymbol{I_0}$ passing through a sample of thickness **x** will get a reduced intensity ***I*** according to the expression:

$$I = I_0 \exp(-\mu x) \qquad \text{---(2.2)}$$

where μ is the linear absorption coefficient, which depends on the types of atom and the density ρ of the material. At certain energies where the absorption increases drastically, gives rise to an absorption edge.

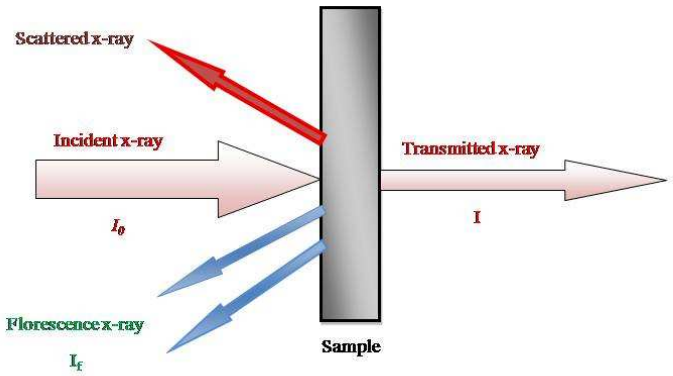

Fig. 2.5. *Schematic diagram of x-ray absorption phenomenon.*

Each such edge occurs when the energy of the incident photon is just sufficient to cause excitation of a core electron of the absorbing atom to a continuum state, i.e. to produce a photoelectron. Thus, the energies of the absorbed radiation at these edges correspond to the binding energies of electrons in the K, L, M, etc, shells of the absorbing elements. The absorption edges are labeled in the order of increasing energy, K, L_I, L_{II}, L_{III}, M_I,…., corresponding to the excitation of an electron from the 1s ($^2S_{1/2}$), 2s ($^2S_{1/2}$), 2p ($^2P_{1/2}$), 2p ($^2P_{3/2}$), 3s ($^2S_{1/2}$), … orbitals (states), respectively. An x-ray absorption spectrum is generally divided into four sections (see Fig. 2.6): (i) pre-edge ($E < E_0$); (ii) x-ray absorption near edge structure (XANES), where the energy of the incident x-ray beam is $E = E_0 \pm 10$ eV; (iii) near edge x-ray absorption fine structure (NEXAFS), in the region between 10 eV up to 50 eV above the edge; and (iv) extended x-ray absorption fine structure (EXAFS), which starts approximately from 50 eV and continues up to 1000 eV above the edge. The minor features in the pre-edge region are usually due to the electron transitions from the core level to the higher unfilled or half-filled orbitals (e.g, $s \rightarrow p$, or $p \rightarrow d$). In the XANES region, transitions of core electrons to non-bound levels with close energy occur. Because of the high probability of such transition, a sudden rise in absorption process is observed.

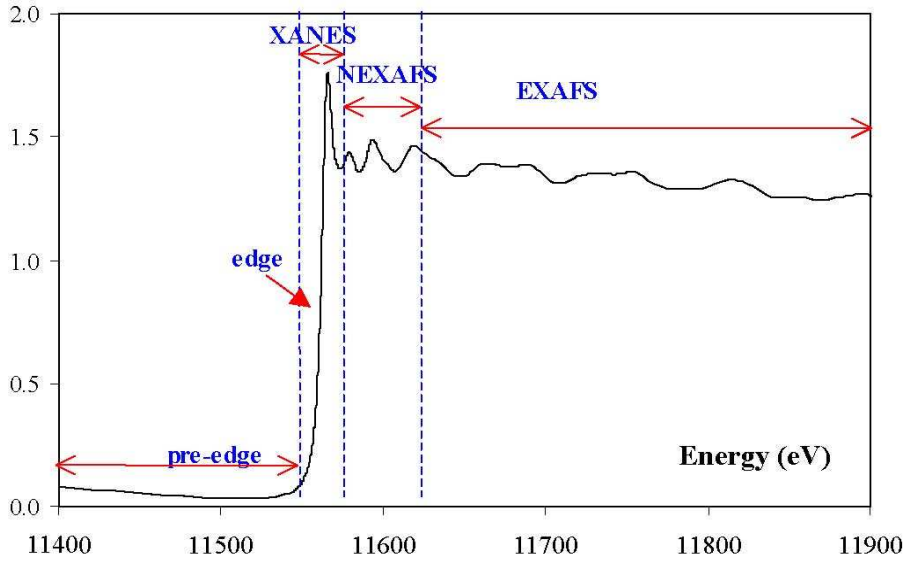

Fig. 2.6. *X-ray absorption spectrum in pre-edge, XANES, NEXAFS and EXAFS regions*

In NEXAFS, the ejected photoelectrons have low kinetic energy ($E-E_0$ is small) and experience strong multiple scattering by the first and even higher coordinating shells. In the EXAFS region, the photoelectrons have high kinetic energy ($E-E_0$ is large) and single scattering by the nearest neighboring atoms normally dominates.

In the present work NEXAFS measurements of $Bi_xCo_{2-x}MnO_4$ ($0.0 \leq x \leq 0.3$) along with Co_3O_4, CoO, MnO, MnO_2, and Bi_2O_3 at O K, Co $L_{3,2}$ and Mn $L_{3,2}$ edges were performed at the soft x-ray beam line 7B1 XAS KIST of the Pohang Light Source (PLS), operating at 2.5 GeV with a maximum storage current of 200 mA. All the samples were scraped with diamond foil prior to the measurements in order to remove the surface contaminants. The spectra were simultaneously collected in the total electron yield (TEY) mode and the fluorescence yield (FY) mode at room temperature in a vacuum better than $1.5x10^{-8}$ Torr. The spectra in the two modes turned out to be nearly identical indicating that the systems are so stable that the surface contamination effects are negligible even in the TEY mode. All the spectra were normalized to incident photon flux and the energy resolution was better than 0.2 eV.

2.3.3 X-ray Magnetic Circular Dichroism (XMCD) studies

In optics, the term "dichroism" refers to changes in the absorption of polarized light on passing through a material in two different directions. First verification of XMCD was done in 1987 by Schutz *et al.* [41] and thereafter this technique in XAS has become a widely useful tool as a probe for the element-specific characterization of magnetic materials. The growing interest in XMCD stems partly from the growing availability of tunable high brilliance x-rays (synchrotron) and is partly from the unique possibility to analyze the magnetic moments not only element specific, but also separated into their spin and orbital contributions. The concepts of XMCD are illustrated in Fig. 2.7 [42]. Simple sum rules can be used to separate out the spin and orbital contributions to the magnetism [43, 44]. The first x-ray absorption sum rule links the total intensity of the L_3 and L_2 resonances with the N number of empty d states (holes). The d valence shell can hold up to 10 electrons which are filled into band states up to the Fermi level and the

number of filled states is therefore 10 -N. For a magnetic material the d shell has a spin moment which is given by the imbalance of spin-up and spin-down electrons or equivalently (except for the sign) by the imbalance of spin-up and spin-down holes. In order to measure the difference in the number of d holes with up and down spin, we need to make the x-ray absorption process spin dependent. This is done by the use of right or left circularly polarized photons which transfer their angular momentum to the excited photoelectron.

Fig. 2.7 represents the electronic transitions in conventional L-edge x-ray absorption (a), and x-ray magnetic circular x-ray dichroism (b, c), illustrated in a one-electron model. The transitions occur from the spin-orbit split 2p core shell to empty conduction band states. In conventional x-ray absorption, the total transition intensity of the two peaks is proportional to the number of d holes (first sum rule). By use of circularly polarized x-rays, the spin moment (b) and orbital moment (c) can be determined from linear combinations of the dichroic difference intensities A and B, according to other sum rules. To separate the spin and the orbital part of the magnetic moment contribution of transition metal (TM), following formulae is used as per sum rule [43, 44]:

$$\langle L_z \rangle = \frac{2(A+B)}{3C} N \qquad \text{---(2.3)}$$

$$\langle S_z \rangle = \frac{(A-2B)}{2C} N \qquad \text{---(2.4)}$$

In the above equations, *A* and *B* are the areas under the L_3- and L_2-edge respectively for the XMCD curves. *C* in the above equations is the area under the $L_{3,2}$-edge XANES spectra and *N* is the number of holes in the *3d* orbital of TM. The sum rules have been tested by comparison with experimental measurements and theoretical calculations [45]; they are generally accurate within about 10% error. One possible source of error is found for the early transition metals, such as Cr, where the multiplet effects are larger than the 2*p* spin-orbit coupling and hence the L_2 and L_3-edges cannot be separated, however, it will not be the case here.

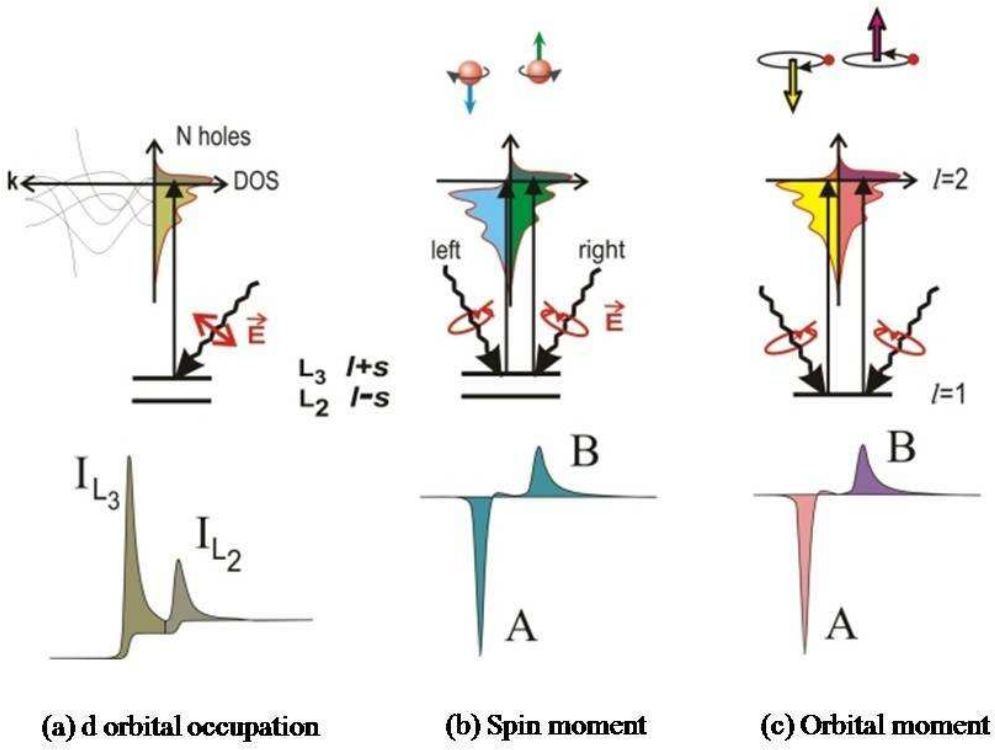

Fig. 2.7. *Concepts of XMCD.*

XMCD measurements presented in this thesis at Co $L_{3,2}$ and Mn $L_{3,2}$ edges were performed at the European Synchrotron Radiation Facility (ESRF) ID08 beam line, which uses an APPLE II type undulator giving ~ 100 % linear/circular polarization. All scans were collected simultaneously in both total electron yield (TEY) and total fluorescence yield (TFY) modes, ensuring both surface and bulk sensitivities. The spectra were normalized to incident photon flux and the base pressure of the experimental chamber was better than 3×10^{-10} Torr.

2.3.4 Raman spectroscopy

When light is scattered by a molecule most photons are elastically scattered. The scattered photons have the same energy (frequency) and therefore the same wavelength, as that of incident photons. However, a small fraction of light (~ 1 in 10^7 photons) is scattered at optical frequencies different from, and usually lower than, the frequency of the incident photons. The process leading to this inelastic scattering is called the Raman effect [46].

Raman scattering can occur with a change in vibrational, rotational or electronic energy of a molecule. The difference in energy between incident photon and Raman scattered photon is equal to the energy of vibration of the scattering molecule. A plot of the intensity of scattered light versus energy difference is the Raman spectrum. Raman spectroscopy is a spectroscopic technique used in condensed matter physics and chemistry to study the vibrational, rotational and other low frequency modes in a system. It relies on inelastic scattering, or Raman scattering of monochromatic light, usually from a laser in the visible, near infrared or near ultraviolet range. The laser light interacts with phonons or other excitations in the system, causing the energy of the laser photons being shifted up or down. The shift in energy gives information about the phonon modes in the system. Typically, a sample is illuminated with a laser beam and then light from the illuminated spot is collected with a lens, and sent through a monochromator. Wavelengths close to the laser beam, due to elastic Rayleigh scattering, are filtered out while the rest of the collected light is dispersed onto a detector. Spontaneous Raman scattering is typically very weak, and as a result the main difficulty of Raman spectroscopy is the separation of the weak inelastically scattered light from the intense Rayleigh scattered laser light. Raman spectrometers typically use holographic diffraction gratings and multiple dispersion stages to achieve a high degree of laser rejection. In the past, photomultiplier tube (PMT) was used as detectors for the dispersive Raman setups, which necessitated longer acquisition times. However the recent use of charged coupled devices (CCD) detectors facilitated dispersive Raman spectra, where acquisition is much faster.

Basic theory

The Raman Effect occurs when light impinges upon a molecule and interacts with the electron cloud**s** of the bonds of that molecule. The incident photon excites one of the electrons into a virtual state. For the spontaneous Raman Effect, the molecule will be excited from the ground state to a virtual energy state, and relax into a vibrational excited state, which generates Stokes Raman scattering. If the molecule was already in an elevated vibrational energy state, the Raman scattering is then called Anti-Stokes Raman scattering (Fig.2.8).

A change in molecular polarizability or the deformation of the electron cloud with respect to the vibrational coordinate is required for the molecule to exhibit the Raman Effect. The change of polarizability will determine the intensity of Raman spectra, where the Raman shift is equal to the vibrational levels involved.

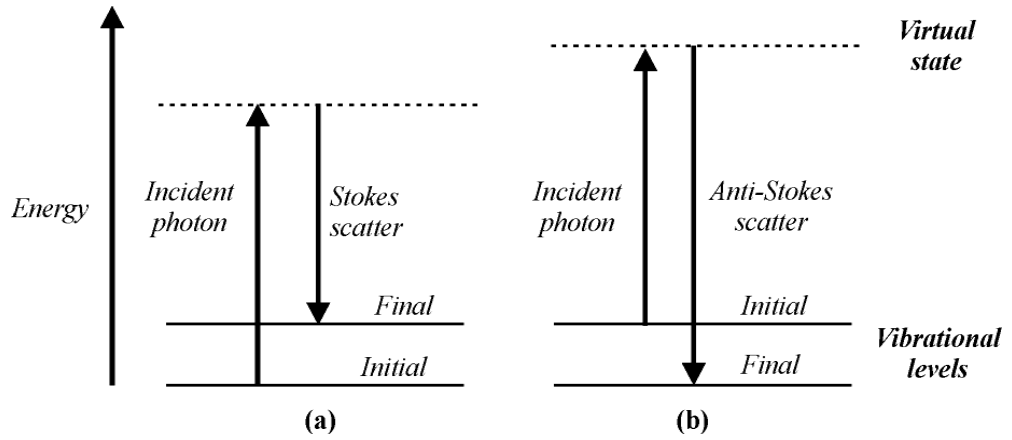

Fig. 2.8. *Energy level diagram of Raman scattering.*

In this work, Raman measurements were performed by using Micro Raman spectrometer(Model HR-800, Jobin Yvon) employing He-Ne laser (λ = 488 nm). The measured resolution of the spectrometer is 1 cm^{-1}. Spectra were collected in backscattering geometry using charge coupled device (CCD) with laser power 9 mW and incident laser beam focused into a diameter of 2µm. Notch filter is used to suppress the Rayleigh light.

2.3.5 Scanning Electron Microscopy (SEM)

Scanning electron microscope (SEM), shown in Fig. 2.9, is used for probing of the surfaces and microstructural characterization of the solid samples [47]. This technique is widely used to get information about the topographical features, morphology, phase distribution, crystal structure, crystal orientation and the presence and location of defects. In SEM, the electron beams are moved by the electric field to scan the sample. In this technique, a beam of electron is produced by heating of a metallic filament. The electron beams, focused with the help of electromagnetic lenses, falls on the sample with energy typically ~30 keV. When the beam strikes on the surface of the sample; backscattered electrons, secondary

electrons, Auger electrons and photons are ejected from the sample with typical energy values.

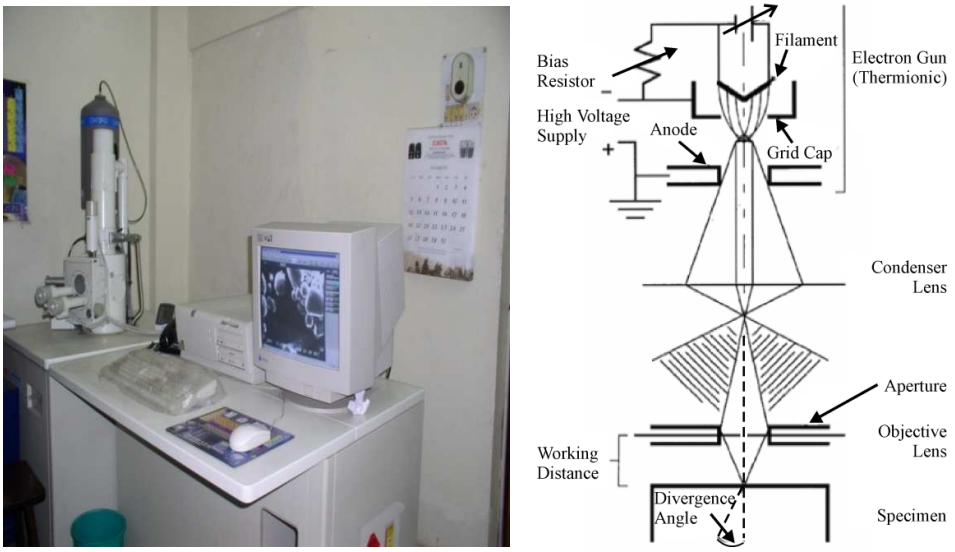

(a) **(b)**

Fig. 2.9. (a) *Automated SEM set up and* (b) *Schematic diagram of scanning electron microscope (SEM)*

Detectors collect the secondary or backscattered electrons and an image is produced on a cathode ray tube screen by recording the intensity of the detected signal as a function of position. The signal magnitude varies as a result of differences in surface topography as the electron beam is scanned across the sample surface. In this way, SEM can be employed to visualize surface features with a good resolution of the order of nanometers.

In this work, morphological and microstructural features of $Bi_xCo_{2-x}MnO_4$ were investigated with a scanning electron microscope, SEM Hitachi (Japan) model No: S3400N and quantitative analysis was made with an electron beam microanalyser equipped with an energy dispersive x-ray analysis (EDAX) capability.

2.3.6 Atomic Force Microscopy (AFM)

Atomic force microscopy [48] is a powerful technique for probing the surface of the thin film and deducing valuable information of its topological features fastly and accurately. AFM operates by scanning using a very sharp and tiny tip attached to the end of a cantilever across the sample surface (Fig. 2.10). The tip approaches the surface of the sample and interacts with it via Vander Waals forces. The interaction translates in a cantilever deflection or a change in the cantilever's oscillating frequency, depending on the operational mode of the AFM; contact or tapping. The deflection or the frequency changes of the cantilever are detected by an optical system consisting of a laser beam, which is reflected on the cantilever. The vertical and the horizontal deflections are measured using a split photodiode detector that analyses the reflected beam. The displacement of the cantilever in the three directions is done by means of a piezoelectric scanner, combining independently operated piezo-electrodes, for X, Y and Z direction into a single tube. The two operating modes that have been used, contact–AFM and tapping–AFM, are described in more detail in the following text.

2.3.6.1 Contact mode AFM

As mentioned already, the changes in the cantilever's deflection are monitored with a split photodiode detector when the tip is scanning the sample surface [49]. A feedback loop maintains a constant deflection between the cantilever and the sample by vertically moving the scanner at each data point to maintain a 'set-point' deflection. By maintaining a constant cantilever deflection, the force between the tip and the sample remains constant. The force F is calculated from Hook's law: $\boldsymbol{F} = -k\,\boldsymbol{x}$, where k is the spring constant and $\boldsymbol{x}$ is the deflection. Spring constants usually range from 0.01 to 1.0 N/m, resulting in forces ranging from nN to μN. The distance that scanner moves vertically at each point (x, y), is stored by the computer to form the topographic image of the surface.

2.3.6.2 Tapping mode AFM

In tapping mode, the cantilever is oscillated near its resonance frequency with the amplitude ranging typically from 20 to 100 nm. The tip lightly 'taps' the surface while scanning, and make contact with the surface at the bottom of its swing. The feedback loop maintains constant oscillation amplitude by maintaining a constant RMS of the oscillation signal acquired by the split photodiode detector. In order to maintain constant oscillation amplitude, the scanner has to move vertically at each point (x, y). The vertical position of the scanner is stored by the computer, to form the topographic image of the sample surface. In this work, to study topographic and morphology of the Bi-substituted Co_2MnO_4 thin films, AFM measurements have been carried out using Nanoscope III a (Digital Instruments) at Inter-University Accelerator Center, New Delhi, INDIA.

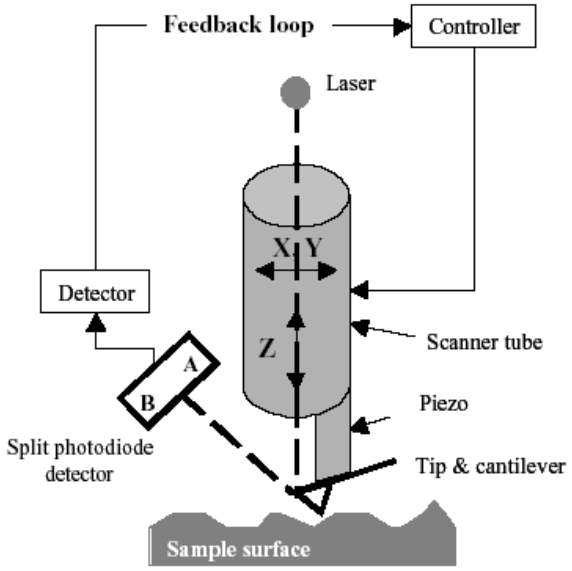

Fig. 2.10. *Schematic diagram of Atomic Force Microscope (AFM)*

2.3.7 Magnetic Force Microscopy (MFM)

The magnetic force imaging is a feature provided by the magnetic force microscope. This method is similar to AFM but the tip of AFM is changed to the magnetic tip of silicon nitrite coated with cobalt/chromium. Magnetic force

Microscope was operated in a phase detection mode whereby a cantilever is forced to oscillate at its resonance frequency and small change in phase due to magnetic interaction is detected. The image obtained is that of the force gradient dF/dz above the sample such that $\Delta\varphi = -Q(dF/dz)/k$, where Q is the quality factor of the cantilever and k is the spring constant. The force acting on the magnetic tip in the z direction is related to the interaction energy E, such that $F_z = dE/dz$.

In MFM, measurement tip is first scanned over the sample in order to obtain the topographic information. After each scan line, the feedback is turned off and the tip is raised above the sample to a user-defined height (20-100 nm) to perform a second scan of the surface measuring any far field contribution, such as magnetic forces (at that height only long range forces can be detected, while Vander Walls forces related to the topography are negligible). The topography data acquired during the first scan are used to maintain the tip at a constant height. The existence of magnetic forces shifts the resonant frequency of the cantilever by an amount proportional to vertical gradients in the magnetic forces on the tip. Resonant frequency shifts are very small (from 1 to 5 Hz for a resonant frequency of about 100 Hz) and can be detected either by phase detection mode or by amplitude detection mode. Phase detection measures the cantilever's oscillation phase relative to the piezo-drive, and amplitude detection measures the oscillation amplitude. In both cases, the measured signal is proportional to the second derivative of the stray field, emanated from the sample [50]. Phase detection is much superior to amplitude detection. In the present work, to probe the domain pattern in the thin films, Magnetic Force Microscopy (MFM) has been carried out on a Nanoscope III a (Digital Instruments) at Inter-University Accelerator Centre, New Delhi, INDIA.

2.3.8 Electrical transport measurements

In the present work, the dc conductivity measurements of the samples were performed by an automated resistance measuring set up at IUAC, New Delhi; consisting a standard four-probe unit and Keithley electrometer (Model 617), in the temperature range 150 K to 400 K. A cryostat consisting of variable temperature probe, inserted in liquid nitrogen (LN_2) container (Fig. 2.11) is used for the

measurement. The temperature was controlled with accuracy of ±50 mK using Lakeshore (Model 340) temperature controller.

2.3.9 Dielectric measurement set up

The dielectric properties of the multiferroic $Bi_xCo_{2-x}MnO_4$ samples have been carried out with the automated dielectric measurement set up at IUAC, New Delhi. The dielectric constant as a function of temperature reveals the ferroelectric property of the material. For measuring the dielectric constant of ferroelectric materials as well as high dielectric materials at low temperature, a variable temperature probe has been utilized. By inserting this in liquid nitrogen (LN_2) container, one can vary the temperature from 77 – 500K. The detail of the setup is shown in Fig. 2.11. The system is capable for following type of measurements:

1. Frequency dependent dielectric properties.
2. Temperature (80 K – 500 K) dependent dielectric properties.
3. Temperature (80 K – 500 K) dependent C-V measurement.

The sample can be electrically connected using silver paste. The temperature of the sample is controlled using the Lakeshore temperature controller (Model 340) and stabilized within ±50 mK. This setup is fully automated and program has been written using LabView software. The dielectric constant for the bulk sample was calculated by measuring the capacitance of the material. The capacitance as a function of frequency and temperature was measured using HP4192 precision LCR meter. Shielded test leads were used for the electrical connections from the analyzer to the sample in order to avoid any parasitic impedance. The samples in the form of circular pellets were used for the dielectric measurements. Before starting the measurement the samples were heated at 100 ^{O}C for 1 hour, so as to homogenize the charge carriers and to remove the moisture content, if any.

For the dielectric measurement, surfaces of the pellets were polished and silver coated, which were kept at 200°C for 2 hours for stabilization of electrodes. The value of the dielectric constant (ε′) was calculated using the formula;

$$\varepsilon' = C/C_0 \qquad \text{---- (2.5)}$$

where is the real part of the dielectric constant, *C* is the capacitance of the material inserted between the electrodes and C_0 is the capacitance of the medium as air or no medium between the electrodes. The C_0 for the parallel plate capacitor can be calculated using the following relation,

$$C_0 = \varepsilon_0 A/t \qquad \text{---- (2.6)}$$

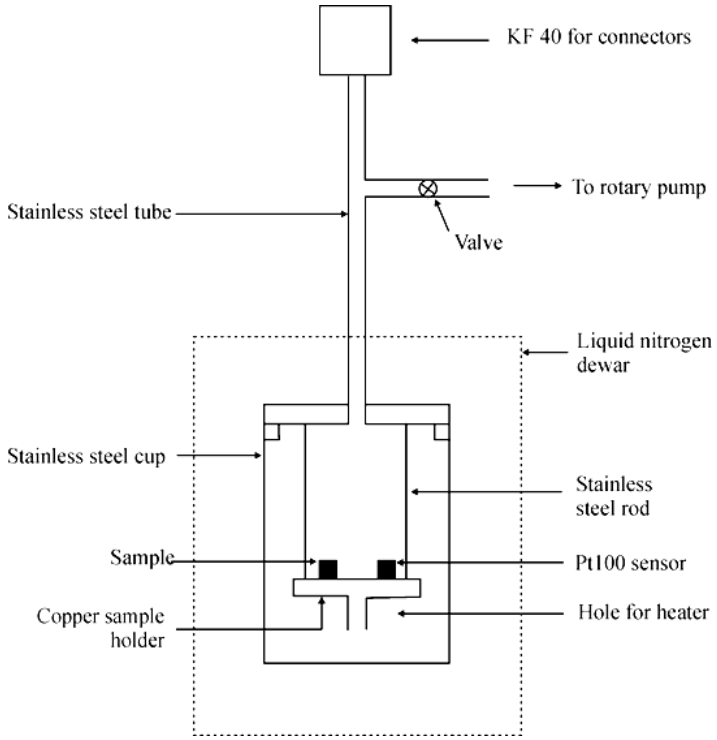

Fig. 2.11. *Schematic diagram of the cryostat.*

For calculating the dielectric constant, the dimensions of the pellet used for measurement were measured with the vernier calipers. Using equations 2.3 & 2.4, we get following relation for the calculating the dielectric constant

$$\varepsilon' = C \times t/\varepsilon_0 A \qquad \text{---- (2.7)}$$

where ε_o is permittivity in vacuum ~ 8.854 X 10^{-12} F/m, C is the capacitance of the specimen, t is the sample thickness and A is the area of the specimen in m^2. The imaginary component of dielectric constant (ε″) is calculated using the formula;

$$\varepsilon'' = \varepsilon' \tan\delta \qquad \text{---- (2.8)}$$

where tanδ is the loss tangent, proportional to the 'loss' of energy from the applied field into the sample (in fact this energy is dissipated into heat) and therefore denoted as dielectric loss. The ac conductivity is calculated from the data of dielectric constant and loss tangent (tanδ) using the relation

$$\sigma_{ac} = \varepsilon' \varepsilon_0 \omega \tan\delta \qquad \text{---- (2.9)}$$

where $\omega = 2\pi f$.

2.3.10 Vibrating Sample Magnetometer (VSM)

Most widely used technique for determining the magnetic properties of wide variety of magnetic samples is Vibrating Sample Magnetometer (VSM). With this technique, the magnetic moment of a sample can be measured with high accuracy. An illustration of VSM is shown in Fig. 2.12. The VSM is based upon Faraday's law, according to which an e.m.f is induced in a conductor by a time-varying magnetic flux. In VSM, a material is subjected to a uniform magnetic field and is made to undergo mechanical vibrations in the vicinity of pick-up coil, which causes the change in magnetic flux. This induces a voltage in the pick-up coils, which is proportional to the magnetic moment of the sample.

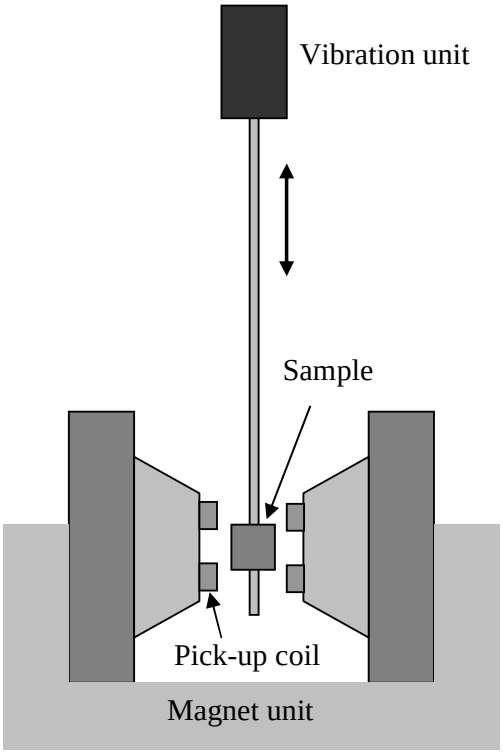

Fig. 2.12. *An illustration of Vibrating Sample Magnetometer.*

In this study we have used the VSM for the magnetization measurement of $Bi_xCo_{2-x}MnO_4$ bulk samples from 5 K to the room temperature. The magnetization measurements were carried out using the VSM option of PPMS set up (Quantum design), within a temperature range, 5 - 300 K in zero field cooled (ZFC) and field cooled (FC) modes under a constant magnetic field (H = 1 kOe). Field dependent magnetization measurements (M-H) were performed at various fixed temperatures. All the measurements were carried out in warming up cycles.

2.3.11 Magnetoelectric measurements

The low temperature high magnetic field facility[51] used for magnetoelectric measurement can cool down to 1.6 K in temperature and can generate magnetic field up to 8 tesla magnetic field without liquid cryogen. With separate attachments the sample space can be cooled to 300 mK (helium 3) and heated up to 1000K (encapsulated oven). It is a single compressor open-ended system purchased from M/s Cryogenics of UK. The compressor is water cooled and requires continuous supply of chilled water (~ 15°C) at the rate 7 lit/minute. The cooling powers at the first and second stage cold heads are 34 W @ 40 K and 1 W @ 4.2 K, respectively. The second stage cooling is shared between the sample space and the Nb-Ti superconducting magnet *(T_c* = 9 K). The first stage is connected to an ultra pure aluminium radiation shield. The magnet is latched to the second stage of the compressor. A condensation pot is attached to the magnet.

When low pressure helium gas from a separate close cycle reservoir is brought in contact with condensation pot the gas liquefies and with suitable pumping, the base temperature of 1.6 K can be achieved. It is to be emphasized that the process is entirely liquid cryogen free. Further since the sample space is always cooled by the helium vapour, the vibrations due to mechanical movement of displacer do not interfere with the measurements. The block diagram of the cryogen-free system is shown in Fig. 2.13. The cryostat also includes a vertical column where the sample is inserted using a dip-stick (variable temperature insert or VTl), a superconducting magnet and a condensation pot. The temperature of the superconducting magnet always remains at ~ 4 K except for small variation of the

order of 0.5 K during charging and discharging of the magnet. The condensation pot is connected to a separate helium gas recycle consisting of a reservoir (50 litre helium gas at 3 psi pressure), an air filter and a dry pump. The helium gas gets liquefied locally at the pot and its vapour flow (and therefore the temperature) in VTI chamber is controlled by a needle valve. To reach 1.6 K, a pressure of 8 mbar is maintained in the VTI chamber. Controlled heating by a 25 W-heater near VTI base, dictates the temperature of the helium vapour at the sample space.

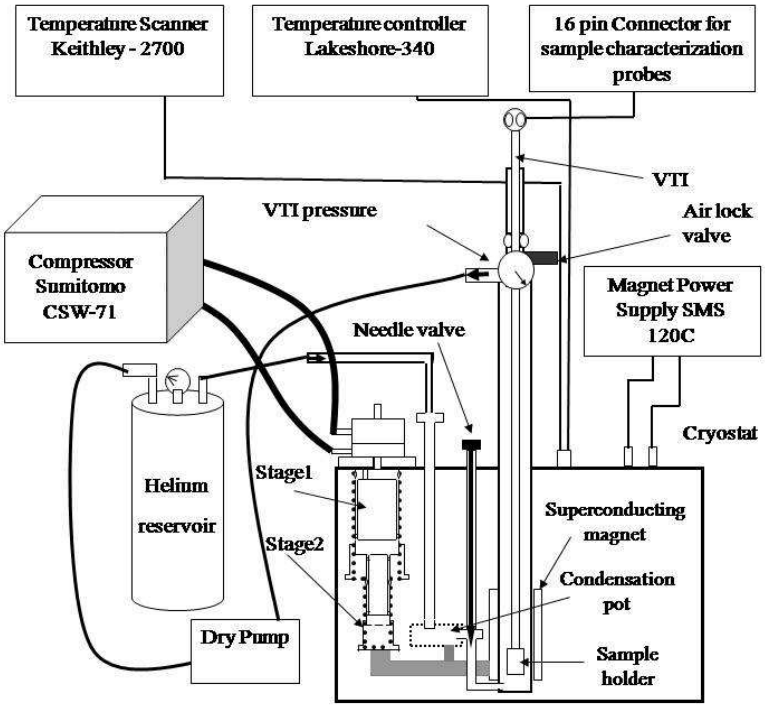

Fig. 2.13. *Block diagram of the GM cycle based cryocooler and cryostat.*

Resistive temperature sensors are placed at various points in the cryostat such as the first stage, shield, second stage, magnet, condensation pot, and exchanger exhaust to continuously monitor the system parameters. The resistance (temperature) at these points is measured using a Keithley 2700 multimeter with a 10 channel scanner. The temperature in the VTI and on the sample holder is measured and controlled by Cernox sensors using a Lakeshore 340 temperature controller. The Magnet power supply is cryogenic Model SMS 120 C. The

maximum of 8 tesla magnetic field requires current flow of 108 Ampere. The magnet is fitted with a persistent switch that enables very stable homogeneous field.

The various attachments already implemented with this system installed at JNU, New Delhi; include *dc* and *ac*, resistivity, Hall effect, magneto-resistance, dielectric constant, and *RF* penetration depth. The interfacing software and automation have been developed using LabView software. The attachments and the sample can be taken out of the system without warming the system to room temperature (unlike the Quantum Design PPMS). This is achieved by an airlock valve. In this work magnetocapacitance studies has been performed by measuring capacitance as a function of temperature with applied magnetic field ranging from 0 to 3 Tesla on the bulk and thin film samples. The field is applied parallel to the *ab* plane of the thin film samples.

2.4. Swift Heavy Ion (SHI) Irradiation

To understand the impact of swift heavy ion irradiation on the magnetoelectric properties of $Bi_xCo_{2-x}MnO_4$ thin films, we have utilized Pelletron accelerator and materials science beam line at IUAC, New Delhi.

2.4.1 Pelletron accelerator

The 15 UD Pelletron, as shown in Fig. 2.14, is a versatile, tandem type of electrostatic heavy ion accelerator. This is installed in a vertical configuration in an insulating tank of 26.5-meter height and 5.5 meter in diameter. In this machine, negative ions are produced and pre-accelerated to ~300 keV by the cesium sputter ion source known as SNICS (Source of Negative Ions by Cesium Sputtering) (Now it has been replaced by MCSNICS (Multi Cathode SNICS). The pre-accelerated ions are injected into strong electrical field inside an accelerator tank filled with SF_6 insulating gas maintained at a pressure of 6 to 7 atmospheres. The ion beam is selected by injector magnet, which selects the mass of the ion using mass spectroscopy. The ions are mass analyzed by a dipole magnet called injector magnet and are tuned vertically to downward direction. The ions then enter in the strong

electrical field inside the accelerator. A terminal shell of about 1.52 meter in diameter and 3.61 meter in height is located at the center of the tank, which can be charged to a high voltage (~15 MV) by a pellet charging system. The negative ions on traversing through the accelerating tubes from the column top of the tank to the positive terminal get accelerated. On reaching the terminal they pass through the stripper (foil or gas), which removes electrons from the negative ions and transforms the negative ions into positive ions with high charge state. For very heavy ions (A > 50), the lifetime of the carbon foils used in the stripper are limited to a few hours due to radiation damage. Therefore a gas filled canal or a combination of the gas stripper followed by a foil stripper is used for heavy ions. The transformed positive ions are then repelled away from the positively charged terminal and are accelerated towards ground potential to bottom of the tank. In this way same terminal potential is used twice to accelerate the ion in tandem. Hence, the name given to this accelerator is a Tandem Pelletron Accelerator.

The final energy of the emerging ions from the accelerator is given by,

$$E_i = [E_{decpot} + (1 + q_i) V] \qquad \text{----(2.10)}$$

where E_i is the energy of the ions having a charge state q_i after stripping, V is the terminal potential in MV and E_{decpot} is the deck potential of the SNICS source. On exciting from the tank, the ions are bent into horizontal plane using analyzing magnet. This magnet works as an energy analyzer and depending on the dipole magnetic field, ions of particular energy travel in the horizontal direction. The switching magnet diverts the high-energy ion beam into selected beam line of the beam hall. The ion beam kept centered and focused using steering magnets and quadruple triplet magnets.

The beam line of the accelerator is in ultra high vacuum (UHV) condition (~10^{-10} mbar). The beam is monitored by beam profile meter (BPM) and the current is observed using Faraday cups. The entire machine is computer controlled and is operated from the control room. The accelerator can accelerate ions from proton to uranium from a few MeV to hundreds of MeV (200 MeV) depending upon the ion.

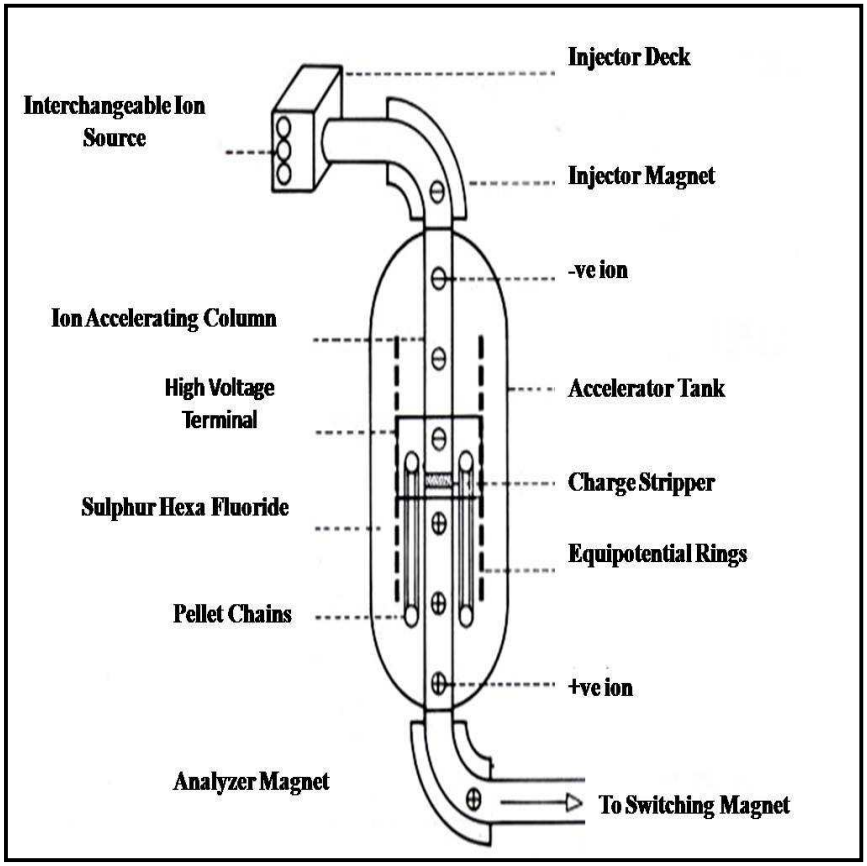

Fig. 2.14. *Schematics of the 15UD Pelletron at IUAC, New Delhi, INDIA.*

2.4.2 Materials science beam line

The accelerated beam from the Pelletron accelerator is brought to the beam hall and can be switched to any of the seven beam lines by using the switching magnet. Materials Science beam line is at 15^{o} to the right with respect to the zero degree beam line. This beam line has three chambers-high vacuum chambers, ultra high vacuum chamber and goniometry chamber. The high vacuum chamber is a cylindrical shaped multiport stainless steel chamber. A view of the high vacuum chamber is shown in Fig. 2.15 (a). The irradiation experiments were performed in high vacuum chamber (~ 10^{-6} mbar) at room temperature in materials science beam line (see Fig. 2.15(b)). Thin film samples to be irradiated were mounted on the four sides of the target ladder (on copper block). The whole body of the ladder is made of stainless steel and a perforated square copper block is brazed at the end of the

ladder. The target ladder is mounted through a Wilson seal from the top flange of the chamber. This top flange is connected to the chamber through a flexible bellow that can be expanding up to 11 cm from its minimum position.

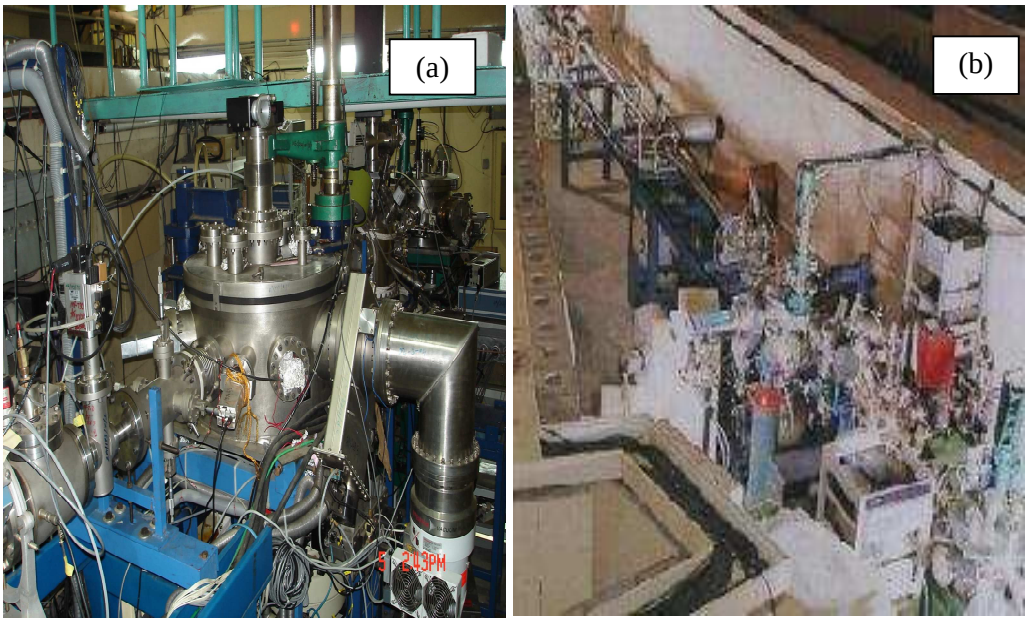

Fig. 2.15. *An overview of (a) Experimental chamber and (b) materials science beam line at Inter-University Accelerator Center, New Delhi, India.*

A stepper motor in conjunction with suitable mechanical assembly is used to control the up and down motion of the ladder. The beam on the ladder can be observed by observing the luminescence of the beam on the quartz crystal mounted on all sides of the ladder. After the observation of the beam on the quartz, the sample to be irradiated is brought to the same position as that on the quartz by moving the ladder in the desirable position. A CCD camera is attached to one of the ports of the chamber for viewing the sample and the quartz position. The positions can be monitored using close circuit television (CCTV) in the data acquisition room. The magnetic scanner (that can sweep the beam by 15 mm in x-direction and 15 mm in y-direction) ensures the uniform irradiation of samples. A cylindrical enclosure of stainless steel surrounds the sample ladder, which is kept at a negative potential of 120 V. This enclosure suppresses the secondary electrons coming out of the sample during the irradiation. An opening in the suppressor allows the ion beam to fall on

the sample. The total number of particles/charges falling on the sample can be estimated by a combination of the current integrator and the pulse counter (Faraday cup) from which the irradiation fluence/dose can be measured.

The counts for the desired ion fluence for each sample can be calculated using the following relation:

$$No.of\ Counts = \frac{Dose \times q \times 1.6 \times 10^{-19}}{Pulse\ Height} \quad \text{---- (2.11)}$$

2.4.3 Ion solid interaction

When an energetic ion passes through the matter, it experiences a series of elastic and inelastic collisions with the atoms which lie in its path. These collisions occur because of the electrical forces between the nucleus and electrons of the projectile and those of the atoms which constitute the solid target. During this collision the energetic ions transfer its energy to nuclei (by elastic atomic collision) and electron (by ionization and excitation) of the target material by two processes:

1. Elastic collision with the target atoms leading to displacement of atoms from their regular lattice sites. This mode of energy transfer is known as nuclear energy loss denoted by $(dE/dX)_n$ or S_n. It is well known mechanism of defect creation in the low energy regime (10 keV ~ few hundreds of keV) and it has negligible contribution in high energy regime (10 MeV and above).

2. Inelastic collision with the target electrons causing their excitation/ ionization. This mode of energy transfer is referred to as electronic energy loss $(dE/dX)_e$ or S_e.

Fig. 2.16 shows the schematic of the two mechanisms that occur during the ion solid interaction. It is well known fact that when a material is bombarded by the heavy ion irradiation, it creates damage zones in the material. When swift heavy ion passes through, the material in the vicinity of the ions trajectory may be transformed into a disordered state, giving rise to the so called latent track (damage zone created along the path of the swift heavy ion).

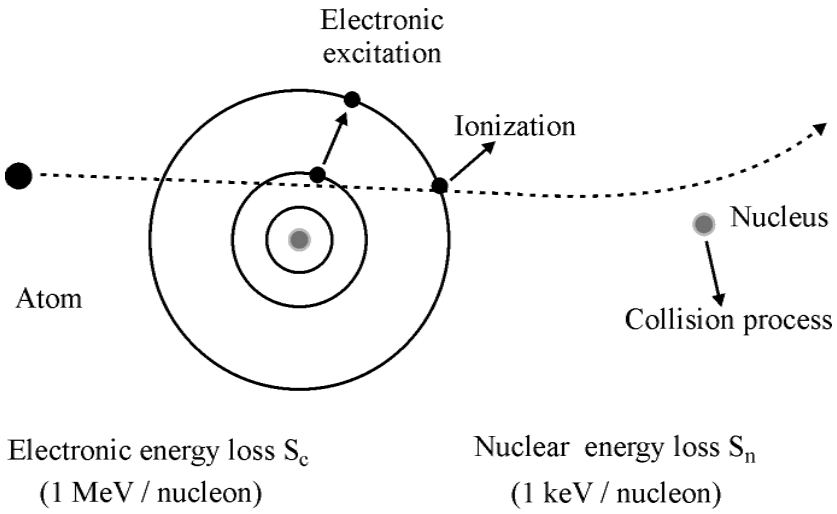

Fig. 2.16. *Ion-solid interaction: Demonstration of electronic and nuclear energy loss of an ion.*

In case of SHI irradiation, electronic energy loss is the most considerable energy loss process. The emergence of these traces is the result of local electronic energy deposition along the ion path. Therefore, a number of experimental results have shown that the higher electronic excitations can induce the structural modifications. This implies that all the S_e dependent effects induced in different materials are probably related to the basic energy transfer between the incident ions and the target atoms. Two basic models of microscopic energy transfer mechanism, namely thermal spike and the coulomb explosion have been used to establish the relevant parameters governing the basic energy transfer process.

2.4.3.1 Thermal spike model

Thermal spike model is based on the transient thermal process. This model was developed to explain the phase transformation after the SHI irradiation. According to this model the heavy ion irradiation may increase the lattice temperature that induces solid to liquid phase transformation into a localized zone of few nanometer (nm), which is followed by the thermal quenching (10^{-13} K/s) of a cylindrical molten liquid along the ion track. This results in the formation of amorphized latent track. The threshold value for the creation of the latent tracks is associated with the energy needed to induce a liquid phase along the ion path [52, 53].

In this process, the incoming ion gives its energy to the electron gas in ~10^{-17} s which is calculated from the collision time of ion with electron. The local thermalization in electronic system will take 10^{-15} s to complete. Heat transfer from the electronic to atomic subsystem becomes substantial in 10^{-14} to 10^{-12} s depending on the magnitude of the coupling (electron-electron coupling and electron-phonon coupling) between the subsystems. The electron- phonon coupling implies the ability of electrons to transfer their energy to the lattice.

2.4.3.2 Coulomb explosion model

In the Coulomb explosion model [54, 55], it is assumed that the incoming ions scatter the target electrons and create a column/cylinder of ionized atoms and the excited electrons are ejected by the Coulomb repulsion. The electron excitation energy is rapidly shared with other electrons via electron phonon interaction. The mutual Coulomb repulsion of the ions produces atomic displacements leading to a dense cloud of interstitial atoms and vacancies along the original ion trajectory. This model seems to be well suited for the insulating materials. In metals, which have large electronic mean free path, the free electrons carry away the excitation energy so efficiently that the sample warms up as a whole without considerable atomic motion.

In the present work, the thin films of $Bi_xCo_{2-x}MnO_4$ samples deposited on various substrates have been irradiated with 200 MeV Ag ions. The Ag ions were selected to create the columnar defects.

References:

1. G. H. Jonker and J. H. Van Santen, Physica B **16** (1950) 337.
2. P. Schiffer, A. P. Ramirez, W. Bao and S. W. Cheong, Phys. Rev. Lett. **75** (1995) 3336.
3. R. Mahendran, R. Mahesh, N. Rangavittal, S. K. Tiwari, A. K. Raychaudhuri, T. V. Ramkrishnan and C. N. R. Rao, Phys. Rev. B **53** (1996) 3348.
4. P. G. Radaelli, G. Iannone, M. Marezio, H. Y. Hwang, S. W. Cheong, J. D. Jorgensen and D. N. Argyriou, Phys. Rev. B **56** (1997) 8265.
5. S. B. Ogale, R. Shreekala, R. Bathe, S. K. Date, S. I. Patil, B. Hannoyer, F. Patit and G. Marest, Phys. Rev. B **57** (1998) 7841.
6. P. Mandal and S. Das, Phys. Rev. B **56** (1997) 15073.
7. R. D. Sanchez, J. Rivas, C. V. Vazquez, A. L. Quintela, M. T. Causa, M. Tovar and S. Oseroff, Appl. Phys. Lett. **68** (1996) 1334.
8. P. Barboux, J. M. Tarascon, L. H. Greene, G. W. Hull, B. G. Bagley, J. Appl. Phys. **63** (1988) 2725.
9. X. Z. Wang, M. Henry, J. Livage, Solid State Comm. **64** (1987) 881.
10. D. B. Chrisey and G. H. Hubler, *Pulsed Laser Deposition of Thin Films*, (Wiley Interscience, NewYork, 1994).
11. N. D. Mathur, G. Burnell, S. P. Isaac, T. J. Jackson, B. S. Teo, J. L. M. Dricoll, L. F. Cohen, J. E. Evetts and M. G. Blamire, Nature **387** (1997) 266.
12. R. Bathe, S.K.Date, S.R.Shinde, L.V.Saraf, S.B.Ogale, S.I.Patil, Ravi Kumar, S. K. Arora and G.K.Mehta, J. Appl. Phys. **83** (1998) 7174.
13. R. Shreekala, M. Rajeswari, K. Ghosh, A. Goyal, J.Y. Gu, C. Kwon, Z. Trazanovic, T. Boettcher, R.L. Green and T. Venkatesan, Appl. Phys. Lett. **71** (1997) 282.

14. J. Q. Guo, H. Takeda, N. S. Kazama, K. Fukamichi and M. Tachiki, J. Appl. Phys. **81** (1997) 7445.

15. W. Zhang, X. Wang and I. W. Boyd, Appl. Phys. Lett. **73** (1998) 2745.

16. P. K. Boyer, G. A. Roche, W. H. Ritchie and G. J. Collins, Appl. Phys. Lett. **40** (1982) 716.

17. G. H. Snyder, R. Hiskes, S. DiCarolis, M. R. Beasley and T. H. Geballe, Phys. Rev. B **53** (1996) 14434.

18. E. S. Gillman, M. Li and K. H. Dahmen, J. Appl. Phys. **84** (1998) 6217.

19. J. J. Heremans, M. Carris, S. Watts, X. Yu, L. H. Dahmen and S. Von Molnar, J. Appl. Phys. **81** (1997) 4967.

20. S. Pignard, H. Vincent, J. P. Senateur, J. Pierre and A. Abrutis, J. Appl. Phys. **82** (1997) 4445.

21. J. L. Vossen and W. Kern, *Thin Film Processes*, (Academic Press, New York, 1982).

22. K. Chahara, T. Ohno, M. Kasai and Y. Kosono, Appl. Phys. Lett. **63** (1993) 1990.

23. X. T. Zeng and H. K. Wong, Appl. Phys. Lett. **66** (1995) 3371.

24. E. Leja, T. Pisarkiewicz, and A. Kolodziej, Thin Solid Films **67** (1980) 45.

25. K. Choi and Y. Yamazaki, Jpn. J. Appl. Phys. **38** (1999) 56.

26. M. Leskela, J. K. Truman, C. H. Mueller and P. H. Holloway, J. Vac. Sc. Tech. A **7** (1989) 3147.

27. R. B. Labowitz, R. H. Koch, P. Chaudhuri, R. H. Gambino, Phys. Rev. B **35** (1987) 8821.

28. G. Critchlow and T. M. Racheva, Thin Solid Films **292** (1997) 299.

29. Shailja Tiwari, Ram Prakash, R J Choudhary1 and D M Phase, J. Phys. D: Appl. Phys. **40** (2007) 4943.

30. M.C. Terzzoli, S. Duhalde, S. Jacobo, L. Steren and C. Moina, Journal of Alloys and Compounds **369** (2004) 209.

31. M A Khan, A Garg, and A J Bell, Journal of Physics: Conference Series **26** (2006) 288.

32. Y. Yamamoto, H. Tanaka and T. Kawai, J. Mag. Mag. Mater. **261** (2003) 263.

33. Y. Muraoka, K. Ueda, H. Tabata and T. Kawai, Vacuum **59** (2000) 622.

34. J. Matsuno, Y. Okimoto, Z. Fang, X. Z. Yu, Y. Matsui, N. Nagaosa, M. Kawasaki, and Y. Tokura, Phys. Rev. Lett. **93** (2004) 167202.

35. M. H. Mahmoud, C.M. Williams, J. Cai, I. Siu, J.C. Walker, J. Mag. Mag. Mater. **261** (2003) 314.

36. G. A. Farnan, M. P. McCurry, C. C. Smith, R. J. Turner and D. G. Walmsley, Supercond. Sci. Technol. **13** (2000) 262.

37. A. Michel and V. Hove, *Surface physics of materials* http:// electron. lbl. gov/ coursees/SScourses.html.

38. B. D. Cullity, *Elements of X-ray Diffraction*, Addison-Wesley Pub. Co. (Reading, Mass, 1978).

39. C. Dong, J. Appl. Cryst. **32** (1999) 838.

40. J. E. Penner-Hahn, Coordination Chemistry Reviews, **190-192** (1999) 1101.

41. G. Sch¨utz, W. Wagner, W. Wilhelm, P. Kienle, R. Zeller, R. Frahm, and G. Materlik, Phys. Rev. Lett., **58** (1987) 737.

42. http://www-ssrl.slac.stanford.edu/stohr/xmcd.htm

43. B. T. Thole, P. Carra, F. Sette, and G. van der Laan, Phys. Rev. Lett. **68** (1992) 1943.

44. P. Carra, B. T. Thole, M. Altarelli, and X. Wang, Phys. Rev. Lett. **70** (1993) 694.

45. T. Funk, A. Deb, S. J. George, H. Wang and S. P. Cramer, Coordination chemistry reviews, **249** (2005) 3.

46. D. J. Gardiner and P. R. Graves, *Practical Raman Spectroscopy* (Springer-Verlag, London).

47. J. I. Goldstein, D. E. Newbury, P. Echlin, D. C. Joy, C. Fiori and E. Lifshin *Scanning Electron Microscopy and X-ray Microanalysis*, (Plenum, New York, 1981).

48. G. Binnig, C. F. Quate and G. Gerber, Phys. Rev. Lett. 56 (1986) 9300.

49. Y. Martin and H. K. Wickramasinghe, Appl. Phys. Lett. 50 (1987) 1455.

50. P. Grütter, H. J. Mamin and D. Rugar, *Scanning Tunnelling Microscopy II* & R. Wiesendanger and H. J. Guntherodt, *Further Applications and Related Scanning Techniques* (Springer, Berlin, 1995).

51. S. D Kaushik, A. K Singh, D. Srikala & S. Patnaik, Indian J. Pure & Appl. Phys **46** (2008) 334.

52. M. Toulemonde, Nucl. Instr. And Meth. B **156** (1999) 1.

53. Z. G. Wang, C. Dufour, E. Paumier, M. Toulemonde, J. Phys. Condens. Matter **6** (1994) 6733.

54. R. L. Fleischer, P. B. Price and R. M. Walker, Phys. Rev. **156** (1967) 2353.

55. D. Leseur and A. Dunlap, Radiat. Eff. and Def. Solids, **126** (1993) 163.

Chapter 3

Structural and Electrical Studies of $Bi_xCo_{2-x}MnO_4$ ($0 \leq x \leq 0.3$)

This chapter presents detailed study of structural and electrical, properties of the series of polycrystalline multiferroic $Bi_xCo_{2-x}MnO_4$ system prepared by a solid-state reaction route. The effect of Bi^{3+} substitutions in Co_2MnO_4 has been studied using x-ray diffraction (XRD), Scanning Electron Microscopy (SEM), frequency and temperature dependent dielectric, and dc & ac conductivity measurements.

3.1. Introduction

Mixed transition metal oxides with general formulae AB_2O_4 (A = Zn, Fe, Co, Ni, Mn, Mg, Cd etc; B = Co, Fe, Cr, Al, Ga, Mn, etc.) where A and B represent divalent and trivalent cations respectively, are time honored systems owing to their interesting magnetic and electric properties, which can be tuned accurately by changing the chemical composition through cation redistribution [1–5]. The crystal structure of a cubic spinel AB_2O_4 belongs to F*d3m* (site symmetry O_h^7) space group. Each unit cell contains 8[AB_2O_4] formula units and therefore 32 O^{2-} ions. This close packing contains 64 tetrahedral interstices and 32 octahedral interstices coordinated with O^{2-} ions. The charge distribution of the normal spinel is represented by $[A^{2+}]_{8a}[B_2^{3+}]_{16d}[O_4^{2-}]_{32e}$, in which Wyckoff positions 8*a* denote the tetrahedral sites and 16*d* the octahedral sites surrounded by O^{2-} ions at 32*e* sites. Empty interstitial space is comprised of 16 octahedral sites (16*c*) and 56 tetrahedral sites (8*b* and 48*f*). All spinel-like structures are characterized by an oxygen parameter *u* having a value around 0.375. For $u = 0.375$, the arrangement of O^{2-} ions is exactly a cubic close packing (FCC structure). In actual spinel lattice, there is deviation from the ideal pattern, with $u > 0.375$, resulting in a deformation of oxygen tetrahedrons and octahedrons [6, 7].

Depending on the species and stoichiometry of cations occupying A and B sites, some of the spinel phase may show multiferroic property. In case of magnetic spinel chromites, appearance of ferroelectricity has been explained based on the conical spin modulation [8]. Spin related ferroelectricity was also observed in many distorted perovskite type magnetic systems [9, 10]. Ferroelectric and ferromagnetic properties exhibited by bismuth based magnetic perovskites were attributed to the covalent bonding between bismuth and oxygen atoms [11, 12]. Recently, first principles calculations have shown that it is more realistic to have ferrimagnetism, instead of ferromagnetism, through B-site cation ordering in the multiferroic oxides [13]. Subsequently, different ferrimagnetic oxides have been experimentally probed for the multiferroic properties. $MnWO_4$ [14], $TmFe_2O_4$ [15], $MnCr_2O_4$ [16] etc

belong to the class of ferrimagnetic multiferroics, which are explored by many research groups and much progress has been made in understanding their mechanisms. The geometrical frustration of the lattice degrees of freedom is considered as the origin of multiferroic behavior of cubic sulpho-spinels [17]. We have chosen Co_3O_4 as a starting compound, a very interesting material, which exhibits an antiferromagnetic ordering at very low temperature (T_N ~ 20K) and two non-equivalent sites of Co. In this material, the octahedrally coordinated Co^{3+} exists in low spin state and the antiferromagnetic ordering is due to weak A-A interactions. From the substitution point of view, there is a lot of scope to substitute various trivalent cations by replacing fraction of Co^{3+} ions by Al, Mn, Ni, Cr, Ti etc [18]. It is well known that the cobalt manganese ($Mn_xCo_{3-x}O_4$) spinel oxides [19, 20] crystallize in cubic form (space group F*d3m*) for x < 1.2 and tetragonal (*I* 41/amd) type structure for x > 1.2.

The motivation behind the substitution of Bi^{3+} ions having $6s^2$ lone pair of electrons was to develop the new class of multiferroic materials with sufficient magnetoelectric coupling, since it is well known from the literature that Bi can introduce noncentrosymmetric charge ordering and consequent polarization [12, 21] in transition metal oxides that lead into multiferroic property. The improved ferroelectric property with Bi-substitution in Co_2MnO_4 suggests that this material is a good candidate for the technological applications, involving magnetoelectric multiferroics. In this chapter, we studied the effect of Bi ion on the structural and electrical properties of Co_2MnO_4.

3.2 Results and discussion

3.2.1 Structural (XRD) and morphological (SEM) characterizations

The X-ray diffraction (XRD) patterns obtained at room temperature for $Bi_xCo_{2-x}MnO_4$, with x = 0.0, 0.1, 0.2 and 0.3 are shown in Fig.3.1. Results of indexing and refinement of XRD patterns indicate the presence of a single-phase polycrystalline structure for the synthesized materials. The X-ray patterns confirm the existence of spinel structure with the reflection arising from 111, 220, 311, 222,

400, 422, 333, 440 and 533 planes. All the samples have good crystallinity and can be indexed with the Joint Committee on Powder Diffraction Standards (JCPDS) file 80-1544, assuming face centered cubic (FCC) structure. The prepared samples correspond to the space group F*d3m*, as a disordered spinel in which cations occupy two non-equivalent sites; tetrahedral *8a* (A Sites) and octahedral *16d* (B sites).

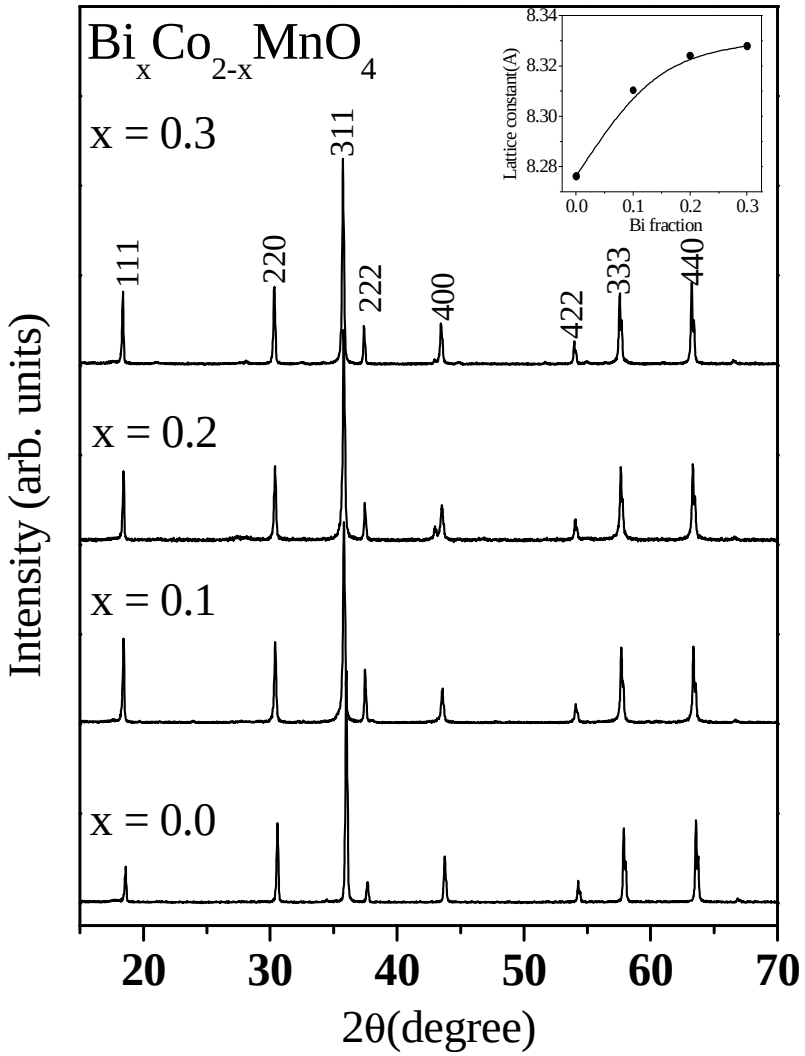

Fig. 3.1. *X-ray diffraction pattern for the samples $Bi_xCo_{2-x}MnO_4$ (x = 0, 0.1. 0.2 and 0.3) measured at 300 K and Inset shows the variation of* ***a*** *with composition.*

From Fig.3.1, the shift of planes towards lower 2θ with the increase in Bi substitution is clearly observed, indicating the lattice expansion due to the substitution of Co^{3+} by Bi^{3+}. This could be attributed to the fact that ionic radius of

Bi^{3+} (1.17A°) is greater than that of Co^{3+} (0.65A°) and Mn^{3+} (0.785 A°). The lattice parameter '***a***' obtained from the analysis of XRD pattern for the samples with cubic unit cell for different compositions are given in the Table. 3.1.

Table 3.1. *Lattice constant and unit cell volume for $Bi_xCo_{2-x}MnO_4$.*

Composition	Lattice constant, *a* (Å)	Unit cell Volume $(Å)^3$
x =0.0	8.27268	566.1593
x =0.1	8.31045	573.9494
x =0.2	8.32425	576.8134
x =0.3	8.32796	577.5849

From the XRD results we infer that $Bi_xCo_{2-x}MnO_4$ is having single phase cubic spinel structure in space group F*d3m* and the lattice constant increases almost linearly with Bi content up to 0.2, obeying Vegard's law [22]. However, for x = 0.3, a small increase in '***a***' is noticed (did not follow the linear behavior, see inset of Fig.3.1.), which suggests that the system has approached to the solubility limit of Bi in the system. In these circumstances, it is not unfair to say that only a small amount of Bi^{3+} can be substituted in the system.

Fig. 3.2 shows the SEM micrographs of the $Bi_xCo_{2-x}MnO_4$ ($0.0 \leq x \leq 0.3$) samples taken at room temperature. The SEM images show a uniformly developed grain morphology and dense microstructure. The micrographs of the samples with x > 0 (Bi substituted) showed relatively greater homogeneity in the microstructure along with increased grain size. Histograms shown in the inset of each SEM micrographs quantitatively represent the increased grain size (~1μm to ~8 μm) due to Bi substitution.

Table 3.2. *The compositional analysis of $Bi_xCo_{2-x}MnO_4$, extracted from EDAX.*

Nominal composition	Bi	Co	Mn	Actual composition	Grain size(SEM) (μm)
$Bi_{0.0}Co_2MnO_4$	0.00	2.0	1.0	Co_2MnO_4	1.75
$Bi_{0.1}Co_{1.9}MnO_4$	0.09	1.9	1.0	$Bi_{0.09}Co_{1.9}MnO_4$	3.82
$Bi_{0.2}Co_{1.8}MnO_4$	0.18	1.8	1.0	$Bi_{0.18}Co_{1.8}MnO_4$	5.90
$Bi_{0.3}Co_{1.7}MnO_4$	0.26	1.7	1.0	$Bi_{0.26}Co_{1.7}MnO_4$	7.42

This suggests that Bi-substituted compositions have higher fraction of bigger crystalline grains. The stoichiometry of the above compositions was calculated by means of an electron beam microanalyser (EDAX) attached to SEM and is shown in the Table 3.2. It is important to mention that, for higher Bi concentration, stoichiometry of the sintered composition is found to deviate slightly from that of the nominal composition.

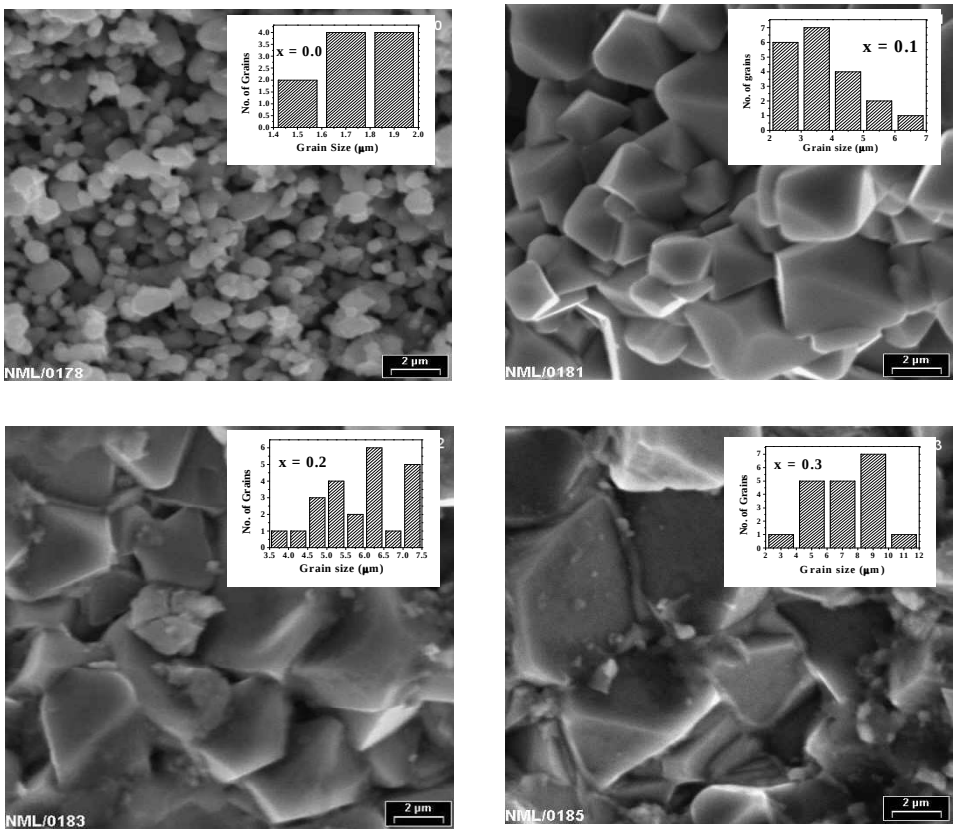

Fig.3.2. *SEM micrographs of $Bi_xCo_{2-x}MnO_4$, for x = 0.0, 0.1, 0.2 and 0.3. Insets show the respective histograms of grain sizes.*

3.2.2 DC conductivity studies

The dc conductivity measured in the temperature range 150 - 400 K exhibits semiconducting behavior, with resistivity reducing from 600 Ω-cm to 300 Ω-cm at room temperature, on increasing Bi-substitution (Fig. 3.3). For the sample with x = 0, the resistivity is of the order of kΩ-cm. The decrease in resistivity can be

attributed to the Bi-induced stabilization of the solid solution in comparison to less conducting pure phase, which is evidenced by an increase of grain size that reduces the number of grain boundaries. Also the number of charge carriers increases as the number of Co^{3+} ions in low spins state decreases on Bi-substitution. The basic conduction mechanism is taken as the hopping of electrons between non-equivalent valence states existing at octahedral and tetrahedral sites.

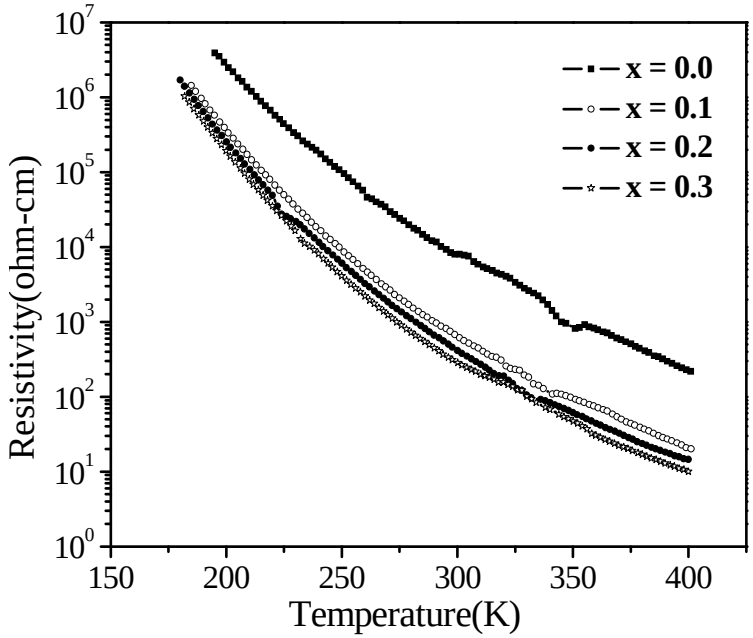

Fig. 3.3. *Plot of dc resistivity as a function of temperature for $Bi_xCo_{2-x}MnO_4$ (x = 0.0, 0.1. 0.2 and 0.3) samples.*

The dc conductivity behaviour can be explained using the Arrhenius relation,

$$\sigma_{dc} T = \sigma_0 \exp(-E_{act}/k_B T) \quad \text{---- (3.1)}$$

where σ_0 is the pre-exponential factor and is a characteristics of the material depending on lattice parameter and phonon frequency [23], k_B is Boltzmann's constant, T is absolute temperature and E_{act} is the activation energy associated with the hopping process. The deviation from linearity in the log $\sigma_{dc}T$ vs. 1000/T plots indicates that the small polaron hopping model is valid only at relatively higher temperatures for lower Bi-substitution and over a wider temperature range for higher Bi-substitution (see Fig. 3.4). The Debye temperature θ_D, is approximately obtained as the twice the temperature where curves of log $\sigma_{dc}T$ vs. 1000/T deviates from

linearity [24]. θ_D, phonon frequency (ν_{ph}, obtained from θ_D) and E_{act} calculated from the plots of log $\sigma_{dc}T$ vs. 1000/T for all the compositions is given in Table 3.3. E_{act} is found to decrease with Bi-substitution in the higher temperature region. The value of ν_{ph} decreases with the increasing Bi-substitution, resulting in the weakening of Co-Mn coupling. Thus, the substitution of Bi in the system tends to delocalize the charges and improve the electrical conductivity.

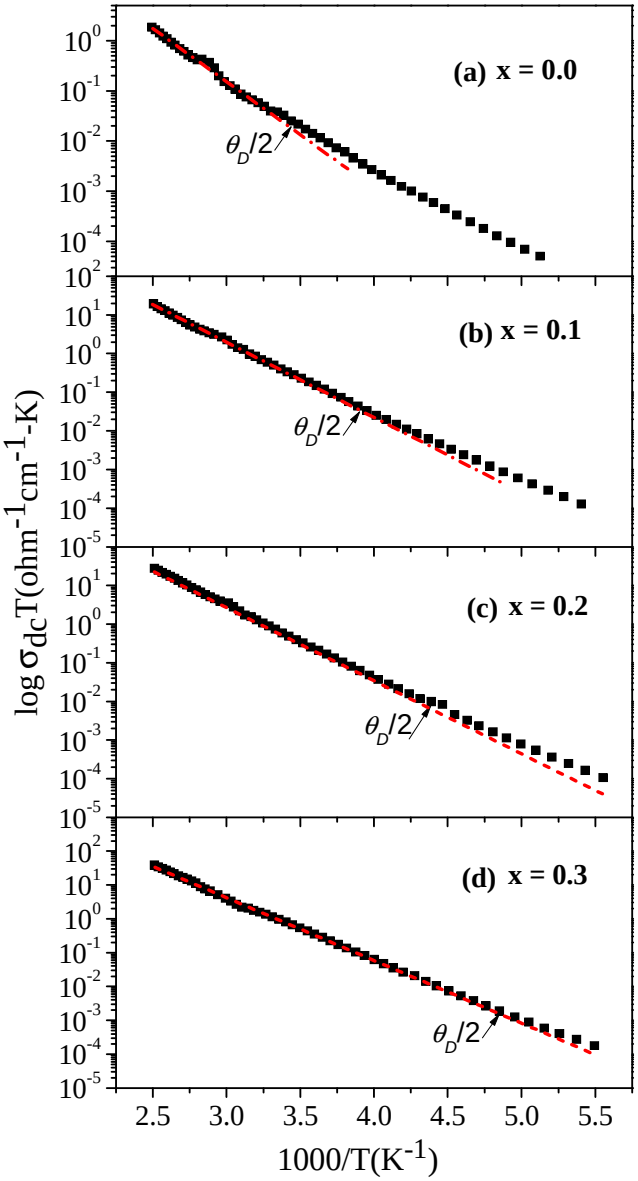

Fig. 3.4. *Log $\sigma_{dc}T$ vs. 1000/T plots for $Bi_xCo_{2-x}MnO_4$ (x = 0, 0.1. 0.2 and 0.3) samples. The dashed lines are fit to the data obtained using equation (3.1).*

Table 3.3. *DC activation energy, Debye temperature and phonon frequency at 300 K for* $Bi_xCo_{2-x}MnO_4$.

Composition	dc activation energy(eV)	Debye Temperature, θ_D (K)	Phonon frequency ($\times 10^{13}$) Hertz
x = 0.0	0.1813	629	1.31
x = 0.1	0.1651	589	1.23
x = 0.2	0.1628	473	0.98
x = 0.3	0.1591	429	0.89

According to VRH Model, the dc conductivity (σ_{dc}) is proportional to exp $(-T_0/T)^{1/4}$, T_0 being the characteristic temperature. In the low temperature region, the conduction may follow the variable range hopping (VRH) model [25-27]. Figure 3.5 shows the variation of log σ_{dc} vs. $T^{-1/4}$ which fits linearly in low temperature regime, indicating the validity of variable range hopping mechanism.

According to VRH theory [25],

$$k_B T_0 = 18\alpha^3 / N(E) \qquad \text{---- (3.2)}$$

where N(E) is the density of states at the Fermi level and $1/\alpha$ corresponds to the localization length. From Fig. 3.5, we have found that the value of T_0 increases with Bi-substitution ($T_0^{1/4}$ varying from 100 for x = 0.0 to 118 for x = 0.3), which suggests the modification of the density of states. The plots clearly reveal that VRH model is applicable in the lower temperature range of measurement. The mean hopping distance $R_h(T)$ and hopping energy $E_h(T)$ can be written at a given temperature, T , as [28],

$$R_h(T) = \frac{3}{8}(\alpha^{-1})\left(\frac{T_0}{T}\right)^{1/4} \qquad \text{---- (3.3)}$$

$$E_h(T) = \frac{1}{4} k_B T^{3/4} T_0^{1/4} \qquad \text{---- (3.4)}$$

Using the fitted values of T_0, in the above equations, the values of $N(E_F)$, R_h(250 K) and E_h(250 K) were estimated by taking the localization length as 0.14 nm, the value reported by Cheng *et al* [29] for this type of material. The above parameters for $Bi_xCo_{2-x}MnO_4$ (x = 0.0, 0.1 and 0.3) are tabulated in Table 3.4.

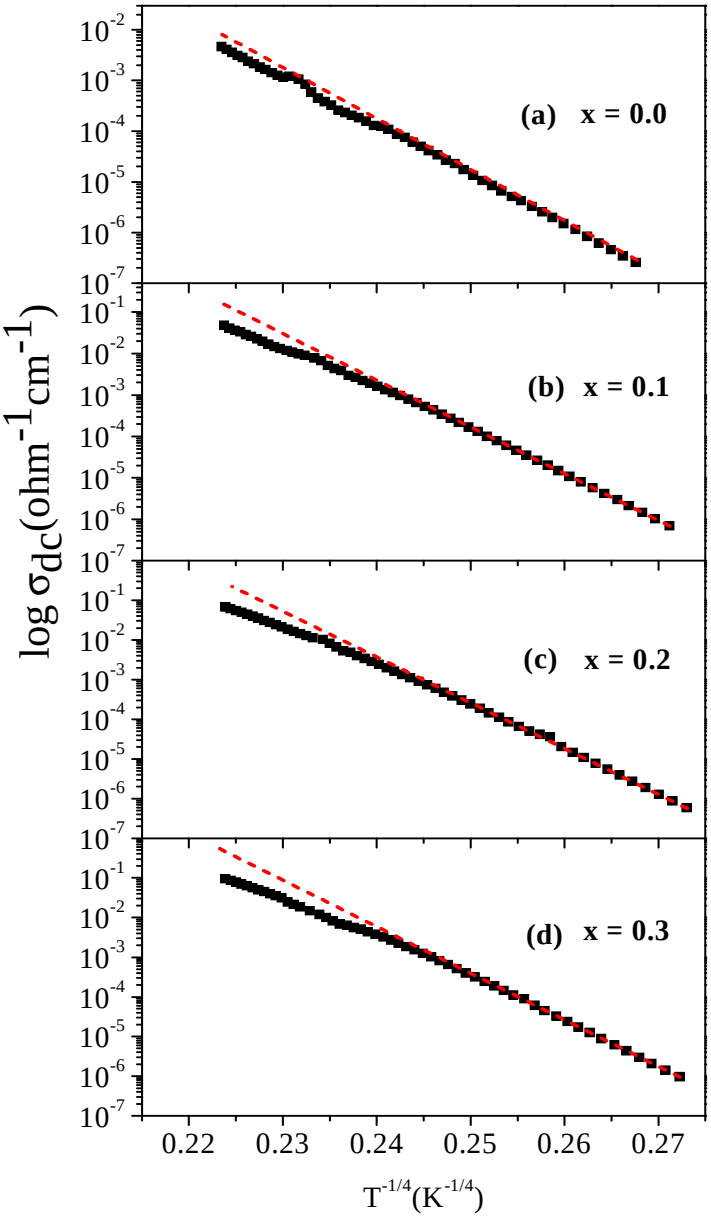

Fig. 3.5. *Log (σ_{dc}) vs. $1/T^{1/4}$ plots for $Bi_xCo_{2-x}MnO_4$ (x = 0, 0.1. 0.2 and 0.3).*

It is observed that $N(E_F)$ decreases along with an increase in the hopping energy E_h (250K) values with increasing Bi concentration. Also, the value of hopping distance R_h (250K) is found to increase. This happens for the lowered concentration of charge carriers at the Fermi level that decreases the electrical conductivity of the system.

Table 3.4. *Density of states at Fermi level $N(E_F)$, hopping distance (R_h) and hopping energy (E_h) for $Bi_xCo_{2-x}MnO_4$.*

Composition	$N(E_F)$ $(eV^{-1}cm^{-3}) \times 10^{20}$	R_h (nm) (250K)	E_h (eV) (250K)
x = 0.0	7.605	1.205	0.135
x = 0.1	4.834	1.349	0.152
x = 0.3	3.922	1.422	0.159

On comparing the two models for the dc conductivity of the $Bi_xCo_{2-x}MnO_4$ samples reveal that small polaron hopping model is more fitting, with the exhibited conductivity.

3.2.3 Dielectric constant and dielectric loss

Figure 3.6 (a-d) show the dielectric constant (ε′) as a function of temperature (T) at various frequencies (100 kHz to 1.1 MHz), for $Bi_xCo_{2-x}MnO_4$ ($0.0 \leq x \leq 0.3$) samples. It is evident from Fig. 3.6 (a) that for x = 0 composition, the dielectric constant remains almost constant up to 204 K at 100 kHz, then increased sharply with the increase in temperature. Within the investigated temperature range, no peak is observed in ε′ vs. T dependence. With the Bi substitution (x = 0.1) the overall dielectric constant values are increased and the temperature up to which the dielectric constant remains constant is also increased to T = 230 K (for 100 kHz). However, a well defined broad peak-like structure (FE transition) appears at a temperature T_c = 366 K.

This peak temperature is found to shift towards a higher temperature with the increase in frequency. With further increase in the Bi-substitution (x = 0.2), the dielectric behaviour is modified and exhibits two transitions, first transition is observed at 307 K and the second one at 413 K, for 100 kHz. The peak-like structures in temperature dependent ε′ and the shift in transition temperature (corresponds to ε'_m) towards higher temperature with the increase in frequency indicates that these materials exhibit relaxor ferroelectric behaviour.

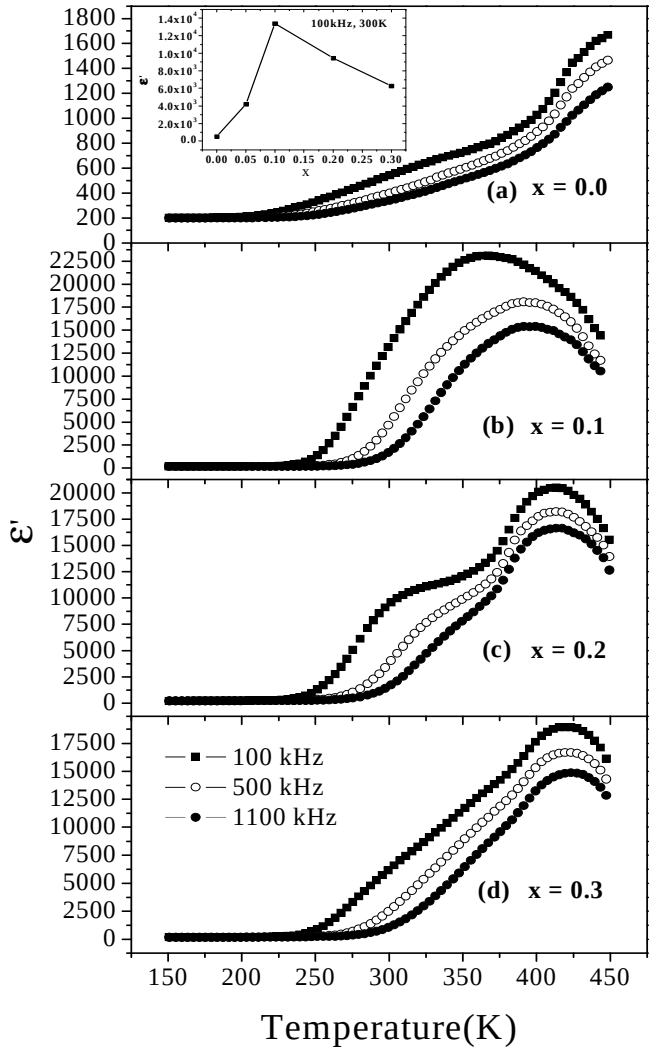

Fig. 3.6. *Plot of dielectric constant, ε′ as a function of temperature for $Bi_xCo_{2-x}MnO_4$ (x = 0.0, 0.1, 0.2 and 0.3). The inset shows the composition dependence of ε′.*

The first transition has strong relaxor behaviour, whereas the second one does not change appreciably with the frequency. It has been observed that the dielectric constant falls slightly for higher Bi-substituted compound (x = 0.2 and x = 0.3). Also, for x = 0.3, low temperature FE transition is found to disappear and high temperature transition became almost non-relaxor in nature. This may be due to the polarization associated with the $6s^2$ lone pair electrons of Bi, and stabilization of grain growth. Notable broadening at FE transition indicates a diffusive phase

transition. Inset of Fig. 3.6 shows the value of the dielectric constant as a function of Bi-substitution measured at 300 K and 100 kHz.

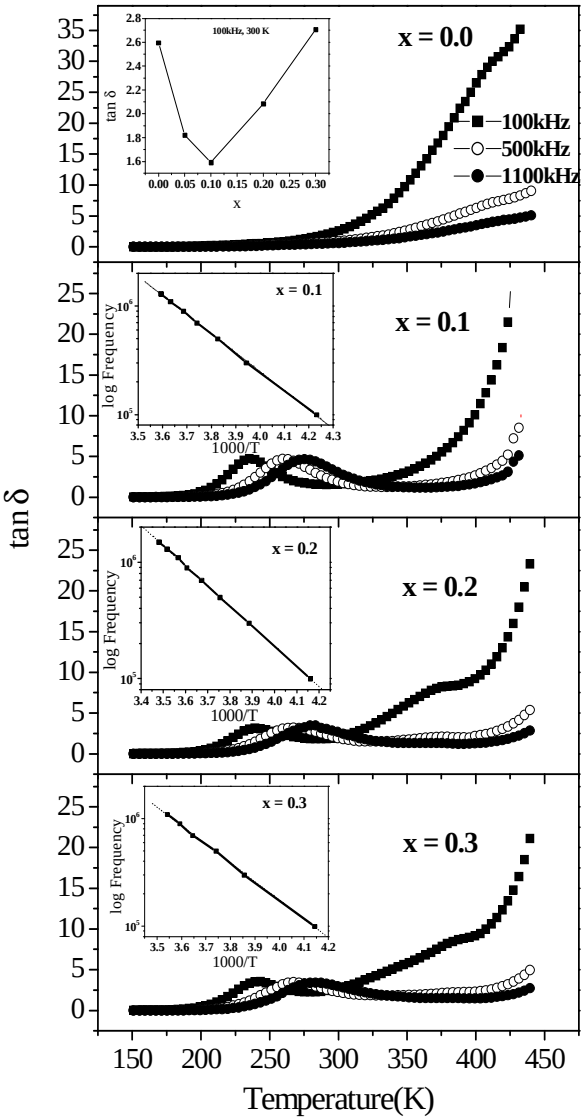

Fig. 3.7. *The plot of tan δ as a function of temperature for $Bi_xCo_{2-x}MnO_4$ (x = 0.0, 0.1. 0.2 and 0.3). The inset shows the composition dependence of tan δ and lower insets are depicting the loss relaxation.*

The temperature dependence of the dielectric loss (*tanδ*), for all the samples, at selected frequencies is shown in Fig.3.7. At low temperature (below 200K), *tanδ* is found to be almost independent of frequency for all the samples. However for a

given composition and temperature, ε′ and $tan\delta$ were found to decrease with the increase in the frequency. The overall higher values of tan δ are observed in all Bi-substituted samples, which may be due to an increase in dc conductivity of the materials with the Bi substitution. A peak like structure in $tan\delta$ as a function of temperature has been observed for Bi-substituted samples. The temperature, at which the peak in $tan\delta$ appears, shifts with frequency. Typical relaxor type behaviour is again demonstrated using Arrhenius relation, as shown in the inset of Fig.3.7. The strong frequency dependent dielectric properties are attributed to the interaction among the free carriers (electrons or holes) with potential barriers at grain boundaries, resulting in the enhancement of conductivity [30]. To further establish the relaxor behaviour, frequency dependence of the dielectric properties has been investigated. Fig. 3.8 shows the variation of ε′ and $tan\delta$ (Inset of Fig.3.8) with frequency at room temperature. It is clear that, both ε′ and $tan\delta$ decrease with increase in frequency which is the normal dispersion behaviour semiconducting oxides. This attributed to the relatively higher conductivity of the materials, due to the existence of space charge and trapped charges.

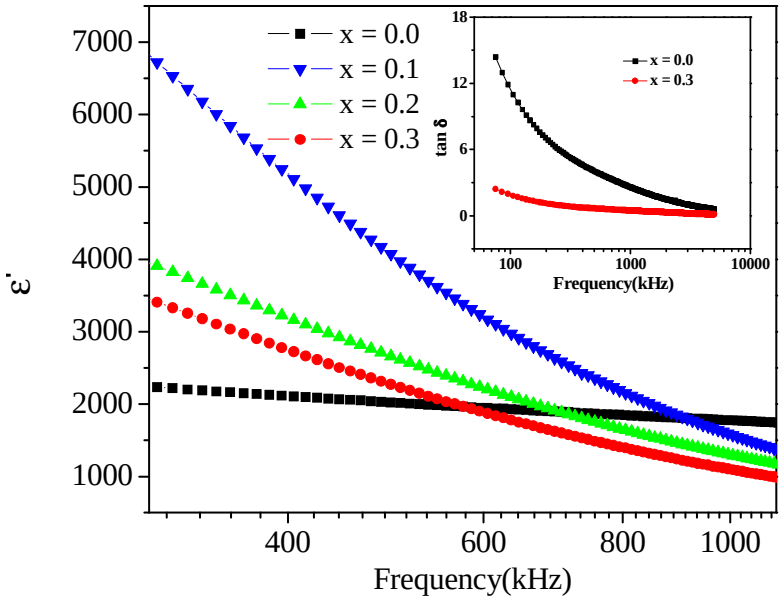

Fig. 3.8. *Frequency dispersion of ε′ for $Bi_xCo_{2-x}MnO_4$ (x = 0, 0.1. 0.2 and 0.3) and Inset: $tan\delta$ vs. frequency $Bi_xCo_{2-x}MnO_4$ (x = 0. 0 and 0.3) at room temperature.*

Among the various contributions to polarization such as electronic, ionic, dipolar and space charge polarizations, the contribution of space charge depends upon the purity of the system. In the present case, Bi ions are likely to occupy octahedral positions and create bonding defects. Capacitance measurements on these samples have been carried out in the high frequency range starting from 100 kHz to 1.1MHz, greater than the frequencies corresponding to the time constants (RC) suggested by the Catalan [31]. This rule out the possibility of contribution from Maxwell–Wagner interfacial polarization (dominant at low frequencies) to the capacitance. At high frequencies most of the systems exhibits the intrinsic capacitance and need not be an artifact effect. Wang *et al* [32] observed two kinds of capacitive contribution above 100 K in $TbMnO_3$ system by grains (dipolar effect i.e. hopping of charge carriers within the grain) and grain boundary effect (i.e. internal layer barrier capacitor, IBLC) and the system followed the universal dielectric response (UDR). In UDR model, localized charge carriers hopping between spatially fluctuating lattice potentials not only produce the conductivity but also give rise to dipolar effects. Accordingly, at a given temperature a linear behaviour should be obtained in the plot of log (fε´) vs log (f), where f is the frequency.

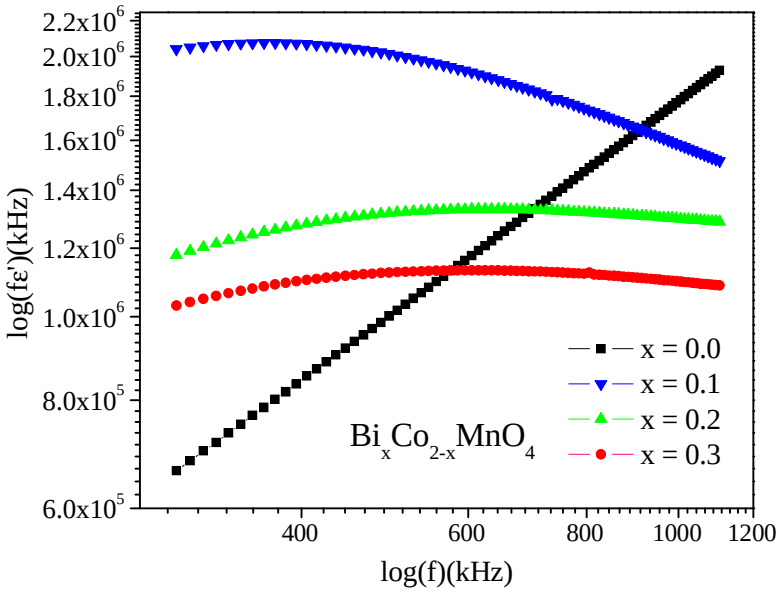

Fig. 3.9. *Plot of log (fε´) vs. log f for the $Bi_xCo_{2-x}MnO_4$ (x = 0, 0.1. 0.2 and 0.3) at 300K.*

Figure 3.9 represents the log (fε′) vs log (f) plot for $Bi_xCo_{2-x}MnO_4$ samples at room temperature and f in the range 100 kHz to 1.1 MHz, where exact straight line behaviour for undoped system i.e. Co_2MnO_4 is observed whereas for doped samples it is not the case. This analysis straight away rules out the possibility of any kind of conductivity contribution in dielectric constant as per UDR, in Bi substituted system. Again it is well known that the exponential increasing background in loss tangent implies that the background is associated with the hopping conductivity. The loss tangent vs. temperature shown for Bi substituted Co_2MnO_4 does not show the exponential increase and further support to the fact that these samples do not follow the UDR behavior.

From the above mentioned results it is evident that the present system exhibit relaxor ferroelectric behaviour for all the samples. To understand the nature of relaxor behaviour, the well known method is to construct the Cole-Cole plot [33]. In this conventional method ε' is plotted as a function of ε'' (imaginary part of dielectric constant, i.e. dielectric loss factor) to get information on the distribution of relaxation times. For the Debye type relaxor behavior the data fits into a semicircular curve. However, the Cole-Cole plots for $Bi_xCo_{2-x}MnO_4$ ($0.0 \leq x \leq 0.3$) samples are not semi-circular, owing to relatively higher conductivity of the samples [34].

From the plots representing the temperature dependence of the real part of the dielectric constant, ε' at different frequencies (Fig. 3.6), it is observed that ε' varies very slowly with temperature up to a temperature $\theta_D/2$, where θ_D is the Debye temperature [35]. Above $\theta_D/2$, the values of ε' for all the samples increase with increase of temperature and decreases with an increase in the frequency. Such a behavior indicates the Debye-type dielectric relaxation process. Frequency dependent shift in ε'_m (dielectric constant maxima) towards the higher temperature was also exhibited by the samples, up to $x = 0.3$, as expected in relaxor ferroelectric materials.

Further, to understand the relaxation behaviour, we have calculated the real and imaginary part of M* (complex dielectric modulus) [24, 36]. The main advantage of using M* is to eliminate the electrode effect [37].

Complex dielectric modulus of a system can be represented as,

$$M^* = M' + iM'' \quad \text{---- (3.5)}$$

According to Macedo *et al* [36], the real and the imaginary parts of dielectric modulus are related to ε' and ε'' as,

$$M' = \frac{\varepsilon'}{\varepsilon'^2 + \varepsilon''^2} \quad \text{---- (3.6)}$$

$$M'' = \frac{\varepsilon''}{\varepsilon'^2 + \varepsilon''^2} \quad \text{---- (3.7)}$$

where, $M''/M' = \varepsilon'' / \varepsilon' = \tan\delta$, the dielectric loss factor which gives directly the phase difference due to absorption of energy. The dielectric modulus, M*, provides information when the dc conductivity is large compared with ac conductivity. Figure 3.10 and 3.11 show the temperature dependence of M' and M'' respectively at different fixed frequencies for the $Bi_xCo_{2-x}MnO_4$ ($0.0 \leq x \leq 0.3$) samples.

M' remains constant for all frequencies at lower temperature, and tends to reach a constant value, which shifts to a higher temperature region for higher frequencies. This indicates the thermally activated behaviour of dielectric constant for these samples. The plots of M'' vs. T show maxima, which shifts, to higher temperature for higher frequencies. This shift of peak temperatures at different frequencies also shows the signature of Debye – type relaxation behavior with a distribution of relaxation times. The corresponding frequency at the maxima of M'' is equal to the relaxation frequency f_r' at that temperature.

$$f_r = f_0 \exp(-\Delta/k_BT) \quad \text{---- (3.8)}$$

where f_0 – Debye phonon frequency ($k_B\theta_D/h$), k_B is Boltzmann's constant and Δ is the relaxation activation energy. At this frequency, hopping rate of the carriers is equal to that of the externally applied electric field. The obtained peaks in M''-T

plots indicate Debye-type relaxation behavior [38]. Broader peaks can be interpreted as being the consequence of distribution of relaxation times.

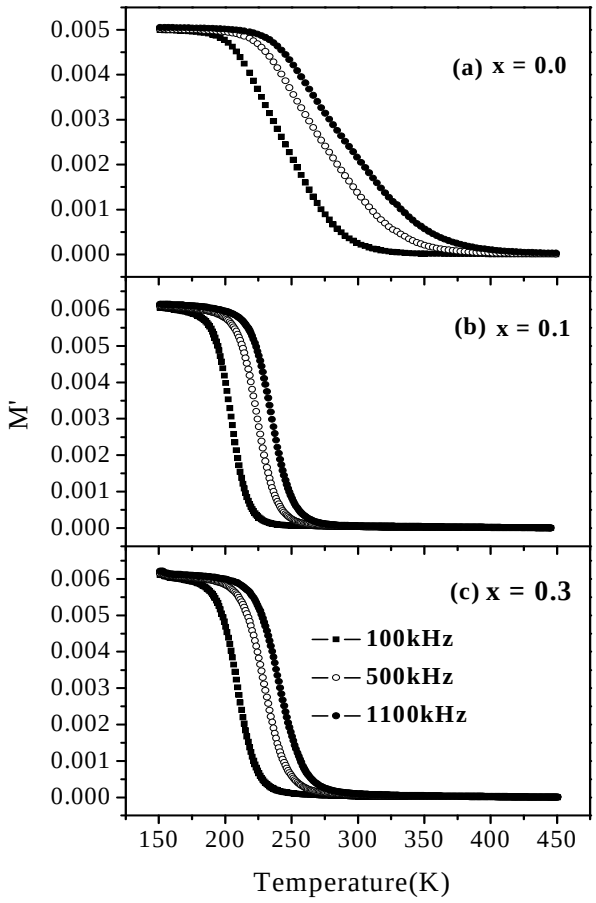

Fig. 3.10. *Temperature dependence of M´for $Bi_xCo_{2-x}MnO_4$ (x = 0.0, 0.1 and 0.3).*

The temperature dependence of the relaxation rate of $Bi_xCo_{2-x}MnO_4$ ($0.0 \leq x \leq 0.3$) samples is shown in the form of Arrhenius plots in insets of fig. 3.10 and relaxation activation energy is calculated. The values of activation energy deduced from dielectric relaxation are approximately equal to that obtained from dc conductivity. This may be due to the local displacement of electrons exchanged between $Mn^{2+/3+/4+}$ and Co^{3+} at octahedral sites in the distorted lattice, in the direction of applied field, eventually resulting the polarization in the materials, as reported for polarization in the aluminates [39]. This is in addition to the polarization appearing due to the $6s^2$ lone pair electrons of Bi.

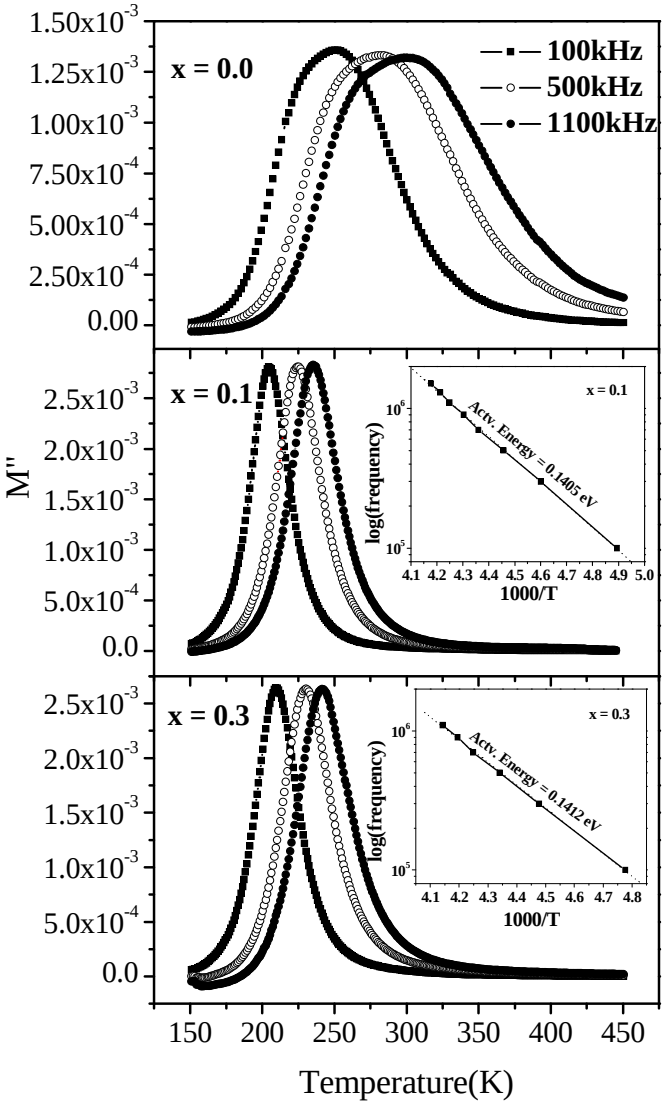

Fig. 3.11. *Temperature dependence of M″ for $Bi_xCo_{2-x}MnO_4$ (x = 0.0, 0.1 and 0.3), with insets showing the relaxation activation.*

The dielectric constant, ε′ of the $Bi_xCo_{2-x}MnO_4$ samples with x = 0, was about an order of magnitude smaller as compared to samples with x=0.1 and 0.2. The FE transition was not visible from the ε′ vs. T plots, within the high temperature limit (450 K) of our experimental setup. In other samples ($Bi_xCo_{2-x}MnO_4$ with x = 0.1, 0.2 and 0.3), FE transition was observed within the high temperature limit of the setup, with increased diffuseness.

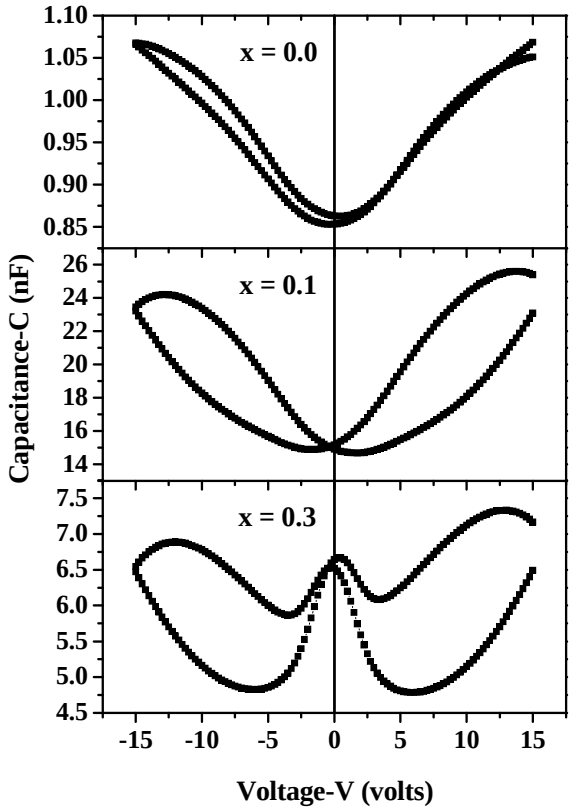

Fig.3.12. *Capacitance versus voltage behaviour for $Bi_xCo_{2-x}MnO_4$ (a) x = 0.0 (b) x = 0.1 and (c) x = 0.3.*

Finally, the variation in the dielectric constant and dielectric loss appears to be non-linear with the composition (shown in the top insets of Figures 3.6 and 3.7). It is due to the stabilization of structure with the increase in Bi substitution up to x = 0.2. Also there is chance of the formation of vacancies at the octahedral sites as the Bi content increases. The capacitance versus voltage (C-V) measurements of the $Bi_xCo_{2-x}MnO_4$ with x = 0 to 0.3 (using an applied voltage of 15 V) showed a typical butterfly-shaped loop in the C-V curves (very narrow for x = 0), as shown in Fig. 3.12. This demonstrates the ferroelectric nature of the Bi-substituted samples. Similar to the dielectric constant (ε′) measurement, the C-V curves show diffuseness that increases with x, and may be attributed to the strain induced by Bi-substitution, owing to its larger ionic radius compared to the other cations.

In normal dielectric behaviour, the dielectric constant remains almost constant in high frequency region because beyond a certain frequency of electric

field, the charge carriers do not get enough time for long range hopping before the reversal of field. Only some short range hopping of carriers within the range of one lattice spacing prevails. So the polarization decreases as the frequency of applied field is increased. In MHz region, the charge carriers would not have even started to move before the field reversal and ε' will have only a small value at very high frequency [40].

3.2.4 AC conductivity studies

The ac conductivity (σ_{ac}) was studied over a frequency range of 100 kHz to 5 MHz, for temperature varying from 150 K to 425 K. The σ_{ac} was calculated from the dielectric data, using following equation,

$$\sigma_{ac} = \varepsilon_0 \varepsilon' \omega \tan \delta \qquad \text{---- (3.9)}$$

σ_{ac} is found to increase for the $Bi_xCo_{2-x}MnO_4$ ($0.0 \leq x \leq 0.3$) samples with a greater Bi content especially in the high frequency region (Fig. 3.13). This indicates that the movement or hopping of the charge carriers is influenced by the neighborhood, i.e. enhanced by presence of Bi^{3+} ions. At higher frequencies (~ 2 MHz), σ_{ac} is decreased for all compositions (not shown here), indicating the inability of hopping of charges to follow the high frequency of the applied field. The total conductivity of the material at a frequency can be written as,

$$\sigma_{total}(\omega) = \sigma_{dc} + \sigma_{ac}(\omega) \qquad \text{---- (3.10)}$$

where, hopping conduction arising from Bi-substitution is responsible for the enhancement of both dc and ac conductivities. The dc conductivity is the $\omega \rightarrow 0$ limit of $\sigma_{total}(\omega)$. For semiconductors and disordered systems the ac conductivity follows the power law behaviour [41],

$$\sigma_{ac}(\omega) = A\,\omega^s \qquad \text{---- (3.11)}$$

where A is temperature dependent constant and s is the frequency exponent ($s \leq 1$).

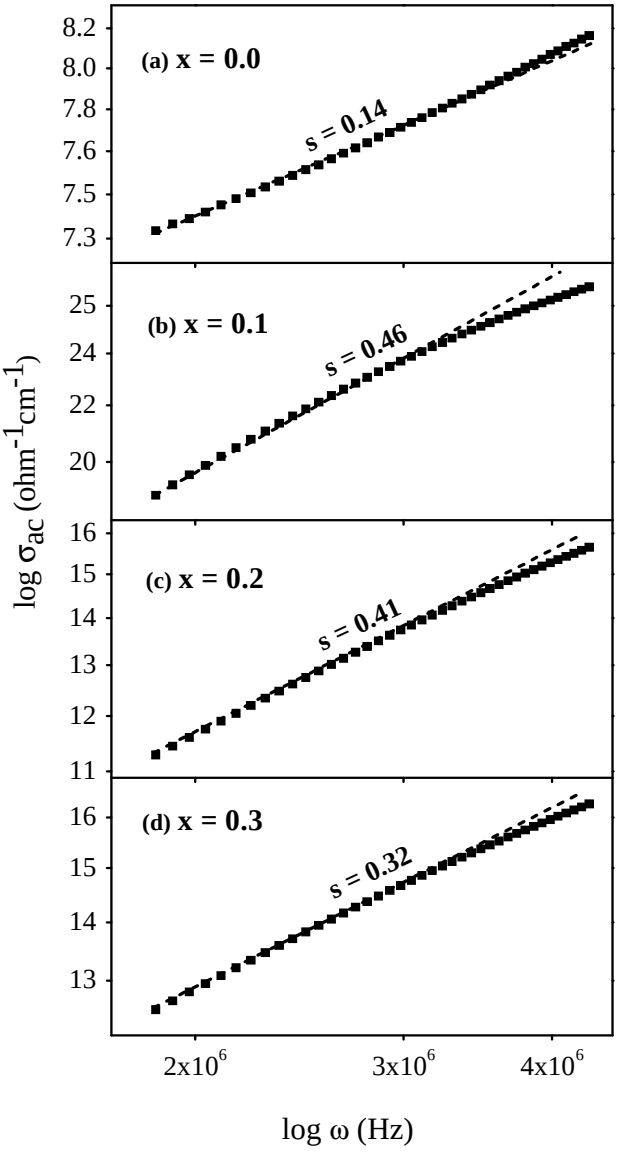

Fig. 3.13. *Log σ_{ac} vs. log ω at 300K, for $Bi_xCo_{2-x}MnO_4$ (x = 0, 0.1. 0.2 and 0.3).*

From the log-log plots drawn for σ_{ac} vs. ω (Fig.3.13) for the different compositions at room temperature, the slope directly provides the value of dimensionless frequency exponent, s and it is clear that s varies with Bi content. Also it can be noted that, magnitude of s starts to decrease towards higher frequency, for the Bi-substituted compositions. This further establishes absence of any contribution from UDR (where s increases with increase in frequency), in deciding the dielectric property of the Bi-substituted Co_2MnO_4 system.

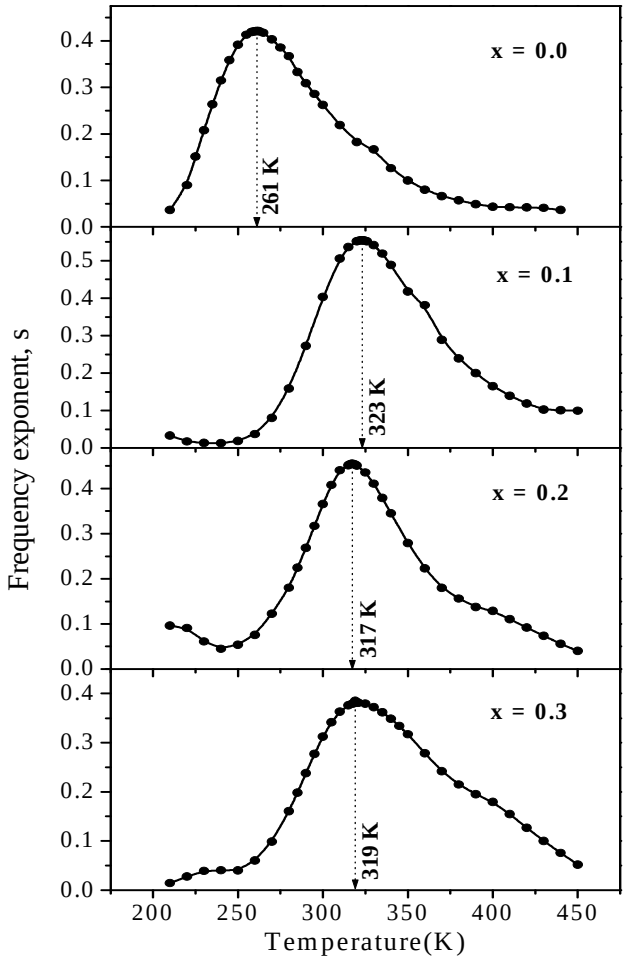

Fig. 3.14. *Temperature dependence of frequency exponent,* ***s*** *for* $Bi_xCo_{2-x}MnO_4$ *(x = 0.0, 0.1, 0.2 and 0.3).*

The ac conductivity also shows frequency dependent dispersion similar to dielectric behaviour discussed earlier. In the case of disordered solids, σ_{ac} is an increasing function of frequency. The temperature dependence of frequency exponent s is shown in Fig.3.14. Frequency exponent s is a measure of correlation between σ_{ac} and frequency. For random hopping of carriers, s should be 0 (frequency independent σ_{ac}) and tends to 1, as correlation between σ_{ac} and ω increases. Qualitatively small polaron tunneling (SPT), usually associated with an increase of s with the increase in temperature indicates the activated behaviour of polarons, which is independent of intersite separation. On the other hand correlated barrier hopping (CBH) shows a decrease in s with increasing temperature, indicating the thermally

activated behavior of electron transfer over the barrier between two sites having their own coulombic potential wells. Temperature dependence arising from the correlation between barrier height and intersite separation are the characteristics of CBH model [21]. From the temperature dependent plots of s (Fig.3.13), it is clear that for pure Co_2MnO_4, the frequency exponent, s increases up to 260 K and then decreases. For this sample, SPT model is suitable up to 260 K at which maximum correlation is exhibited between σ_{ac} and ω. Above 260 K, CBH model is valid, where dc conductivity contribution is not negligible. For the Bi-substituted samples also, SPT and CBHs models seem to fit, which explain the conduction mechanism with better correlation at higher temperature ~ 320 K.

3.3 Conclusions

In summary, we have successfully synthesized polycrystalline bulk samples of $Bi_xCo_{2-x}MnO_4$ ($0 \leq x \leq 0.3$) by standard solid state reaction technique. The effect of the substitution of non magnetic Bi^{3+} ion in Co_2MnO_4 was investigated by means of structural, microstructural and electrical studies. The following observations have been made on the basis of the experiments performed with the bulk samples.

(i) The XRD analysis of $Bi_xCo_{2-x}MnO_4$ ($0 \leq x \leq 0.3$) indicates that all samples exhibit a single phase nature. All the samples are indexed in cubic spinel structure and lattice parameter '*a*' is found to increase with Bi content. Analysis of XRD data and SEM micrographs shows that Bi content $x > 0.3$ is difficult to accommodate, while retaining the cubic spinel structure.

(ii) The temperature dependent dielectric data represents a diffused ferroelectric phase transition; with an increasing ferroelectric T_c as the Bi content increases. Bi-substituted samples have moderately high dielectric constant depicting better ferroelectric characteristics along with Debye-type relaxation behavior.

(iii) The dispersion of ac conductivity has been estimated in terms of frequency exponent s, which varies with temperature and is explained using small polaron tunneling (SPT) model and correlated barrier hopping (CBH) model.

(iv) The dc conductivity analysis revealed the semiconducting nature of the spinel compounds. The hopping of charges between cations with different valence states at the octahedral sites is considered to be the origin of all the dielectric and electrical properties of the Bi-substituted Co_2MnO_4.

The establishment of tunable ferroelectric nature of the multiferroic Bi-substituted Co_2MnO_4 proposes the candidature of these materials for various technological applications, including ferroelectric RAMs.

References

1. B. Antic, G. F. Goya, H. R. Rechenberg, V. Kusigerski, N. Jovic and M. Mitric., J. Phys.:Condens. Matter **16** (2004) 651.

2. S. Kumar, Alimuddin, R. Kumar, A. Dogra, V.R.Reddy and A. Banerjee., J. Appl. Phys. **99** (2006) 08M910.

3. N. Fujiwara, H. Yasuoka and Y. Ueda, Phys. Rev. B **57** (1981) 3539.

4. J. L. Dormann and M. Nogues., J. Phys.: Condense.Matter. **2** (1990) 1223.

5. G. Srinivasan, E.T.Rasmussen and R.Hayes, Phys. Rev. B **67** (2003) 014418.

6. E. J. W. Verwey and E. L. Heilmann., J.Chem.Phys **15** (1947) 174.

7. Y. Ikedo, J. Sugiyama, H. Nozaki, H. Itahara, J. H. Brewer, E. J. Ansaldo, G. D. Morris, D. Andreica and A. Amato, Phys.Rev.B **75** (2007) 054424.

8. Y. Yamasaki, S. Miyasaka, Y. Kaneko, J. P. He, T. Arima and Y. Tokura, Phys. Rev. Lett. **96** (2006) 207204.

9. T. Kimura, T. Goto, H. Shintani, K. Ishizaka, T. Arima and Y. Tokura, Nature **426** (2003) 53.

10. T. Goto, T.Kimura, G. Lawes, A. P.Ramirez and Y. Tokura, Phys. Rev. Lett. **92** (2004) 257201.

11. D. K. Shukla, S. Mollah, R. Kumar, P. Thakur, K. H. Chae, W. K. Choi and A. Banerjee, J. Appl. Phys. **104** (2008) 033707.

12. W Prellier, M P Singh and P Murugavel., J. Phys.: Condens. Matter **17** (2005) R803.

13. P. Baettig and N. A. Spaldin, Appl. Phys. Lett. **86 (**2005) 012505.

14. O. Heyer, N. Hollmann, I. Klassen, S. Jodlauk, L .Bohat´y, P. Becker, J. A. Mydosh, T. Lorenz and D. Khomskii, J. Phys.: Condens. Matter **18** (2006) L471.

15. K. Yoshiia, N. Ikedab, S. Moric, J. Mag. Mag. Mater. **310** (2007) 1154.

16. T. Suzuki, K. Adachi, T. Katsufuji, J. Mag. Mag. Mater. **310** (2007) 780.

17. J. Hemberger, P. Lunkenheimer, R.Fichtl, H.A.Krug von Nida and V.Tsurkan, A.Loidl, Nature **434** (2005) 364.

18. D. Pyke, K. K. Mallick, R. Reynolds and A. K. Bhattacharya, J. Mater. Chem. **8** (1998) 1095.

19. H. T. Zhnag and X. H. Chen, Nanotechonlogy **17** (2006) 1384.

20. J. L. Martin de Vidales, E. Vila, R. M. Rojas and O. Garefa-Martinez, Chem. Mater **7** (1995) 1716.

21. J. Wang, A. Scholl, H. Zheng, S. B. Ogale, Viehland, and R. Ramesh, Science **307** (2005) 1203b.

22. X. Liu, F. Gao, and C. Tian, Materials Research Bulletin **43** (2008) 693.

23. V. Massarotti, D. Capsoni, M. Bini, and G. Chiodelli, Journal of Solid state Chemistry, **131** (1997) 94.

24. D. K. Shukla, S. Mollah and R. Kumar, J. Appl. Phys **101** (2007) 13708.

25. N. F.Mott, J.Non-Cryst Solids **1** (1968) 1.

26. M. Viret, L. Ranno, J. M. D. Coey, Phys. Rev. B **55** (1997) 8067.

27. K. De, R. Ray, R. N. Panda, S. Giri, H. Nakamura and T. Kohara, J. Mag. Mag. Mater. **288** (2005) 339.

28. S. Ravi and M. Kar, Physica B 348 (2004) 169.

29. C. S. Cheng, M. Serizawa, H. Sakata, T. Hirayama, Mate. Chem. Phys. **53** (1998) 225.

30. O. Raymond, R. Font, N. Suarez-Almodovar, J. Portelles and J. M. Siqueiros., J. Appl. Phys. **97** (2005) 084107.

31. G. Catalan, Appl. Phys. Lett. **88** (2006) 102902.

32. C. C. Wang, Y. M. Cui and Y. W. Zhang, Appl. Phys. Lett. **90** (2007) 012904.

33. K. S. Cole and R. H. Cole J. Chem. phys. **9** (1941) 341.

34. F. A. Grant, J. Appl. Phys. **29** (1957) 176.

35. A. H. Elsayed and A. M. Haffz, Egypt. J.Solids **28** (2005) 53.

36. P. B. Macedo, C. T. Moynihan and R. Bose , J.Chem. Glasses **13** (1972) 171.

37. Y. Suzhu, P. Hing and H. Xiao, J. Appl. Phys. **88** (2000) 398.

38. K. K. Som, S. Mollah, K. Bose and B. K. Chaudhuri., Phys. Rev. B **47** (1993) 534.

39. I. Halevy, D. Dragoi and E. Ustunday, J.Phys. Condens. Matter **14** (2002) 10511.

40. S. Kurien, J. Mathew, S. Sebastian, S. N. Potty and K. C. George; Mat. Chem. Phys. **98** (2006) 470.

41. S.R. Elliot, Adv. Phys. **36** (1987) 135.

Chapter 4

Electronic, Magnetic and Magnetoelectric Studies of $Bi_xCo_{2-x}MnO_4$ ($0 \leq x \leq 0.3$)

This chapter presents detailed study of electronic, magnetic and magnetoelectric properties of a series of polycrystalline multiferroic $Bi_xCo_{2-x}MnO_4$ system prepared by a solid-state reaction route. Raman spectroscopic measurements have been utilized to confirm the octahedral occupation of trivalent cations. The effect of Bi^{3+} substitutions in Co_2MnO_4 on the distribution of magnetic moments has been studied through NEXAFS, isothermal magnetization hysteresis, temperature dependent magnetization and magnetic field dependent dielectric measurements.

4.1 Introduction

In multiferroic materials, magnetism and ferroelectricity coexist and these materials enfold physics for various future technological applications and have received the world wide attention from scientific community working in the field of materials sciences [1-9]. The simultaneous occurrence of ferromagnetism/ ferrimagnetism (FM) and ferroelectricity (FE) and the coupling between these two order parameters could lead to the emergence of new storage media, which enable electrically reading/writing of the magnetic memories and vice versa, yielding more degrees of freedom from device application point of view. Coupling between electric and magnetic ordering could also provide basis for using these materials for magnetic field sensor applications. Among recently established magnetoelectric multiferroic materials, frustrated magnets and geometrical frustration of lattice degrees of freedom have been found to be the leading mechanisms for perovskite manganites and cubic spinels systems respectively [10]. However it is difficult to develop multiferroic materials with a sufficient amount of magnetoelectric coupling, because of the contrasting origins of these properties. Various alternate mechanisms have been proposed as a solution to the above problem, including the approach of achieving the ferromagnetism with non metallicity or ferroelectricity in centrosymmetric systems [7, 11]. In this context, for FE and FM to coexist in single phase, the atom which moves off centre to induce the electric dipole moment should be different from those that carry the magnetic moment (atoms with partially filled *d* orbitals, responsible for FM). Recent *ab* initio calculations, for existing ferroelectrics suggest that atoms with d^0 configuration create more off centre distortion [4, 6]. In principle, coexistence of FE and FM can be achieved through either an alternative mechanism like a non–*d* electron for magnetism or through an alternative mechanism for ferroelectricity. In practice alternative mechanisms for ferroelectricity are pursued [1]. One such alternative followed is the induction of non magnetic ions having stereochemically active lone pair of electrons that may introduce off centering in the structure containing transition metal ions (TMI) [12]. Spinel oxides exhibit a variety of interesting functional properties such as

magnetoelectric multiferroic properties, thermoelectric property, colossal magnetoresistivity (CMR), spintronics, magnetic recording, etc., depending on the species and stoichiometry of cations occupying the A and B sites in AB_2O_4 type structure [13 - 19]. Multiferroic property in many of the spinel oxides have been predicted [20] and studied, but found to possess only weak magnetoelectric coupling [21]. The crystal symmetry in spinel oxides offers ample space to material-scientists for testing/designing of new functional properties with numerous permutations and combinations possible among A and B sites. These materials are time honored systems owing to their extraordinary magnetic and electric properties that became the source of most fascinating magnetoelectric property, which can be tuned accurately by changing the chemical composition through cation redistribution.

In the Co based spinel oxides the substituted trivalent metal ion occupies the octahedral sites while cobalt ions are distributed over both octahedral (Co^{3+} ions in low spin $t_{2g}^6\ e_g^0$ state) and tetrahedral sites (magnetic Co^{2+} ions in high spin $e_g^4 t_{2g}^3$ state) [19]. Bi substituted Co_2MnO_4, is found to crystallize in normal spinel with a space group O_h^7-$F\,d\,\bar{3}\,m$ [22]. Bi-substitution leads in to the competition between the preference of occupancies of Co^{3+}/Mn^{3+} cations at octahedral site, which effect their electrical and magnetic properties [23, 24]. In $Bi_xCo_{2-x}MnO_4$ samples, Bi^{3+} with $6s^2$ lone pair electrons at the octahedral sites instead of magnetic ions distorts the oxygen octahedron, consequently introduces ferroelectricity and influences the ferrimagnetic ordering of the parent system. Co_2MnO_4 exhibited ferrimagnetic behaviour with low coercivity and moderate magnetic saturation. Ferrimagnetism along with improved ferroelectric property with Bi-substitution in Co_2MnO_4 suggest that this material is a good candidate for the technological applications, involving magnetoelectric multiferroics. Mixed valence states of cations in spinel oxide are playing a key role in determining their electrical and magnetic characteristics, which needs fundamental understanding about the intriguing nature of spin state distribution and hybridization states. Knowledge of the electronic structure of the aforementioned material is desirable for designing the new multiferroic materials as well as important from the basic physics point of view. Owing to its simplicity and universality, near edge x-ray absorption fine structure (NEXAFS) technique is most

widely used in determining the valence states of atom and local symmetries in solids. In this chapter, NEXAFS spectra at the O K-, Mn $L_{3,2}$- and Co $L_{3,2}$- edges of $Bi_xCo_{2-x}MnO_4$ ($0 \leq x \leq 0.3$) samples along with the reference compounds Bi_2O_3, CoO, $LiCoO_2$, MnO and MnO_2, and Raman spectra are presented to explain the effect of Bi ion on magnetic and magnetoelectric properties of Co_2MnO_4.

4.2 Results and discussions

4.2.1 Raman scattering studies

The parent compound, Co_3O_4 that crystallizes in the normal spinel structure with O_h^7 spectroscopic symmetry, was shown to possess five Raman active modes, as $A_{1g} + E_g + 3F_{2g}$, with wave numbers 194.4 cm^{-1} (F^1_{2g}), 482.4 cm^{-1} (E_g), 521.6 cm^{-1} (F^2_{2g}), 618.4 cm^{-1} (F^3_{2g}) and 691 cm^{-1} (A_{1g}) [25]. The Raman mode at ~ 691 cm^{-1} (A_{1g}) is attributed to the characteristics of octahedral (o_h) sites (CoO_6) in the O_h^7 spectroscopic symmetry and the mode at ~ 195 cm^{-1} (F^1_{2g}) is attributed to the tetrahedral (t_d) sites (CoO_4). The broadening and shifting of Raman modes on Mn-substitution into the Co_3O_4 lattice, is already reported [26].

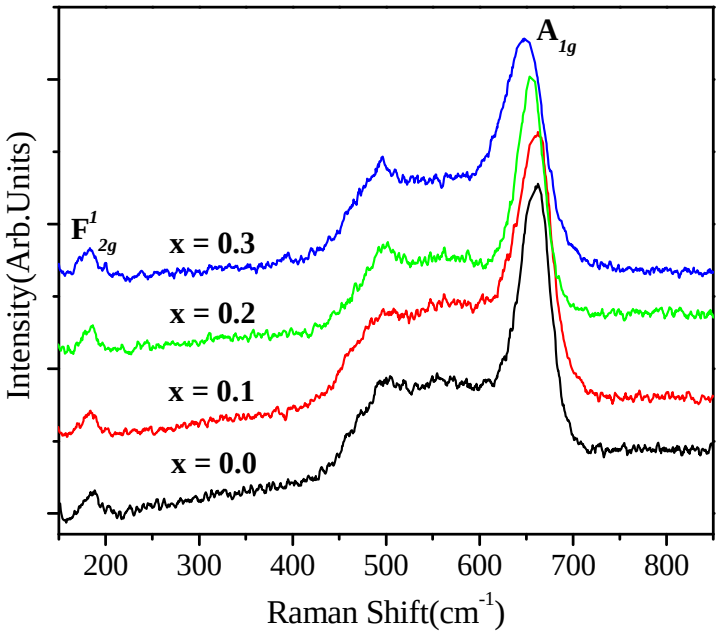

Fig. 4.1. *Raman scattering spectra collected at room temperature for $Bi_xCo_{2-x}MnO_4$ (x = 0.0, 0.1, 0.2 and 0.3).*

Raman spectra studies of the $Bi_xCo_{2-x}MnO_4$ (x = 0.0, 0.1, 0.2 and 0.3) showed shift in peak position towards lower wave number (A_{1g} shifted from 664 cm^{-1} to 650 cm^{-1} & F^1_{2g} shifted from 188 cm^{-1} to 183 cm^{-1}, for x = 0.0 to x = 0.3) due to increased unit cell parameters with Bi substitution (Fig. 4.1). The greater shift in A_{1g} mode indicates that most of the substituted Bi and Mn cations are occupying the octahedral sites ($Co/Bi/MnO_6$).

4.2.2 NEXAFS studies

Spinel oxides exhibit variety of exciting physical properties due to the active role of the orbital degrees of freedom within its complicated structure that can be typically observed in the lattice and electronic response. As a matter of fact, such properties appear to have their origin in the unique electronic structure derived from the hybridized transition metal ions' (TMI) 3*d* and O 2*p* orbitals in the structural and chemical environment of a spinel oxide [27]. Therefore, the resulting intra-atomic exchanges and the orbital degrees of freedom of TMI' 3*d* electrons play vital roles in this spinel system. NEXAFS spectra were assessed at the Mn/Co $L_{3,2}$ edges and at the O K edges for $Bi_xCo_{2-x}MnO_4$ (x = 0.0, 0.1, 0.2 & 0.3) samples. The former directly proves the unoccupied Mn/Co 3*d* states via $2p \rightarrow 3d$ transitions, whereas, the latter establishes the unoccupied O 2*p* states via O $1s \rightarrow 2p$ dipolar transitions [28], together providing the information on the Mn/Co 3*d* occupancy and the effect of Bi^{3+} ion substitution on the hybridization between the O 2*p* and Mn/Co 3*d* orbitals. It is noticed that the substituted Bi^{3+} ion with $6s^2$ lone pair introduces the non-centrosymmetric charge ordering leading to ferroelectricity in Co_2MnO_4, however, the consequent increase in magnetic moment [22] indicates the considerable change in the hybridization of lowest unoccupied energy levels of Mn/Co 3*d* with O 2*p* levels. The larger ionic radii of Bi^{3+}, causes the redistribution of cations among the occupied 8*a*-t_d and 16*d*-o_h sites and the participation of unoccupied 16 octahedral sites (16*c*) and 56 tetrahedral sites (8*b* and 48*f*) in a distorted environment due to Bi induced chemical pressure.

It is well known that the peak positions and the line shapes of the Co/Mn $L_{3,2}$ edge NEXAFS spectrum depend on the local electronic structure of Co/Mn ions. So the L edge spectrum provides the information on the valence state of the Co/Mn ions

[29, 30]. Figure 4.1 shows the normalized Co $L_{3,2}$-edge NEXAFS spectra of $Bi_xCo_{2-x}MnO_4$. Generally, NEXAFS spectra are sensitive to the crystal field symmetry primarily due to the 2*p*-3*d* transition of TMI'. The spin-orbit interaction of the Co 2*p* core states splits the spectrum into two broad multiplets, namely, the L_3 ($2p_{3/2}$) and L_2 ($2p_{1/2}$) ~ 15 eV apart. Each of these two regions further splits into t_{2g} and e_g orbital features because of the crystal field effect of neighboring ions. The intensity of these peaks is the direct measure of total unoccupied Co 3*d* states. In Co_2MnO_4, the Co ions distributed at A and B site (in AB_2O_4 structure) are in t_d (Co^{2+}) and o_h (Co^{3+}) symmetry.

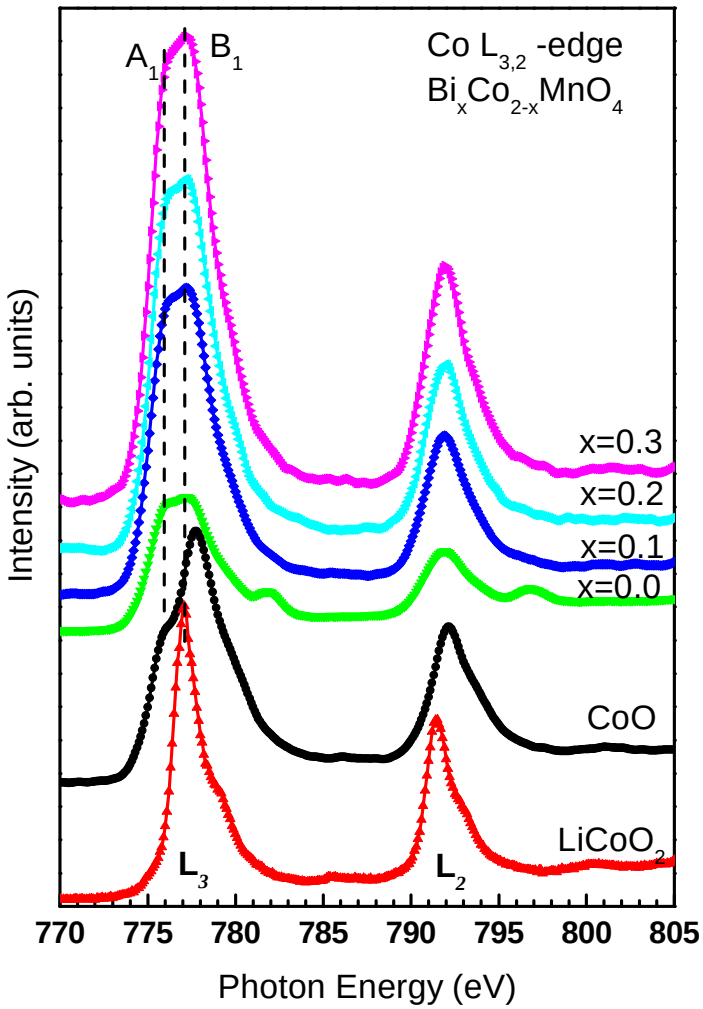

Fig. 4.2. *Normalized Co $L_{3,2}$-spectra of $Bi_xCo_{2-x}MnO_4$ (x = 0.0, 0.1, 0.2 and 0.3) along with the spectra of CoO and $LiCoO_2$.*

Co^{3+} at B (o_h) site has the higher crystal field splitting energy, so all the valence electron are in lower orbital t_{2g} ($t_{2g}^6\ e_g^0$) only, whereas, the e_g subbands are lower than t_{2g} in t_d symmetry and the associated lower crystal field splitting energy results in the high spin state of Co^{2+} ($e_g^4 t_{2g}^3$). The L_3 region contains two spectral features, A_1 and B_1, at 778.3 eV and 779.1 eV, which correspond to Co^{2+} and Co^{3+} valence state, respectively. To determine the valence states of Co ions, Co $L_{3,2}$ edge has been compared with that of CoO and $LiCoO_2$ spectra. For the starting composition Co_2MnO_4 (x = 0.0), the intensity ratio of B_1/A_1 is almost equals to one indicating that distribution of Co^{2+} ions at t_d and Co^{3+} ions at o_h, respectively are equal. B_1/A_1 ratio is found increased on increasing Bi-substitution, clearly showing that Co^{2+} content is reduced. This reveals that substitution of Bi at o_h site enforces the relocation of Mn ions between o_h and t_d sites. This element specific observation complements to our structural measurement XRD, as described in chapter 2 [22] and Raman scattering.

Figure 4.3 shows the Mn $L_{3,2}$ spectra of $Bi_xCo_{2-x}MnO_4$ along with the reference compounds MnO and MnO_2. Similar to Co $L_{3,2}$ edge spectra (Fig. 4.2) due to the spin-orbit interaction, Mn 2*p* core states split the spectrum into two broad multiplets, namely, the L_3 ($2p_{3/2}$) and L_2 ($2p_{1/2}$) ~ 11 eV, apart. Each of these two regions further splits into t_{2g} and e_g orbital features because of the crystal field effect of neighboring ions. The intensity of these peaks measures the total unoccupied Mn 3*d* states. These spectra show a valence-specific multiplet structure with a chemical shift due to change in oxidation state. The inflection points of the Mn L_3 edge for manganese oxides ($Mn^{2+}O$ and $Mn^{4+}O_2$ shown in plot and $Mn_2^{3+}O_3$ from Ref: 31-33) are subsequently at higher energies, corresponding to the increase in the valence number of Mn. The L_3 region in both MnO_2 and MnO contains two spectral features, which are assigned to Mn t_{2g} and Mn e_g d subbands. Mn ions in MnO have a +2 charge state with orbitals each filled by majority spin electrons, so that features at lower energy can be attributed to t_{2g} and higher energy feature is attributed to e_g subbands.

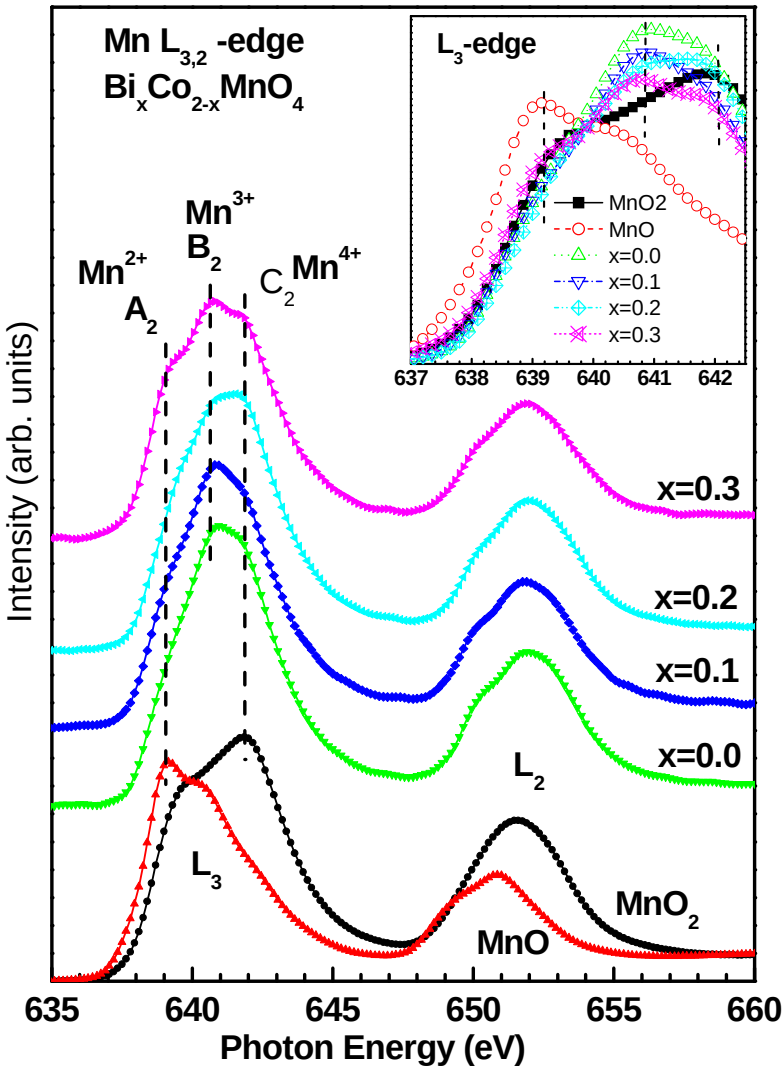

Fig. 4.3. *Normalized Mn $L_{3,2}$-spectra of $Bi_xCo_{2-x}MnO_4$ (x = 0.0, 0.1, 0.2 and 0.3) along with the spectra of MnO and MnO_2. Inset: Zoomed-normalized Mn L_3-edge region.*

The larger intensity of lower energy peak is due to the fact that there are three t_{2g} orbitals and only two e_g orbitals and t_{2g} having more unoccupied states. In MnO_2, Mn ions have +4 oxidation state with the e_g subband empty. So the unoccupied part of the e_g subband will contribute to higher energy peak of the Mn $L_{3,2}$-edge spectrum, and is more intense. Similarly in case of Mn_2O_3 also L_3 edge is dominated by e_g subbands only [from Ref: 31-33]. The L_3 region in Mn $L_{3,2}$ spectra of doped $Bi_xCo_{2-x}MnO_4$ contains three spectral features, A_2, B_2 and C_2, which can be

directly compared with the three valence states (2+, 3+ and 4+) of Mn ions (see Fig. 4.3). Spectra of the parent composition (x=0) matches well with that to the spectra of Mn^{3+} [from Ref 31-33]. However, the increase in the intensity of peak features A_2 and C_2 with Bi-substitution at o_h site reveal that more of Mn^{3+} ions are converted into Mn^{2+}/Mn^{4+}. For more closer view, the zoomed-normalized Mn L_3-edge region is shown as an inset in Fig.4.3, where increased Mn^{2+} and Mn^{4+} at the expense of Mn^{3+} is clearly displayed. Mn^{2+} occupies the t_d sites, complementing our observation of the reduced Co^{2+} in Co $L_{3,2}$ spectra, whereas Mn^{4+} ions are in o_h sites only, as the signature of Mn^{4+} is similar to MnO_2 spectra vindicating o_h geometry. The increase in Mn^{2+} and Mn^{4+} at the expense of Mn^{3+} results in the enhancement of net magnetic moment.

Figure 4.4 shows the measured O K edge NEXAFS spectra of the $Bi_xCo_{2-x}MnO_4$, along with the spectra of reference compounds CoO, $LiCoO_2$, Bi_2O_3, MnO and MnO_2. O K edge NEXAFS spectra, which represents the orbital nature of the spectral features of the O 2*p* unoccupied states in the conduction bands can be efficiently used to explore all kind of possible hybridizations with different cations (Co, Mn and Bi).

Based on the existing literature and band structure calculations, [34-37] four features marked by A_3, B_3, C_3, and D_3 in $Bi_xCo_{2-x}MnO_4$ (x=0.1) are identified. Except the spectral feature B_3 all other are present in parent composition (x=0.0), reason being B_3 originates from Bi 6s /O 2*p* hybridizations. The O K- edge spectra of pure (x = 0.0) sample indicates that low energy features resembles with Co_3O_4 [from Ref:38] and spectral feature B_3 at ~ 532 eV observed for doped compositions follows the behaviour of highly polarizable $6s^2$ lone pair of electrons of Bi^{3+} ion. The orientation of the Bi $6s^2$ lone pair towards a surrounding O^{2-} ion can produce local distortion and hybridization between $6s^2$ Bi-orbital and O 2p orbital, resulting in ferroelectric properties in doped compounds. As a matter of fact, increase of Bi content at o_h site induces more Mn^{2+}/Mn^{4+} crystal symmetries, which can be clearly observed in the O K edge spectra of optimally doped (x=0.3) sample, where A_3 is more prominent.

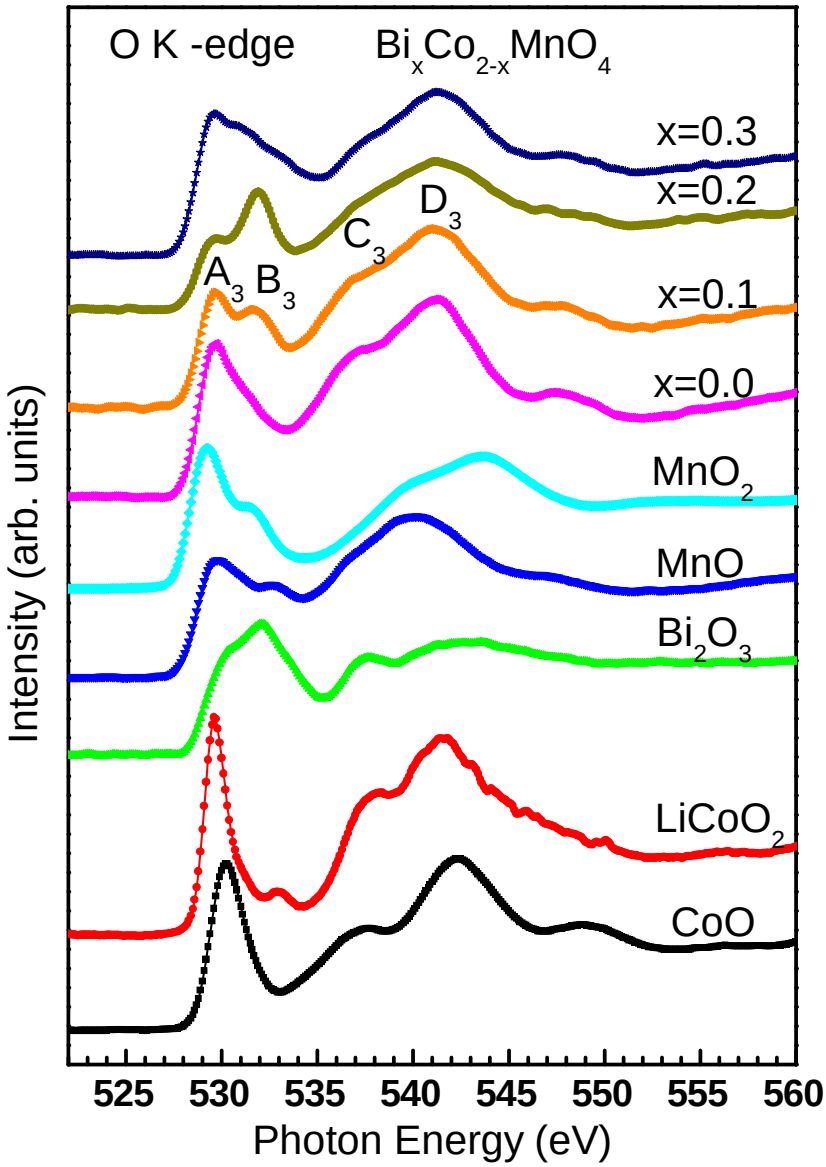

Fig. 4.4. *Normalized O-K edge spectra of $Bi_xCo_{2-x}MnO_4$ (x = 0.0, 0.1, 0.2 and 0.3) along with that of reference compounds CoO, $LiCoO_2$, MnO, MnO_2 and Bi_2O_3.*

On the whole, the spectral feature of peaks A_3, B_3, C_3, and D_3 clearly represents the presence of Bi^{3+}, $Mn^{2+/3+/4+}$ and $Co^{2+/3+}$ ions in Bi-substituted samples. The above observation is in conformity to the $L_{3,2}$ spectra of Co/Mn.

4.2.3 Magnetization measurements

Temperature dependence of the field cooled (FC) and zero field cooled (ZFC) magnetization of $Bi_xCo_{2-x}MnO_4$, with x = 0.0, 0.1 and 0.3, in the presence of an applied magnetic field of 0.1 T are shown in the Fig.4.5.

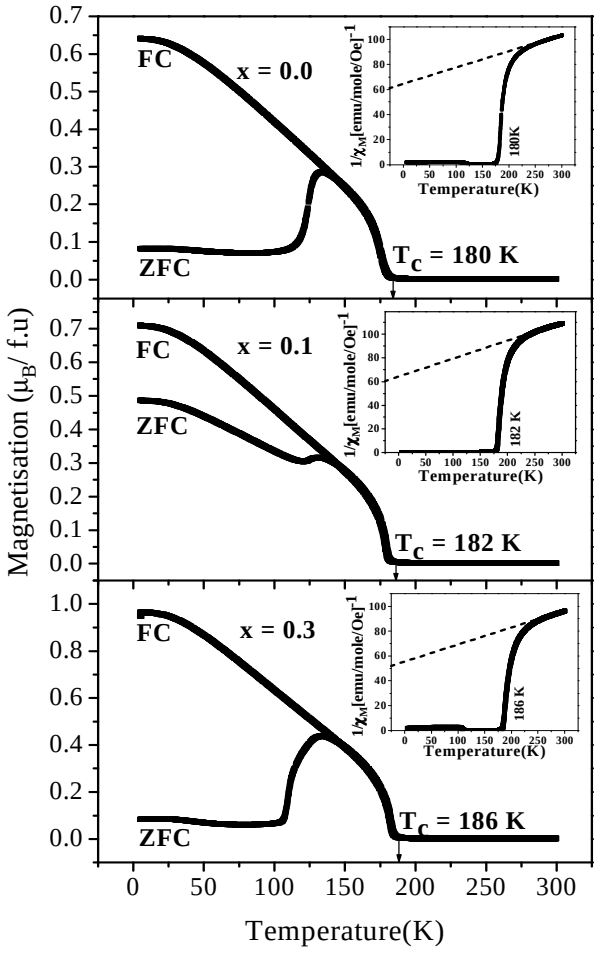

Fig. 4.5. *Zero field cooled (ZFC) and field cooled (FC) magnetization data plotted as a function of temperature of $Bi_xCo_{2-x}MnO_4$ (x = 0, 0.1. and 0.3). Insets shows the respective temperature dependence of $1/\chi_M$.*

It has been found that these samples obey the Curie-Weiss law and exhibits ferrimagnetic transition in the temperature range 180-186 K depending on Bi-content with a divergence of FC and ZFC at lower temperatures (~143-147 K).

Below the divergence point the FC magnetization increases linearly, whereas ZFC curve exhibit a wide maximum around 133 K. Inverse susceptibility ($1/\chi_M$) obtained for these samples are plotted in the insets of Fig.4.5, which revealed that the ferrimagnetic transition occurred at slightly varied temperature depending on Bi concentration.

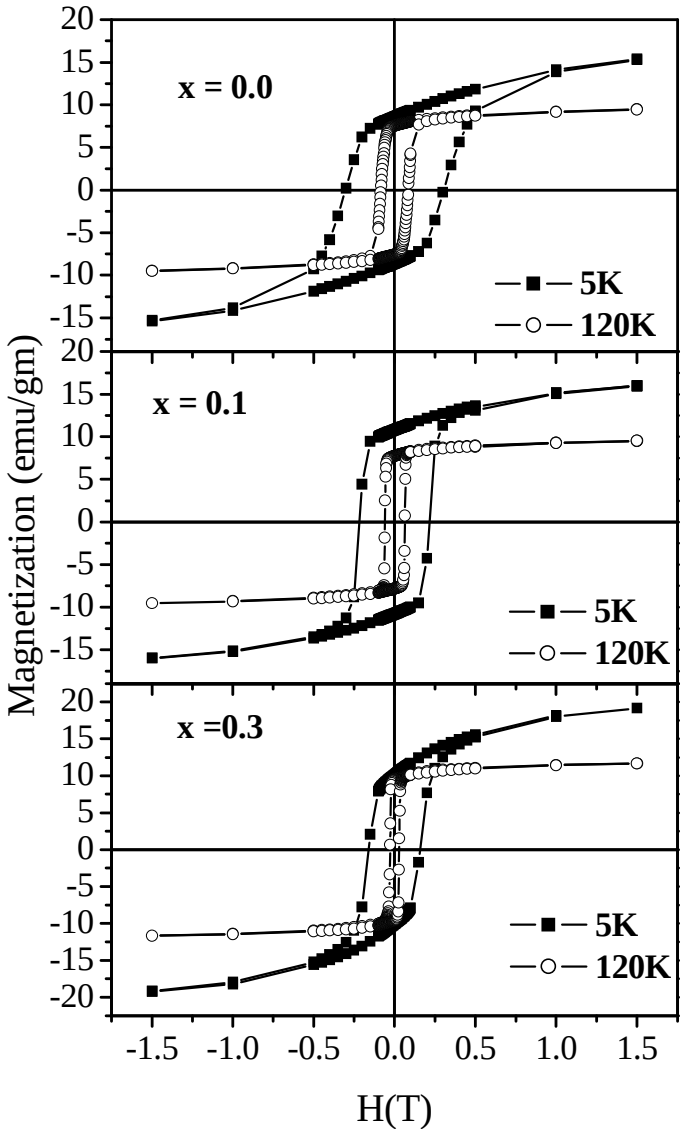

Fig. 4.6. *Isothermal magnetization hysteresis of $Bi_xCo_{2-x}MnO_4$ (x = 0, 0.1 and 0.3) at 5K and 120K.*

Isothermal Magnetization hysteresis for $Bi_xCo_{2-x}MnO_4$ ($0.0 \leq x \leq 0.3$) samples have been performed at various temperatures below the transition temperature. In Fig.4.6 the M-H plots at T = 5 K and 120 K for $Bi_xCo_{2-x}MnO_4$ ($0.0 \leq x \leq 0.3$) samples are shown, clearly depicting ferrimagnetic behaviour. Larger loop area at lower temperature indicates increased magnetization. At all measured temperatures, saturation magnetization (M_S) is found to be increasing with the increasing Bi content. Remnant magnetization (M_R) observed in these compounds was not so high. The coercive field (H_C) was found to decrease with Bi-substitution owing to a larger grain size, which results in the reduction of uncompensated spins.

Regarding the magnetic behaviour of spinel oxides, there are mainly three types of magnetic interactions possible between the ions at A-site and B-sites through the intermediate oxygen ions (O^{2-}) via intrasite A-O-A (J_{AA}) and B-O-B ($J_{BB,}$) and intersite A-O-B (J_{AB}) superexchange interactions. Since cation-cation distances are large, direct interactions, J_{AA} and J_{BB} are weakly antiferromagnetic (AFM). It has been verified experimentally that these interaction energies are negative favouring antiferromagnetism when the *d* orbitals of the metal ions are half filled or more than half filled, while a positive interaction accompanied by ferrimagnetism appears when *d* orbital is less than half filled. In Co_2MnO_4 these interaction (J_{AA} and J_{BB}) energies are negative favoring AFM, simultaneously a positive, J_{AB}, superexchange interaction result in to FM, which is originating from Mn ions occupying the octahedral sites. In addition, with Bi-substitution, weak, J_{AA}, super exchange interaction between A-sites (Co^{2+} - Co^{2+}) mediated through O^{2-} and Co^{3+} that maintains the AFM ordering is affected due to the redistribution of Co/Mn ions. The ferrimagnetic behaviour appears to evolve due to the Bi-substitution induced competition among J_{AB} (Co^{2+}-O-Mn^{4+}, Co^{2+}-O-Mn^{3+}, Mn^{2+}-O-Mn^{3+}, Mn^{2+}-O-Mn^{4+}), J_{AA} (Co^{2+}-O-Co^{2+}, Mn^{2+}-O-Mn^{2+}, Co^{2+}-O-Mn^{2+}), J_{BB} (Mn^{3+}- O - Mn^{3+}, Mn^{4+} - O - Mn^{4+}, Mn^{3+}-O-Mn^{4+}) superexchange interactions and consequent magnetic frustration [39].

Also, the appearance of ferrimagnetism in this compound may be attributed to either the canting of the antiferromagnetically ordered spins by the structural

distortion or a breakdown of the balance between the antiparallel sublattice magnetization of Co^{2+} due to the substitution of Mn/Bi ions with different valence states [40]. In other words the presence of Bi and Mn at the cation sites modifies the magnetic behaviour of the parent compound Co_3O_4 because of the competition among intrasite (J_{AA} & J_{BB}) and intersite (J_{AB}) interactions that leads to the magnetic frustration. This disrupts the antiferromagnetic ordering in Co^{2+} sublattice and results in ferrimagnetism [40, 41].

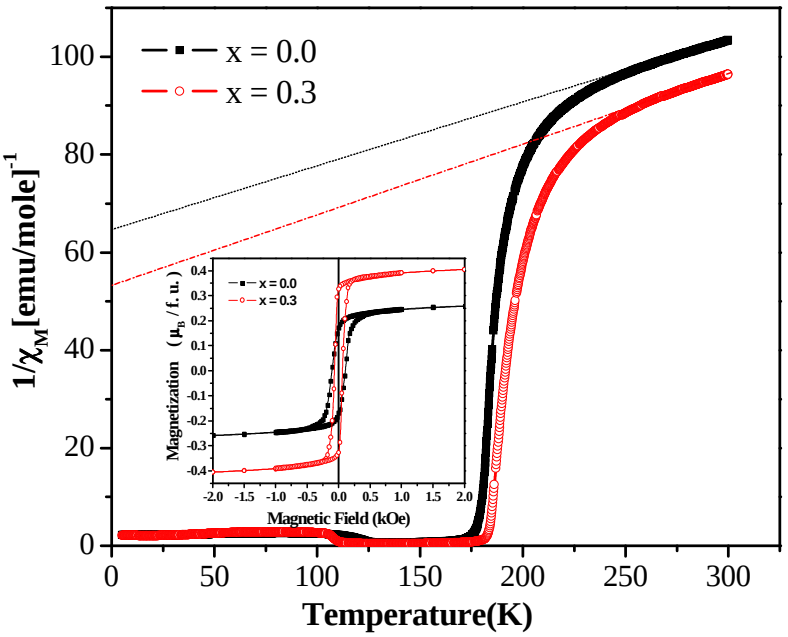

Fig. 4.7. *$1/\chi_M$ - T plots $Bi_xCo_{2-x}MnO_4$ (x = 0.0 and 0.3) and Inset: M-H loops $Bi_xCo_{2-x}MnO_4$ (x = 0.0and 0.3) measured at 150 K.*

Analysis of temperature dependence of inverse susceptibility showed that Curie-Weiss constant, θ_{CW} is highly negative, indicating that strong antiferromagnetic interactions exist in the compound, besides the ferrimagnetic character, which sets at T_c. So the compound shows ferrimagnetism, as in the case of many other spinel oxides. The improvement in ferrimagnetic (FM) property was confirmed through the rise in T_c/θ_{CW} [42] (0.364 to 0.502, for x = 0.0 to x = 0.3) from $1/\chi_M$ vs. T plots (inverse of molar susceptibility vs. temperature, Fig. 4.7), which represents the increase in frustration among the antiferromagnetic ordering in the system, as Bi-

content increases. In other words, this can be interpreted by looking at the fall in negative Curie-Weiss constant, θ_{CW} (-494 to -370, for x = 0.0 to x = 0.3; obtained as the intersecting point of extrapolation of high temperature region of $1/\chi_M$ vs. T plots), which directly represent the fall in negative molecular field and consequent rise in AFM frustration, finally leading to improved FM. The increase in net magnetic moment because of the evolution of Mn^{2+} and Mn^{4+} at the expense of Mn^{3+} due to the Bi-substitution is evident in M-H plots (inset of Fig.4.6). However, it is to be mentioned that the well defined ferrimagnetic behaviour exhibited by these compositions cannot be explained completely by the AFM frustration discussed so far. The canting of the spins by the Bi-induced structural distortion also contributes to ferrimagnetism. Therefore the source of increasing FM ordering with the Bi-substitution in $Bi_xCo_{2-x}MnO_4$ ($0.0 \leq x \leq 0.3$) originates from the complex magnetic ordering attained and consequent enhancement in magnetic interactions. NEXAFS study substantiates that the complex magnetic ordering is induced in the Bi-substituted spinel Co_2MnO_4.

4.2.4. Magnetoelectric studies

Magnetoelectric property of $Bi_xCo_{2-x}MnO_4$ (x = 0.3) have been determined through the magnetocapacitive effect as shown in Fig. 4.8. The percentage variation of dielectric constant $\left[\frac{\varepsilon'(H)-\varepsilon'(0)}{\varepsilon'(0)}\times 100\right]$ versus temperature measured at 3 T and 0 T shows a maxima at FM transition temperature, T_C (186 K) indicating magnetocapacitive coupling. This confirms the magnetic origin of ferroelectricity and can be correlated to the inverse of Dsyaloshinskii-Moriya type of interaction occurring in complex magnetic structures like non collinear canted antiferromagnets, where the canted spin polarizes the O 2*p* orbital through electron-lattice interaction [5, 8, and 10]. The decrease in magnetoelectric coupling, i.e., fall in dielectric constant at high temperature can be attributed to the flip of polarization that was originated from complex magnetic structure against the polarization related to the

"proper" ferroelectricity [8]. This type of polarization flip is shown in $TbMnO_3$ on tuning by magnetic field [43].

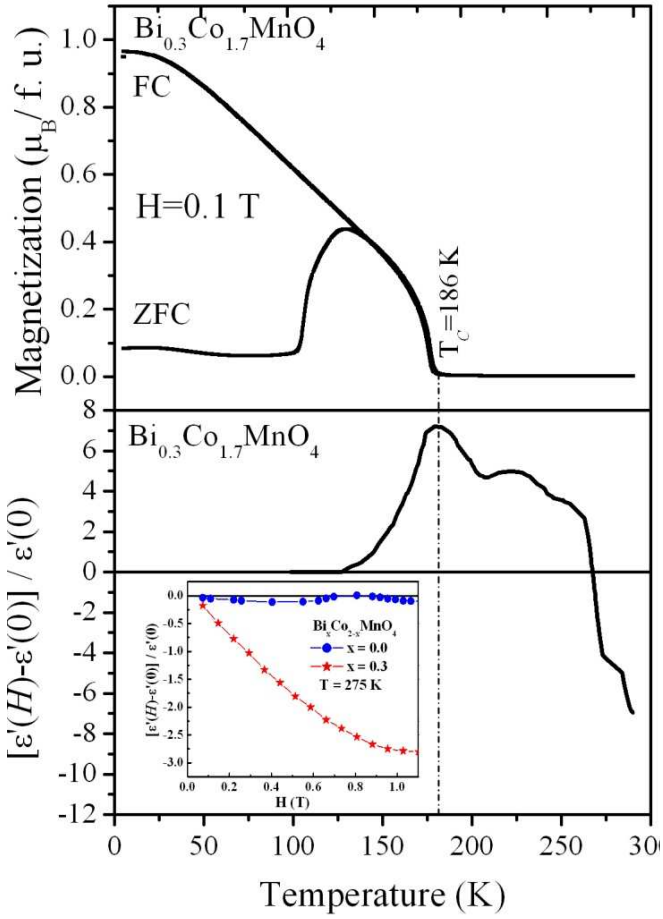

FIG. 4.8. *Upper part shows the temperature dependent magnetization for $Bi_xCo_{2-x}MnO_4$ (x = 0.3)measured during the warming (ZFC) and cooling (FC) cycles, whereas lower part shows magnetocapacitive coupling* $\left[\frac{\varepsilon'(H)-\varepsilon'(0)}{\varepsilon'(0)}\right]$ *versus temperature for the same sample.*

Magnetically tunable ferroelectricity exhibited by the Bi-substituted Co_2MnO_4 at 275 K is depicted in the bottom inset of Fig.4.8, where the parent compound shows almost zero response. This is attributed to non linear magnetic ordering occurring due to the geometrical frustration with Bi-substitution. The clear nonappearance of magnetoelectric coupling at lower temperature (below FM T_c) can be attributed to the collinear magnetic ordering, as in case of hexaferrites [11].

4.3 Conclusions

The effect of the substitution of non magnetic Bi^{3+} ion in Co_2MnO_4 was analyzed using magnetic, magnetoelectric, Raman spectroscopy and NEXAFS studies. The following observations have been made on the basis of the experiments performed with the bulk samples.

(i) The investigation of electronic structure of $Bi_XCo_{2-x}MnO_4$ ($0.0 \leq x \leq 0.3$) using NEXAFS spectra at O K edge and $L_{3,2}$ edge of Co/Mn revealed that increase in net magnetic moment and more ordered ferrimagnetism with Bi substitution is due to cationic redistribution. More of Mn^{3+} ions are converted into Mn^{2+} and Mn^{4+} and redistributed to t_d and o_h sites. O K edge spectra confirm the highly polarizable behaviour of Bi $6s^2$ lone pair of electron. Raman spectra of the samples confirm the greater occupation of substituted cations in the octahedral sites.

(ii) The dc magnetization measurements show that all the samples are ferrimagnetically ordered, with $T_c < 190$ K and saturation magnetization increases with increasing the concentration of Bi^{3+} ions due to the softening of the lattice arising from the redistribution of cations at the octahedral sites. Lowered negative molecular field is depicted by the decrease in Curie – Weiss constant, which indicates the increased AFM frustration with Bi-substitution, favoring FM.

(iii) The magnetoelectric coupling obtained as the variation of dielectric constant in response to the applied magnetic field exhibited maxima at FM T_c, for the Bi-substituted samples, confirming the magnetic origin of ferroelectricity. This can be correlated to the inverse of Dsyaloshinskii-Moriya type of interaction occurring in complex magnetic structures like non collinear canted antiferromagnets arising from the geometrical frustration with Bi-substitution.

Bi substitution introduces a radical change in cationic distribution, favoring the ferrimagnetism along with the ferroelectricity. The coexistence of ferroelectric and magnetic properties proposes the candidature of this material for the future multiferroic application.

References

1. R. Ramesh and N. A. Spaldin, Nature Materials, **6** (2007) 21.
2. M. Bibes and A. Barthelemy, Nature Materials, **7** (2008) 425.
3. W. Prellier, M. P. Singh, and P. Murugavel, J. Phys. Condens. Matter. **17** (2005) R803.
4. W. Erenstein, N. D. Mathur and J. F. Scott, Nature **442** (2006) 17.
5. C. J. Fennie, and K. M. Rabe, Phys. Rev. B **72** (2005) 214123.
6. D. I. Khomskii, J. Mag. Mag. Mater. **306** (2006) 1.
7. Y. Yamasaki, S. Miyasuka, Y. Kaniko, J. P. He, T. Arima, and Y. Tokura., Phys. Rev. Lett. **96** (2006) 207204.
8. S. W. Cheong, and M. Mostovoy, Nature **6** (2007) 13.
9. D. K. Shukla, S. Mollah, R. Kumar, P. Thakur, K. H. Chae, W. K. Choi, and A. Banerjee, J. Appl.Phys. **104** (2008) 033707.
10. T. Kimura, Annu. Rev. Mater. Res. **37** (2007) 387.
11. Ce-Wen Nan, M. I. Bichurin, S. Dong, D. Viehland and G. Srinivasan, J. Appl. Phys, **103** (2008) 031101.
12. V. A. Khomchenko, D. A. Kiselev, J. M.Vieira, and L. Kholkin., Appl. Phys. Lett. **90** (2007) 242901.
13. A. K. M. Akther Hossain, M. Seki, T. Kawai, and H. Tabata, J. Appl. Phys. **96** (2004) 1273.
14. S. A. Wolf, D. D. Awschalom, R. A. Buhrman, J. M. Daughton, S. von Molnár, M. L. Roukes, A. Y. Chtchelkanova, D. M. Treger, Science **294** (2001) 1488.
15. M. J. Carey, S. Maat, P. Rice, R. F. C. Farrow, R. F. Marks, A. Kellock, P. Nguyen, B. A. Gumey, Appl. Phys. Lett. **81**(2002) 1044.

16. M. L Kahn and Z. J. Zhang, Appl. Phys. Lett. **78** (2001) 3651.

17. B. Antic, G. F. Goya, H. R. Rechenberg, V. Kusigerski, N. Jovic and M. Mitric**,** J.Phys.: Condens.Matter. **16** (2004) 651.

18. S. Kumar, Alimuddin, R. Kumar, A. Dogra, V.R.Reddy and A. Banerjee, J. Appl. Phys. **99** (2006) 08M910.

19. Y. Ikedo, J. Sugiyama, H. Nozaki, H. Itahara, J. H. Brewer, E. J. Ansaldo, G. D. Morris, D. Andreica and A. Amato , Phys. Rev. B **75** (2007) 054424.

20. J. F. Scott, Rep. Prog. Phys. **12** (1979) 1055.

21. M. Fiebig, J. Phys. D: Appl. Phys. **38** (2005) R123.

22. N. E. Rajeevan, P. P. Pradyumnan, R. Kumar, D. K. Shukla, S. Kumar, A. K. Singh, S. Patnaik, S. K. Arora, and I. V. Shvets, Appl. Phys. Lett **92** (2008) 102910.

23. A. C. Tavares, M. A. M. Cartaxo, M. I. da Silva Pereira and F. M. A. Costa, J.Solid state Electrochem. **5** (2001) 57.

24. M.H. Mendonca, M.I. Godinho, M.A. Catarino, M.I. da Silva Pereira and F.M. Costa, Solid State Sciences **4** (2002) 175.

25. V. G. Hadjiev, M. N. Iliev, and I. V Vergilov, J. Phy. C: Solid State Phys. **21** (1988) L199.

26. F. Kovanda, and T. Rojka, J. Solid State Chem. **179** (2006) 812.

27. H. J. Lee, G. Kim, D. H. Kim, J. S. Kang, C. L. Zhang, S. W. Cheong, J. H. Shim, S. Lee, H. Lee, J. Y. Kim, B. H. Kim and B. I. Min, J.Phys.: Condens. Matter **20** (2008) 295203.

28. F. M. F. de Groot, M. Grioni, J. C. Fuggle, J. Ghizsen, G. A. Sawatzky and H. Petersen, Phys. Rev. B **40** (1989) 5715.

29. F. M. F. de Groot, J. C. Fuggle, B. T. Thole, and G. A. Sawatzky, Phys. Rev. B **42** (1990) 5459.

30. G. van der Laan and I. W. Kirkman, J. Phys.: Condens. Matter **4** (1992) 4189.

31. S. Voss, M. Fonin, and U. Rüdiger, Phys. Rev. B **75** (2007) 045102.

32. S. Mukherjee and A. K. Pal, Phys.Rev. B **74** (2006) 104413.

33. W. A. Harrison, Phys. Rev. B **77** (2008) 245103.

34. E. Pellegrin, L. H. Tjeng, F. M. F de Groot, R. Hesper, G. A. Sawatzky, Y. Moritomo, and Y. Tokura, J. Electron Spectrosc. Relat. Phenom. **86** (1997) 115.

35. J. H. Park, T. Kimura, and Y. Tokura, Phys. Rev. B **58** (1998) R13330.

36. D. S. Dessau, Y. D. Chuang, A. Gromko, T. Saitoh, T. Kimura, and Y. Tokura, J. Electron Spectrosc. Relat. Phenom. **117–118** (2001) 265.

37. N. A. Hill and K. M. Rabe, Phys. Rev. B **59** (1999) 8759.

38. J. van Elp, J. L.Wieland, H. Eskes, P. Kuiper, G. A. Sawatzky, F. M. F. de Groot, T. S. Turner, Phys. Rev. B **44** (1991) 609.

39. T. Suzuki, H. Nagai, M. Nohara and H. Takagi, J.Phys.: Condens. Matter **19** (2007) 145265.

40. R. N. Bhowmik, R. Ranganathan and R. Nagarajan,, J. Mag. Mag. Mater. **299** (2006) 327.

41. T. Kimura, T. Goto, H. Shintani, K. Ishizaka, T. Arima, and Y. Tokura, Nature **426** (2003) 55.

42. G. Jeffrey Snyder, C. H. Booth, F. Bridges, R. Hiskes, S. DiCarolis, M. R. Beasley and T. H. Geballe, Phys. Rev. B **55** (1997) 6453.

43. K. Ueda, H. Tabata and T. Kawai Appl. Phys. Lett. **75** (1999) 555.

Chapter 5

Study of Structural and Magnetoelectric Properties of $Bi_xCo_{2-x}MnO_4$ Thin Films

This chapter presents the study of structural and magnetoelectric properties of multiferroic $Bi_xCo_{2-x}MnO_4$ thin films deposited on different substrates such as amorphous quartz, $LaAlO_3$ (LAO) and $YBa_2Cu_3O_7$ (YBCO)-coated LAO.

5.1 Introduction

Magnetoelectric multiferroic materials possess at least two order parameters among ferromagnetic (FM)/antiferromagnetic (AF), ferroelectricity (FE) and ferroelasticity over a certain range of temperature and promise applications in the development of multifunctional devices. Recent studies showed that coupling between these properties offered multiple state memory and logic device applications [1-3].Unlike the natural multiferroics having weak magnetoelectric coupling, newly developed multiferroic composites are expected to yield giant magnetoelectric coupling response near to the room temperature, enabling itself for wider technological applications in information storage and spintronics including magnetoelectric sensors and magnetocapacitive devices [4]. Ferroelectric polarization and magnetization are used to encode binary information in FE-RAMs (ferroelectric random access memories) and MRAMs (magnetic random access memories) respectively. Multiferroic materials, possessing these two properties allow the realization of four-state logic devices [5]. However, because of the contrasting origins of FM and FE properties, there are only very few multiferroic materials, naturally existing, with sufficient amount of magnetoelectric coupling. In practice, the coexistence of FE and FM are achieved through the induction of nonmagnetic ions having stereochemically active lone pair of electrons that can introduce off centering in the structure containing magnetic transition metal oxides [3, 6]. As described in chapter 2, the induction of Bi has introduced the noncentrosymmetric charge ordering and consequently polarization (FE) in the bulk Co_2MnO_4 spinel material along with the frustrated antiferromagnetic ordering among the Co^{2+} sublattices that lead to ferrimagnetism, and magnetoelectric effect [7]. Very few efforts have been made to study multiferroic properties of Bi-substituted spinel oxides in thin film form. Modern technology requires compactness of the materials, which enables the reduction in size of the devices. In these circumstances, thin film deposition of these materials is of great importance. Advances in thin film technology offer new routes to the structures and phases that

can be hardly achieved through traditional technologies, and allows the properties of the existing materials to be modified by strain engineering and cation redistribution [8]. There are several deposition techniques to grow thin films of ferrite materials, such as sol-gel method, pulsed laser deposition technique (PLD), rf sputtering, magnetron sputtering etc. Among these deposition techniques, PLD is the widely used method for thin film growth of complex oxides. In the present work PLD technique is used due to its versatility (see details in chapter 2). In addition, the stoichiometry of the target is faithfully reproduced in the film, by PLD with carefully set conditions. Deposition of the multilayer thin films carried out by varying the gas pressure or the substrate temperature or the target is also possible with PLD. However, it suffers from certain drawbacks such as difficulty in large area film deposition due to narrow angular distribution of the plasma plume. To overcome this problem, substrate can be scanned vertically/horizontally or laser beam can be scanned over the large area of the target. Another major disadvantage is the "splashing effect" causing large particulates to nucleate on the film. This causes significant surface roughness. Sanding the target before deposition and continuous scanning of the target during deposition can minimize this effect. Few research groups have initiated growing the thin films of spinel oxide and other oxide systems using PLD technique. Highly oriented (111) and epitaxial (100) $CoFe_2O_4$ thin films, with single phase spinel structure has been grown by PLD and found exhibiting high perpendicular coercive fields, even at room temperature [9]. Growth of a stoichiometric $(BiFeO_3)_{0.7}$-$(PbTiO_3)_{0.3}$ phase in thin films using PLD, was observed depending on substrate temperature ~ 450ºC and the lack of phase formation at higher substrate temperatures was attributed to the loss of volatile constituents of bismuth and lead [10]. Epitaxially oriented thin films of $Zn_xMg_{1-x}Fe_2O_4$, have been fabricated on a sapphire (0001) substrate by the PLD method. Changing the ratio of zinc ion to magnesium ion, the ferrimagnetic transition temperatures systematically decrease from 650 to 350K just as in the bulk, indicating that the thin films maintain an ion configuration similar to the bulk compound [11]. Thin films of (111)-oriented $Mg_{1.5}FeTi_{0.5}O_4$ spinel have been successfully prepared by PLD technique on Al_2O_3 (0001) substrates. The value of the lattice parameter of the (111) out-of-plane and

the Neel temperature of the films depend on the film thickness. Freezing temperature of the spin-glass behavior of this spinel is observed to vary with oxygen partial pressure during film preparation, which exhibits the adaptability of the PLD technique in controlling the magnetic properties of films [12]. Highly oriented Fe_3O_4 thin films were deposited directly on semiconducting substrates such as silicon and GaAs, and on amorphous float glass substrates. The films on glass were grown completely relaxed, resulted the lattice parameters to be very close to that of the bulk values, as the glass being amorphous does not cause any substrate induced strain [13]. Thin films of $CuCr_2Se_4$ were successfully grown by PLD on isostructural $MgAl_2O_4$ substrates followed by annealing in a Se-rich environment. X-ray absorption spectroscopy studies indicated that the chemical structure at the surface of the films is similar to that of bulk $CuCr_2Se_4$ single crystals and X-ray magnetic circular dichroism measurements (XMCD) showed that magnetic order persists to the surface of the film [14]. Single-crystalline thin film Sr_2CoO_4 with square-lattice CoO_2 sheets of thickness of 40 nm were grown by PLD from the target with a nominal composition of Sr_2CoO_4, prepared by conventional solid-state reaction and films exhibited metallic ferromagnetic behaviour. The fairly high T_C (250 K) of Sr_2CoO_4 is supposed to provide opportunities to explore the spintronic functionality of CoO_2 layers [15]. Multiferroic composite thin films of multilayered $Pb(Zr_{0.53}Ti_{0.47})O_3 – CoFe_2O_4$ prepared by PLD on platinized silicon substrate was found to have high dielectric constant and showed reduction in ferroelectric polarization with the application of external magnetic field [16]. P. Samarasekara *et al.* [17] have reported the growth of single crystal (111) textured $NiFe_2O_4$ ferrite thin films and polycrystalline-textured thin films on C-plane and R-plane sapphire substrates, respectively. In general, we can say that the physical properties of the thin films are highly dependent upon the deposition technique and parameters like substrate orientation and temperature, oxygen partial pressure etc. It is important to mention here that we need these properties in thin film form, from device realization point of view. During the last few years, a lot of efforts have been made on thin films of a variety of spinel oxides, but there is no report available on the thin films of Bi-substituted Co_2MnO_4, exhibiting multiferroic property. In this work, Bi_xCo_{2-}

$_xMnO_4$(x=0.0, 0.1, 0.2 and 0.3) thin films have been synthesized on amorphous (quartz) and crystalline $LaAlO_3$ (LAO) and $YBa_2Cu_3O_7$ coated LAO substrates using PLD and studied the crystal structure, ferroelectric, magnetic and magnetoelectric behaviour of these thin films.

5.2 Pulsed laser deposition conditions for the growth of $Bi_xCo_{2-x}MnO_4$ thin films

The thin films of spinel $Bi_xCo_{2-x}MnO_4$ (x = 0.0, 0.1, and 0.3) were grown by PLD technique (KrF Excimer Laser source-Lambda Physik-COMPEX-201, λ = 248 nm, repetition rate of 10 Hz and pulse laser energy of 220 mJ) using single phased targets on cleaned amorphous quartz, LAO(001) and YBCO coated LAO substrates. The targets were synthesized by the conventional solid state reaction, as described in Chapter 3. The target was mounted at an angle of 45^o to laser beam inside vacuum chamber, where a base pressure of 2×10^{-5} Torr was achieved through a turbo-mechanical pump and rotated at 10 rpm. To optimize the film growth conditions, the quartz substrates were kept at the temperature of 700°C and the other two substrates were kept at 650°C during the deposition along with oxygen at a pressure of 60 mTorr in the deposition chamber. The substrates of size $10mm^2$ were mounted on the heatable sample holder using silver paste. The distance between the target and the substrates was 5 cm. The deposition were carried out for 60 minutes, to achieve a film thickness ~ 350 nm, as measured by the off-line thickness profilometer (Ambios Inc, USA) with 0.5 nm resolution. After the deposition, substrates were cooled at the rate of 5°C per minute in the same oxygen environment as used during the deposition. For the purpose of bottom electrode, YBCO film of thickness 200 nm was deposited on one set of LAO substrates using PLD under optimal conditions, as given elsewhere [8]. The in-house YBCO target was made by pressing a pellet obtained from precursor oxides, sintering at 920^o C, then regrinding, pressing and repeated sintering. The single phase orthorhombic nature of the YBCO target (as per the JCPDS: 860477 file) and the preferentially oriented crystallization, (004) and (008) of the YBCO films on LAO substrate were revealed through X-ray diffraction. YBCO was chosen as the bottom electrode, as the conventional Pt/Si electrode are unsuitable, owing to the high temperature processing conditions required for the stable growth of the Bi-substituted Co_2MnO_4 films.

5.3 Results and discussion

5.3.1 Structural (XRD) and morphological (AFM) characterizations

X-ray diffraction has been carried out for the structural analysis of $Bi_xCo_{2-x}MnO_4$ (x = 0.0, 0.1, 0.2 & 0.3) thin films. θ-2θ geometry was used to get the XRD pattern of the thin film deposited on all the substrates. Experimentally observed XRD patterns of oriented polycrystalline films have been indexed using PowderX software developed by C. Dong [18].

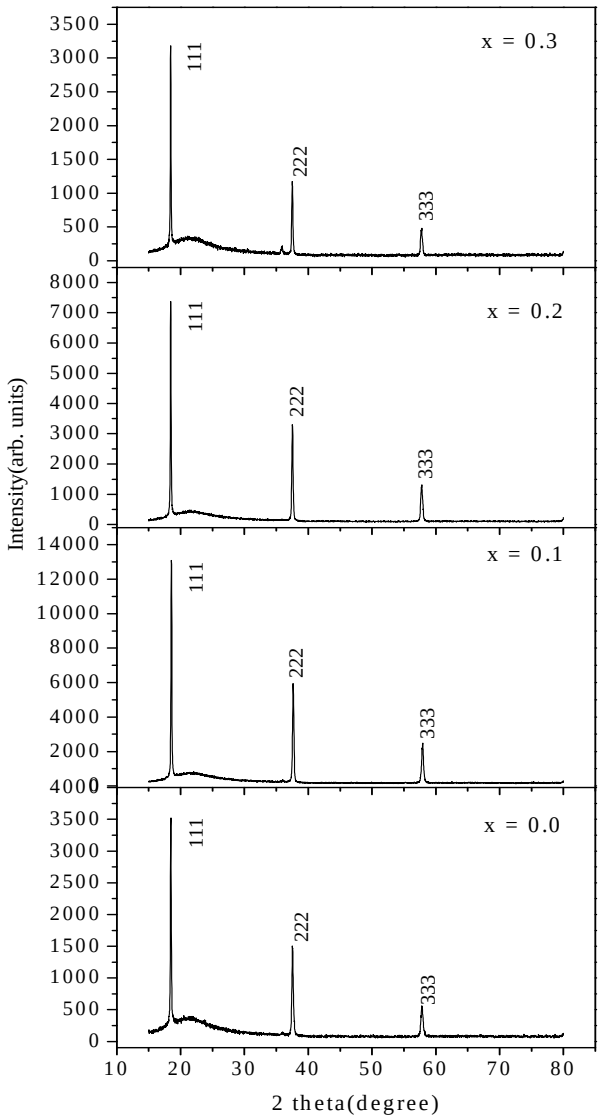

Fig. 5.1. *XRD pattern for the films of $Bi_xCo_{2-x}MnO_4$ (x = 0.0, 0.1, 0.2 and 0.3) on quartz substrates.*

In Fig. 5.1, XRD patterns of thin films of $Bi_xCo_{2-x}MnO_4$ (x = 0.0, 0.1, 0.2 & 0.3) on amorphous quartz substrates clearly show the single phase nature of thin films and supports to the fact that films are oriented in (111) plane. The lattice parameters of the films are close to that of bulk. This is because, the quartz substrate being amorphous does not cause any substrate induced strain and the film grows completely relaxed with preferential (111) orientation. Also, for the films on both LAO and YBCO coated LAO (YBCO/LAO) substrates, the single phase polycrystalline growth has been observed.

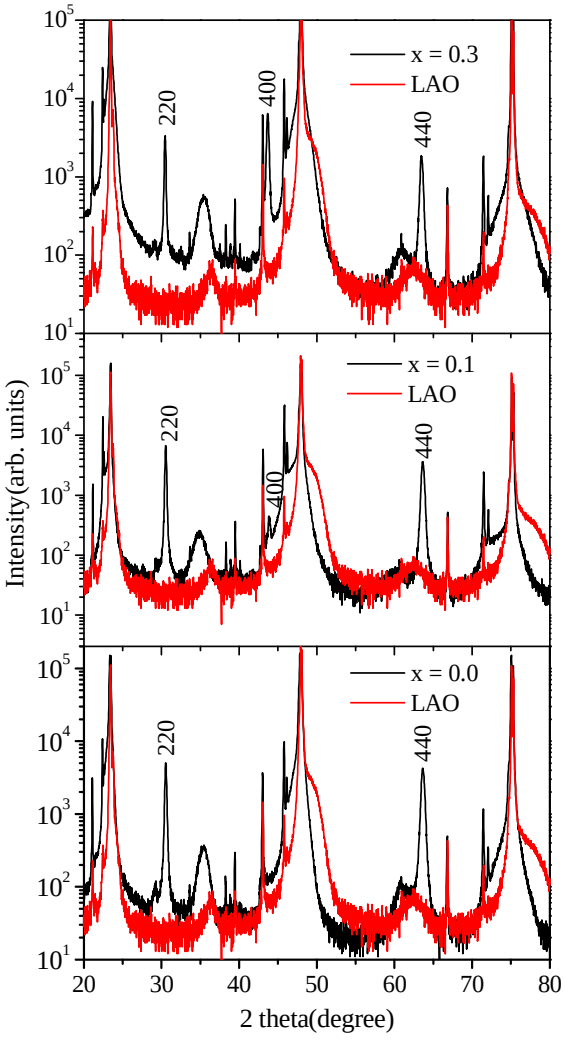

Fig. 5.2. *XRD pattern for the thin films of $Bi_xCo_{2-x}MnO_4$ (x = 0.0, 0.1, and 0.3) on LAO substrate.*

On LAO (001), films were grown with preferential (220), (400) and (440) planes, as depicted in Fig. 5.2. On YBCO/LAO also films were preferential grown in (222), (400) and (422) planes (Fig. 5.3).

The XRD reflection peaks from the films on all the three substrates belong to cubic spinel structure, revealing the single phase nature of the films grown. However, it is clear from the figures 5.1, 5.2 and 5.3 that all the peaks corresponding to the Bi-substituted Co_2MnO_4 bulk, are not observed in the thin films and the intensities of the peaks are also quite different from that of bulk; for example, (311) is the lowest intensity peak in the thin films on quartz, whereas, it is of the highest intensity peak in the bulk.

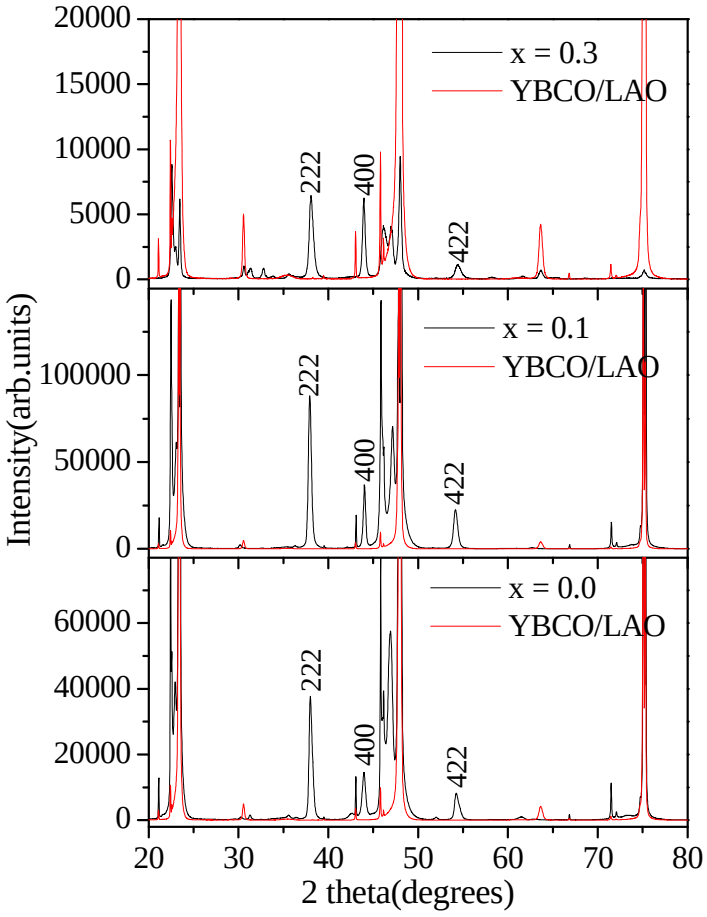

Fig. 5.3. *XRD pattern of film $Bi_xCo_{2-x}MnO_4$ (x = 0.0, 0.1 and 0.3) on YBCO/LAO substrate.*

The appearance of (220) in the film deposited on LAO and (222) in the film deposited on YBCO/LAO, as a dominant peak signifies a slow texturing in the thin films on these substrates. It is well known that the surface to volume ratio is very large in case of films; therefore, surface energy plays an important role in the thin film texturing. In spinel $Bi_xCo_{2-x}MnO_4$ thin films, the oriented growth along (111) is the most favoured, as it offers lower surface energy and greater oxygen packing density than the other crystallographic planes.

The lattice parameters as obtained from the XRD patterns of films on YBCO/LAO substrate were found slightly more deviated in comparison with the films on quartz and LAO substrates with respect to that of the bulk composition, indicating lattice contraction (Table 5.1). This may be due to the greater strain induced by the YBCO-electrode on the films owing to the lattice mismatch (for YBCO, a = 3.81 Å, b =3.88 Å, c = 11.68 Å).

Table 5.1. *Lattice constant (in Å) for* $Bi_xCo_{2-x}MnO_4$.

$Bi_xCo_{2-x}MnO_4$	Quartz substrate	LAO substrate	YBCO/LAO substrate	Bulk
x = 0.0	8.2751	8.2713	8.2355	8.2735
x = 0.1	8.3038	8.2803	8.2467	8.3186
x = 0.3	8.3343	8.2986	8.2497	8.3376

Surface morphology of the thin films is characterized by the atomic force microscopy (AFM). Figures 5.4(a), (b), (c) and (d) show the room temperature AFM images of $Bi_xCo_{2-x}MnO_4$ thin films deposited on LAO substrates. The AFM used in the present work is a commercial optical deflection microscope (Nanoscope, Digital Instruments) operating in air. The samples were mounted on a piezo-ceramic which controls the motion in the three directions. The deflection of the laser beam on the cantilever is used to monitor the height displacement via a photodiode and a feedback loop. Using this technique one can measure the height variations of the order of 0.1 nm. For all these measurements the data have been acquired in the tapping mode with 512×512 data points in the length of 5μm, which gives a sampling rate of 5μm/512 ≈ 9.76 nm. These results have been discussed on the basis of the root mean square (rms) of the roughness height and grain size. Fine observation of the AFM images reveals the dense growth of crystallites.

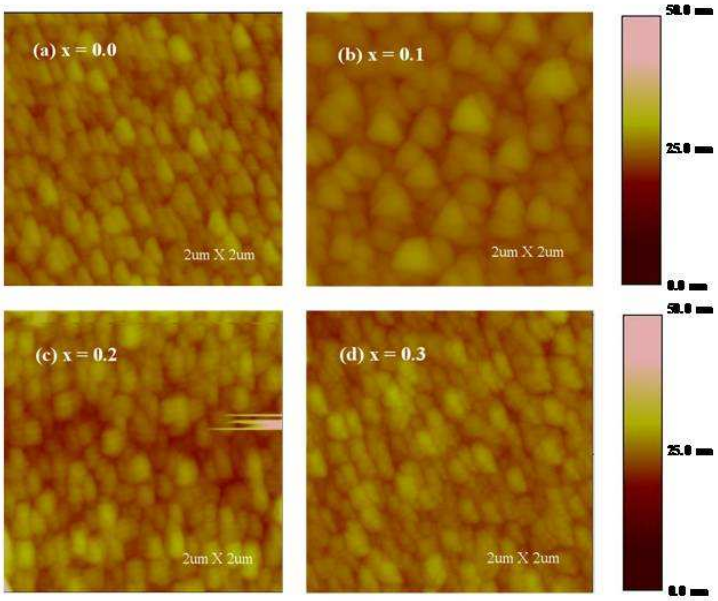

Fig. 5.4. *(a), (b), (c) & (d); AFM images of $Bi_xCo_{2-x}MnO_4$ (x = 0.0, 0.1, 0.2 and 0.3).*

The roughness and average dimension of the grains were found increasing with Bi-substitution (RMS roughness increased from 2.67 nm to 9.30 nm and grain size increased from 150 nm to 200 nm, see Fig. 5.5).

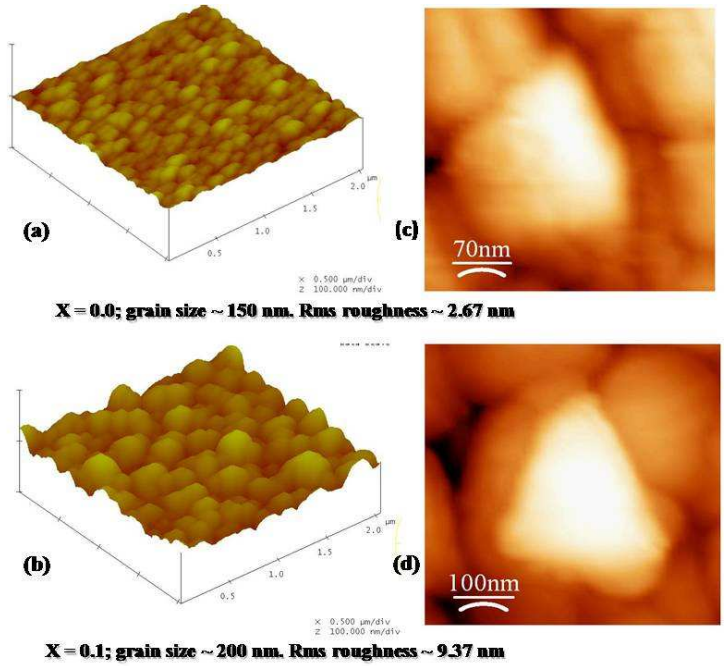

Fig. 5.5 *(a) & (b); 3d-AFM images of $Bi_xCo_{2-x}MnO_4$ (x = 0.0 & 0.1) and (c) & (d), zoomed grains of the respective compositions.*

5.3.2 Raman scattering studies

As in the case of bulk compositions discussed in chapter 3, Raman modes of the films on different substrates were analyzed in respect to the parent compound, Co_3O_4, which crystallizes in the normal spinel structure with O_h^7 spectroscopic space group. Five Raman active modes, as A_{1g} + E_g + $3F_{2g}$ (at 194.4 (F^1_{2g} - tetrahedral), 482.4 (E_g), 521.6 (F^2_{2g}), 618.4 (F^3_{2g}), and 691 (A_{1g} - octahedral)) are observed. In Fig. 5.6 Raman spectra of Bi-substituted Co_2MnO_4 spinels thin films grown on quartz (x= 0.0 & x= 0.3), LAO (x = 0.3) and YBCO/LAO (x = 0.3) are shown. It is observed that F^1_{2g} mode is shifted to the wave number ranging in 185 – 191 cm^{-1} and A_{1g} mode is shifted to the wave number ranging in 654 - 659 cm^{-1} depending on the film composition and substrates. The E_g (482.4 cm^{-1}) and F^2_{2g} (521.6 cm^{-1}) modes appear to be coalesced to 503 cm^{-1}. The greater shift in A_{1g} mode (Table 5.2) is indicative of fact that most of the substituted Bi and Mn cations are occupying the octahedral sites (Co/Bi/MnO_6). In the case of film with x = 0.3 deposited on YBCO/LAO substrates, A_{1g} and F^1_{2g} modes were found slightly shifted to higher wave number compared to the films on quartz substrate (see Table 5.2).

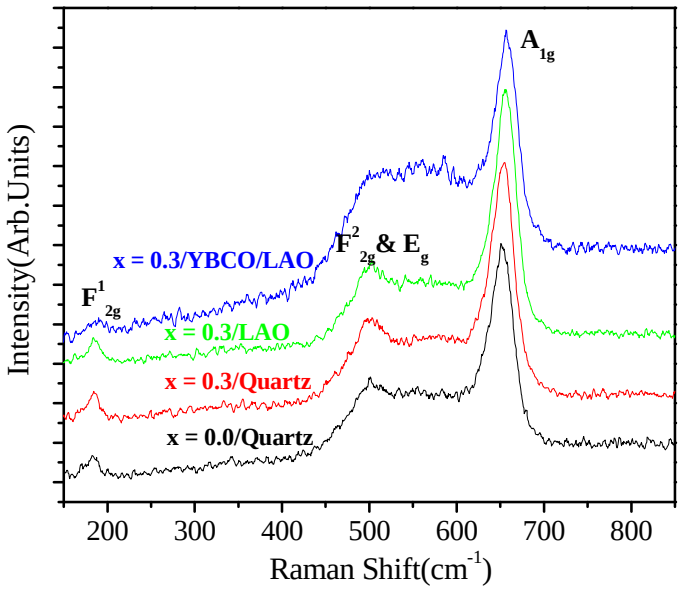

Fig. 5.6. *Raman Spectra for the films of $Bi_xCo_{2-x}MnO_4$ (x = 0 and 0.3) on quartz, x = 0.3 on LAO substrate and x = 0.3 on YBCO/LAO substrate.*

This hardening is indicative of slight contraction of unit cell and strain induced on the film lattice by the YBCO bottom layer. Hence Raman scattering studies also show the single phase character of $Bi_xCo_{2-x}MnO_4$ (x= 0.0, 0.1 and 0.3) thin films grown on quartz, LAO and YBCO/LAO substrates.

Table 5.2. Raman modes (in cm^{-1}) of $Bi_xCo_{2-x}MnO_4$ (x = 0.3).

Modes	Quartz substrate	LAO substrate	YBCO/LAO substrate	Bulk
F^1_{2g}	185.0	185.4	190.7	183.1
A_{1g}	654.8	656.6	658.5	655.4

5.3.3 Ferroelectric studies

For the ferroelectric(FE) measurements, thin films of $Bi_xCo_{2-x}MnO_4$ (x = 0.0, 0.1, 0.2 and 0.3) deposited on YBCO/LAO substrates were used, for which the lower YBCO conducting layer and upper layer of good quality silver paste act as pair of electrodes. Dielectric measurements were carried out with an automated dielectric set up consisting variable temperature probe and precision LCR meter. Dielectric constant (ε') for $Bi_xCo_{2-x}MnO_4$ (x = 0.0, 0.1, 0.2 and 0.3) films deposited on YBCO/LAO substrates measured as a function of temperature, at selected frequencies, are shown in Fig. 5.7. The films with x = 0.0 and 0.1 depicted two ferroelectric transition peaks, one at lower temperatures (at ~168 K for x = 0.0 & at ~181 K for x = 0.1) and other at high temperatures (at ~ 436 K for x = 0.0 & at ~ 443 K for x = 0.1) at 100 kHz.

In higher temperature regime, ε' is lesser for pure film compared to the Bi-substituted ones and both the transition temperatures corresponding to the two ferroelectric peaks are found to increase with Bi-substitution, possibly due to the polarization induced by the $6s^2$ lone pair of electrons. Temperature dependent variation of tan δ also exhibited peak like structure, with increasing trend on Bi-substitution (Fig.5.8), as in the bulk samples, establishing that stoichiometry of the bulk composition is retained in the films.

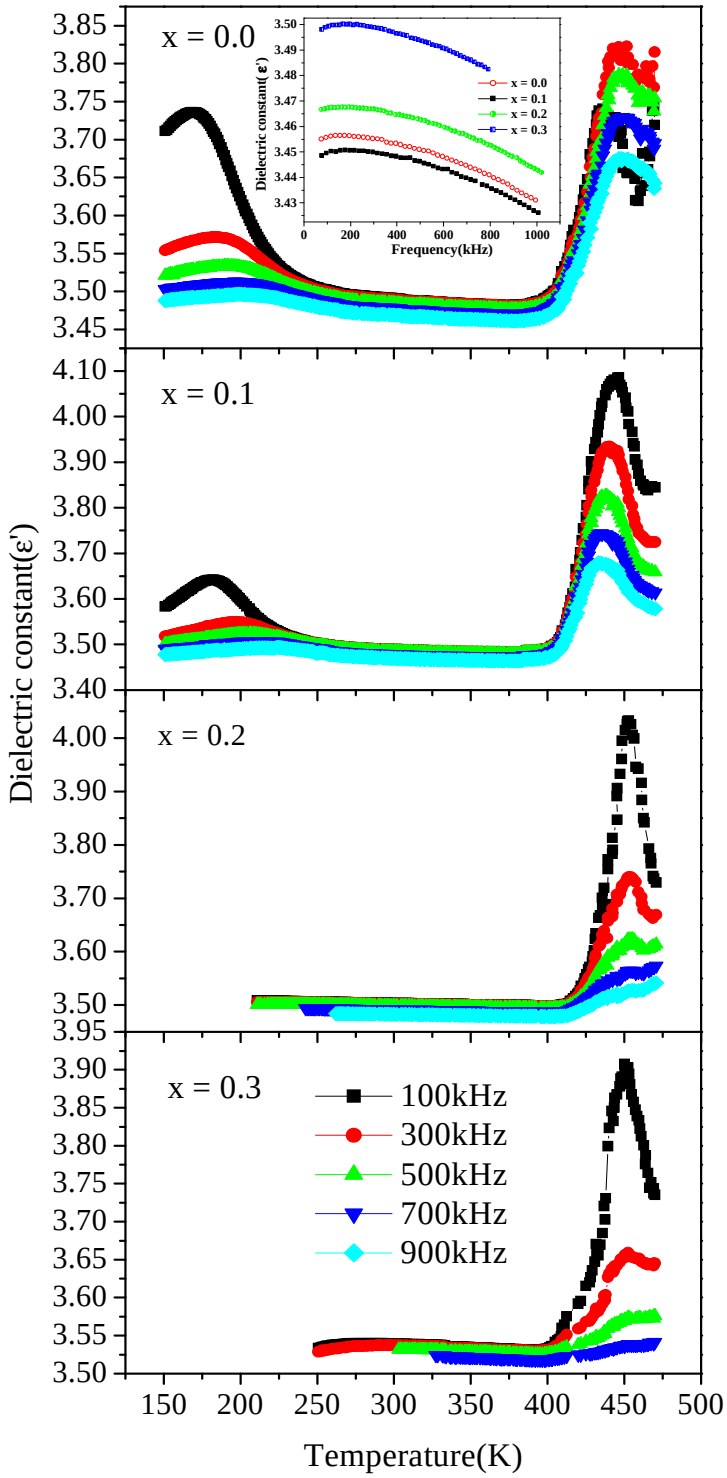

Fig. 5.7. *Dielectric constant (ε΄) vs. Temperature for $Bi_xCo_{2-x}MnO_4$ (x = 0.0, 0.1, 0.2 and 0.3)* and *Inset: Frequency dispersion of ε΄at room temperature.*

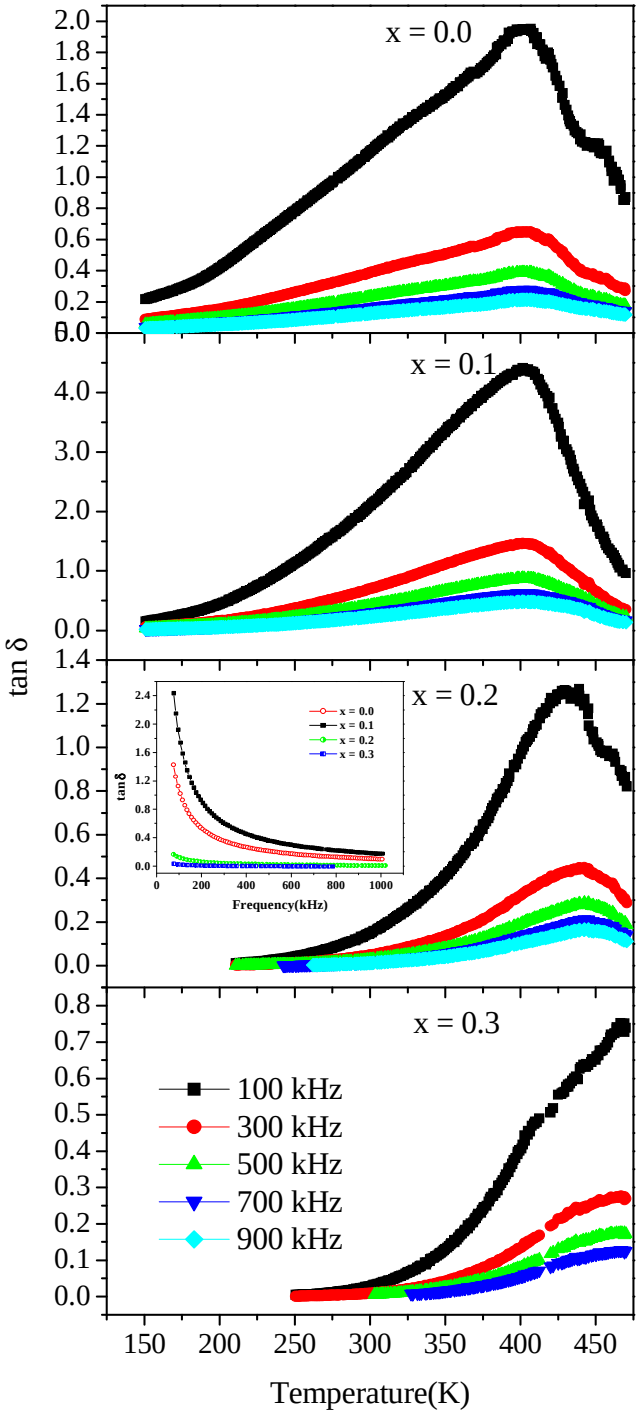

Fig. 5.8. *Tan δ vs. temperature for $Bi_xCo_{2-x}MnO_4$ (x = 0.0, 0.1, 0.2 and 0.3). Inset: Frequency dispersion of loss factor (tanδ) at room temperature.*

Lower value of loss factor possessed by the films with higher Bi-content is conducive for the practical applications using these films. Although the thin film and bulk properties are qualitatively similar, the thin film samples show a usual reduction in FE polarization and dielectric response, compared with the corresponding single crystal-materials [19], the same is exhibited by the presently investigated Bi-substituted Co_2MnO_4 thin films also. This can be due to the substrate-imposed pinning of the domains, which is known to suppress the ferroelectric response in thin films and reduce the dielectric constant. The inset of Fig. 5.7 shows the frequency dispersion of ε′ at room temperature. This shows the distribution of relaxation time associated with the non-identical polarizable species, mainly the oppositely charged Bi and oxygen vacancies, created due to the high temperature required for the film deposition which indicates a weak relaxor type dielectric behaviour of the $Bi_xCo_{2-x}MnO_4$ thin films. FE behaviour of Bi-substituted films is again demonstrated through the Capacitance-Voltage (C-V) characteristics performed for films on YBCO/LAO substrate, at 400 K (the film showed more pronounced FE characteristics at higher temperature than room temperature) and 100 kHz.

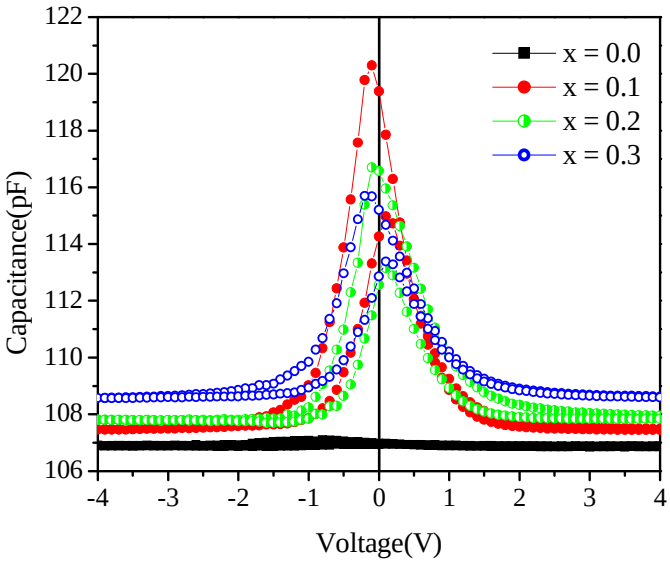

Fig. 5.9. *C-V plot of the $Bi_xCo_{2-x}MnO_4$ (x = 0.1) film at 400K and 100 kHz.*

The nearly butterfly nature of the C-V loop is a signature of FE nature of the Bi-substituted films (Fig.5.9). The asymmetric loop in the C-V plot may be attributed to the different types of electrodes (YBCO & Ag).

5.3.4 Magnetization studies

DC magnetization studies were carried out for the films deposited on LAO substrates, using the VSM option of PPMS set up. Fig. 5.10 illustrates the temperature dependent magnetization for $Bi_xCo_{2-x}MnO_4$ films, measured under magnetic field 0.1 T and shows that ferrimagnetic transition temperature (T_C) slightly vary depending on Bi-content. With Bi substitution the ferrimagnetic-T_C is increased just as observed in the case of bulk.

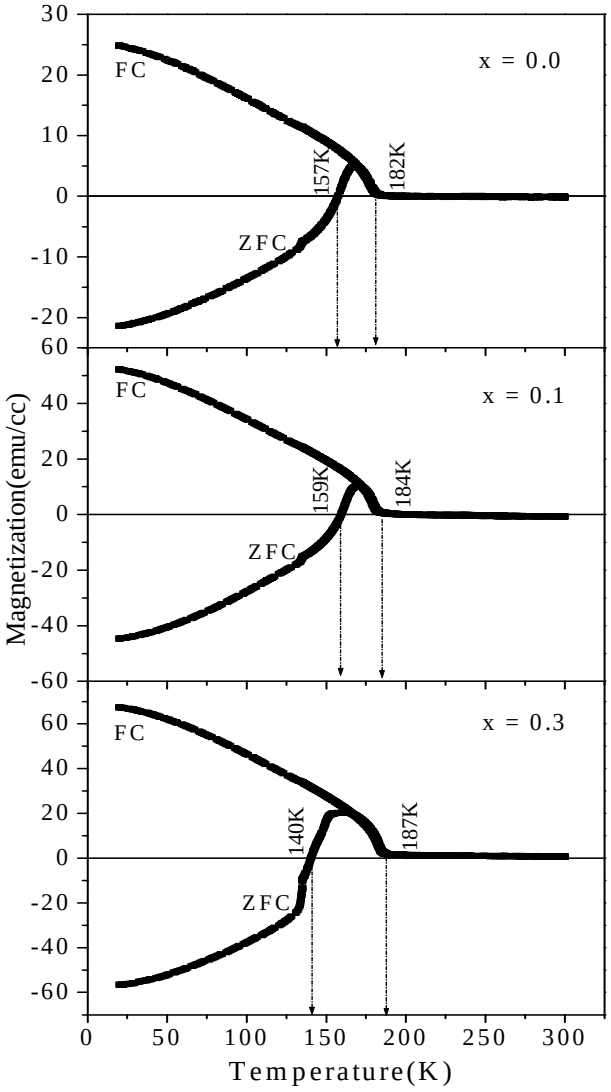

Fig. 5.10. *Magnetization vs. Temperature for $Bi_xCo_{2-x}MnO_4$ (x = 0.0, 0.1 and 0.3) films, at 0.1 T.*

The magnetization (M) versus applied magnetic field (H) at 150 K demonstrated hysteresis loops, depicting ferrimagnetic behaviour of the films, as shown in Fig. 5.11. Saturation magnetization (M_S) is found to increase from 15 emu/cc for x = 0.0 film to 34 emu/cc for Bi-substituted (x = 0.3) film, along with drop in coercive field, H_C (1016 Oe to 597 Oe).

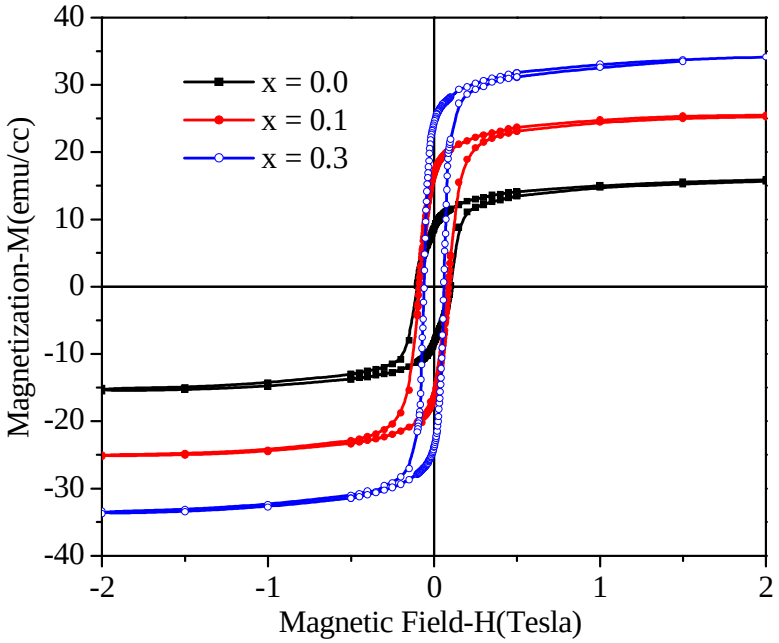

Fig. 5.11. *M-H loops for the $Bi_xCo_{2-x}MnO_4$ (x = 0.0, 0.1 and 0.3) films with at 150 K.*

As evident, from Fig. 5.10 and Fig. 5.11, magnetic behaviour of the films is almost identical with that of the bulk samples of the respective compositions, as described in chapter 4 and supports that thin films maintain the cation configuration similar to that of bulk. Therefore, it is reasonable to attribute the ferrimagnetic nature of $Bi_xCo_{2-x}MnO_4$ films to the canting of the antiferromagnetically ordered spins by the structural distortion [20] and a breakdown of the balance between the antiparallel magnetization at Co^{2+} sublattices due to the substitution of Mn and Bi ions at Co^{3+} sites, arising from the affect on the super exchange interaction, Co^{2+}-O^{2-}-Co^{3+}-O^{2-}-Co^{2+}, that maintains the antiferromagnetism [21]. In other words, the overall ferrimagnetic behaviour of these spinel films with AB_2O_4 structure is found to be effected by the Bi-substitution induced competition among intrasite A-O-A (J_{AA}), B-O-B (J_{BB}) and intersite A-O-B (J_{AB}) superexchange interactions and consequent

magnetic frustration. The increase in ferrimagnetic-T_C (182 K for x = 0.0 to 187 K for x = 0.3) indicates the magnetic frustration, that resulted in lowering of negative molecular field. The increase in net magnetic moment, as demonstrated in Fig. 5.10 and fig. 5.11, is attributed to the evolution of Mn^{2+} and Mn^{4+} at the expense of Mn^{3+} due to the Bi-substitution at octahedral site.

DC magnetization during zero field cooling (ZFC) for all the films is found to undergo a crossover from positive to negative values, which necessitates a magnetic compensation between the opposite contributions of magnetic moments from Co and Mn ions. This characteristic behaviour was not exhibited by the bulk samples. This may be the outcome of the oriented crystalline nature of the films formed on LAO, which hardens (pinning) one set of magnetic moments. The crossover temperature, T_{CR}, is found shifted from 157 K for x = 0.0 to 155 K for x = 0.2 and to 140 K for x = 0.3. This further supports the influence of Bi-substitution in controlling the net magnetic moment of the presently probed thin films. The crossover to negative magnetization originates from the switching of the state with greater moment contribution of Mn ions to the state that provides greater moment contribution of Co ions, with effective coercive field. However this crossover is not visible in field cooled (FC) magnetization, as both the moments reorient towards the applied field. This kind of crossover of magnetization is already reported by Kukarni *et al* [22], for $Nd_{0.75}Gd_{0.25}Rh_3B_2$ alloy at nominal zero fields. Anyhow the film with x = 0.1, showed anomalous behaviour in this regard, with slight increase in T_{CR} (159 K) compared with film without Bi. This calls for further investigation to understand the negative magnetization exhibited by $Bi_xCo_{2-x}MnO_4$ thin films.

5.3.5 X-ray magnetic circular dichroism (XMCD) studies

The magnetic behaviour of the films is observed to be almost identical with that of the bulk samples of the respective compositions, as described in chapter 4 and supports that thin films maintain an ion configuration similar to that of bulk. This is substantiated by the near edge x-ray absorption fine structure (NEXAFS) and XMCD measurements of the thin films, as depicted in Fig. 5.12, which shows the normalized XMCD spectra at Co $L_{3,2}$ and Mn $L_{3,2}$edges of the $Bi_xCo_{2-x}MnO_4$ thin film with x = 0.3, collected at 150 K. Upper panel in both the figures 5.12(a) & 5.12(b) corresponds to NEXAFS spectra for left and right circularly polarized x-

rays, where as lower panel is XMCD signal. From Fig. 5.12(a) it is clear that Co $L_{3,2}$ spectrum is splitted into two broad multiplets, namely, the L_3 ($2p_{3/2}$) and L_2 ($2p_{1/2}$) ~ 15 eV apart, owing to the spin orbit interaction of Co core 2*p* states, as explained for the bulk sample having same composition, in chapter 4. Each of these two regions further splits into t_{2g} and e_g orbital features because of the crystal field effect of neighboring ions. The spectral features observed at 778.5 eV and 780.0 eV correspond to Co^{2+} (in tetrahedral symmetry) and Co^{3+} (in octahedral symmetry) valence state, respectively. The lower intensity of the Co^{2+} peak than the Co^{3+} peak indicates Bi-induced transition of Co^{2+} to Co^{3+}. Substitution of Bi^{3+} at octahedral sites imposes the distribution of Mn ions between octahedral and tetrahedral sites. This is evident in Mn $L_{3,2}$ spectra of the same film shown in Fig. 5.12(b). Like its bulk counterpart, Mn 2*p* core states also split the spectrum into two broad multiplets, namely, the L_3 ($2p_{3/2}$) and L_2 ($2p_{1/2}$) ~ 11 eV, apart. The inflection points of the Mn L_3 edge with identical spectral features as that of the bulk, shown are subsequently at higher energies and correspond to Mn^{2+} (in tetrahedral symmetry), Mn^{3+} and Mn^{4+} (both in octahedral symmetry). This vindicates that the mixed valance states of Mn and Co ions of the film synthesized are exactly matching with that of the bulk.

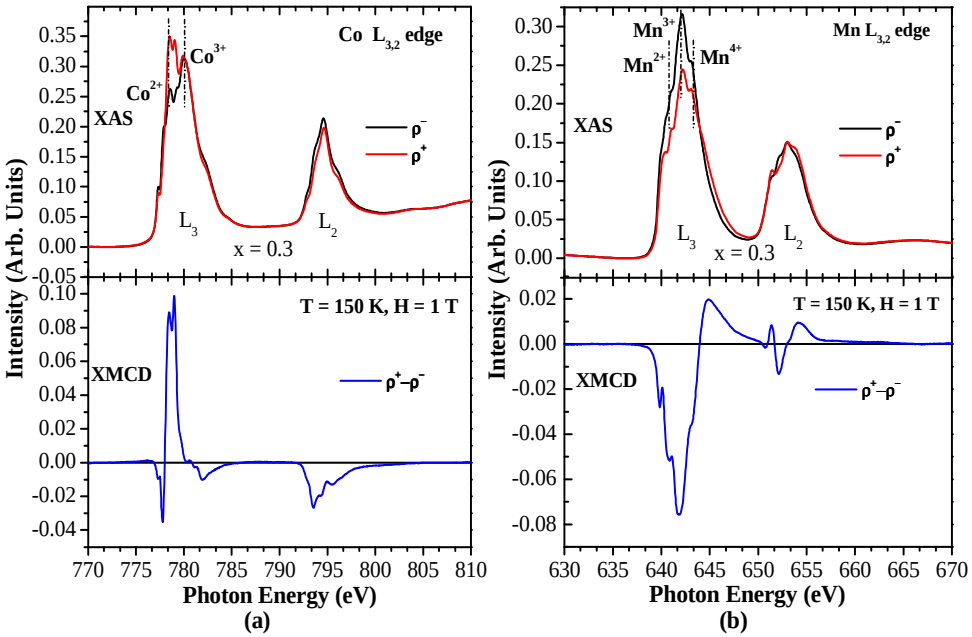

Fig. 5.12. (a) *Co $L_{3,2}$ XAS and XMCD (ρ^+ - ρ^-) and (b)Mn $L_{3,2}$ XAS and XMCD (ρ^+ - ρ^-) signals of $Bi_xCo_{2-x}MnO_4$ thin film with x = 0.3.*

The use of right or left circularly polarized photons which transfer their angular momentum to the excited photoelectron measure the difference in the number of *d* holes and consequently reflected in the XMCD spectra. The polarity of the Mn 2*p* XMCD spectra is opposite to that of the Co 2*p* XMCD spectra at 150 K, well below ferrimagnetic T_C of the material. This indicates the antiparallel alignment of the spin moments between Mn and Co ions as shown in Fig. 5.12(a) and Fig. 5.12(b). Although there is a little dependence of the NEXAFS signal on the polarization of the incident x-ray photon, there is a clear reproducible difference between the NEXAFS collected for the photon helicity parallel and antiparallel with the applied magnetic field (1 T), which is the XMCD signal. In Fig. 5.12(a), the XMCD signal of Co^{2+} at energy ~ 778.5 eV is clearly observed, which is in agreement with the spectral position of Co^{2+} observed in NEXAFS spectra of the film. Likewise, XMCD signal of Mn^{3+} at 642 eV can be identified with the Mn^{3+} spectral position in the NEXAFS spectra. Thus the observed crossover of ZFC magnetization to negative values at 140 K, for film with x= 0.3 (the representative film considered) can be correlated with the imbalance in the contributions spin moments of Co ions and Mn ions which are aligned antiparallel, as clearly depicted in XMCD spectra.

5.3.6 Magnetoelectric studies

The magnetoelectric coupling studies of the films on YBCO/LAO substrates have been carried out using a cryogen free low temperature high magnetic field set up. Dielectric constant was measured without a magnetic field as ε′(0T) and with a magnetic field of 3 Tesla as ε′(3T) during warming cycle, after zero-field cooling. Distinct variation in ε′(3T) was observed for $Bi_xCo_{2-x}MnO_4$ film (x = 0.3), relative to ε′(0T), during the entire range of temperature (100-300 K). For the film of composition x = 0, hardly any distinction between ε′(3T) and ε′(0T) was visible and film with x = 0.1 displayed weak dependence of ε′ on magnetic field (Fig. 5.13). Inset of Fig. 5.13 shows the relative percentage variation in dielectric constant under an applied magnetic field (magnetoelectric coupling) and is determined as $\left[\frac{\varepsilon'(3T)-\varepsilon'(0T)}{\varepsilon'(0T)}\times 100\right]$, for the film with x = 0.3. The maximum magnetoelectric coupling was observed at ~ 183 K; just below the ferrimagnetic transition

temperature of the film material, and the magnetoelectric response was found reduced at lower and higher temperature regimes of the measurement carried out. Similar magnetoelectric effect was achieved in the bulk composition and therefore it is sensible to exclude extrinsic contribution like the strain effect induced by the substrates on the film grown [19]. The negative magnetoelectric response exhibited by the film when the magnetic field is applied perpendicular to it, in contrast to the positive dielectric response exhibited by the respective composition in bulk form, is supposed to appear from the suppression of the excitation from a singly occupied state to another state by the magnetic field, arising from the preferentially oriented growth of the films.

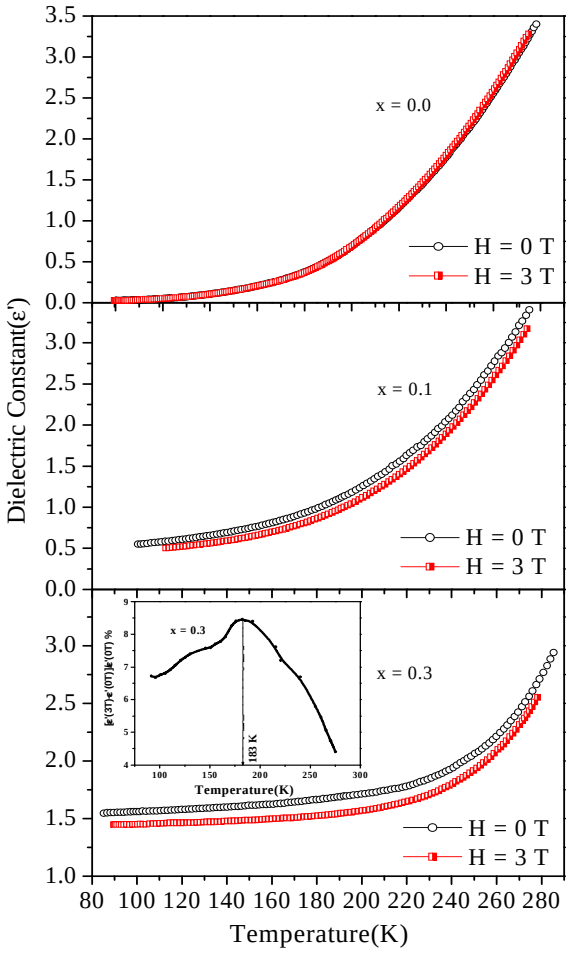

Fig. 5.13. *Magnetic field dependent variation of ε' with temperature* & Inset: *Magnetoelectric coupling* $\left[\frac{\varepsilon'(H)-\varepsilon'(0)}{\varepsilon'(0)}\right]$ *versus temperature for* $Bi_xCo_{2-x}MnO_4$ *film (x = 0.3).*

Similar behavior was observed in $Bi_6Fe_2Ti_3O_{18}$ films by Lu *et al* [23]. The magnetoelectric response the Bi-substituted Co_2MnO_4 films is originating from the non-collinear magnetic ordering occurring due to the geometrical frustration of the lattice on cation substitution that affect the collinear antiferromagnetic ordering of the parent composition Co_3O_4, arising from the substitution by Mn^{3+} and Bi^{3+} cations in the spinel lattice. This results in the magnetic origin of ferroelectricity as in the inversed Dsyaloshinskii-Moriya interaction occurring in complex magnetic structures such as non-collinearly canted antiferromagnets where the canted spins displaces the oxygen sandwiched between them and leads to electric polarization through electron-phonon interaction [24, 25]. The diminution of the magnetoelectric effect at high temperature may be due to the order-disorder transition of magnetic ions in the complex magnetic structure of the Bi_xCo_{2-x} MnO_4 (x = 0.3) film which results in the flip of polarization against the normal ferroelectric polarization. The reduction in the magnetoelectric effect at lower temperature can be attributed to the collinear magnetic ordering. The ferroelectric as well as magnetoelectric measurements of these films have been carried out at high frequency (100 kHz and above) to rule out the contribution of polarization of arising from magnetoresistance combined with Maxwell-Wagner effect [26], as discussed in chapter 3.

5.4 Conclusions

The results of the study of thin films of $Bi_xCo_{2-x}MnO_4$ grown by PLD on different substrates lead to following conclusions:

(i) XRD pattern and AFM images of thin films of $Bi_xCo_{2-x}MnO_4$, show that good quality, single phased polycrystalline films of Bi_xCo_{2-x} MnO_4 (x = 0.0, 0.1, 0.2 & 0.3) with preferred orientation was grown by PLD on amorphous quartz, LAO and YBCO/LAO substrates. The growth of the single phase films were confirmed by Raman spectra. Moreover, from the XRD study, it is observed that the film deposited on YBCO/LAO has smaller grain size than that of the film deposited on quartz and LAO. AFM images depicted the increase in grain size and roughness.

(ii) Dielectric data of the $Bi_xCo_{2-x}MnO_4$ films reveals the weak ferroelectric behaviour and FE-T_C increases as Bi content increases. Films are found to possess lower dielectric constant compare to that of the bulk samples and exhibited better ferroelectric nature at higher temperature. Similar variations of dielectric loss factor, tan δ with temperature supports that the stoichiometry of the bulk samples are retained in the films.

(iii) DC magnetization studies show that the thin films of $Bi_xCo_{2-x}MnO_4$ deposited on LAO exhibited well defined hysteresis loop at 150 K, which revealed its ferrimagnetic behaviour. Both M_S and ferrimagnetic-T_C increase as Bi-content increases in the films, owing to the Bi-induced redistribution of cations at the octahedral sites, similar to the bulk samples. This indicates that the thin films maintain an ion configuration similar to the bulk. Magnetization exhibited crossover from positive to negative values at ZFC.

(iv) $Bi_xCo_{2-x}MnO_4$ films with higher Bi-content demonstrated magnetoelectric coupling, as the variation of dielectric constant in response to the applied magnetic field and exhibited maxima at ferrimagnetic-T_C, similar to bulk samples. This suggests that the effect of substrate induced strain, if any, can be ruled out for the Bi-substituted samples, confirming the magnetic origin of ferroelectricity. Magnetoelectric coupling is supposed to originate from the interplay between structural distortion and magnetic exchange interaction.

The films exhibited both the ferroelectric and ferrimagnetic properties, revealing the multiferroic characteristics along with magnetoelectric effect which strongly support the candidature of this film material for multiferroic device applications.

References

1. M. Li, M. Ning, Y. Ma, Q. Wu and C K Ong, J. Phys D: Appl. Phys **40** (2007) 1603.

2. Y. H. Chu, L. W. Martin, M. B. Holcomb, M. Gajek, S. J Han, Q. He, N. Balke, C. H. Yang, D. Lee, W. Hu, Q. Zhan, P. L Yang, A. F. Rodriguez, A. Scholl, S. X. Wang and R. Ramesh, Nature Mater. **7** (2008) 478.

3. D. K. Shukla, S. Mollah, R. Kumar, P. Thakur, K. H. Chae, W. K. Choi and A. Banerjee, J. Appl. Phys. **104** (2008) 033707.

4. Ce-Wen Nan, M. I. Bichurin, S. Dong, D. Viehland, and G. Srinivasan, J. Appl. Phys. **103** (2008) 031101.

5. M. Gajek, M. Bibes, S. Fusil, K. Bouzehouane, J. Fontcuberta, A. Barthélémy, and A. Fert, Nature Mater. **6** (2007) 296.

6. V. A. Khomchenko, D. A. Kiselev, J. M.Vieira, and L. Kholkin, Appl. Phys. Lett. **90** (2007) 242901.

7. N. E. Rajeevan, P. P. Pradyumnan, R. Kumar, D. K. Shukla, S. Kumar, A. K. Singh, S. Patnaik, S. K.Arora, and I. V. Shvets, Appl. Phys. Lett. **92** (2008) 102910.

8. D. G. Schlom, J. H. Haeni, J. Lettieri, C. D. Theis, W. Tian, J. C. Jiang, X. Q. Pan, Mater. Sci. Engg. B **87** (2001) 282.

9. M. C. Terzzoli, S. Duhalde, S. Jacobo, L. Steren, C. Moina, J. Alloys and Comp. **369** (2004) 209.

10. M. A. Khan, A. Garg, and A. J. Bell, J. Phys.: Conference Series **26** (2006) 288.

11. Y. Yamamoto, H. Tanaka, T. Kawai, J. Mag. Mag. Mater. **261** (2003) 263.

12. Y. Muraoka, K. Ueda, H. Tabata, T. Kawai, Vacuum **59** (2000) 622.

13. S. Tiwari, R. Prakash, R. J. Choudhary and D. M. Phase, J. Phys. D: Appl. Phys. **40** (2007) 4943.

14. J. S. Bettinger, R. V. Chopdekar, M. Liberati, J. R. Neulinger, M. Chshiev, Y. Takamura, L. M. B. Alldredge, E. Arenholz, Y. U. Idzerda, A. M. Stacy, W. H. Butler, Y. Suzuki, J. Mag. Mag. Mater. **318** (2007) 65.

15. J. Matsuno, Y. Okimoto, Z. Fang, X. Z. Yu, Y. Matsui, N. Nagaosa, M. Kawasaki, and Y. Tokura; Phys. Rev. Lett. **93** (2004) 167202.

16. N. Ortega, P. Bhattacharya, and R. S. Katiyar, P. Dutta, A. Manivannan, M. S. Seehra, I. Takeuchi and S. B. Majumder, J. Appl. Phys. **100** (2006) 126105.

17. P. Samarasekara, R. Rani, F. J. Cadieu and S.A. Shaheen, J. Appl. Phys. **79** (1996) 8.

18. C. Dong, J. Appl. Cryst. **32** (1999) 838.

19. R. Ramesh and N. A Spaldin, Nature Mater. **6** (2007) 21.

20. T. Suzuki, H. Nagai, M. Nohara, and H. Takagi, J. Phys.: Condens. Matter. **19** (2007) 145265.

21. Y. Yamasaki, S. Miyasuka, Y. Kaniko, J. P. He, T. arima, and Y. Tokura, Phys. Rev. Lett. **96** (2006) 207204.

22. P. D. Kulkarni, U. V. Vaidya, V. C. Rakhecha, A. Thamizhavel, S. K. Dhar, A. K. Nigam, S. Ramakrishnan, and A. K. Grover, Phys. Rev. B **78** (2008) 064426.

23. J. Lu, L. J. Quio, X. Q. Ma and W. Y. Chu, J. Phys.: Condens. Matter **18** (2006) 4801.

24. S. W. Cheong, and M. Mostovoy, Nature Mater. **6** (2007) 13.

25. I. A. Sergienko and E. Dagotto, Phys. Rev. B **73** (2006) 094434.

26. G. Catalan Appl. Phys.Lett. **88** (2006) 102902.

Chapter 6

Effect of Swift Heavy Ion Irradiation on the Structural, Dielectric and Magnetic Properties of $Bi_XCo_{2-x}MnO_4$ Thin Films

This chapter presents the effect of 200 MeV Ag^{15+} ions irradiation on the structural, dielectric and magnetic properties of $Bi_xCo_{2-x}MnO_4$ thin films grown on Quartz, LAO and YBCO-coated LAO substrates.

6.1 Introduction

Recently efforts have been made to synthesize multiferroic thin films from single phase ferroelectric and magnetic compounds. Multiferroic thin films reveal a range of interesting phenomena and stimulated the exploration of new device heterostructures [1-3]. From literature, it is found that there is a constant interest in the optimization of the properties of multiferroic thin films, as it envisages a wide variety of smart devices such as multiple memory devices, electric field controlled ferromagnetic resonance devices, and transducers with magnetically modulated piezoelectricity etc. It has been well established that structural, electrical and magnetic properties of spinel oxide films are extremely sensitive to the external pressure or stress/strain induced in the system. This may be possible through different routes like changing the ionic radii of the substituted cation, creating cation-oxygen vacancies or by swift heavy ion (SHI) irradiation [4-5]. Among these methods, SHI irradiation is found to be a unique method for engineering the properties of a material [6]. SHI radiation is known to introduce controlled defects and structural disorder and can modify the strain, electrical and magnetic properties in the films. Significant changes in the magnetic hysteresis features were observed for nanoparticles of $Ni_{0.8}Cu_{0.2}Fe_2O_4$ having spinel cubic structures on irradiation by 100 MeV Ni ions, and was attributed to the SHI induced formation of cluster of defects in the nanocrystalline samples [7]. Modifications on structural, electrical transport and magnetic properties of epitaxial magnetite (Fe_3O_4) thin films grown on MgO (100) oriented substrate have been reported by Ravi Kumar et al [4] and they have explained on the basis of structural strain and disorder induced by SHI (200 MeV Ag 15^+), which lead to modification in the inter-ionic Coulomb potential at octahedral sublattices and bandwidth in this system. 200MeV Ag^{15+} ion irradiated thin films of Fe-doped ZnO, deposited on α-Al_2O_3 (0001) single crystal substrates using plasma assisted molecular beam epitaxy (PAMBE) exhibited room temperature ferromagnetism and a metal–semiconductor transition at 227K [8]. The characteristic Verwey-transition temperature of the epitaxially grown thin films of Fe_3O_4 was found to increase with SHI irradiation by 200 MeV Ag^{15+} and this

behaviour was associated to the release of substrate induced strain after ion irradiation [9]. A metallic catalyst assisted growth of magnetic nanopillars was reported, in the thin films of $Mg_{0.95}Mn_{0.05}Fe_2O_4$ after SHI irradiation by 200MeV $Ag15^+$ ion [10]. The degradation of ferroelectric properties of $Pb(Zr_{0.53}Ti_{0.47})O_3$ and $SrBi_2Ta_2O_9$ thin films irradiated by 50 MeV Li^{3+} were ascribed to the irradiation-induced partial amorphisation and the pinning of the ferroelectric domains by the trapped charges and found that after annealing former partially regained the ferroelectric properties, while latter did not. The regaining of properties after annealing is attributed to the thermal annealing of the defects, generated during the irradiation [11]. The decrease in dielectric property exhibited by 190 MeV Ag^{15+} ion irradiated $NiMn_{0.05}Fe_{1.95}O_4$ thin film compared to the pristine film was explained as the consequence of the fall in the number of ferrous sites, required for polarization and the obstruction of flow of space charge carriers that could build up space charge polarization, in the irradiated films [5]. The SHI is known to generate the controlled defect states such as structural strain, point/cluster of defects and columnar defects depending upon the type of ion, energy, fluence and the target material. It is well established and reported that swift heavy ions lose their energy via two nearly independent processes. When the swift heavy ions pass through the material, the ions either excite or ionize the atoms by inelastic collisions or displace atoms of the target by elastic collisions. Elastic collisions are dominant in low energy regime, whereas inelastic collision process dominates at high-energy regime. From the literature, it is evident that electronic energy loss S_e due to inelastic collision is able to generate point/cluster defects provided S_e is less than the threshold value of electronic energy loss,S_{eth} [12]. Nuclear energy loss (S_n), following the elastic collision of the ions has only low profile, if the striking ions possess high energy (~ 100 MeV). Investigations by many research groups revealed that the threshold, S_{eth} to create the columnar defects/latent tracks is about ~ 10 - 14 keV/nm for the spinel oxides [7, 10, 12-15]. For the present Bi-doped spinel oxide system, we chose the condition $S_e > S_{eth}$ because the strain induced by defects and amorphisation following the origination of latent tracks are also responsible for drastic changes in the structural, dielectric and magnetic properties [16-18]. Studies

on the magnetoelectric properties of the Bi-substituted Co_2MnO_4 spinel in bulk and thin films has been reported [19, 20, 21, 22], the details of which are given in chapter 3, 4 and 5. In this chapter, the irradiation effect of 200 MeV Ag^{15+} ions on the structural, dielectric and magnetic properties of the Bi-substituted Co_2MnO_4 thin films prepared by pulsed laser deposition (PLD) is presented.

The thin films of $Bi_xCo_{2-x}MnO_4$ on amorphous quartz, LAO and YBCO/LAO substrates were cut into four pieces, each of 5 mm × 5 mm size. This set of four pieces was used for irradiation and further study in order to keep the growth conditions uniform for all the samples. One piece of film was kept pristine while the other pieces of the thin film were irradiated at the room temperature with 200 MeV Ag^{15+} ion beam using the 15 UD tandem accelerator at the Inter-University Accelerator Centre, New Delhi, INDIA, with different fluence value such as 1×10^{11}, 5×10^{11} and 1×10^{12} ions/cm^2. The irradiation was performed under high vacuum condition (base pressure 2×10^{-6} Torr). The incident angle of the ion beam was kept slightly away from the normal to the sample surface to avoid the channeling effects and also the beam current was kept 0.1 pnA to avoid the heating. The ion beam was focused to a spot of 1 mm diameter and scanned over the entire area of the film using a magnetic scanner. The fluence values were confirmed by measuring the charge falling over the sample surface, in the secondary electron suppressed geometry. The ladder current was measured with a digital current integrator and a scalar counter.

6.2 Results and discussion

In the present research work, 200 MeV Ag^{15+} ions have been used for the irradiation on $Bi_xCo_{2-x}MnO_4$ thin films on amorphous quartz, LAO and YBCO/LAO substrates grown by PLD. The electronic energy loss (S_e), nuclear energy loss (S_n) and range of ion (R_p) have been calculated by using SRIM2008 (Stopping and Range of Ions in Matter) simulation program and are found as 20.7 keV/nm, 55.6 eV/nm and 15.5 µm, respectively. From these values it is clear that S_n is two orders of magnitude smaller than S_e and ion range is much larger than the film thickness (350 nm). The S_{eth} to create columnar defects in this spinel oxide materials is 14 keV/nm and the S_e opted (Table 6.1 and Fig.6.1) is greater than the required threshold.

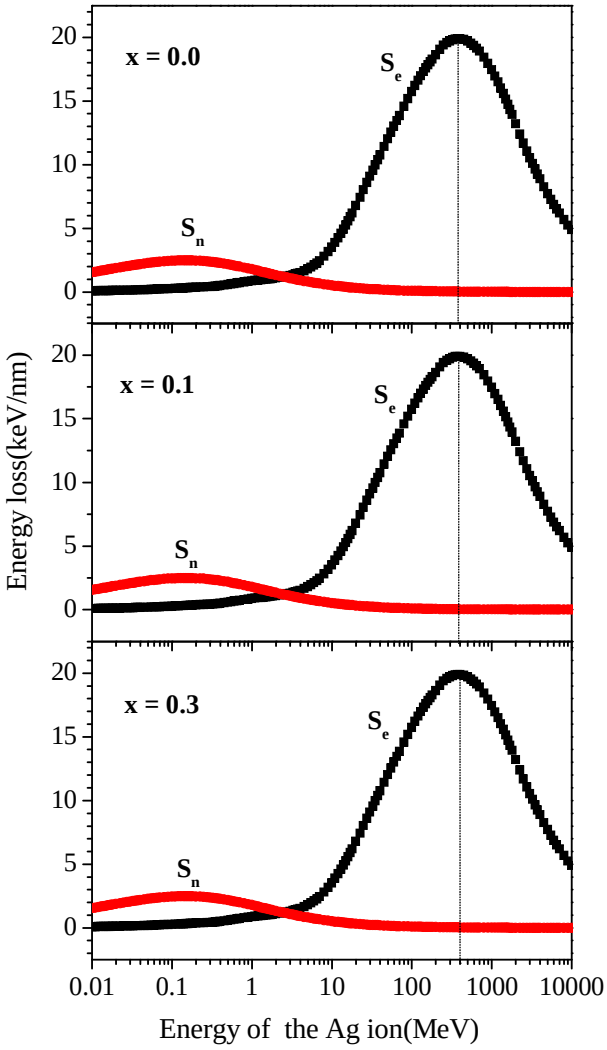

Fig. 6.1. *Variation of $(dE/dx)_e$ and $(dE/dx)_n$ versus energy in $Bi_xCo_{2-x}MnO_4$ for 200 MeV Ag ions.*

Table 6.1. *The electronic stopping power (S_e), nuclear stopping power (S_n), and range (R_p) of 200 MeV Ag^{15+} ions $Bi_xCo_{2-x}MnO_4$ calculated using the SRIM-2008.*

$Bi_xCo_{2-x}MnO_4$	$S_e = (dE/dX)_e$ (keV/nm)	$S_n = (dE/dX)_n$ (eV/nm)	S_e/S_n	R_p (µm)
x = 0.0	20.73	55.66	372.43	15.48
x = 0.1	19.94	54.18	368.03	16.09
x = 0.2	19.25	52.88	364.03	16.67
x = 0.3	18.63	51.73	360.13	17.23

6.2.1 Structural (XRD) and morphological (AFM) characterizations

X-ray diffraction (XRD) using Bruker D8 X-ray Diffractometer with Cu K_α radiation at room temperature has been performed in standard θ/2θ mode for the identification of phase and the orientation of the thin films. XRD pattern confirms the single phase nature and oriented growth of the $Bi_xCo_{2-x}MnO_4$ thin films on all the three sets of substrates; quartz, LAO and YBCO/LAO.

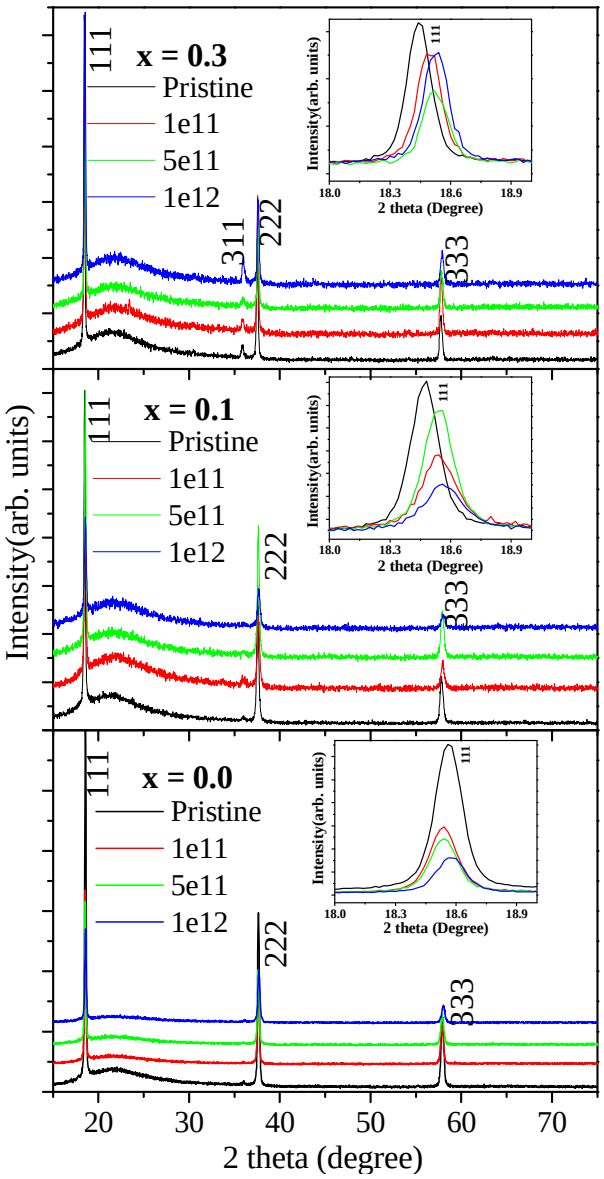

Fig. 6.2. *XRD pattern for the pristine and irradiated films of $Bi_xCo_{2-x}MnO_4$ (x = 0.0, 0.1, and 0.3) on quartz substrates.*

Crystal structure of the films is found matching well with the cubic spinel structure (F*d3m* space group) of the bulk target material. Figure 6.2 shows the XRD patterns of pristine thin films of $Bi_xCo_{2-x}MnO_4$ grown on quartz substrates and of the same film irradiated at different fluences, 1×10^{11}, 5×10^{11}, 1×10^{12} ions/cm^2. XRD pattern reveals (111) oriented nature of $Bi_xCo_{2-x}MnO_4$ films on amorphous quartz substrates. The insets of Fig. 6.2 depict the zoomed (111) reflection of the pristine and 200 MeV Ag^{15+} ion irradiated films grown from different compositions of varying Bi-content on quartz substrates. It is found that, on increasing the fluence in the order 1×10^{11}, 5×10^{11} and 1×10^{12} ions/cm^2, lattice constant '*a*' decreases and full width half maximum (FWHM) in respect of (111) reflection increases (Table 6.2).

Table 6.2. *XRD analysis of $Bi_xCo_{2-x}MnO_4$ thin films on amorphous quartz substrates.*

$Bi_x Co_{2-x} MnO_4$	Ion Fluence (cm^{-2})	Lattice constant(in Å)	FWHM (degrees)	Strain
x = 0.0	Pristine	8.2752	0.1341	0.0016
	1×10^{11}	8.29012	0.1597	0.0019
	5×10^{11}	8.29012	0.1439	0.0017
x = 0.1	Pristine	8.31645	0.1308	0.0016
	1×10^{11}	8.29012	0.1320	0.0016
	5×10^{11}	8.28138	0.1294	0.0015
x = 0.3	Pristine	8.3343	0.1160	0.0014
	1×10^{11}	8.3164	0.1187	0.0014
	5×10^{11}	8.2988	0.1284	0.0015

The lattice strain (*T)* in the film is calculated using the relation [23],

$$T \tan\theta = (\lambda/D \cos\theta) - B \qquad \text{---- (6.1)}$$

where B is FWHM, λ is X-ray wavelength (1.54 Å for Cu K_α) and θ is the Bragg's angle in degrees and D, the grain size obtained using Debye-Scherrer formula. The strain calculated for the Bi_xCo_{2-x} MnO_4 thin films on amorphous quartz substrates are shown in Table 6.2. It is clear that film deposited on quartz substrate maintains almost constant strain in pristine and irradiated samples. The nature of irradiation induced defects may be the extended defects and partial amorphisation. It has been noticed that, for the films irradiated at fluence 5×10^{11} ions/cm^2, FWHM is decreased

with increased intensity of the peaks and is indicative of the release of strain present in the film. So, 5×10^{11} ions/cm^2 appears to be the optimum ion fluence rate for the growth of well textured thin films.

The $Bi_xCo_{2-x}MnO_4$ thin films grown on crystalline LAO substrates are found to possess almost similar lattice parameters, as in the case of quartz substrates revealing the lower strain that is conducive to retain a better crystallinity in the films (Fig. 6.3 and table 6.3).

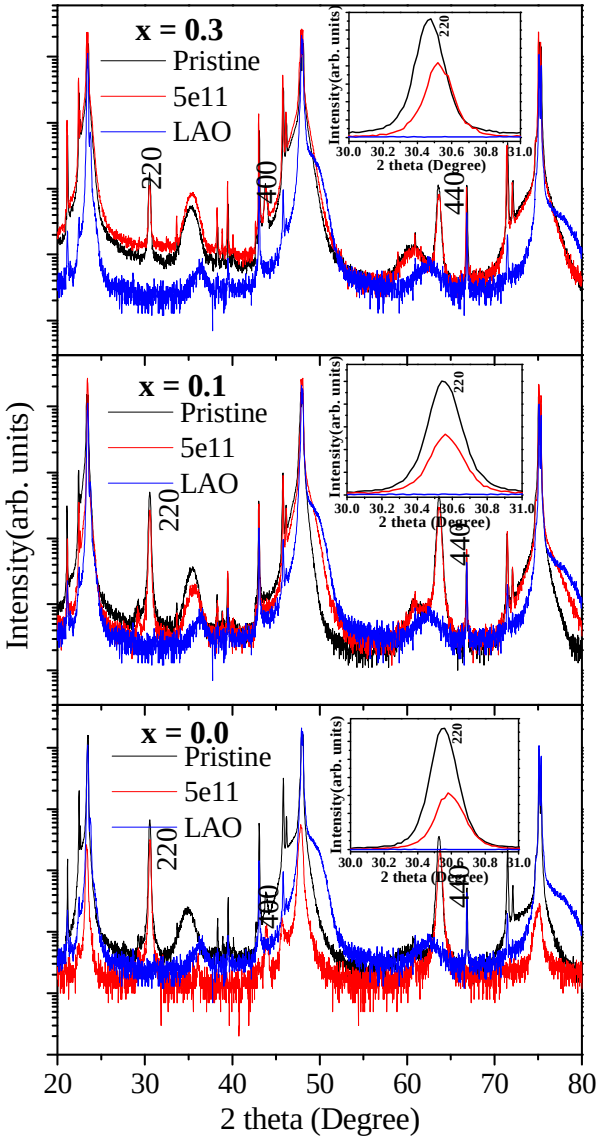

Fig. 6.3. *XRD patterns for the pristine and irradiated films of $Bi_xCo_{2-x}MnO_4$ (x = 0.0, 0.1, and 0.3) on LAO substrates.*

With irradiation at fluence 5×10^{11} ions/cm^2, a marginally reduced lattice constant and lower strain is observed, which indicates that the films grown on LAO possess better crystallinity among all three substrates.

Table 6.3. *XRD analysis of $Bi_xCo_{2-x}MnO_4$ thin films on LAO substrates.*

$Bi_xCo_{2-x}MnO_4$	Ion Fluence (ion-cm^{-2})	Lattice constant(in Å)	FWHM (degrees)	Strain
x = 0.0	Pristine	8.2752	0.1939	0.0014
	5×10^{11}	8.2671	0.1954	0.0014
x = 0.1	Pristine	8.2803	0.1649	0.0014
	5×10^{11}	8.2722	0.1713	0.0012
x = 0.3	Pristine	8.2986	0.1633	0.0013
	5×10^{11}	8.2857	0.1703	0.0013

However, slightly increased strain and FWHM along with noticeably deviated lattice constant were observed for the films grown on YBCO/LAO (Table.6.4 and Fig. 6.4), which is attributed to the lattice mismatch of $Bi_xCo_{2-x}MnO_4$ with YBCO bottom layer, as explained in chapter 5.

Table 6.4. *XRD analysis of $Bi_xCo_{2-x}MnO_4$ thin films on YBCO/LAO substrates.*

$Bi_xCo_{2-x}MnO_4$	Ion Fluence (cm^{-2})	Lattice constant(in Å)	FWHM (degrees)	Strain
x = 0.0	Pristine	8.2613	0.3632	0.0021
	1×10^{11}	8.2577	0.5681	0.0032
	5×10^{11}	8.2757	0.3245	0.0018
x = 0.1	Pristine	8.2976	0.3306	0.0019
	1×10^{11}	8.2812	0.4006	0.0023
	5×10^{11}	8.3287	0.2683	0.0015
x = 0.3	Pristine	8.2776	0.2690	0.0022
	1×10^{11}	8.2703	0.2806	0.0023
	5×10^{11}	8.3067	0.2503	0.0022

In this series of films, irradiation at fluence 5×10^{11} ions/cm^2 leads to the release of the strain to a certain extent and can be regarded as the optimum ion fluence value for improving the crystallinity of $Bi_xCo_{2-x}MnO_4$ thin films grown.

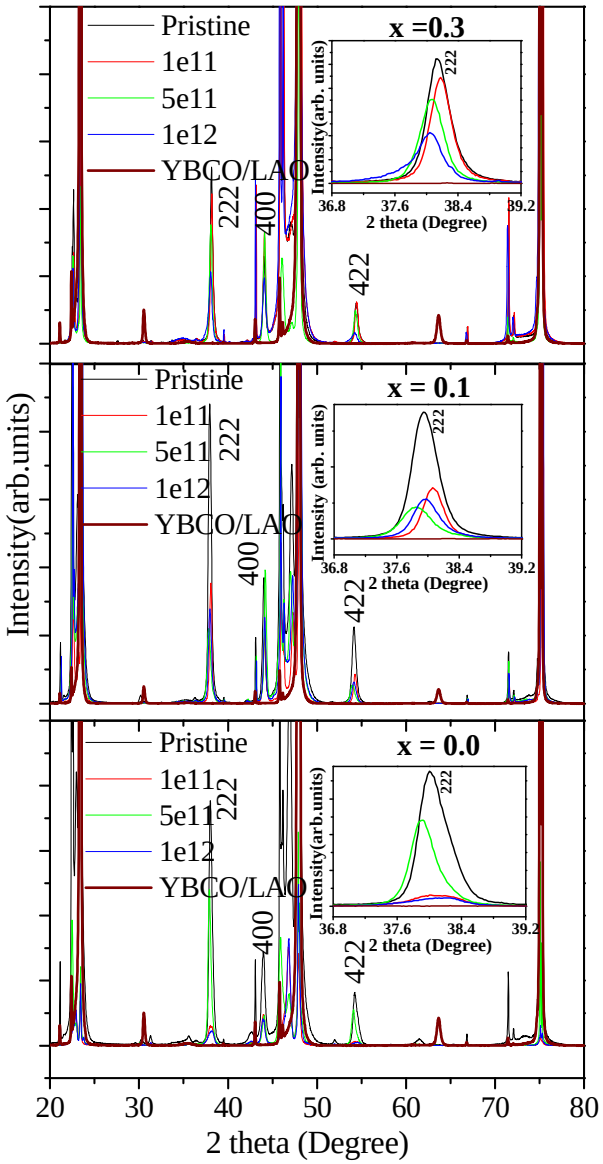

Fig. 6.4. *XRD pattern for the pristine and irradiated films of $Bi_xCo_{2-x}MnO_4$ (x = 0.0, 0.1, and 0.3) on YBCO/LAO substrates.*

From the XRD analysis, it was observed that all the Bi_xCo_{2-x} MnO_4 films grown on amorphous quartz, crystalline LAO and YBCO/LAO substrates exhibited single phase cubic spinel structure before and after the irradiation. The irradiation at 5×10^{11} ions/cm^2 appears to be the optimum fluence, considering the crystallinity, which can be attributed to the release of the strain. From the XRD spectra it is clear that there is no structural transformation occurred in thin film materials with SHI irradiation,

except small variation of their peak intensities and peak broadening. The fall in intensity of the XRD reflection peaks is suggestive of the partial amorphisation in the irradiated films. Further, investigation of the changes produced by the SHI irradiation o the surface morphology of these films has been carried out utilizing atomic force microscopy (AFM).

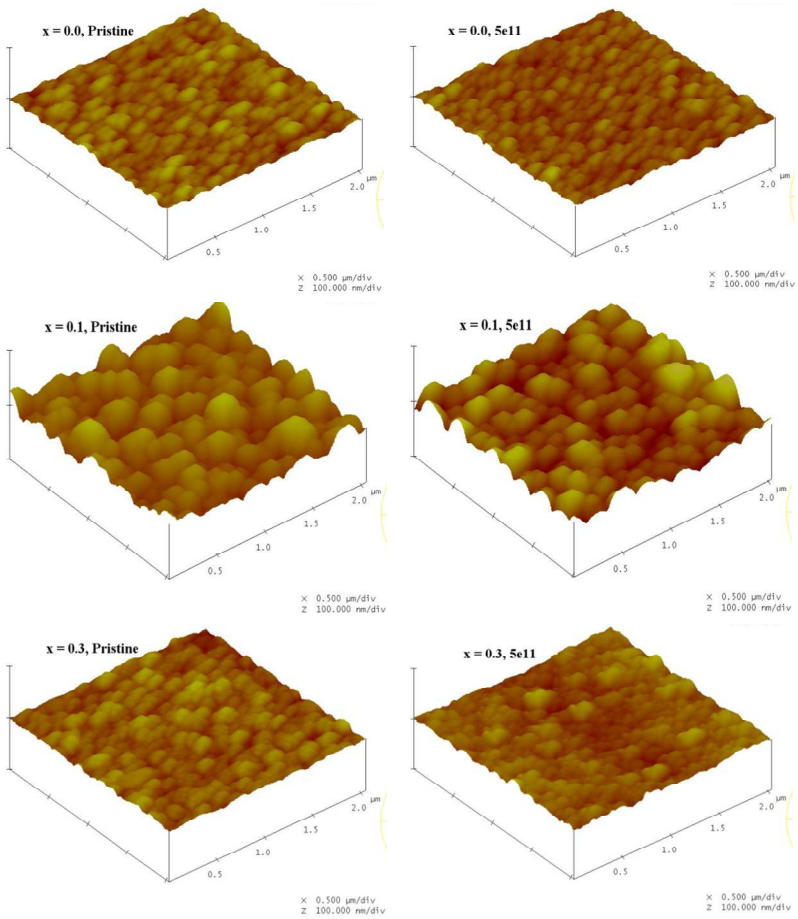

Fig. 6.5. *AFM images of pristine and irradiated thin films of $Bi_xCo_{2-x}MnO_4$ (x = 0.0, 0.1, and 0.3) grown on LAO.*

Surface morphology of the thin films is characterized by the AFM technique, as described in chapter 5. Fig. 6.5 show the room temperature AFM images of pristine as well as irradiated $Bi_xCo_{2-x}MnO_4$ thin films deposited on LAO substrates. The findings have been correlated considering the root mean square (rms) of the roughness height and grain size. The roughness is found increasing with irradiation. RMS roughness increased from 2.67 nm to 3.03 nm in the Bi_xCo_{2-x} MnO_4 film for x

= 0.0 and 2.10nm to 2.23nm in the Bi_xCo_{2-x} MnO_4 film for x = 0.3, with the irradiation at 5×10^{11} ions/cm^2. Average diameter of the grains was found decreasing with irradiation, as a consequence of irradiation induced grain fragmentation. However the grain size and roughness were relatively higher for the film with x = 0.1, as the bulk target composition of this particular Bi-content exhibited more stabilized growth (Chapter 3).

6.2.2 Raman scattering studies

As discussed in chapter 4 and chapter 5, Raman modes of the pristine and irradiated $Bi_xCo_{2-x}MnO_4$ thin films on different substrates were analyzed in respect to the parent compound, Co_3O_4, with normal spinel structure having O_h^7 spectroscopic space group. Co_3O_4 possess five Raman active modes; $A_{1g} + E_g + 3F_{2g}$, as 194.4 cm^{-1} (F^1_{2g} - tetrahedral), 482.4 cm^{-1} (E_g), 521.6 cm^{-1} (F^2_{2g}), 618.4 cm^{-1} (F^3_{2g}), and 691 cm^{-1} (A_{1g} - octahedral).

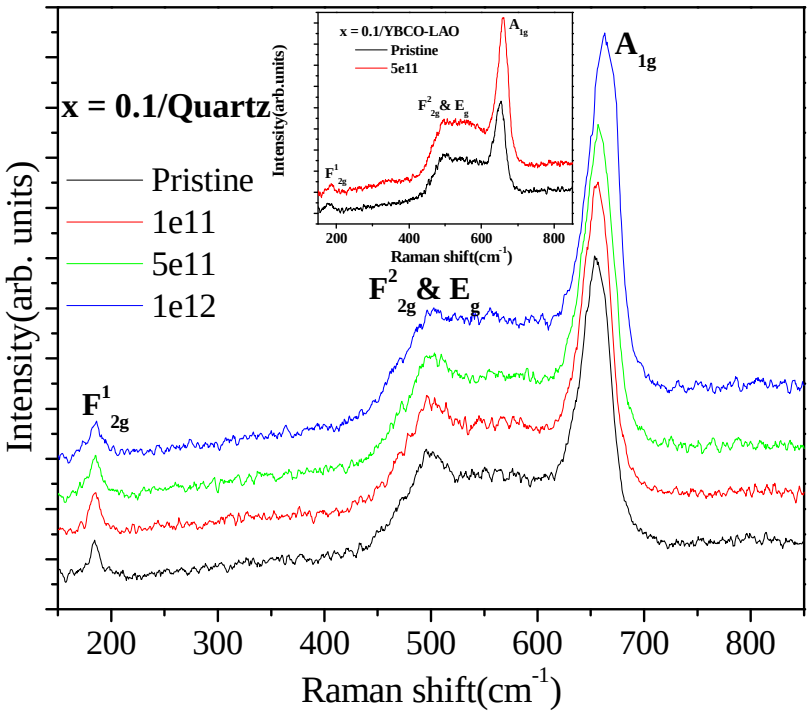

Fig. 6.6. *Raman Spectra for the films of $Bi_xCo_{2-x}MnO_4$ for x = 0.1 on quartz substrates and Inset: Raman Spectra for the films of $Bi_xCo_{2-x}MnO_4$ for x = 0.1 on YBCO/LAO substrates.*

Fig.6.6 depicts the Raman spectra of the pristine and irradiated films grown on quartz and YBCO/LAO (Inset) substrates, for x = 0.1. All the pristine and irradiated films displayed the characteristic Raman modes corresponding to octahedral (A_{1g} ~ 650-655 cm^{-1}) and tetrahedral (F^1_{2g} ~ 180-185cm^{-1}) sites, and coalesced E_g - F^2_{2g} mode at ~ 500 cm^{-1} indicating that there is no structural change with irradiation.

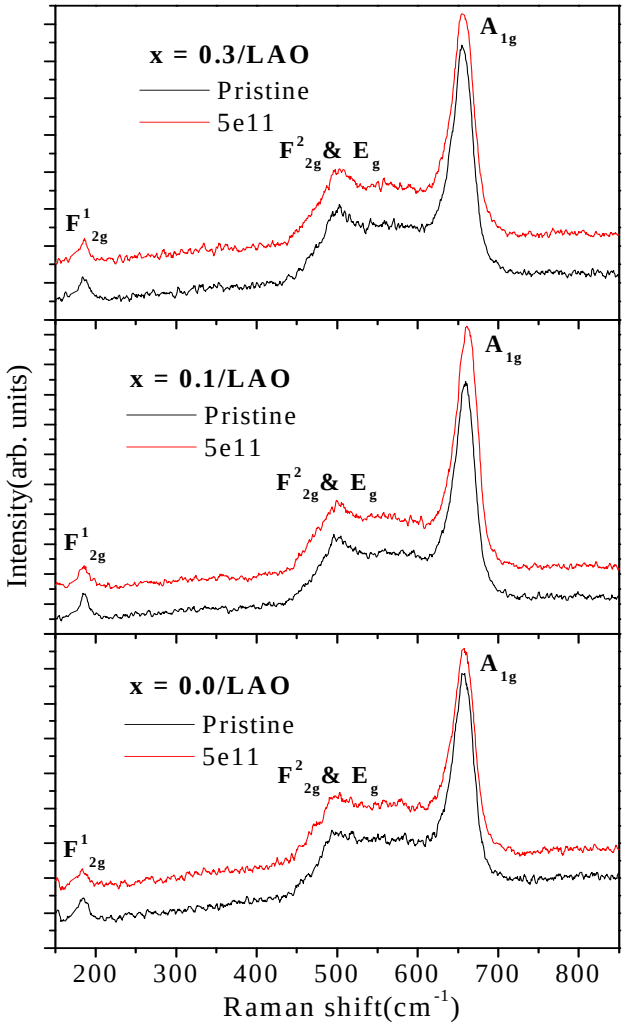

Fig. 6.7. *Raman Spectra for the films of $Bi_xCo_{2-x}MnO_4$ (x = 0.0, 0.1 and 0.3) on LAO substrates.*

In Fig. 6.7 Raman spectra of thin films grown on LAO (x= 0.0, 0.1 & 0.3) are shown. For all films the characteristic modes were found shifted towards higher

wave number with irradiation (Table 6.5). This hardening is indicative of slight contraction of unit cell and strain induced on the film lattice by the SHI irradiation, which is in conformity with the results discussed in the XRD analysis. Weak, but noticeable profile broadening of modes implies the increased anharmonicity due to structural distortion [24]; in the form of induction of defects and amorphisation with irradiation for the $Bi_xCo_{2-x}MnO_4$ films. In general, the Raman spectra with a flat background is indicative of only phonon structure present in the system, but the increased background at higher wave numbers has been observed in large number of reports on superconductors [25] due to increased electronic scattering. Here, for both the pristine and irradiated $Bi_xCo_{2-x}MnO_4$ films, considerable increase in background at higher wave numbers were observed, which indicates that multiferroic property of this film material, which is strongly dependent on electron-phonon coupling, are not affected by the irradiation.

Table 6.5. *Raman modes (in cm^{-1}) for $Bi_xCo_{2-x}MnO_4$ thin films.*

on quartz						
Bi-content	x = 0.0		x = 0.1		x = 0.3	
Raman mode → Ion fluence (cm^{-2})	A_{1g}	F^1_{2g}	A_{1g}	F^1_{2g}	A_{1g}	F^1_{2g}
Pristine	651.25	183.91	654.84	184.65	652.61	184.49
5×10^{11}	652.42	184.20	657.13	185.00	654.23	184.67
on LAO						
Bi-content	x = 0.0		x = 0.1		x = 0.3	
Raman mode → Ion fluence (cm^{-2})	A_{1g}	F^1_{2g}	A_{1g}	F^1_{2g}	A_{1g}	F^1_{2g}
Pristine	656.50	184.25	658.22	187.87	655.46	185.37
5×10^{11}	656.64	183.37	660.80	185.11	656.07	185.75
on YBCO/LAO						
Bi-content	x = 0.0		x = 0.1		x = 0.3	
Raman mode → Ion fluence (cm^{-2})	A_{1g}	F^1_{2g}	A_{1g}	F^1_{2g}	A_{1g}	F^1_{2g}
Pristine	654.29	185.52	651.08	185.13	656.66	187.78
5×10^{11}	655.21	183.83	659.35	186.43	658.92	189.91

6.2.3 Ferroelectric studies

The ferroelectric (FE) nature of the pristine and irradiated thin films of $Bi_xCo_{2-x}MnO_4$ (x = 0.0, 0.1 and 0.3) deposited on YBCO/LAO substrates were investigated through dielectric measurements, as described in chapter 5. The dielectric constant ε′ and dielectric loss tangent, tan δ measured at room temperature as a function of frequency for as deposited and irradiated films, are shown in the Fig.6.8 and Fig.6.9 respectively.

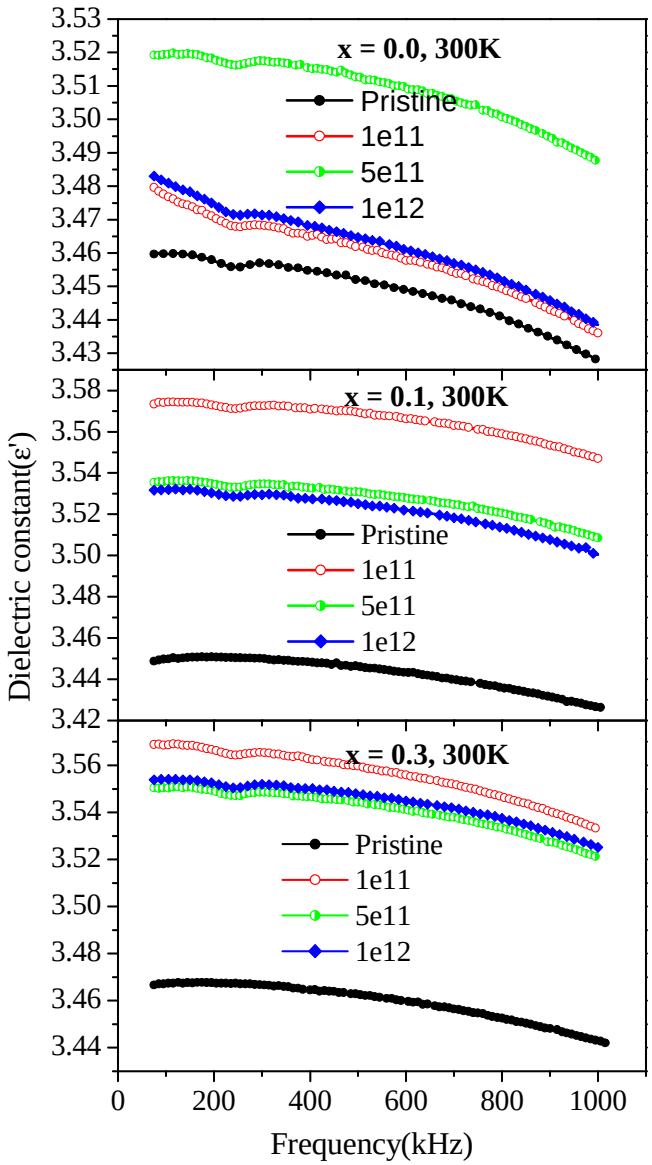

Fig. 6.8. *ε′ vs. frequency for $Bi_xCo_{2-x}MnO_4$ (x = 0.0, 0.1 and 0.3).*

It is observed that both pristine and irradiated films exhibit the frequency dispersion of ε′ and is found to enhance with irradiation along with slight reduction in dielectric loss. The frequency dispersion of dielectric properties at room temperature reveals the distribution of relaxation times associated with the oppositely charged Bi and oxygen vacancies, as described in chapter 5.

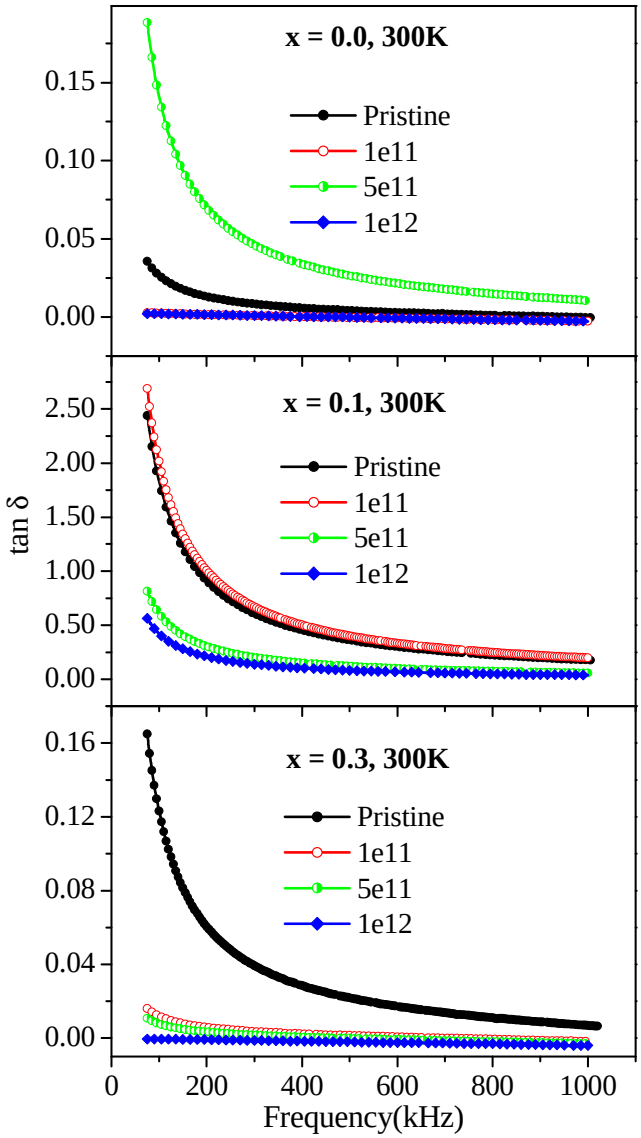

Fig. 6.9: *Loss factor (tanδ) vs. frequency at room temperature.*

The improvement in dielectric properties on irradiation especially in the case Bi substituted films may be attributed to the generation of defects in the form of

increased cation-anion (Bi^{+}-O) vacancies at the octahedral sites. The reduction in the size of unit cell as confirmed by XRD and Raman spectroscopy studies also supports that there will be a fall in dielectric loss and consequent increase in dielectric constant due to the compactness achieved in the lattice.

Dielectric constant (ε′) for the pristine and irradiated $Bi_xCo_{2-x}MnO_4$ (x = 0.0, 0.1, and 0.3) thin films measured as a function of temperature are shown in Fig.6.10. Both the pristine and irradiated films demonstrated two ferroelectric transition peaks, one at lower temperature (~ 200 K) and the other at high temperature (~ 400 K).

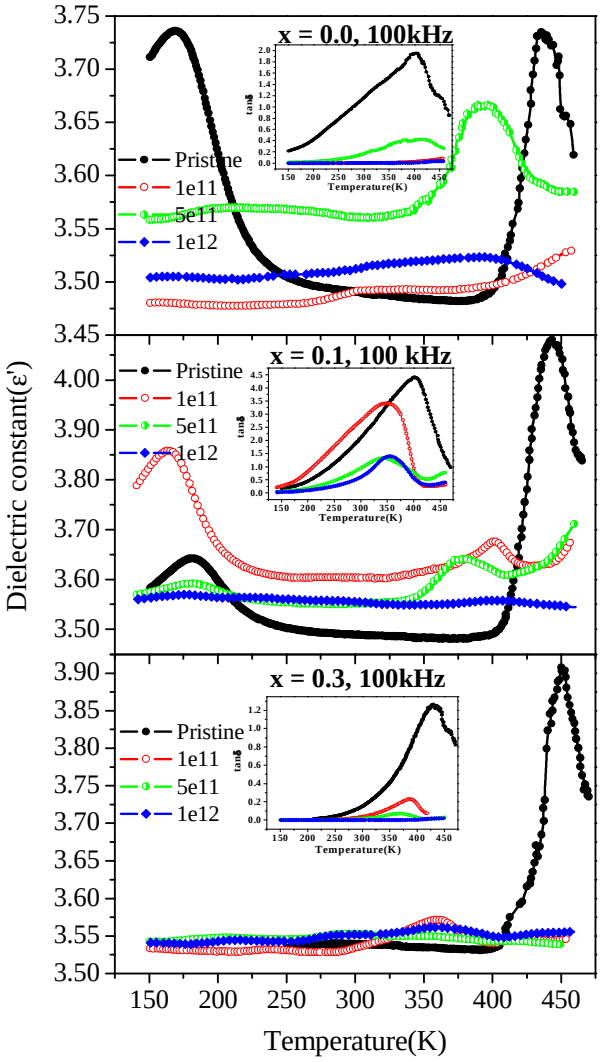

Fig. 6.10. *ε′ vs. temperature for pristine and irradiated $Bi_xCo_{2-x}MnO_4$ (x = 0.0, 0.1, and 0.3)* thin films and *Inset:* tan δ *vs. temperature for the same samples.*

For the wider part of the temperature range of measurement (200 – 400 K), ε′ is found lesser in pristine film compared to the irradiated films. Also the difference in temperature corresponding to the two transition peaks is found to shrink with irradiation. The shrinkage of the range of temperature between the ferroelectric transitions is because of the partial amorphisation of the film material with irradiation. Temperature dependent variation of tan δ also showed peak like structure, but with decreasing trend on irradiation (Insets of Fig.6.10). Charges trapped by the radiation-induced defects also can influence the FE nature, as it can control the ferroelectric domains and the consequent polarization. Both the higher temperature and higher ion fluence appear to destroy the ferroelectric nature of these films. At lower ion-irradiation fluences annealing of the pre-existing defects are dominant, while the higher fluences resulting in more amorphisation in the films. For this film material, thus fluence up to 5×10^{11} ions/cm^2 is the limit regarding FE property.

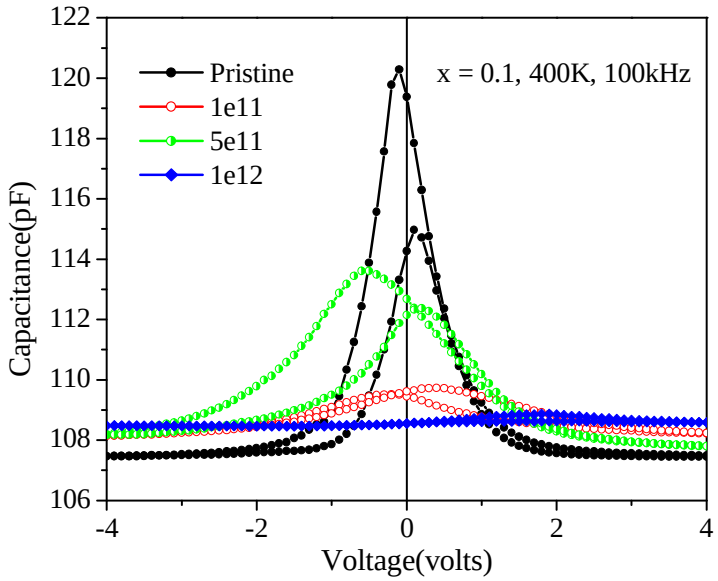

Fig. 6.11. *C-V plot of the $Bi_xCo_{2-x}MnO_4$ film (x = 0.1) at 400K and 100 kHz.*

The Capacitance-Voltage (C-V) characteristic curves (before and after irradiation) for the $Bi_xCo_{2-x}MnO_4$ thin films (x = 0.1) are shown in Fig.6.11. For both the pristine and irradiated films (up to 5×10^{11} ion/cm^2), characteristic butterfly shaped loop with two maxima corresponding to the forward and backward switching

voltages is observed supporting the ferroelectric behaviour. The irradiation has increased the gap between switching voltages from 0.2 volts for pristine to 0.5 volts for film irradiated with 5×10^{11} ions/cm^2. Further increase in the fluence seems to distort the C-V loop indicating the weakening of ferroelectric behaviour, owing to the increased amorphisation. The variation in the switching voltages and capacitance demonstrated in C-V loops can be attributed to the creation of cation-anion vacancies and charges trapped in the film material during irradiation, which alters the local field and there by affecting the switching characteristic as a function of applied voltage [11]. The asymmetric C-V loop (different values of capacitance on the two sides of C-V curve) is due to the difference in electrode materials. The two surfaces of the films have two different electrodes, silver on the top and YBCO at the bottom. Any how this asymmetric nature in C-V curve is found to subside with irradiation at higher fluence indicating that electrodes are also affected.

6.2.4 Magnetization studies

DC magnetization studies were carried out for the films deposited on LAO substrates, using the VSM option of PPMS set up. To study the effect of 200 MeV Ag^{15+} ion irradiations on the magnetic behavior of these thin film samples, magnetization (M) versus temperature (T) measurements were performed in the temperature range from 5 to 300 K in the presence of an external magnetic field of 0.1 Tesla in the zero-field-cooled (ZFC) and field-cooled (FC) modes (Fig. 6.12).

The ferrimagnetic behaviour of these spinel films with AB_2O_4 structure is influenced by the Bi-substitution induced competition among intrasite A-O-A (J_{AA}), B-O-B (J_{BB}) and intersite A-O-B (J_{AB}) superexchange interactions and consequent magnetic frustration, as explained in chapter 4 and chapter 5. Canting of spins arising from the Bi-induced distortion of the lattice, also contribute to the ferrimagnetic behaviour. Ferrimagnetic transition temperature (T_C) appears insensitive to irradiation, which reveals that irradiation could not induce cationic redistribution or further frustration in the magnetic ordering. Irreversibility between ZFC and FC magnetization curves is observed close to T_C for both pristine and irradiated films.

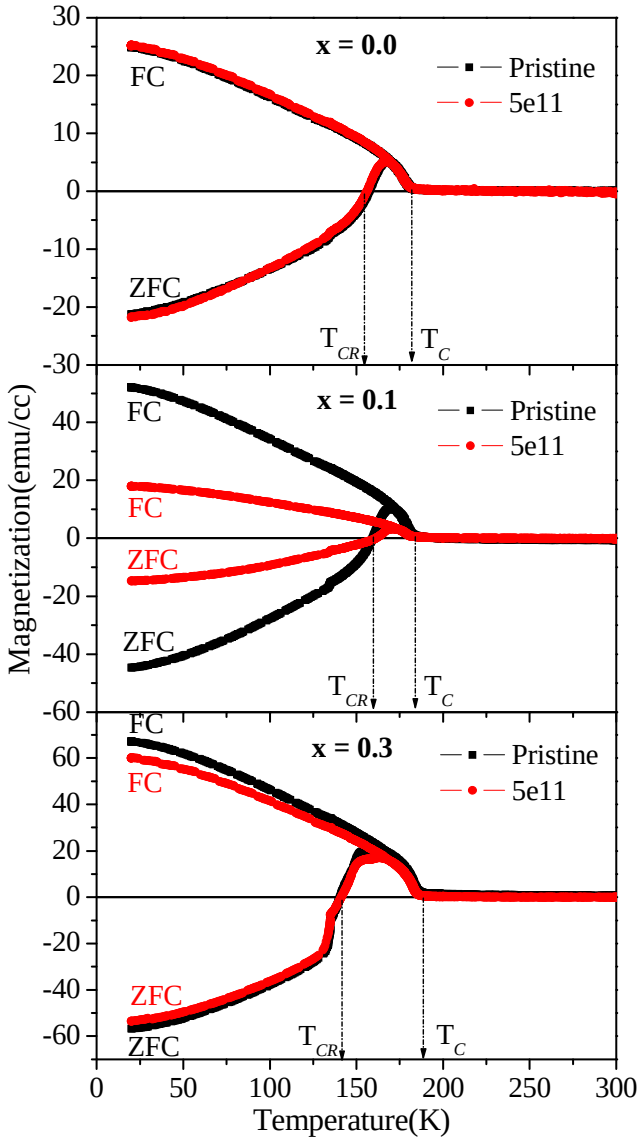

Fig. 6.12. *Magnetization vs. Temperature for $Bi_xCo_{2-x}MnO_4$ (x = 0.0, 0.1 and 0.3) films.*

The unusual behaviour of ZFC magnetization undergoing a crossover from positive to negative values is exhibited by irradiated films also, the details of which is explained in chapter 5. The crossover temperature, T_{CR}, is found unaffected by the irradiation, which further confirm that the origin of magnetism in this material is more or less stable against irradiation.

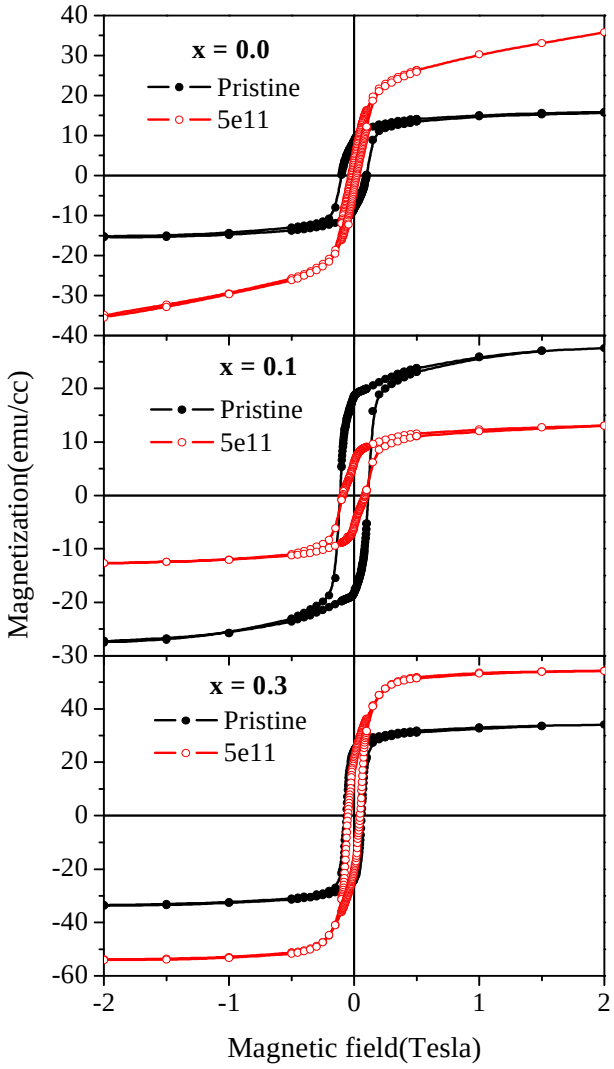

Fig. 6.13. *M-H loops for the pristine and irradiated $Bi_xCo_{2-x}MnO_4$ (x = 0.0, 0.1 and 0.3) films with at 150 K.*

Fig. 6.13 shows the isothermal dc magnetization hysteresis curves for unirradiated and 200MeV Ag ion irradiated $Bi_xCo_{2-x}MnO_4$ thin films grown on LAO substrates. Thin films show increase in the saturation magnetization (M_s) value with irradiation at a chosen fluence of 5×10^{11} ions/cm^2, which is the optimal fluence concerning structural and ferroelectric properties. These results clearly indicate that the ion irradiation plays a major role to texture the $Bi_xCo_{2-x}MnO_4$ thin films, which is complementing with the results of XRD and Raman spectra. However for the film with x = 0.1, M_s is found to decrease with irradiation. This decrease in the

magnetization suggests that these films are more susceptible for irradiation induced amorphisation, which may be due to the larger size of the grains it contains, as evident in AFM images, leading to lower texturing. The decrease in M_s also reveals that the magnetic moments of the material do not completely participate in the magnetization since they get trapped in the stressed domains created due to the irradiation.

Table 6.6. *Coercive field (H_C), remnant magnetization (M_R) and saturation magnetization (M_S) of pristine and irradiated $Bi_xCo_{2-x}MnO_4$ thin films.*

Bi-content	M_S(emu/cc)		M_R(emu/cc)		H_C(Oersted)	
	Pristine	5×10^{11} ions/cm^2	Pristine	5×10^{11} ions/cm^2	Pristine	5×10^{11} ions/cm^2
x = 0.0	15.5	35.9	8.7	3.5	1000	748
x = 0.1	27.5	13.5	18.6	6.2	1116	894
x = 0.3	34.4	54.1	24.4	21.7	597	497

It is obvious from the table that the M_S of Bi-substituted thin film exceeds the M_S of pure Co_2MnO_4 after irradiation. This supports that the Bi-substitution helps the system to retain its magnetization even at higher fluences of the ion beam. The decrease in the saturation magnetization in the case of the film with low Bi-substitution can also be due to the loss of oxygen content from the stoichiometric system. It is also possible that the deficiency of oxygen content will affect the interatomic distances and oxidation number of Co/Mn ions which reduces the magnetization [15, 26]. It is observed that coercivity values, H_C decreases for all the films after the irradiation at 5×10^{11} ions/cm^2 (see Table 6.6), which is attributed to the annealing of the pre-existing defects trapped in, during the growth of the pristine films in the form of grain boundary and point defects, which act as the pinning sites for domain walls [10]. The higher value of remnant magnetization, M_R retained in the Bi-substituted samples even after the optimally selected irradiation rate 5×10^{11} ions/cm^2, once again vindicates the profound effect of Bi in controlling the magnetization of this multiferroic material, which enhances the ferroelectric property too.

6.2.5 X-ray magnetic circular dichroism (XMCD) studies

The 200 MeV Ag^{15+} ion irradiated $Bi_xCo_{2-x}MnO_4$ ($0 \leq x \leq 0.3$) films exhibited a magnetic behaviour identical to that of the pristine films and confirms that ion configuration is not disturbed by irradiation. This has been substantiated by the near edge X-ray absorption fine structure (NEXAFS) and XMCD measurements of the films, as depicted in Fig. 6.14 and 6.15, which show the normalized XMCD spectra at Co $L_{3,2}$ and Mn $L_{3,2}$edges of the $Bi_xCo_{2-x}MnO_4$ thin film with x = 0.0 and 0.3, collected at 150 K. Upper panel in both the Figures 6.14(a) & 6.14(b) correspond to NEXAFS spectra of Co $L_{3,2}$ edge for left and right circularly polarized X-rays, for pristine and irradiated films with x = 0.0, whereas lower panel is XMCD signal. Similarly figures 6.14(c) & 6.14(d) correspond to NEXAFS spectra of Mn $L_{3,2}$ edge for left and right circularly polarized X-rays, for pristine and irradiated films with x = 0.0, and lower panel is XMCD signal. In the same way figures 6.15(a), (b), (c) and (d) represent the NEXAFS and XMCD signals of pristine and irradiated films with x = 0.3. From the figures 6.14(a) & (b) and 6.15(a) & (b), it is clear that Co $L_{3,2}$ spectrum is split into two broad multiplets, namely, the L_3 ($2p_{3/2}$) and L_2 ($2p_{1/2}$) ~ 15 eV apart, owing to the spin orbit interaction of Co core 2*p* states, as explained in chapter 5. Each of these two regions further splits due to crystal field effect of neighboring ions and correspond to t_{2g} and e_g subbands. Also, the spectral features of Co^{2+} (in tetrahedral symmetry) and Co^{3+} (in octahedral symmetry) valence states are retained after irradiation. Likewise Mn 2*p* core states also split the spectrum into two broad multiplets, namely, the L_3 ($2p_{3/2}$) and L_2 ($2p_{1/2}$) ~ 11 eV, apart, as evident in figures 6.14(c) & (d) and 6.15(c) & (d). For the pristine films, the inflection points of the Mn L_3 edge are subsequently at higher energies and correspond to Mn^{2+} (in tetrahedral symmetry), Mn^{3+} and Mn^{4+} (both in octahedral symmetry). The same spectral features are exhibited by the irradiated films. This reveals that the mixed valance states of Mn and Co ions of the irradiated films are identical to that of the pristine.

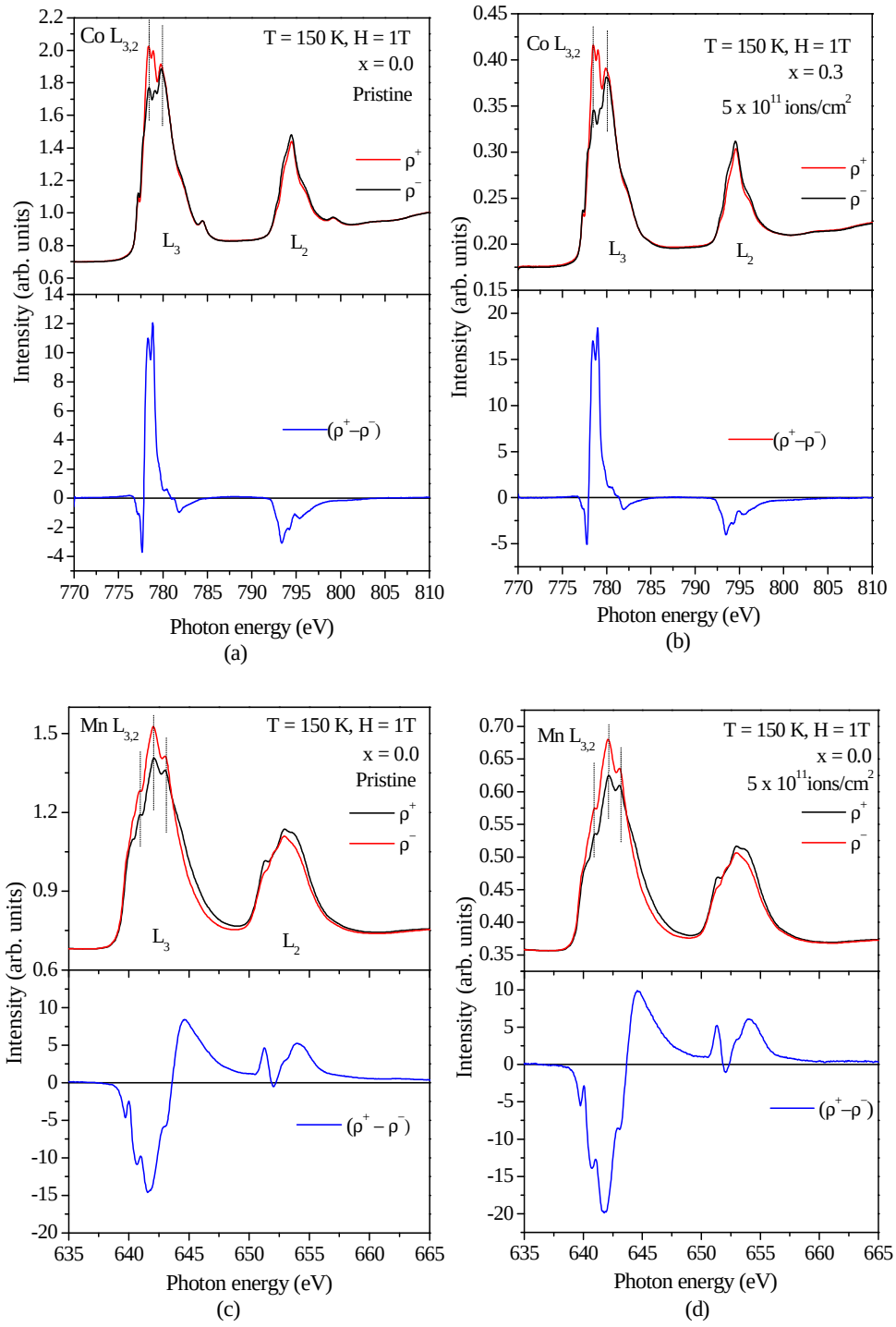

Fig. 6.14. *XAS and XMCD (ρ^+ - ρ^-) signals of (a) Co $L_{3,2}$-edge of pristine and (b) Co $L_{3,2}$-edge of Ag^{15+} ion irradiated at 5 x 10^{11} ions/cm^2 (c) Mn $L_{3,2}$-edge of pristine and (d) Mn $L_{3,2}$-edge of Ag^{15+} ion irradiated at 5 x 10^{11} ions/cm^2 of $Bi_xCo_{2-x}MnO_4$ thin film with x = 0.0 at 150 K.*

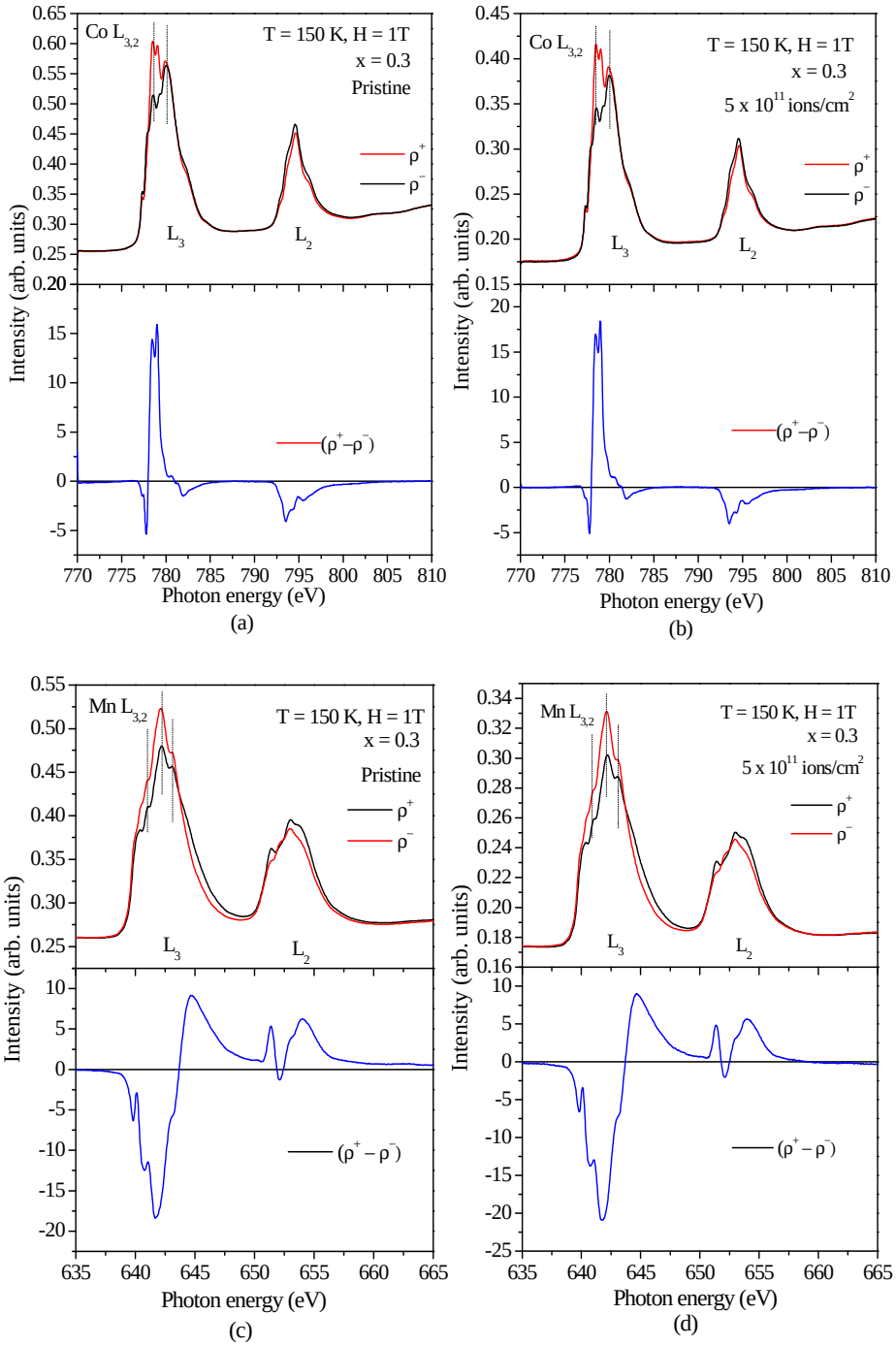

Fig. 6.15. *XAS and XMCD (ρ^+ - ρ^-) signals of (a) Co $L_{3,2}$-edge of pristine and (b) Co $L_{3,2}$-edge of Ag^{15+} ion irradiated at 5 x 10^{11} ions/cm^2 (c) Mn $L_{3,2}$-edge of pristine and (d) Mn $L_{3,2}$-edge of Ag^{15+} ion irradiated at 5 x 10^{11} ions/cm^2 of $Bi_xCo_{2-x}MnO_4$ thin film with x = 0.3 at 150 K.*

With the help of XMCD spectra, it is possible to measure the difference in the number of *d* holes, using right or left circularly polarized photons, which transfer their angular momentum to the excited photoelectron. From the figures 6.14 and 6.15 it is clear that the polarity of the Mn 2*p* XMCD is opposite to that of the Co 2*p* XMCD spectra at 150 K, for the pristine as well as irradiated films. This indicates the antiparallel alignment of the spin moments of Mn and Co ions, below ferrimagnetic transition temperature. In the XMCD spectra shown in Fig. 6.14 and 6.15, the XMCD signal of Co^{2+} at 778.5 eV is found to have spectral position of Co^{2+} observed in NEXAFS spectra of the film. Likewise, XMCD signal of Mn^{3+} at 642 eV can be identified with the Mn^{3+} spectral position in the NEXAFS spectra. The net magnetic moment exhibited by the films arises from the imbalance in the contributions of spin moments from Co ions and Mn ions which are aligned antiparallel. This is clearly depicted in XMCD spectra. Moreover, the intensity of XMCD signals corresponding to magnetic moments of both Co and Mn are found increasing with irradiation. This can be correlated with the enhancement in saturation magnetization (M_s) observed in dc magnetization hysteresis loop of SHI irradiated $Bi_xCo_{2-x}MnO_4$ films (Fig. 6.13). Thus the XMCD studies are in conformity with the magnetization measurements.

6.3 Conclusions

Polycrystalline oriented thin films of $Bi_xCo_{2-x}MnO_4$ (x = 0.0, 0.1 and 0.3) were successfully grown on amorphous quartz, crystalline LAO and YBCO/ LAO substrates by PLD. The thin films where irradiated with 200 MeV Ag^{15+} ions at the fluence values 1×10^{11}, 5×10^{11} and 1×10^{12} ions/cm^2. The results of comparative study of the as grown and irradiated $Bi_xCo_{2-x}MnO_4$ thin films leads to following conclusions:

(i) From the XRD analysis, it was observed that all the Bi_xCo_{2-x} MnO_4 films grown on amorphous quartz, crystalline LAO and YBCO/LAO substrates exhibited single phase cubic spinel structure before and after the irradiation with lower strain. This supports that there is no structural transformation. The irradiation at 5×10^{11} ions/cm^2 appears to be the optimum fluence for the better texturing in the films. For higher fluence, amorphisation dominates

over texturing. From the analysis of the AFM micrograph of the film deposited on LAO, enhancement in the RMS surface roughness has been observed along with a slight reduction in grain size, due to the irradiation induced fragmentation.

(ii) Raman scattering studies also showed that the basic crystal structure of the thin films are not affected by the irradiation except the hardening of the Raman modes taken place following the slight contraction of the unit cell and partial amorphisation. The increasing background towards the higher wave numbers of the Raman spectra, retained even after the irradiation of the Bi_xCo_{2-x} MnO_4 films on all the substrates, is suggestive of the strong electron-phonon coupling.

(iii) The ferroelectric properties are improved in the films after irradiation, for a wider part of the temperature range (up to ~ 400 K) for lower ion fluences. But both the higher temperature and higher ion fluence values appear to be detrimental for the ferroelectric nature of these films. This can be attributed to the annealing effect of ion irradiation at the lower fluences, while the higher fluences resulting in more amorphisation in the films. The observed changes in the FE property are explained in terms of the radiation induced partial amorphisation and the trapping of charges by the radiation-induced defects, which can control the ferroelectric domains and the consequent polarization. The distortion of the CV loop also indicates the weakening of FE characteristics at higher ion fluences.

(iv) From dc magnetization hysteresis loop study, it is observed that the film deposited on LAO substrates exhibited a ferrimagnetic ordering at ~ 150 K. The increase in M_s with the irradiation at optimal fluence rate 5×10^{11} ions/cm^2 is due to improved texturing and increased crystallinity of the films. The temperature dependent magnetization studies reveal that irradiation could not induce cationic redistribution or further frustration in the magnetic ordering.

The tunable ferroelectric and ferrimagnetic nature exhibited by the $Bi_xCo_{2-x}MnO_4$ thin films is supposed to assure a position in multiferroic device applications.

References

1. Ce-Wen Nan, M. I. Bichurin, S. Dong, D. Viehland, and G. Srinivasan, J. Appl. Phys. **103** (2008) 031101.

2. M. Li, M. Ning, Y. Ma, Q. Wu, and C. K. Ong, J. Phys D: Appl. Phys **40** (2007) 1603.

3. R. Ramesh and N. A. Spaldin, Nature Mater. **6** (2007) 21.

4. R. Kumar, M. W. Khan, J. P. Shrivastava, S. K. Arora, R. G. S. Sofin, R. J. Choudhary and I.V. Shvets, J. Appl. Phys. **100** (2006) 033703.

5. A. Dogra, M. Singh, V. V. Siva Kumar, N. Kumar, R. Kumar, Nucl. Instr. and Meth. B, **212** (2003) 184.

6. S. E. Donnelly and R. C. Birtcher, Proc. SPIE **3413** (1998) 174.

7. S. N. Dolia, R. Kumar, S. K. Sharma, M. P. Sharma, S. Chander, M. Singh, Curr. Appl. Phys. **8** (2008) 620.

8. R. Kumar, A. P. Singh, P. Thakur, K. H. Chae, W. K. Choi, B. Angadi, S. D. Kaushik and S. Patnaik, J. Phys. D: Appl. Phys. **41** (2008) 155002.

9. R. Prakash, R. J. Choudhary, S. Tiwari, D. M. Phase and R. Kumar, Nucl. Instr. and Meth. B **266** (2008) 1242.

10. S. Kumar, S.K. Sharma, Alimuddin, R. J. Choudhary, D. M. Phase, R. Kumar, Nucl. Instr. and Meth. B **266** (2008) 1741.

11. B. Angadi , P. Victor, V. M. Jali, M. T. Lagare, R. Kumar, S. B. Krupanidhi, Thin Solid Films **434** (2003) 40.

12. G. Szenes, Phys. Rev.B **51** (1995) 8026.

13. S. J. Zinkle, V. A. Skuratov, Nucl. Instr. and Meth. B **141** (1998) 737.

14. A. Dogra, R. Kumar, S. A. Khan, V. V. Siva Kumar, N. Kumar, M. Singh, Nucl. Instr. and Meth. B **225** (2004) 283.

15. M. C. Chantbar, K. B. Modi, G. J. Baldha, H. H. Joshi, R. V. Upadhyay, R. Kumar, NIM B **244** (2006) 124.

16. C. Houpert, F. Studer, D.Groult, M. Toulmonde, NIM B **39** (1989) 720Y723.

17. R. Kumar., S. B. Samantra, S. K. Arora, A. Gupta, D. Kanjilal. R. Pinto, A. V. Narlikar, Solid State Commun, **106(12)**, 805Y810 (1998).

18. R. Kumar, S. K. Arora, D. Kanjilal, G. K. Mehta, R. Bache, S. K. Date, S. R. Shinde, L. V. Saraf, S. B. Ogale, S. I. Patil, Radiat. Eff. Defects Solids **147**, 187 (1999).

19. N. E. Rajeevan, P. P. Pradyumnan, R. Kumar, D. K. Shukla, S. Kumar, A. K.S ingh, S. Patnaik, S. K. Arora, and I. V.Shvets, Appl. Phys.Lett **92,** 102910 (2008).

20. R. Kumar, S. K. Arora, I. V.Shvets, N. E. Rajeevan, P.P.Pradyumnan and D. K. Shukla, J. Appl. Phys. **105** (2009) 07D910.

21. N. E. Rajeevan, R. Kumar, D.K. Shukla, P. P. Pradyumnan, S. K. Arora, and I. V. Shvets, "Structural, Electrical and Magnetic Properties of Bi-substituted Co_2MnO_4" (*communicated*).

22. N. E. Rajeevan, R. Kumar, D. K. Shukla, R. J. Choudhary, P. P.Pradyumnan, A.K. Singh, S. Patnaik, S. K. Arora, and I.V. Shvets, "Magnetoelectric Studies of Bi-Substituted Co_2MnO_4 thin films" (*communicated*).

23. S. Tiwari, R. J. Choudhary, R. Prakash and D. M. Phase, J. Phys.: Condens. Matter 19 (2007) 176002

24. D. K. Shukla, R. Kumar, S. Mollah, R. J. Choudhary, P. N. Vishwakarma, V. Ganesan and V. G. Sathe, "Specific heat and Raman scattering anomalies in Ti substituted BiMn2O5 multiferroics", *(communicated).*

25. M. N. Iliev V. G. Hadjiev, S. Jandl, D. Le Boeuf, V. N. Popov, D. Bonn, R. Liang, and W. N. Hardy, Phys. Rev. B **77** (2008) 174302.

26. Y. Yamamoto, H. Tanaka, T. Kawai, Jpn. J. Appl. Phys. **40** (2000) L545.

Chapter 7

Summary and Future Scope

This chapter present the summary of the research work carried on the magnetoelectric-multiferroic properties of Bi-substituted cobalt manganite spinel oxide and future scope of the present work.

7.1 Scope of the present work

Research work presented in this thesis includes studies on structural, electrical, electronic structure, magnetic and magnetoelectric characteristics of $Bi_xCo_{2-x}MnO_4$ ($0 \leq x \leq 0.3$) spinel oxide. We have synthesized Bi-substituted Co_2MnO_4 bulk using solid state reaction technique and their thin films using Pulsed Laser Deposition (PLD) method onto amorphous quartz, crystalline $LaAlO_3$ (LAO) and $YBa_2Cu_3O_7$ (YBCO) coated LAO substrates, in view of device applications. It is well established that structural, electrical and magnetic properties of spinel oxide films are extremely sensitive to the external pressure or stress/strain that can be induced in the system through different routes like changing the ionic radii of the substituted cation, creating cation-oxygen vacancies or by swift heavy ion (SHI) irradiation. Among these different routes, SHI irradiation is considered to be a unique method for engineering the properties of a material, and is opted for the present work.

Substitution of non-magnetic Bi^{3+} having stereochemically active $6s^2$ lone pair of electrons in Co_2MnO_4 spinel oxide is found to effect the ferroelectric (FE) properties in the form of drastic change in the dielectric properties and variation of FE transition temperature through the non centrosymmetric charge ordering induced in the structure of the material. Interestingly, Bi-substitution also modified the ferrimagnetic property through the frustration in antiferromagnetic ordering of sublattices by effecting the superexchange interactions between magnetic cations. Most importantly, Bi-substituted Co_2MnO_4 samples exhibited the magnetoelectric effect owing to the electron lattice interaction arising from structural distortion.

7.2 Resume of important results and conclusions from the present thesis work

7.2.1 Bulk $Bi_xCo_{2-x}MnO_4$ ($0 \leq x \leq 0.3$) synthesized by solid state reaction

The substitution effect of Bi^{3+} ions on structural, electrical, electronic structure, magnetic and magnetoelectric properties have been studied using different techniques such as X-Ray Diffraction (XRD), Scanning Electron Microscopy

(SEM), Raman spectroscopy, Near Edge X-ray Absorption Fine Structure Spectroscopy (NEXAFS), DC conductivity, Dielectric, DC magnetization and magnetocapacitance measurements.

(i) The XRD analysis of $Bi_xCo_{2-x}MnO_4$ ($0 \leq x \leq 0.3$) indicates that all samples exhibit a single phase nature. All the samples are indexed in cubic spinel structure and lattice parameter '*a*' is found to increase with Bi content. Analysis of XRD data and SEM micrographs shows that Bi content $x > 0.3$ is difficult to accommodate, while retaining the cubic spinel structure.

(ii) The temperature dependent dielectric data represents a diffused ferroelectric phase transition; with an increasing ferroelectric T_c as the Bi content increases. Bi-substituted samples have moderately high dielectric constant depicting better ferroelectric characteristics along with Debye-type relaxation behavior.

(iii) The dispersion of ac conductivity has been estimated in terms of frequency exponent s, which varies with temperature and is explained using small polaron tunneling (SPT) model and correlated barrier hopping (CBH) model.

(iv) The dc conductivity analysis revealed the semiconducting nature of the spinel compounds. The hopping of charges between cations with different valence states at the octahedral sites is considered to be the origin of all the dielectric and electrical properties of the Bi-substituted Co_2MnO_4.

(v) The investigation of electronic structure of $Bi_xCo_{2-x}MnO_4$ ($0.0 \leq x \leq 0.3$) using NEXAFS spectra at O K edge and $L_{3,2}$ edge of Co/Mn revealed that increase in net magnetic moment and more ordered ferrimagnetism with Bi substitution is due to cationic redistribution. A part of Mn^{3+} ions are converted into Mn^{2+} and Mn^{4+} and redistributed to tetrahedral and octahedral sites. O K edge spectra confirm the highly polarizable behaviour of Bi $6s^2$ lone pair of electrons. Raman spectra of the samples confirm the greater occupation of substituted cations in the octahedral sites.

(vi) The dc magnetization measurements show that all the samples are ferrimagnetically ordered, with $T_c < 190$ K and saturation magnetization increases with increasing the concentration of Bi^{3+} ions due to the softening of the lattice arising from the redistribution of cations at the octahedral sites. Lowered negative molecular field is depicted by the decrease in Curie–Weiss constant, which indicates the increased AF frustration with Bi-substitution, favoring ferrimagnetism.

(vii) The magnetoelectric coupling obtained as the variation of dielectric constant in response to the applied magnetic field exhibited maxima at ferrimagnetic T_c, for the Bi-substituted samples, confirming the magnetic origin of ferroelectricity. This can be correlated to the inverse of Dsyaloshinskii-Moriya type of interaction occurring in complex magnetic structures like non collinear canted antiferromagnets arising from the geometrical frustration with Bi-substitution.

Bi substitution introduces a radical change in cationic distribution, favoring the tunable ferrimagnetism as well as the ferroelectricity. The coexistence of ferroelectric and magnetic properties proposes the candidature of Bi-substituted Co_2MnO_4 for the future magnetoelectric multiferroic applications.

7.2.2 Thin films of $Bi_xCo_{2-x}MnO_4$ ($0.0 \leq x \leq 0.3$) grown by PLD

Thin films were characterized using X-Ray Diffraction (XRD), Atomic Force Microscopy (AFM), Raman spectroscopy, Dielectric, dc Magnetization and magnetoelectric measurements. The results of the experimental investigations of thin films of $Bi_xCo_{2-x}MnO_4$ ($0.0 \leq x \leq 0.3$) grown on different substrates by PLD leads to following conclusions:

(i) XRD pattern and AFM images of thin films of $Bi_xCo_{2-x}MnO_4$, show that good quality, single phased polycrystalline films of $Bi_xCo_{2-x}MnO_4$ (x = 0.0, 0.1, & 0.3) with preferred orientation were grown on amorphous quartz, LAO and YBCO/LAO substrates. The single phase growth was confirmed from x-ray diffraction and Raman spectrum. In Raman spectra, all peaks as

observed for the respective bulk sample are not found for the thin films and the intensities of the peaks are also quite different from that of the bulk.

(ii) Dielectric data of the $Bi_xCo_{2-x}MnO_4$ films reveals the weak ferroelectric behaviour and ferroelectric-T_C increases as Bi content increases. Films are found to possess lower dielectric constant compared to that of the bulk samples and exhibited better ferroelectric nature at higher temperature, which indicates that the films are highly oriented. Similar variations of dielectric loss factor, tan δ with temperature supports that the stoichiometry of the bulk samples are retained in the films.

(iii) DC magnetization studies show that the thin films of $Bi_xCo_{2-x}MnO_4$ deposited on LAO exhibited well defined hysteresis loop at 150 K, which revealed its ferrimagnetic behaviour. Both saturation magnetization and ferrimagnetic-T_C increase as Bi-content increases in the films, owing to the Bi-induced redistribution of cations at the octahedral sites, similar to that of the bulk samples. This indicates that the thin films maintain an ion configuration of the bulk. Magnetization exhibited crossover from positive to negative values in zero field cooled magnetization vs. temperature cycle.

(iv) $Bi_xCo_{2-x}MnO_4$ films with higher Bi-content demonstrated magnetoelectric coupling, as the variation of dielectric constant in response to the applied magnetic field and exhibited maxima at ferrimagnetic-T_C, similar to bulk samples. This suggests that the effect of substrate induced strain, if any, can be ruled out for the Bi-substituted samples, confirming the magnetic origin of ferroelectricity. Magnetoelectric coupling is supposed to originate from the interplay between structural distortion and magnetic exchange interaction.

The films exhibited both the ferroelectric and ferrimagnetic properties, revealing the multiferroic characteristics along with magnetoelectric effect which strongly support the candidature of this film material for multiferroic device applications.

7.2.3 Effect of 200 MeV Ag^{15+} irradiation on $Bi_XCo_{2-x}MnO_4$ ($0.0 \leq x \leq 0.3$) thin films

The thin films were irradiated with 200 MeV Ag^{15+} ions at the fluence values 1×10^{11}, 5×10^{11} and 1×10^{12} ions/cm^2. The results of comparative study of the as grown and irradiated $Bi_xCo_{2-x}MnO_4$ thin films can be summarized as;

(i) From the XRD analysis, it was observed that all the Bi_xCo_{2-x} MnO_4 films grown on amorphous quartz, crystalline LAO and YBCO/LAO substrates exhibited single phase cubic spinel structure before and after the irradiation with lower strain. This supports that there is no structural transformation. The irradiation at 5×10^{11} ions/cm^2 appears to be the optimum fluence for the better texturing in the films. For higher fluence, amorphisation dominates over texturing. From the analysis of the AFM micrograph of the film deposited on LAO, enhancement in the RMS surface roughness has been observed along with a slight reduction in grain size, due to the irradiation induced fragmentation.

(ii) Raman scattering studies also showed that the basic crystal structure of the thin films are not affected by the irradiation except the hardening of the Raman modes taken place following the slight contraction of the unit cell and partial amorphisation. The increasing background towards the higher wave numbers of the Raman spectra, retained even after the irradiation of the Bi_xCo_{2-x} MnO_4 films on all the substrates is suggestive of the strong electron-phonon coupling.

(iii) The ferroelectric properties are improved in film after irradiation, for a wider part of the temperature range (up to ~ 400 K) for lower ion fluences. But both the higher temperature and higher ion fluence values appear to be detrimental for the ferroelectric nature of these films. This can be attributed to the annealing effect of ion irradiation at the lower fluences, while the higher fluences resulting in more amorphisation in the films. The observed changes in the FE property are explained in terms of the radiation induced partial amorphisation and the trapping of charges by the radiation-induced

defects, which can control the ferroelectric domains and the consequent polarization. The distortion of the CV loop also indicates the weakening of FE characteristics at higher ion fluences.

(iv) From dc magnetization hysteresis loop study, it is observed that the film deposited on LAO substrates exhibited a ferrimagnetic ordering at ~ 150 K and the saturation magnetization increased by the irradiation at optimal fluence rate 5×10^{11} ions/cm^2 due to improved texturing and increase in crystallinity of the film. From the magnetization (M) vs. temperature (T) curves, it is observed that ferrimagnetic transition temperature (T_C) appears insensitive to irradiation, which reveals that irradiation could not induce cationic redistribution or further frustration in the magnetic ordering.

The tunable ferroelectric and ferrimagnetic nature exhibited by the $Bi_xCo_{2-x}MnO_4$ thin films is supposed to assure a position in multiferroic device applications. Further investigations are pursued on to study the effect of SHI irradiation on the magnetoelectric properties of these multiferroic thin films.

7.3 Future Scope

From the technological point of view, synthesization of multiferroics in thin film form that can yield applications at useful temperature range is a complicated task. In this research work, such a task has been carried out. The outcome of the effort put in is encouraging in the sense that the newly synthesized system; Bi-substituted Co_2MnO_4 exhibited stable magnetoelectric properties in bulk and thin film forms. The high tuneability of the magnetically induced electric polarization and dielectric constant demonstrated by the $Bi_xCo_{2-x}MnO_4$ thin films is expected to provide a new impulse in the design and development of multifunctional devices like four-state logical memory, data storage and accessing with more degrees of freedom etc. A series of smart multiferroic devices will soon emerge as there are advanced techniques to grow high-quality films with precisely controlled composition, atomic arrangements and interfaces. In this regard choice of superior conducting substrates and optimization of oxygen partial pressures is necessitated. Further advancements in the quality and efficiency of $Bi_xCo_{2-x}MnO_4$ thin films for

improved magnetoelectric behaviour will be carried out utilizing swift heavy ion irradiation with ions having suitable energy and fluence.

Electric field versus polarization will provide more insight about the ferroelectricity in these materials. Here, due to the limitations of the ferroelectric loop set up in tracing the hysteresis of semiconducting multiferroic oxides, Capacitance-Voltage loop measurements has been carried out. To rule out the ambiguity, if any, regarding ferroelectric characteristics of Bi-substituted Co_2MnO_4, it is proposed to carry out ferroelectric loop tracing also in future. Theoretical modeling of the magnetoelectric behaviour of this complex, non magnetic Bi incorporated magnetic spinel oxide, supposed to be challenging, is also a future aim. Also, to minimize the substrate induced strain that affects the ferroelectric as well as magnetoelectric properties, growing vertical structures with nanopillar geometry is envisaged to be carried out. The advantage of the nanopillar structure over the horizontal-structured films is that former is free off substrate-imposed mechanical clamping, which is known to suppress both the ferroelectric response and the magnetoelectric coupling.

An order of magnitude increase in spin canting angle would yield magnetizations that are comparable to those in existing magnetic devices. It will be very exciting as well as more enlightening towards fundamental understanding to explore whether the spin canting angle can be increased, as the canting angle of adjacent magnetic moments is influenced by the strain, on symmetry modification through different heterstructures, on the chemistry of the non-magnetic ions and external pressure like swift heavy ion irradiation. Of course, the converse effect, tuning magnetic behaviour of newly synthesized $Bi_xCo_{2-x}MnO_4$ with an electric field, is also an enticing prospect considering the expensive generation of large magnetic fields (of several Tesla) necessary to accomplish magnetoelectric effect. The electrically controlled magnetism that can lead to the emergence of new devices within the framework of spintronics, information storage and communication; is also a ripe area for future studies.

****

Research Papers Published /Communicated:

1. "Magnetoelectric properties of $Bi_xCo_{2-x}MnO_4$ ($0 \leq x \leq 0.3$)", ***N. E. Rajeevan****, P. P. Pradyumnan, Ravi Kumar,, D. K. Shukla, S. Kumar, A. K. Singh, S. Patnaik, S. K. Arora, and I. V. Shvets,* **Appled Physics Letters 92** (2008) 102910.

2. "Structural and transport properties of Bi-substituted Co_2MnO_4", *Ravi Kumar, S. K. Arora, I. V. Shvets,,* ***N. E. Rajeevan****, P.P.Pradyumnan and D.K. Shukla,* **Journal of Applied Physics 105** (2009) 07D910.

3. "Multiferroic Properties of Bi-Substituted Co_2MnO_4", ***N. E. Rajeevan****, Ravi Kumar, Shalendra Kumar, D. K. Shukla, P. P. Pradyumnan, S. K. Arora, and I. V. Shvets,* **AIP Conf. Proc- International Conference on Magnetic Materials (ICMM-2007) 1003** (2008) 124.

4. "Structural, Electrical and Magnetic Properties of Bi-substituted Co_2MnO_4", ***N. E. Rajeevan****, Ravi Kumar, D. K. Shukla, P. P. Pradyumnan, S. K. Arora, and I. V. Shvets,* **Mater.Sci.& Engg.B** (Submitted).

5. "Magnetoelectric Studies of Bi-Substituted Co_2MnO_4 thin films" ***N.E.Rajeevan****, Ravi Kumar, D. K. Shukla, R. J. Choudhary, P. P. Pradyumnan, A. K. Singh, S. Patnaik, S. K. Arora, and I. V. Shvets* **Thin solid films** (Submitted).

6. "Bi-substitution induced magnetic moment distribution in spinel $Bi_xCo_{2-x}MnO_4$ multiferroic", ***N. E. Rajeevan****, Ravi Kumar, D. K. Shukla, P. Thakur, N. B. Brookes, K. H. Chae, W. K. Choi, S. Gautam, S. K. Arora, I. V. Shvets and P. P. Pradyumnan,* **Physical Review B** (Submitted).

7. "Effect of swift heavy ion irradiation on the multiferroic behaviour of Bi-substituted Co_2MnO_4 thin films", ***N. E. Rajeevan****, Ravi Kumar, D. K. Shukla, R. J. Choudhary, P. Thakur, N. B. Brookes, S. K. Arora, I. V. Shvets, P. P. Pradyumnan,* **Nuclear Instruments and Methods in Physics Research B** (Submitted).

Research Papers Presented /Accepted in Seminars/Conferences:

8. "Structural and thermoelectric property studies of Co_3O_4 thin films", ***N. E. Rajeevan****, K. S. Shabumon, P. P. Pradyumnan, S. R. Abhilash and D. Kanjilal,* **Kerala Science Congress 2007**, January 29-31, 2007, Kannur, Kerala.

9. "Multiferroic properties of Bi-substituted Co_2MnO_4", ***N. E. Rajeevan****, Ravi Kumar, S. K. Arora, I. V. Shvets and P.P. Pradyumnan,* **52nd DAE-Solid State Physics Symposium**, December 27-31, 2007, University of Mysore, Mysore.

10. "Synthesis and structural characterization of multiferroic $Bi_xCo_{2-x}MnO_4$(x=0.0, 0.1, 0.2 and 0.3) thin films", ***N. E. Rajeevan****, Ravi Kumar, D. K. Shukla, R. J. Choudhary and P. P. Pradyumnan,* **National Conference on Nanophotonic Materials (NCNM-2008)**, October 10-12, 2008, Cochin University of Science and Technology, Kochi-22.

11. "Structural and magnetoelectric studies of Bi-substituted Co_2MnO_4 thin films", ***N. E. Rajeevan****, Ravi Kumar, D. K. Shukla, R. J. Choudhary, S. Patnaik, V. Sathe and P. P. Pradyumnan,* **International Conference on Magnetic Materials and their Applications for 21st Century(MMA 21)**, October 21-23, NPL, New Delhi, 110 012.

12. "Swift Heavy Ion Induced Modifications in Structural and Ferroelectric Properties of Bi-substituted Co_2MnO_4 Thin Films", ***N. E. Rajeevan****, Ravi Kumar, D. K. Shukla, R. J. Choudhary and P. P. Pradyumnan,* **53rd DAE-Solid State Physics Symposium**, December 16-20, 2008, BARC, Mumbai.

13. "Effect of Bi-substitution on the magnetic properties of PLD grown Co_2MnO_4 thin films on LAO", ***N. E. Rajeevan****, Ravi Kumar, D. K. Shukla, R. J. Choudhary, S. K. Arora, I. V. Shvets and P. P. Pradyumnan,* **International Conference on Multifunctional Oxide Materials (IC MOM 2009),** April 16-18, HPU, Shimla (Accepted).

14. "X-ray absorption and magnetic circular dichroism study of the magnetic interactions in spinel $Bi_xCo_{2-x}MnO_4$ thin films", *P. Thakur, Ravi Kumar,* ***N. E. Rajeevan****, N. B. Brookes, R. J. Choudhary, and P. P. Pradyumnan,* **International Conference on Multifunctional Oxide Materials (IC MOM 2009),** April 16-18, HPU, Shimla (Accepted).